MASTER OF PHILOSOPHY

Evaluation of residual stress fields after laser shock peening treatment of aerospace components

Coratella, Stefano

Award date:
2014

Awarding institution:
Coventry University

Evaluation of Residual Stress Fields after Laser Shock Peening Treatment of Aerospace Components

By

Stefano Coratella

October 2014

Evaluation of Residual Stress Fields after Laser Shock Peening Treatment of Aerospace Components

By

Stefano Coratella

October 2014

A thesis submitted in partial fulfilment of the University's requirements for the Degree of Master of Philosophy/Master of Research

To my mum and dad, because as the pioneer of flight said:

Orville Wright

Abstract

The introduction of Residual Stresses (RS) inside structural aerospace components has been widely studied and several techniques are now used in order to retard the crack initiation and propagation process. Among these techniques, Laser Shock Peening (LSP) has been recently applied due to its higher performance in terms of the magnitude and depth of RS introduced. Since only at the end of 1990s was a laser with high repetition rate available, LSP is a very new technique that is being gradually introduced as a method that allows introducing deep RS in both aerospace and nuclear power plant applications. Nevertheless, research around LSP is still intensive due to the large number of metal alloys where this technique can be applied, on a wide range of thickness and geometries. In parallel to the studies carried out to understand the physical phenomenon of LSP and its applications in structural engineering, analyses through the Finite Element Method have been promoted and are widely used in order to predict quickly the RS field and the associated plasticity.

This research was primarily focused on two main areas of LSP research: the understanding of the distribution of the RS in aluminium alloys after LSP treatment; and the possibility to predict them in thick samples through the Eigenstrain approach. The techniques used to measure the RS were incremental hole-drilling, neutron diffraction, and X-ray diffraction.

The investigations carried out on thick samples have shown that, under particular conditions, the Eigenstrain method is able to predict the distribution of the RS in flat areas, blended curves and round edges. Similarly, promising results were obtained where the Eigenstrains were used in order to predict the RS field in a Single Edge Notch sample that was previously Laser Peened and then Shot Peened.

In parallel, a research has been carried out for thin samples subjected to LSP processing. The research involved many thin samples laser peened with different laser settings in order to better understand which laser parameters are affecting the distribution of the RS. This research included both single-face laser peening and a double-opposite-face treatment, and it has been shown that with the use of the proper laser setting it is possible to introduce a fully-compressive RS field through the thickness.

Preface

This thesis is submitted for the degree of Doctor of Philosophy at Coventry University, United Kingdom. The data reported in this dissertation were collected and elaborated during studies initially in the Department of Engineering and Innovation at The Open University, and completion at the Faculty of Engineering and Computing, Coventry University. The whole data and material presented in here were collected and elaborated during the period between October 2011 and October 2014 under the supervision of Professor Michael E. Fitzpatrick and they are not and have not been submitted for any other degree or similar qualification. Part of this research was presented in various conferences as either posters or talks, submitted for peer-reviewed journals, and published in a conference proceeding. The complete list follows:

List of Conference attendances

S. Coratella, Michael E. Fitzpatrick, "*Linear Eigenstrain Theory: calibration of a simple and complex geometry FE models*," Presented at the 3rd Laser shock Peening Conference – October 2011, Osaka, Japan

S. Coratella, Michael E. Fitzpatrick, "*Application of the Eigenstrain method to predict residual stresses at curved edges after Laser Shock Peening*," presented at the International Conference of Residual Stresses 9 - October 2012, Garmisch-Parterkirchen , Germany

S. Coratella, Michael E. Fitzpatrick, "*Evaluation of Residual Stress with Eigenstrain method prediction after Laser Shock Peening treatment*," Presented at the 4th Laser Shock Peening Conference – May 2013, Madrid, Spain

S. Coratella, Michael E. Fitzpatrick, "*Evaluation of Residual Stress with Eigenstrain method prediction after Laser Shock Peening and Shock Peening treatment,.*" presented at MECA SENS 7 – September 2013, Sydney, Australia

S. Coratella, Michael E. Fitzpatrick, "Distribution of Residual Stresses in Double Peened Thin Aluminium Plates," poster at the 11th International Fatigue Congress – March 2014, Melbourne, Australia

S. Coratella, Michael E. Fitzpatrick, "*Evaluation of Residual Stresses in Double Peened Thin Samples with Hole-Drilling and X-Rays Technique,*" presented at the 9th European Conference of Residual Stress - July 2014, Troyes, France

Airbus PhD days

S. Coratella, Michael E. Fitzpatrick, Jim Moffatt, *"Applying the Eigenstrain Theory to Predict Residual Stress in Laser Shock Peened Samples,"* – October 2012, Madrid, Spain

S. Coratella, Michael E. Fitzpatrick, Jim Moffatt, *"The Challenge of Measuring and Predicting Residual Stresses after Laser Shock Peening Treatment"* - October 2013, Bremen, Germany

Publication

Coratella, S., Burak Toparli, M., & Fitzpatrick, M. E. (2014). Application of the Eigenstrain Theory to Predict Residual Stress around Curved Edges after Laser Shock Peening. In Materials Science Forum (Vol. 768–769, pp. 185–192).

S. Coratella, M. Sticchi, M.B. Toparli, M. E. Fitzpatrick, N. Kashaev, "*Application of the Eigenstrain approach to predict the residual stress distribution in laser shock peened AA7050-T7451 samples,"* submitted at Surface & Coatings Technology, under peer review.

Acknowledgments

When I started this PhD programme I'd been told I would have spent the most tough period of my study career: they were all wrong. I honestly spent one of the most enthusiastic and rewarding period of my whole life. This would have not been possible without the constant presence of several people who have been directly or indirectly part of this project.

The first huge thanks goes to my supervisor Prof. Michael E. Fitzpatrick, he has been the coolest supervisor I could have asked for. His constant presence, positive attitude to my job and constructive feed-backs gave me the possibility to never feel under pressure. But most importantly, no matter what I asked for during my PhD, he has always told me "yes, do it!": that was the attitude I was looking for in a supervisor.

The second person who I want to mention and acknowledge is Dr. Domenico Furfari from Airbus Deutschland. Not only he introduced me for the first time to the engineering research world but he constantly pushed me during my PhD to improve my research and my results. I also would like to acknowledge Elke Hombergsmeier and Ulrike Heckenberger from Airbus IW for their constant support in terms of samples and feed-backs. Similarly, during my research I had the pleasure to meet and talk with Prof. Yuji Sano, Toshiba, Japan and Prof. José Luis Ocaña from Universidad Politécnica de Madrid, Spain, who shared with me their precious comments and ideas about my results and they supply samples during my PhD.

At different levels and in different occasions, I had the chance to talk with several people involved in the Laser Shock Peening technology like Prof. Mike Hill from UC Davis, USA, Dr. Kristina Langer and Dr. Thomas J. Spradlin from AFRL, USA, Prof. Claudia Polese from University of Witwatersrand, South Africa, my friend and PhD student Marianna

Sticchi and her supervisor Prof. Nikolai Kashaev at Helmholtz-Zentrum Geesthacht, Germany, my friend and PhD student Sara Taddia and her supervisor Prof. Enrico Troiani from University of Bologna, Italy.

During the time I spent at The Open University, many colleagues were sharing the everyday-life with me. First of all, a big thank goes to Dr. M. Burak Toparli for his constant presence and invaluable patience in teaching me the basics of the residual stress techniques. Life in the office could not have been any better without having J. RodoLSPho Leo, Jefferson Oliveira, Dr. Yéli Traoré, Gerardo Carvajal, Dr. Sanjooram Paddea, Dr. Abdul Khadar Syed, Dr. Suraya Zabeen and Dr. Niall Smith as colleagues: with them there were more funny moments than serious ones. And also: Prof. Mike Hutchings and Dr. Foroogh Hosseinzadeh for their precious critics during my mini-Viva, Stan Hiller and Gordon Imlach for their technical support and heLSP, Paul Courtnage and Angie Swain for their fast resolutions to any problem I had during my life at the campus.

During my trips for tests I met several researchers which I would like to thank for their constant support before, during and after the experiments: Dr. Peter Staron, PETRA III, Germany, Dr. Steven Van Petegem, PSI, Switzerland, Dr. Michael Hoffman, FRM II, Germany, Dr. Michael Ghargouri, Chalk River Nuclear Laboratory, Canada, Dr. Jun-Sun Park, Advanced Photon Source, USA, Dr. Thilo Pirling, ILL, France , Dr. Thomas Connolley and Dr. Robert Atwood, Diamond Light Source, UK.

Life outside the campus wouldn't have been that funny without other crazy-like-me Italians. First, I'd like to thank both Alessandra and Barbara and my friend Marianna from Italy for their constant presence during the whole PhD period and their invaluable friendships. Secondly, but not less important, Camilla and Mauro, Alessandro, Ilaria, Marco, Daniele, Annalisa, Giuseppe: when I spent time with them even English food tasted much better. Among the non-Italian friends: Hannah, Rob H., Maxine, Talib, Lana, Ryan,

Rob P., Roshni, Carlos, Miriam, Lucas, Dasha, Angela and Brandon, Lisa and Mohammed: world looks smaller with you all around.

Last but not the least, my family, to whom I dedicate this thesis, not only for their constant support and love but to have showed me that their happiness is my happiness.

15th October 2014,

Stefano Coratella

London, UK

Table of Contents

List of Figures

List of Tables

Abbreviations in alphabetical order

AA = aluminium alloy

ANL = Argonne National Laboratory

APS = Argonne Photon Source

CCD = Charge-Coupled Device

DLS = Diamond Light Source

EDDI = Energy Dispersive DIffraction

EDM = Electro Discharge Machining

FEA = Finite Element Analysis

FEM = Finite Element Modelling

HEL = Hugoniot Elastic Limit

ILL = Institut Laue-Langevin

JEEP = Joint Engineering, Environmental, and Processing

LPwC = Laser Peening without Coating

LSP = Laser Shock Peening

MIC = Metal Improvement Company

POLDI = Pulse-Overlap DIffractometer

PS = Pseudo Strains

RS = Residual stress

SCC = Stress Corrosion Cracking

SENT = Single Edge Notch Tension

SP = Shot Peening

SR = Synchrotron Radiation

TOF = time of flight

YAG = Yttrium Aluminium Garnet

Glossary of terms

σ (sigma) = components on the Cauchy's tensor (or stress tensor) for the normal stress

τ (tau) = components of the Cauchy's tensor (or stress tensor) for the shear stress

ε (epsilon) = components of the strain tensor for the normal strain . The same letter is used for the Eigenstrain

γ (gamma) = components of the strain tensor for the shear strain

ν (ni) = Poisson ration

E = Young's modulus

G = Shear modulus

1 Introduction

One of the most important aspects of the design of a new airplane is the structural engineering. The most important challenge of this discipline is to keep the weight of the structure the lowest possible without compromising its strength. Usually, the structural components of an airframe are designed in order to be resistant to static loads, impact loads, corrosion and cracking. Since aviation was born in 1903, structures were designed in order to be resistant to maximum load. By increasing the performance of airplanes in terms of speed and loads, a second element appeared as important as the maximum load: the total amount of cracks inside the airframes and their evolution during the life of the airplane. Cracks are small defects present in any aircraft structures and, since close to cracks the ultimate load of the material can be reached, crack can easily grow until it compromises the structural integrity. The fact that fatigue was not taken into consideration during the first 30-40 years of aviation, led to several accidents like the Comet, in civil aviation, and the loss of the prototype of the F-111 after only 100 flight hours.

Fig. 1.1 Cracks position and their growth in the Comet [1]

The Comet demonstrated how important was design against fatigue. Three different philosophies are nowadays used to design the airframes: safe life, fail safe and damage tolerance. Safe Life philosophy has been applied since the aviation was born and it consists of changing any mechanical components that have reached their total predicted life, without checking if this component could still work for some more flight hours and it is usually applied to all the hidden components where cracks cannot be detected. Fail Safe philosophy is usually applied for extremely sensitive components, and it consists of designing a structure which will have still enough structural strength even after a local failure. Damage Tolerance is a philosophy that assumes the airplanes has many cracks and the studies are focused on how this crack can propagate and when their length can compromise the structural integrity.

Since the fatigue life of an airplane is linked with the distribution of the stresses inside a particular component due to the external loads, one of the methods that can improve the fatigue life is the introduction of a pre-stress field or, more simply, a residual stress field. Several techniques are available nowadays to introduce a residual stress field around holes and in thick and thin components. One of the recently-developed technologies to introduce residual stresses which has been demonstrating its versatility and superior performance is Laser Shock Peening (LSP). LSP was patented in 1983 after several studies based on the interaction between a laser and a metallic material but only lately, due to the availability of lasers with high repetition rates, this technique has been used to prevent crack growth in military airframes and nuclear power plants. The studies of this technology have involved several companies and universities all around the world and the interest led to the first Laser Shock Peening Conference in Houston in December 2008.

1.1 Scope of this research

This research was possible thanks to Airbus Deutschland GmbH who sponsored the entire project as well as Airbus Innovation Work (previously EADS IW) who supplied the samples for the research. Others sample suppliers were the Universidad Politécnica de Madrid, and Toshiba. The 3-year project was focused on two different aspects of the LSP: measurements of the residual stress fields after the treatment and the prediction of the residual stress field using the Eigenstrain approach. Two typical aluminium alloys for aerospace components were used: AA2024-T351 and AA7050-T7451. In particular, two different samples made of AA7050 were subjected to residual stress measurements and the possibility to predict them by the Eigenstrain approach was explored. The samples made of AA2024 were 2 mm thin sample, typical sections which reproduce the fuselage and wing skin. With these samples, the possibility of applying LSP on thin samples with a single-face treatment or double-face treatment was explored and the RS field measured.

The thesis contains 8 chapters and their contents are here listed:

In chapter 2 some basics of the stress theory are given as well as a description of RS techniques which are considered competitors of the LSP;

In chapter 3 a brief introduction to the sample used is reported with the material characterizations where available;

In chapter 4 the RS measurement techniques are presented and for each of them the details of the experiments carried out during the research project are reported;

In chapter 5 the Eigenstrain theory is described and the Finite Element analysis approach is reported in order to understand the theory limitations;

In chapter 6 the stepped coupon studies are reported. In particular all the results of the RS measurements are reported as well as the comparison with the Eigenstrain approach;

In chapter 7 the Single Edge Notch preliminary studies are reported and the possibility to predict the RS field with the Eigenstrain approach in a sample that was both Laser Shock Peened and Shot Peened;

In chapter 8 the thin single-face peened samples are presented and all the RS measurements are reported. The results were compared in order to get the best laser peening treatment in this type of sample;

In chapter 9 the thin double- peened samples are presented. The reported results show the distribution of the RS in this peening approach measured mainly with the hole-drilling technique but some results were available also with the X-ray diffraction method. An entire 3D map of the residual stress is presented too and it is considered to be one of the first RS most detailed 3D maps in thin samples ever published.

References

[1] R. J. H. Wanhill, "Milestone Case Histories in Aircraft Structural Integrity," *National Aerospace Laboratory. NLR-TP-2002-521*, 2002. [Online]. Available: http://www.scribd.com/doc/36516087/Milestone-Case-Histories-in-Aircraft-Structural-Integrity. [Accessed: 12-Sep-2014].

2 Literature Review

Continuum mechanics is a branch of classic mechanics that studies the mechanical and kinematic behaviour of continuum bodies: all bodies which have a mass large enough to not be affected by their internal atomic structure. In more details, solid mechanics is a branch of continuum mechanics that studies the stress state deformation within a continuum body. If we consider for simplicity a body made of a metal alloy at room temperature subject to an external load, we can easily recognize two different behaviours of this component: elastic behaviour and the plastic behaviour. Elastic deformation occurs when a body is subjected to external loads and it is reversible as soon as these external loads are not applied anymore on the body. Plastic deformation is a persistent deformation that remains even when the external loads are no longer applied on the body. The stress value that connects these two behaviours is called the yield strength. In aerospace structural engineering, the yield stress is considered the upper stress limit which the airplane must not reach for its entire life. If this happens, the airplane will be grounded for checks to assure the safety of the payload is not compromised.

2.1 Continuum Mechanics

2.1.1 Stress

According to continuum mechanics, the internal stress in a component is a physical measure of the contact forces exerted between the internal parts of a continuous three-dimensional body through its surface [1]. The stress can be either generated by an external load or introduced through an external treatment: in the latter case the stresses are called Residual Stresses (RS).

Taking into account the most general continuous three-dimensional body, the stress state can be defined by considering an infinitesimal cube or unit cell. The stress-state generated by the external applied forces can be discretised into components shown in the following picture:

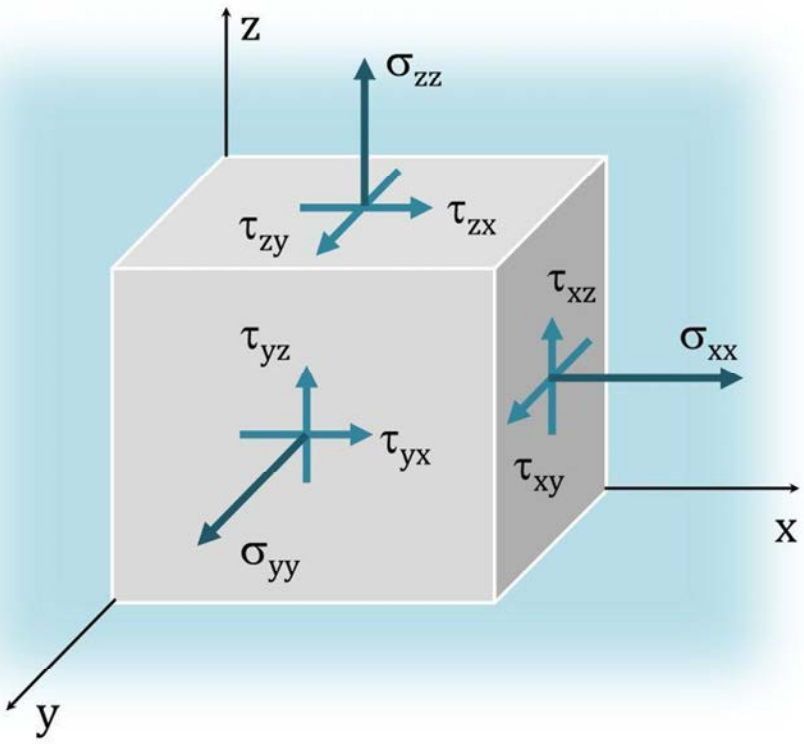

Fig. 2.1 Schematic view of the stress field

Referring to Fig. 2.1, all the components perpendicular to the cube faces are called normal stresses (σ-sigma) while all the components tangential to the cube face are called shear stresses (τ-tau). The subscript in the normal stress indicates the direction of the stress component in the considered coordinate system while in the shear stress the subscript is composed of two letters: the first indicates the direction perpendicular to the plane where the components lies while the second indicates the direction of action of the stress component. It is possible to demonstrate that a generic force vector in a generic point of the body can be seen as a superposition of both normal and shear stress. With the

stress tensor (or Cauchy tensor) it is possible to completely define the stress state within a body:

$$\begin{bmatrix} \sigma_{xx} & \tau_{xy} & \tau_{xz} \\ \tau_{yx} & \sigma_{yy} & \tau_{yz} \\ \tau_{zx} & \tau_{zy} & \sigma_{zz} \end{bmatrix}$$

Equation 2.1

In order to maintain the static equilibrium, both the vector summation of the total forces and the summation of the moments of these forces applied to the body have to be zero and this leads to:

$$\tau_{ij} = \tau_{ji}$$

Equation 2.2

where ij are used to indicate a generic direction of the stress.

Therefore only 6 components out of 9 are left in the Cauchy tensor, i.e. it becomes symmetric. To further decrease the number of elements in the Cauchy tensor, it is possible to use a particular coordinate system which, from an algebraic point of view, transforms the 6 element tensor to a diagonal tensor. From a mechanical points of view, in this particular coordinate system the shear stresses are zero and the remaining normal components are called the Principal Stresses.

$$\begin{bmatrix} \sigma_1 & 0 & 0 \\ 0 & \sigma_2 & 0 \\ 0 & 0 & \sigma_3 \end{bmatrix}$$

Equation 2.3

2.1.2 Strain

In continuum mechanics when an external force acts over a surface of a body, the body starts to deform until the total internal stresses balance the external applied force. In

mechanics it is generally preferred to use the strain rather than the deformation. The true strain is a normalized measure of the deformation relative to a reference length. It is generally expressed as :

$$\boldsymbol{\varepsilon = \frac{l_f - l_i}{l_i} = \frac{\Delta l}{l_i}}$$

Equation 2.4

where l_f is the final length of the component while l_i is its initial length.

Similarly to the stress, that can be divided into the normal and shear components, the same operation can be done with the strains. Considering for simplicity a bar subjected to an external force acting in tension in the bar axis direction, for what has been said the bar will deform elastically in the direction of the load. This is the normal strain. However, the deformation will not only occur in the direction of the load but it will occur also in the direction perpendicular to it. This phenomenon was named the Poisson effect and it can be seen in the following picture:

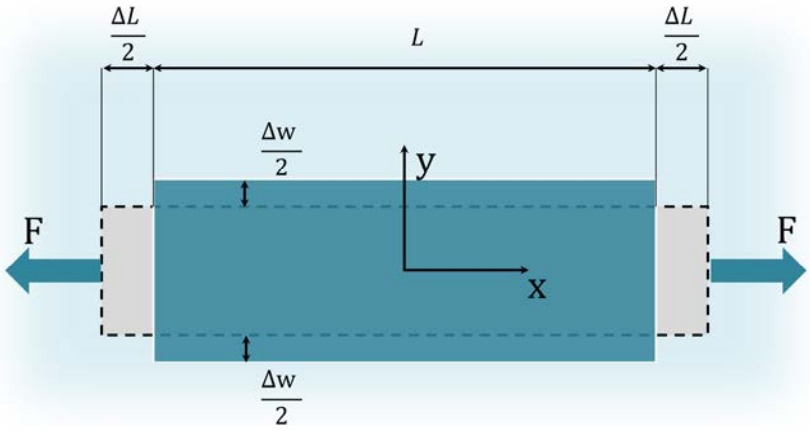

Fig. 2.2 Poisson effect under uniaxial load

It is possible to see in Fig. 2.2 that if a bar with a length L is subjected to an uniaxial stress in the direction x, the bar elongates by a length ΔL in the same direction of the load

and at the same time the bar section undergoes a contraction Δw in the direction perpendicular to the applied load (y in Fig. 2.2). This phenomenon is taken into consideration during the stress analysis with the Poisson's ratio ν.

If the same bar is subjected to a torque for example, an angular distortion will occur. Considering Fig. 2.3, this distortion d normalized with respect to a reference length h is called shear strain and the following picture shows the geometric deformation:

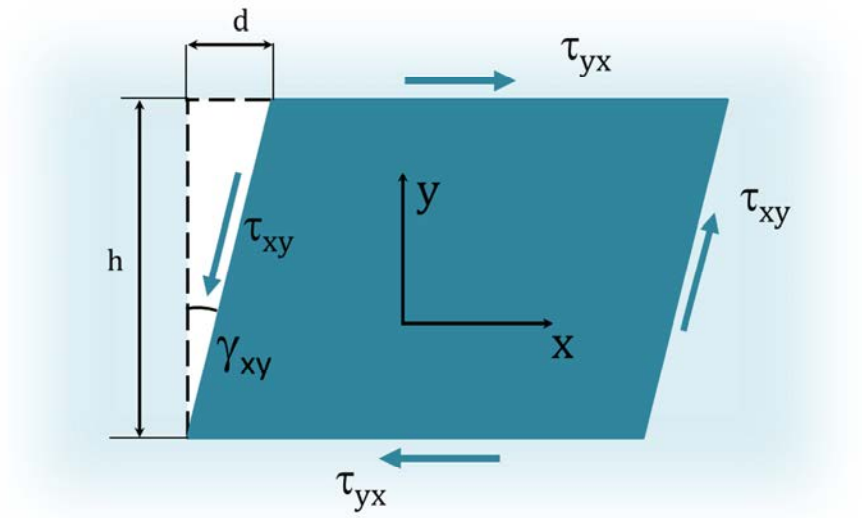

Fig. 2.3 Schematic of the shear strain

By definition the shear strain equation will be:

$$\gamma = \frac{d}{h}$$

Equation 2.5

2.1.3 Constitutive linear-elastic equations

For what has been said so far, each body that undergoes an external applied load will generate both stress and strain. Let's consider a body which is isotropic, linear and elastic. If the external applied load is not bigger than the load which will plastically deform the

body (the so-called yield stress) it is possible to write a linear equation that links the stress and the strain:

$$\sigma = E\varepsilon$$

Equation 2.6

where *E* is the Young's modulus that acts as elastic constant of the material.

Similarly, for the shear stress and strain the following equation can be written:

$$\tau = G\gamma$$

Equation 2.7

where G is the shear modulus.

Generalizing the equation by taking into account the Poisson effect, the final equations for the strains will be:

$$\begin{Bmatrix} \varepsilon_{xx} \\ \varepsilon_{yy} \\ \varepsilon_{zz} \end{Bmatrix} = \frac{1}{E}\begin{bmatrix} 1 & -\nu & -\nu \\ -\nu & 1 & -\nu \\ -\nu & -\nu & 1 \end{bmatrix}\begin{Bmatrix} \sigma_{xx} \\ \sigma_{yy} \\ \sigma_{zz} \end{Bmatrix}$$

Equation 2.8

While the equation to calculate the stress once the strains are known is:

$$\sigma_i = \frac{E}{1-\nu^2}(\varepsilon_i + \nu\varepsilon_j)$$

Equation 2.9

Similarly, the equations for the shear strains can be written as:

$$\gamma_{ij} = \frac{1}{2G}\tau_{ij}$$

Equation 2.10

With all the preceding equations it is possible to completely define the stress-strain state of a body, when its mechanical properties, i.e. *E, ν* and *G*, are known.

2.1.4 Plane stress and plane strain

As seen in the previous section, the final number of equations to know the complete stress-strain field within a body is twelve: six for the stress and six more for the strain. However, in certain conditions, the components can be decreased without losing consistency of the model. This can happen in particular when two different geometric conditions are present: if the sample has a thickness of at least an order of magnitude lower than the length or width, the component of the stress perpendicular to wider surface of the sample can be negligible all through the thickness, thus equal to zero. This is verified by imposing the following conditions:

$$\sigma_{zz} = \tau_{xz} = \tau_{yz} = 0$$

Equation 2.11

This particular case of stress distribution is called plane stress and it is typically applied in thin samples.

In the same way, if the sample has the length an order of magnitude bigger than the other two dimensions, the strain component aligned to this length is considered negligible. In this case the conditions to be applied are:

$$\varepsilon_{zz} = \gamma_{xz} = \gamma_{yz} = 0$$

Equation 2.12

2.2 Residual Stresses

2.2.1 Definition and Nature of Residual Stresses

By definition the Residual Stresses (RS) are the self-balancing locked-in stresses within a body when no external forces are applied [1]. The RS can be generally either introduced on purpose to improve for example the fatigue life of a component or they can be introduced unintentionally during the manufacturing of the sample and in the latter case they can be detrimental for the life in service of the component. The RS in engineering components are caused by incompatible internal permanent strains [2] so RS occur within a body when plastic deformations, thermal deformations or other treatments cause permanent deformations (or misfit). The generally accepted classification of the RS is based on their length scale. According with [3] and Fig. 2.4 there are three types of RS:

Fig. 2.4 Schematic view of the three different types of stress [3]

Type I: are generally called macrostresses and refer to the variation of the stress on a large scale (usually a large fraction of the sample dimensions), so many grains are included. They are typically generated by a macroscopic misfit which occurs when the sample is subjected to an external treatment like plastic deformation, quenching, etc.;

Type II: called microstresses in combination with the Type III stress. This is generally the stress variation from grain to grain, and they are generated by the different mechanical behaviours of the grains due to their different orientations;

Type III: are generally the stresses within a single grain, and derive from defects like interstitial atoms, vacancies, dislocations etc.

This classification is extremely important when we have to deal with the measurement of RS. Different techniques measure different types of RS. Generally speaking, in engineering problems related with the fatigue life of a component, the most important stresses are the macrostresses (or type I) which can be measured with most of the techniques that will be presented in chapter 4.

2.2.2 Residual Stress Techniques

As said in the previous section, RS can be purposely introduced inside an engineering component in order to, for example, increase its fatigue life or prevent stress corrosion cracking. Several techniques have been used, in particular in the aerospace field where the predicted fatigue life of a component plays a fundamental role during the design process of the airplane structures. In this paragraph a brief list and description of the most commonly used RS techniques will be presented. In particular, only the cold-working techniques are presented since a direct comparison with the laser shock peening will be easier since it is a cold-working process itself.

The Cold expansion technique is the most commonly used procedure to introduce a compressive RS field around the holes in riveted aerospace structures, which act as stress concentrator. It consists of drawing an oversized mandrel through a hole in order to plastically deform the circumference of the hole and its surrounding region. This forced misfit is counterbalanced by the generation of compressive RS which significantly decreases crack growth [4]. This technique has been successfully applied for the last 40 years [5], especially in aluminium alloys typically used in the aerospace field like AA2024-T3 [6].

Shot Peening (SP) has been the most important fatigue life improvement technique used in recent decades [7]. It is low-cost and high rate of repeatability allows the SP to be one of the widest used technique to introduce compressive RS in aerospace components. It consists of firing small spheres of glass, metal or ceramic on to a component's surface, causing a local plastic deformation which generates a compressive RS field [8]. The surface roughness generally increases due to the multiple impacts and the compressive RS are typically confined to the few first tenths of a millimetre from the surface. Laser Shock Peening is considered a direct competitor or replacement technology to the SP and for this many several articles have been published on the comparison between the two techniques and some of them will be reported later on this chapter. However, the coupling of both SP and LSP has demonstrated beneficial effect on the fatigue life of components [9] and for this reason a sample that was subjected to both LSP and SP is the subject of RS measurements as presented in chapter 7.

Deep Rolling is a relatively new, cold technique which consist of passing a free-rolling ball on top the sample surface with a normal force applied in order to introduce local plasticity and subsequently generate compressive RS. It has been successfully applied to

prevent the fretting fatigue effects due to low roughness level obtained after the treatment [10].

2.3 Laser Peening

Laser Shock Peening (LSP) is a relatively new surface treatment. Compared with the previously-mentioned techniques, it allows introduction of deeper compressive RS in materials. It has been shown that samples treated with LSP have remarkably improved their fatigue life and stress-corrosion cracking behaviour [11], [12]. Furthermore, the LSP has been used as forming process to achieve final shapes previously unobtainable [13]. In the next sections, a brief history of LSP will be presented as well as all the parameters involved in this technology. A final section is dedicated to the importance of the simulation of this process, to better understand why the Eigenstrain approach, presented in chapter 5, aroused interested within the research community.

2.3.1 History

The first study regarding the interaction between a laser and a metallic material dates back in 1960s, when for the first time the pressure generated on the surface of a metallic component when hit by a pulsed laser was recorded [14]. Further studies allowed researchers to conclude that the pressure generated by the interaction between the laser and the metal was due to a local vaporization of a thin layer of the surface of the component. Successive studies [15], [16] allowed researches to further understand the process and in particular the presence of the plasma which produced shock waves was confirmed.

A major breakthrough in the research on laser peening happened in 1964 when Neuman [17] discovered that the pressure generated by the laser ablation could be

increased by 800% by simply putting a transparent material (a quartz crystal) on top of the peened surface. In this way the transparency would still let the laser reach the metallic surface undisturbed as there is no material on-top of the sample, but the plasma generated from the vaporization of a thin surface layer stayed entrapped between the surface of the metallic component and the quartz increasing its pressure. It was the first demonstration of confined laser shock processing and nowadays this philosophy is still used.

In 1972 researchers at Battelle Memorial Institute in Columbus, Ohio (USA) [18] published some interesting results regarding the beneficial effects of the laser shock peening, first on AA7075 samples and later on iron samples [19]. Subsequently researchers focused their attention on the possibility to improve the fatigue life of metal components, in particular used in the automotive and aeronautic fields. In 1983 the technology and its benefits were officially presented during the Laser and Materials Processing conference held in Los Angeles by Clauer [20] and he obtained the patent for the refined laser shock process [21].

Later, in the 1980s, the first studies carried out in France were published [22]. Although several studies demonstrate the higher fatigue performances reached by several metal alloys used in common engineering applications, the laser system was both extremely expensive and it was not possible to get a high repetition rate, so no further publications were made for some time. Only with the advent of cheaper and more powerful lasers, were studies conducted in order to refine the technique. In particular, LSP technology was first tested with glass as transparent confinement material [23] and only later the introduction of a layer of water and ablation material allowed a higher repetition rate of the process [24], [25]. This allowed increase of the peak pressure up to 5 GPa which was an order of magnitude higher than the pressure reached without the confinement material.

2.3.2 Laser Peening Process

The Laser Shock Peening method consists of firing a pulsed laser on to the sample surface which can be (or not) covered with an ablative layer (in the latter case the technique is called Laser Peening without Coating – LPwC).

Fig. 2.5 Schematic view of the LSP process with and without coating [26]

As soon as the laser shot hits the ablative layer or the metal surface, a thin layer of material is vaporized. The vapour remains entrapped between the metal surface and the confinement material and it increases in pressure and temperature. According to Fabbro *et al.* [27], the temperature reached during the process is of the order of 10,000 K. Once the plasma is generated, it creates shock waves which propagate inside the metal component and, if their pressure is higher than the Hugoniot Elastic Limit (HEL), they introduce plastic tensile strains in the plane of the surface which are constrained by the surrounding elastic material and generate compressive residual stress on the same plane. During the propagation of the shock waves, their pressure reduces and once their value is under the HEL, no more plasticity is introduced.

In more detail the process can be divided into three different phases according to [28]:

- **Heating phase**: this phase happens when the sample surface is irradiated by the laser, for a time length between 3 and 30 ns. In this phase the pressure generated by the plasma generates the shock waves that propagate through the sample thickness;
- **Adiabatic cooling**: this phase starts when the laser pulse is over and it lasts between 2-3 times the length of the laser pulse. In this phase the pressure remains initially constant and then it starts to cool down adiabatically i.e. without the introduction or loss of further heat. Both during the heating and adiabatic phase, the pressure of the plasma is higher than the HEL and plastic deformations occur;
- **Final phase**: occurs over longer times, until the plasma pressure equals the atmospheric pressure. In this phase the gas expansion introduces further deformations in the sample;

If on one hand the pressure does not depend either on the pulse duration nor on the laser wavelength, on the other hand the dielectric breakdown has to be taken into consideration [29]. In more detail, by increasing the power density of the beam, the laser starts to interact with the confinement layer (or transparent layer). This interaction leads to an ionization process of this layer such that it becomes opaque to the laser beam. This process is detrimental for the laser beam which is prevented from reaching the metal surface. When the filtered, i.e. less powerful, laser beam hits the metal surface, the pressure generated by the plasma is necessarily lower. Generally speaking, power values not greater than 10 GW/cm^2 are used for the LSP process.

2.3.3 LSP parameters

2.3.3.1 Lasers

A laser is a device that emits an intense beam of coherent monochromatic light by stimulated emission of photons from excited atoms. Typically two different lasers have been used in the LSP research and applications: Nd:glass and Nd:YAG (Yttrium Aluminium Garnet). The former was developed in 1974 at Battelle Columbus Laboratories (Ohio) and

only in 1995 [30] was a useful version of the laser for LSP built. In particular, the laser can deliver energy between 25-100 J during each pulse with a repetition rate of 1 Hz (compared to the repetition rate of one pulse every 8 minutes of the first ever built Ng:glass). The Nd:YAG has similar characteristics to the Nd:glass laser but a different dopant crystal. Both the lasers use the Q-switching system which allow them to emit a pulsed laser rather than a continuous light beam, and the pulse length is generally between 2 and 50 ns.

These laser systems are able to produce a beam with a wavelength of 1064 nm, and with the utilization of a single crystal, it is possible to produce the second and third harmonics, i.e. a laser with wavelength of 532 nm (green light) and 355 nm (ultraviolet). As it is possible to see in Fig. 2.6, although the 355 nm wavelength generates a higher peak pressure with lower power density, the dielectric breakdown threshold is lower than the 1064 nm and 532 nm wavelength lasers. For this reason the two longer wavelengths are used nowadays in the LSP process.

Fig. 2.6 Generation of peak pressure with different laser wavelength [24], [31]

2.3.3.2 Opaque and Transparent layer

The opaque (also ablative or protective) and transparent layers play a fundamental role in the LSP process since their presence allows the generation of the plasma, its increase in pressure, and the subsequent generation of shock waves. Furthermore, the ablative layer thermally protects the sample surface [19]. Important analyses were carried out to study the best ablative and transparent layers in terms of peak pressure generated. Generally speaking the choice of both the ablative and the transparent layer strongly depends on their acoustic impedances but, since a complete description of the physical process occurring during the ablation process lies outside the scope of this research, only the key results will be reported. As shown in [32], several protective (or ablative) layer have been investigated to assess their thermal protection on metallic targets like aluminium foil or paint, and also black paint [33]. The research concluded that the peak pressure is increased up to 50% compared with the bare material and the layer thickness should be higher than 80 μm to assure that only the ablative layer is vaporized during the peening process. Similar results were concluded by Hong *et al.*[25], and comparing Al foil with black paint, the latter resulted to be more efficient even if the Al foil was easier to apply and its thickness more controllable than the paint layer.

As has been said before, the transparent layer entraps the plasma and allows it to increase its pressure in order to achieve higher RS values [19], [23]. As was done for the protective layer, several transparent layers were studied like quartz [33], silicon rubber, Pb glass and K9 glass [25]. All the results agreed that the materials with higher acoustic impedence generates a higher pressure peak, i.e. quartz and Pb glass. However, it was demonstrated [34] that by increasing the power density up to 4 GW/cm^2 both water and glass confinement were able to generate a pressure high enough to introduce the same RS field. Since the treatment has to be delivered with high repeatability to be competitive in the industrial field, nowadays the most common ablative layer (where used) is aluminium

foil while the most common transparent overlay is water due to its easy application even on complex geometries like curved surfaces or edges.

2.3.3.3 Spot geometry, Size and Overlapping

The laser peening treatment can be applied with both squared and circular spots. The squared geometry was patented by Metal Improvement Company and it was verified that it generates more homogeneous distribution of the shock waves while the circular spot tends to focus the shock waves toward the centre of the spot, increasing the load until the reverse yield effect is present, subsequently reducing the RS field [34] as can be seen in Fig. 2.7. In order to minimize this detrimental effect, the circular spot laser treatment requires an higher overlapping rate.

Fig. 2.7 Differences in RS at the surface for square and circular spots [34]. The x axis shows the distance in mm from the centre of the laser spot.

Generally speaking most of researches for industrial applications used spot sizes between 1 and 5 mm [35]. It has be found that small spot sizes tend to generate spherical shock waves which are easily attenuated within the sample while larger spots tend to have planar fronts which are attenuated at a lower rate.

The overlapping technique is a consolidated process that allows introduction of a more homogeneous compressive RS field at the surface. The following picture shows the surface deformation after three shots with a 5% overlapping:

Fig. 2.8 Surface profile after LSP process [36] measured in respect of the coordinate system of the CMM machine. In all three axis data are reported in mm

As Fig. 2.8 shows, the 5% overlapping allows a homogeneous distribution of the compressive RS between two spots. In order to further improve this effect, two different methods can be applied: either the overlapping distance is increased or, after the first layer of treatment, a second (or more) layer will be applied with a geometrical shift. This latter approach is called multi-peening and it is widely used not only to create a homogeneous RS field at the sample surface but also to increase the RS value as was demonstrated by Peyre *et al.*[11] on aluminium.

2.3.4 Laser Peening induced Residual Stress

The primary aim of the LSP treatment is to introduce plasticity inside the treated component in order to generate a RS field. Using the correct set of laser parameters and considering a sample with a thickness greater than 6 mm, it is possible to introduce a deep

compressive RS profile close to the surface of the sample while the tensile stresses are generally confined through the thickness. A typical distribution of RS after LSP treatment can be seen in the following picture:

Fig. 2.9 Distribution of RS after LSP for various thickness samples [56]

As can be seen in Fig. 2.9, the RS after LSP treatment is divided into two different areas: the compressive region and the tensile region. The compressive RS generally have their largest magnitude at the surface, then the stresses tend to decrease (in magnitude) up to the tensile region where they reach a tensile peak. In the same figure it is possible to see that, by increasing the thickness of the sample, this tensile peak tends to decrease. This happens because the stresses can be balanced over more material. After a certain depth, the stresses linearly decay due to the presence of the stresses automatically generated by the sample in order to balance the stresses introduced by the laser peening process. Generally speaking, the peak in compression reached with the LSP can be similar to the one obtained with shot peening, but the compressive RS are maintained deeper into the material. As reported in [39], [57], the shot peening introduces in aluminium alloy

AA7050-T7451 compressive RS up to 0.8 mm from the surface against a compressive RS up to 4 mm for LSP.

In thin samples it has been demonstrated that the RS profiles can be either in tension or compression at the surface depending on the parameters used for the LSP [58], [36]. These profiles usually present a U-shaped RS field due to the presence of the clad layer and possible reverse yielding due to the Bauschinger effect. The study of LSP for thin samples will be described in more detail in chapters 8 and 9.

2.3.5 LSP suppliers

LSP was invented more than 30 years ago but only lately, as said before, the repetition rate and the lower costs have allowed the technique to be cost-effective for industry. In the last 15 years, different companies around the world started to supply laser peening technology, using various parameters. Since during this 3-year research programme three different laser suppliers were involved, in the following paragraphs a brief introduction to their different laser set-ups is presented.

2.3.5.1 Metal Improvement Company- MIC

Metal Improvement Company (MIC) has been supplying shot peening and other surface treatments since the 1940s. In 1995, a powerful laser was set-up by Dane *et al.* [30] and the LSP technology successfully started to be supplied. The laser system at MIC is composed of an Nd:glass laser with an output energy of 25-30 J/pulse, 150 W and a pulse duration not longer than 14 ns. The laser spot has a square geometry with edge length of 2 to 8 mm and the first engineering applications were successfully published in [37]. Several applications with MIC lasers were made on aluminium alloys due to its wide application in the aerospace field. Preliminary research [38] was conducted in order to understand the process parameters variation on AA7049-T73, and it was concluded that, by increasing the treatment layers, deeper and higher (in magnitude) compressive residual stress are

introduced. MIC uses between 2 and 5 layers of treatments for the laser shock peening. The first layer is usually composed of several spots put side-by-side. In order to avoid the generation of tensile RS at the edge of these spots, a second (or more) treatment is usually performed with a geometrical shift that depends on the final number of treatments. The following pictures shows the geometrical pattern of the spots:

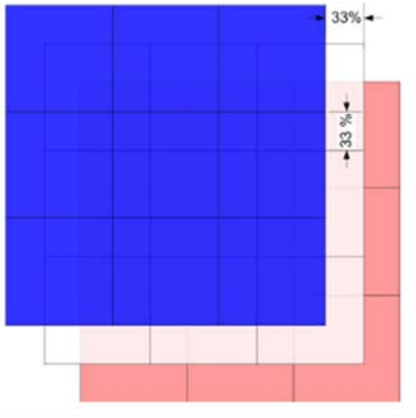

Fig. 2.10 LSP pattern for the first and second layer with a geometrical shift of 10%

Every time a new treatment layer has to be done on the sample surface, the laser has to be stopped and a technician is required to apply the ablative layer, which is a thin aluminium foil. Similar study [39] was conducted with samples made of AA7050-T7451 and their fatigue life was improved by a factor of 7.9 (considering 1 the fatigue life of as-machined material). LSP was demonstrated also to improve the fatigue life of AA2195 after Friction Stir Welding over Shot Peening [40] at elevated and cryogenic temperatures. Similar results were reached with titanium alloy Ti-6Al-4V [41] and after successful tests LSP was used on in-service turbine blades to introduce a pre-stress condition in order to retard the crack growth due to Foreign Object Damage [42]. Nowadays, MIC is able to provide a portable laser system [43] and the first successful application was made on the F-22 Raptor fighter plane in order to improve the fatigue live of the titanium alloy wing attachment lugs [44].

2.3.5.2 Toshiba Company

As has been said before, laser peening was first tested with a protective layer (or ablative layer) in order to protect the surface from the melting generated by the laser interaction. This approach is preferred when the surface of the sample is easily reachable by the technician. During 1990s though, Toshiba was involved in extensive research in order to solve the problem of Stress Corrosion Cracking (SCC) that was affecting the Boiling Water Reactor (BWR) nuclear power plants in Japan. Since it was not possible to extract the assembly to be peened and the local environment was radioactive and under water, the researchers were forced to supply the surface treatment from a remote station. LSP was one of the technologies taken into consideration. The usual wavelength of 1064 nm was not possible to be used due to its relatively poor transmitting properties in the confining medium and, furthermore, due to the inaccessibility of the BWR, researchers investigated the possibility to use the treatment without a sacrificial layer. In order to avoid any detrimental effect at the surface of the material, it was decided to drastically decrease the energy involved in the process, which was in the order of mJ while the laser was doubled its frequency in order to obtain in a wavelength of 532 nm. If on the one hand the reduction of the energy allows the use of optical fibres to guide the laser to the destined area, on the other hand the only way to obtain the same residual stress profile induced by the higher-energy laser was to increase up to 800% the number of layers of treatment. In this way, the RS introduced in the stainless steel components was similar to those introduced by the treatment with the protective layer, and the SCC phenomenon was drastically dropped [45], [46]. Besides that, the same technology demonstrated its versatility on several other materials including aluminium [47], [48] and titanium alloys [49].

2.3.5.3 Centro Laser – Universidad Politécnica de Madrid

At the laser centre of the Universidad Politécnica de Madrid (UPM), a laser with a wave length of 1064 nm, with the possibility to be switched at 532 nm, was developed and successfully tested [50]. In this case the laser is a Q-switched Nd:YAG, able to supply a shot with 9.4 ns pulse length, an energy of 2.8 J/pulse and a circular geometry with a diameter of 1.5 mm. The laser set up can be seen in the following picture:

Fig. 2.11 Laser se-up in UPM [50]

At UPM researchers were able to test the laser peening with and without protective coating [51], [52]. In particular, a paint coating of 13.3 μm was tested in order to evaluate the enhancement in terms of higher residual stress values achievable with the ablative layer. Similarly, the confinement layer was studied by taking into consideration both the thin water layer configuration (as shown in Fig. 2.11) and the full-immersed sample configuration [52], [53]. The laser set-up demonstrated the ability to introduce a deep compressive RS profile with both wavelengths of 1064 and 532 nm in aluminium alloy AA6061-T6 [54] and similar results were achieved in aluminium alloy AA2024-T351 [55].

2.3.6 Laser Peening Simulation

LSP is a complex technique whose modelling requires a good know-how of the laser involved, good knowledge of the plasma generation phenomena and the material response to an impact load. Nevertheless, LSP is quite an expensive technology compared to SP for example, even if the improved results obtained allow this technology to be applied in several engineering cases. In order to decrease as much as possible the expense during the research programme for LSP, a viable way to predict the RS field generated by the LSP is Finite Element Analysis (FEA). The FEA approach though, must include all the modelling of the physics phenomena that occur when the LSP is used. Since most of these were completely clarified only during the 1990s, it is easy to understand why the first ever approach to predict RS introduced by LSP via FEA was done in 1998 [59]. This first analysis demonstrated the basics to simulate the LSP phenomena. ABAQUS software was used because of the possibility to have both linear and non-linear analysis. The latter is called ABAQUS/Explicit and it is usually used for transient analyses while the former, or ABAQUS/Standard, is used primarily for static or natural frequency calculations. According to Braisted and Brockman [59], ABAQUS/Standard can be used to simulate the entire process of a single peened spot but it would not cost-effective and that is why the Explicit package is needed as well.

Generally, the simulation of the LSP technique involves two steps: the application of the pressure on-top of the treated surface and the subsequent generation of plasticity; then the calculation of the stresses, strains and deformation in ABAQUS/Standard once the plasticity input is imported from the previous step. In order to obtain the correct distribution of the plasticity, two important modelling factors have to be taken into account: the model of the pressure and the model of the material response under high strain rates. Based on analytical models [11], [60], the pressure is modelled as a triangular pulse due to the increasing of its value during the first 10-25 ns and its decreasing in the

following 100 ns which is the simulation for the heating phase and the adiabatic cooling as described in section 2.3.2. The modelling of the material behaviour under strain-rates higher than 10^6 per second is complex. Under these conditions the material behaves differently than under quasi-static conditions and both the Young's modulus and the yield strength can change. In order to simulate the material behaviour as close as possible to reality, Braisted and Brockman considered the material as elastic-perfectly plastic, but the yield strength was a function of the HEL rather than the yield strength measured in static conditions. The results published were promising and were confirmed later by Ding *et al.* [61] where also the multi-peening approach was used. Both these approaches were simulated for a 2D model only. Hu *et al.* [62] used the same approach to simulate the LSP in a 3D model with a multi-peening treatment, while a proper systematic analysis of the simulated parameters can be found in [63].

A new approach for the material behaviour modelling was proposed for the first time by Wu *et al.* [64] and nowadays is still used. In this study, the Johnson-Cook constitutive model was proposed to be implemented in the FEA analysis of the LSP. Just for clarification the equation is reported here:

$$\boldsymbol{\sigma = (A + B\overline{\varepsilon^p}^{n})(1 + C \ln \dot{\varepsilon}^{*})(1 - \overline{T^m})}$$

Equation 2.13

where $\overline{\varepsilon^p}$ is the equivalent plastic strain, n in the work-hardening exponent, A, B, C and m are material constants, $\dot{\varepsilon}^{*}$ is the normalized equivalent plastic strain rate and $\overline{T}$ is defined as: $(T-T_{room})/(T_{melt}-T_{room})$. It is possible to see in Equation 2.13 how the strain hardening, strain rate and thermal effects are separate. With this new approach, the results were quite promising. Ever since, the Johnson-Cook approach is a consolidated method used to predict the RS field after LSP peening. The approach has been used to study the LSP phenomena for several factors like the study of the spot geometry [65],

prediction of plasticity distribution in a curved geometry [66], comparison with different material behaviour models [67], the possibility to apply LSP with femtosecond pulse length [68], and the prediction of RS field in several materials like titanium [69], [70] and aluminium alloys [71].

A particular effort was made by the Universidad Politécnica de Madrid to propose a model for the plasma generation of the LSP [72], [73] in order to predict the RS [74].

2.4 Aim & Objectives

In the light of this literature review which described the LSP process, its applications to different samples and the simulation approach used in order to get a preliminary study of the RS distribution, it is possible to conclude that a deeper study of the Eigenstrain approach is needed in order to understand the limit of this promising approach. For example this approach hasn't been studied yet for round edges and no publications have been made so far relatively to the application of Eigenstrain when different surface treatments are applied on the same surface like LSP and SP. Considering the approach that DeWald proposed for its promising results and versatility, both these problems were studied during the PhD research and the final results will be shown in chapter 6 and 7.

Furthermore, even if the LSP has been applied on different materials and samples, only a bunch of studies have been made on the application of the LSP on thin samples even if it is author's opinion that these samples could have several applications in the aerospace structures due to their small thicknesses (around 2 mm). In order to fill this gap, different thin samples were subject to LSP treatment and subsequent RS measurements with different techniques in order to increase the reliability of the obtained data and to get a clear view on how the LSP parameters affect the distribution of RS. Both single and double peened samples were used and the promising data collected will be shown in chapters 8 and 9.

2.5 Conclusions

In this chapter the fundamentals of the Stress theory and the presentation of the laser peening technology has been given. In particular, the LSP technology has been showed to be a superior technique to introduce compressive residual stress in engineering components. All the mentioned suppliers of the treatment were involved during this research and all of them provided one or more samples to be tested during the PhD project for which results will be presented in chapters 6 to 9.

An introduction to the LSP simulation has been given as well in order to better understand why the Eigenstrain approach aroused interest in the research community. In the next chapter a full description of the residual stress measurement techniques used during this research will be presented while in chapter 5 the Eigenstrain theory will be presented as well as the applications made during this research project.

References

[1] W. F. Hosford, *Mechanical Behaviour of Materials*, 1st ed. Cambridge: Cambridge University Press, 2005.

[2] A. M. Korsunsky, "On the modelling of residual stresses due to surface peening using Eigenstrain distributions," *J. Strain Anal.*, vol. 40, pp. 817–824, 2005.

[3] M. Fitzpatrick and A. Lodini, *Analysis of residual stress by diffraction using neutron and synchrotron radiation*. Taylor & Francis, 2003.

[4] D. Ball and D. Lowry, "Experimental investigation on the effects of cold expansion of fastener holes," *Fatigue Fract. Eng. Mater. Struct.*, vol. 21, no. 1, pp. 17–34, Jan. 1998.

[5] M. J. Pavier, C. G. C. Poussard, and D. J. Smith, "Effect of residual stress around cold worked holes on fracture under superimposed mechanical load," *Eng. Fract. Mech.*, vol. 63, no. 6, pp. 751–773, Aug. 1999.

[6] X. Zhang, “Fatigue life improvement in fatigue-aged fastener holes using the cold expansion technique,” *Int. J. Fatigue*, vol. 25, no. 9–11, pp. 1249–1257, Sep. 2003.

[7] L. Wagner, *Shot Peening*. WILEY, 2006, p. 584.

[8] S. Wang, Y. Li, M. Yao, and R. Wang, “Compressive residual stress introduced by shot peening,” *J. Mater. Process. Technol.*, vol. 73, no. 1–3, pp. 64–73, Jan. 1998.

[9] U. C. Heckenberger, V. Holzinger, W. von Bestenbostel, and E. Hombergsmeier, “Laser shock peening to improve the fatigue resistance of AA7050 components,” *Int. J. Struct. Integr.*, vol. 2, no. 1, pp. 22–33, 2011.

[10] G. H. Majzoobi, K. Azadikhah, and J. Nemati, “The effects of deep rolling and shot peening on fretting fatigue resistance of Aluminum-7075-T6,” *Mater. Sci. Eng. A*, vol. 516, no. 1–2, pp. 235–247, Aug. 2009.

[11] P. Peyre, R. Fabbro, P. Merrien, and H. P. Lieurade, “Laser shock processing of aluminium alloys. Application to high cycle fatigue behaviour,” *Mater. Sci. Eng. A*, vol. 210, no. 1–2, pp. 102–113, Jun. 1996.

[12] J. Z. Lu, K. Y. Luo, D. K. Yang, X. N. Cheng, J. L. Hu, F. Z. Dai, H. Qi, L. Zhang, J. S. Zhong, Q. W. Wang, and Y. K. Zhang, “Effects of laser peening on stress corrosion cracking (SCC) of ANSI 304 austenitic stainless steel,” *Corros. Sci.*, vol. 60, pp. 145–152, Jul. 2012.

[13] Y. Shi, Z. Yao, H. Shen, and J. Hu, “Research on the mechanisms of laser forming for the metal plate,” *Int. J. Mach. Tools Manuf.*, vol. 46, no. 12–13, pp. 1689–1697, Oct. 2006.

[14] G. A. Askarya and E. M. Moroz, “Pressure on evaporation of matter in radiation beam,” *Sov. Physics, JEPT*, vol. 16, pp. 1638–1639, 1963.

[15] D. W. Gregg, “Momentum Transfer Produced by Focused Laser Giant Pulses,” *J. Appl. Phys.*, vol. 37, no. 7, p. 2787, Jul. 1966.

[16] N. C. Anderholm, “Laser-Generated Stress Waves,” *Appl. Phys. Lett.*, vol. 16, no. 3, p. 113, Oct. 1970.

[17] F. Neuman, “Momentum Transfer and Cratering Effects Produced by Giant Laser Pulses,” *Appl. Phys. Lett.*, vol. 4, no. 9, p. 167, Dec. 1964.

[18] B. P. Fairand, “Laser shock-induced microstructural and mechanical property changes in 7075 aluminum,” *J. Appl. Phys.*, vol. 43, no. 9, p. 3893, Nov. 1972.

[19] B. P. Fairand, “Quantitative assessment of laser-induced stress waves generated at confined surfaces,” *Appl. Phys. Lett.*, vol. 25, no. 8, p. 431, Oct. 1974.

[20] A. H. Clauer, S. C. Ford, and C. T. Walters, “The Effect of Laser Shock Processing on the Fatigue Properties of AA2024-T3 Aluminum,” *Lasers in Materials Processing, 1983, Los Angeles, California*. 1983. Unpublished research

[21] A. H. Clauer, B. P. Fairand, S. C. Ford, and C. T. Walters, "Laser shock processing in Shock Waves and High-Strain-Rate Phenomena in Metals.," 4401477, 1983.

[22] P. Ballard, J. Fournier, R. Fabbro, J. Frelat, and L. Castex, "Study of the plastification of metallic targets shocked by a laser pulse of high energy," *Le J. Phys. Colloq.*, vol. 49, no. C3, pp. C3–401–C3–406, Sep. 1988.

[23] J. F. R. Fabbro P. Ballard, D. Devaux, J. Virmont, "Physical study of laser-produced plasma in confined geometry," *J. Appl. Phys*, vol. 68, pp. 775–784, 1990.

[24] L. Berthe, R. Fabbro, P. Peyre, L. Tollier, and E. Bartnicki, "Shock waves from a water-confined laser-generated plasma," *J. Appl. Phys.*, vol. 82, no. 6, p. 2826, 1997.

[25] X. Hong, S. Wang, D. Guo, H. Wu, J. Wang, Y. Dai, X. Xia, and Y. Xie, "Confining medium and absorptive overlay," *Opt. Lasers Eng.*, vol. 29, no. 6, pp. 447–455, Jun. 1998.

[26] G. Ivetich, "Residual Stress Effects on Fatigue Phenomena in Aerospace Structures," PhD Thesis, University of Pisa, 2010.

[27] P. Peyre and R. Fabbro, "Laser shock processing: a review of the physics and applications," *Opt. Quantum Electron.*, vol. 27, no. 12, pp. 1213–1229, Dec. 1995.

[28] R. Fabbro, J. Fournier, P. Ballard, D. Devaux, and J. Virmont, "Physical study of laser-produced plasma in confined geometry," *J. Appl. Phys.*, vol. 68, no. 2, p. 775, 1990.

[29] L. Berthe, R. Fabbro, P. Peyre, and E. Bartnicki, "Experimental study of the transmission of breakdown plasma generated during laser shock processing," *Eur. Phys. J. Appl. Phys.*, vol. 3, no. 2, pp. 215–218, Aug. 1998.

[30] C. B. Dane, L. E. Zapata, W. A. Neuman, M. A. Norton, and L. A. Hackel, "Design and operation of a 150 W near diffraction-limited laser amplifier with SBS wavefront correction," *IEEE J. Quantum Electron.*, vol. 31, no. 1, pp. 148–163, 1995.

[31] L. Berthe, R. Fabbro, P. Peyre, and E. Bartnicki, "Wavelength dependent of laser shock-wave generation in the water-confinement regime," *J. Appl. Phys.*, vol. 85, no. 11, p. 7552, 1999.

[32] J. A. Fox, "Effect of water and paint coatings on laser-irradiated targets," *Appl. Phys. Lett.*, vol. 24, no. 10, p. 461, Oct. 1974.

[33] A. H. Clauer and B. P. Fairand, "Interaction of laser-induced stress waves with metals," in *Applications of Lasers in Materials Processing*, 1979.

[34] J.-E. Masse and G. Barreau, "Laser generation of stress waves in metal," *Surf. Coatings Technol.*, vol. 70, no. 2–3, pp. 231–234, Jan. 1995.

[35] R. Fabbro, P. Peyre, L. Berthe, and X. Scherpereel, "Physics and applications of laser-shock processing," *J. Laser Appl.*, vol. 10, no. 6, pp. 265–279, 1998.

[36] M. B. Toparli, “Analysis of Residual Stress Fields in Aerospace Materials After Laser Peening,” PhD Thesis, The Open University, 2012.

[37] G. Hammersley, L. A. Hackel, and F. Harris, “Surface prestressing to improve fatigue strength of components by laser shot peening,” *Opt. Lasers Eng.*, vol. 34, no. 4–6, pp. 327–337, Oct. 2000.

[38] J. E. Rankin, M. R. Hill, and L. A. Hackel, “The effects of process variations on residual stress in laser peened 7049 T73 aluminum alloy,” *Mater. Sci. Eng. A*, vol. 349, no. 1–2, pp. 279–291, May 2003.

[39] H. Luong and M. R. Hill, “The effects of laser peening and shot peening on high cycle fatigue in 7050-T7451 aluminum alloy,” *Mater. Sci. Eng. A*, vol. 527, no. 3, pp. 699–707, 2010.

[40] O. Hatamleh, M. Hill, S. Forth, and D. Garcia, “Fatigue crack growth performance of peened friction stir welded 2195 aluminum alloy joints at elevated and cryogenic temperatures,” *Mater. Sci. Eng. A*, vol. 519, no. 1–2, pp. 61–69, Aug. 2009.

[41] K. K. Liu and M. R. Hill, “The effects of laser peening and shot peening on fretting fatigue in Ti–6Al–4V coupons,” *Tribol. Int.*, vol. 42, no. 9, pp. 1250–1262, 2009.

[42] S. Zabeen, M. Preuss, and P. J. Withers, “Residual stresses caused by head-on and 45° foreign object damage for a laser shock peened Ti–6Al–4V alloy aerofoil,” *Mater. Sci. Eng. A*, vol. 560, pp. 518–527, Jan. 2013.

[43] C. B. Dane, F. Harris, E. Lao, J. Rankin, and R. Hurd, “Advanced beam delivery for mobile laser peening,” in *2nd International Conference on Laser Peening*, 2010. Unpublished research

[44] D. Jensen, “Adaptation of LSP Capability for Use on F-22 Raptor Primary Structure at an Aircraft Modification Depot ,” in *2nd International Conference on Laser Peening*, 2010. Unpublished research

[45] N. Mukai, N. Aoki, M. Obata, A. Ito, Y. Sano, and C. Konagai, “Laser processing for underwater maintenance in nuclear plants,” in *3rd JSME/ASME joint international conference on nuclear engineering*, 1995, pp. 1489–1494.

[46] Y. SANO, “Development and application of laser peening system to prevent stress corrosion cracking of reactor core shroud,” *Proc 8th Int Conf Nucl. Eng.*, 2000. Unpublished research

[47] Y. Sano, K. Masaki, T. Gushi, and T. Sano, “Improvement in fatigue performance of friction stir welded A6061-T6 aluminum alloy by laser peening without coating,” *Mater. Des.*, vol. 36, no. 0, pp. 809–814, 2012.

[48] K. Masaki, Y. Ochi, T. Matsumura, and Y. Sano, “Effects of laser peening treatment on high cycle fatigue properties of degassing-processed cast aluminum alloy,” *Mater. Sci. Eng. A*, vol. 468–470, pp. 171–175, Nov. 2007.

[49] E. Maawad, Y. Sano, L. Wagner, H.-G. Brokmeier, and C. Genzel, "Investigation of laser shock peening effects on residual stress state and fatigue performance of titanium alloys," *Mater. Sci. Eng. A*, vol. 536, pp. 82–91, Feb. 2012.

[50] J. L. Ocaña, M. Díaz, J. A. Porro, L. R. de Lara, and C. Correa, "Effect of Thermal Treatments on the Mechanical Properties Enhancement of High Reliability Metallic Materials by Laser Shock Processing," in *Materials Science Forum*, 2014, vol. 783–786, pp. 2376–2381.

[51] J. L. Ocaña, C. MoLSPeceres, J. A. Porro, G. Gómez, and M. Morales, "Experimental assessment of the influence of irradiation parameters on surface deformation and residual stresses in laser shock processed metallic alloys," *Appl. Surf. Sci.*, vol. 238, no. 1–4, pp. 501–505, Nov. 2004.

[52] C. Rubio-González, G. Gomez-Rosas, J. L. Ocaña, C. MoLSPeceres, A. Banderas, J. Porro, and M. Morales, "Effect of an absorbent overlay on the residual stress field induced by laser shock processing on aluminum samples," *Appl. Surf. Sci.*, vol. 252, no. 18, pp. 6201–6205, 2006.

[53] C. Rubio-González, J. L. Ocaña, G. Gomez-Rosas, C. MoLSPeceres, M. Paredes, A. Banderas, J. Porro, and M. Morales, "Effect of laser shock processing on fatigue crack growth and fracture toughness of 6061-T6 aluminum alloy," *Mater. Sci. Eng. A*, vol. 386, no. 1–2, pp. 291–295, Nov. 2004.

[54] G. Gomez-Rosas, C. Rubio-Gonzalez, J. L. Ocaña, C. MoLSPeceres, J. A. Porro, M. Morales, and F. J. Casillas, "Laser Shock Processing of 6061-T6 Al alloy with 1064nm and 532nm wavelengths," *Appl. Surf. Sci.*, vol. 256, no. 20, pp. 5828–5831, Aug. 2010.

[55] G. Gomez-Rosas, C. Rubio-Gonzalez, J. . Ocaña, C. MoLSPeceres, J. A. Porro, W. Chi-Moreno, and M. Morales, "High level compressive residual stresses produced in aluminum alloys by laser shock processing," *Appl. Surf. Sci.*, vol. 252, no. 4, pp. 883–887, Nov. 2005.

[56] A. T. DeWald and M. R. Hill, "Eigenstrain-based model for prediction of laser peening residual stresses in arbitrary three-dimensional bodies. Part 2: model verification," *J. Strain Anal.*, vol. 44, 2008.

[57] Y. K. Gao, "Improvement of fatigue property in 7050–T7451 aluminum alloy by laser peening and shot peening," *Mater. Sci. Eng. A*, vol. 528, pp. 3823–3828, 2011.

[58] M. B. Toparli and M. E. Fitzpatrick, "Residual stresses induced by laser peening of thin aluminium plates," *Mater. Sci. Forum*, vol. 681, pp. 504–509, 2011.

[59] W. Braisted and R. Brockman, "Finite element simulation of laser shock peening," *Int. J. Fatigue*, vol. 21, no. 7, pp. 719–724, 1999.

[60] P. Peyre, R. Fabbro, L. Berthe, and C. Dubouchet, "Laser shock processing of materials, physical processes involved and examples of applications," *J. Laser Appl.*, vol. 8, no. 3, p. 135, 1996.

[61] K. Ding and L. Ye, "Simulation of multiple laser shock peening of a 35CD4 steel alloy," *J. Mater. Process. Technol.*, vol. 178, no. 1–3, pp. 162–169, Sep. 2006.

[62] Y. Hu, Z. Yao, and J. Hu, "3-D FEM simulation of laser shock processing," *Surf. Coatings Technol.*, vol. 201, no. 3–4, pp. 1426–1435, Oct. 2006.

[63] A. Warren, Y. Gou, and S. Chen, "Massive parallel laser shock peening: Simulation, analysis, and validation," *Int. J. Fatigue*, vol. 30, no. 1, pp. 188–197, Jan. 2008.

[64] X. Wu, C. Huang, X. Wang, and H. Song, "A new effective method to estimate the effect of laser shock peening," *Int. J. Impact Eng.*, vol. 38, no. 5, pp. 322–329, May 2011.

[65] Y. Hu, C. Gong, Z. Yao, and J. Hu, "Investigation on the non-homogeneity of residual stress field induced by laser shock peening," *Surf. Coatings Technol.*, vol. 203, no. 23, pp. 3503–3508, Aug. 2009.

[66] A. Vasu, Y. Hu, and R. V. Grandhi, "Differences in plasticity due to curvature in laser peened components," *Surf. Coatings Technol.*, vol. 235, pp. 648–656, Nov. 2013.

[67] H. K. Amarchinta, K. Langer, D. S. Stargel, and R. V. Grandhi, "Material model validation fro laser shock peening process simulation," *Model. Simul. Mater. Sci. Eng.*, vol. 17, no. 1, 2009.

[68] B. Wu, S. Tao, and S. Lei, "Numerical modeling of laser shock peening with femtosecond laser pulses and comparisons to experiments," *Appl. Surf. Sci.*, vol. 256, no. 13, pp. 4376–4382, Apr. 2010.

[69] H. K. Amarchinta, R. V. Grandhi, A. H. Clauer, K. Langer, and D. S. Stargel, "Simulation of residual stress induced by a laser peening process through inverse optimization of material models," *J. Mater. Process. Technol.*, vol. 210, no. 14, pp. 1997–2006, Nov. 2010.

[70] S. Bhamare, G. Ramakrishnan, S. R. Mannava, K. Langer, V. K. Vasudevan, and D. Qian, "Simulation-based optimization of laser shock peening process for improved bending fatigue life of Ti–6Al–2Sn–4Zr–2Mo alloy," *Surf. Coatings Technol.*, vol. 232, pp. 464–474, Oct. 2013.

[71] N. Hfaiedh, P. Peyre, H. Song, I. Popa, V. Ji, and V. Vignal, "Finite Element analysis of Laser Shock Peening of 2050-T8 aluminum alloy," *Int. J. Fatigue*, Jul. 2014.

[72] J. L. Ocana, C. MoLSPeceres, M. Morales, and A. Garcia-Beltran, "Model for the coupled predictive assessment of plasma expansion and material compression in laser shock processing applications," in *Advanced High-Power Lasers and Applications*, 2000, pp. 252–263.

[73] J. L. Ocaña, M. Morales, C. MoLSPeceres, and J. Torres, "Numerical simulation of surface deformation and residual stresses fields in laser shock processing experiments," *Appl. Surf. Sci.*, vol. 238, no. 1–4, pp. 242–248, 2004.

[74] M. Morales, J. L. Ocaña, C. MoLSPeceres, J. A. Porro, and A. García-Beltrán, "Model based optimization criteria for the generation of deep compressive residual stress fields in high elastic limit metallic alloys by ns-laser shock processing," *Surf. Coatings Technol.*, vol. 202, no. 11, pp. 2257–2262, Feb. 2008.

3 Materials and Samples used for the experiments

During this research several samples were subjected to residual stress measurements with different techniques after laser shock peening process. All the samples were made of aluminium alloys typical of aerospace applications such as AA2024-T351 and T7050-T451. In this chapter a brief introduction of the samples used will be given with the description of their materials, geometry and laser peening treatments.

3.1 Introduction

The first use of aluminium is dated back to the Roman empire where crystals of Alum were used for different purposes. Only at the start of the 19th century was it possible to obtain pure aluminium but the costs were so prohibitive that aluminium was considered for decades a precious metal like silver. Only with the advent of the aerospace industry, has aluminum started being widely used, and the cost of its production was drastically decreased when a method to recycle aluminum was put in practice during the 1960s.

The aluminum alloys are mainly divided into two different groups: wrought and cast alloys. Both have subgroup classifications based on the presence of the second major alloying element. In this thesis two different wrought alloys were used: AA2024 and AA7050. In the next sections these two alloys will be presented and the samples described.

3.2 AA7050-T7451

The aluminium alloy AA7050 has been extensively used in aerospace structure due to its high strength, high resistance to exfoliation corrosion, stress-corrosion cracking, high fracture toughness and fatigue resistance. During this research, two samples of aluminium alloy AA7050 were used and the heat treatment for both was the so-designated T7451

where T stands for temper and the numbering 7451 indicates solution heat-treated, stress-relieved by controlled stretching and then artificially over-aged. This particular treatment is usually reserved for components susceptible to stress-corrosion cracking. The most of the chemical composition of AA7050 is reported in the following table while minor metallic components were present and they were not reported in the table:

Element	Al	Zn	Mg	Cu	Zr
Weight %	89.0	6.2	2.3	2.3	0.12

Table 3.1

The Young's modulus E=72 GPa while the Poisson's ratio is ν=0.33.

Two samples made of AA7050 were available for residual stress measurement, the Stepped Coupon and the Single Edge Notch (SEN), both of them were supplied by Airbus Innovation Works (previously EADS Innovation Works). A brief description of both samples follows.

3.2.1 Stepped Coupon

The stepped coupon was designed with the intention of reaching a certain stress concentration factor where the change of the section is present. The sample is shown in Fig. 3.1:

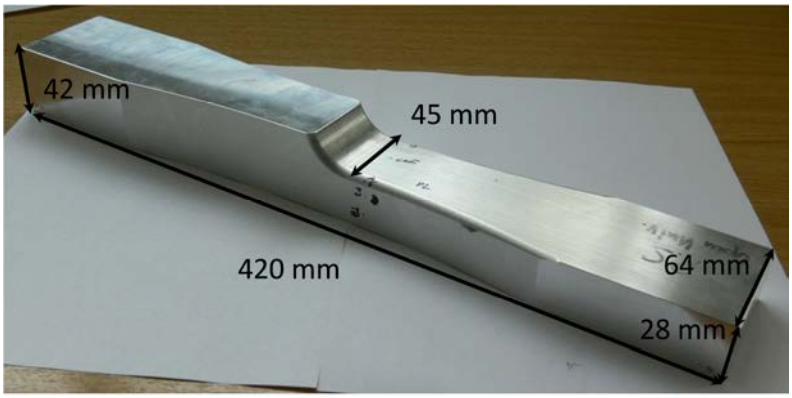

Fig. 3.1 Stepped Coupon

As shown in Fig. 3.1, the stepped coupon is a 420 mm long bar with two different sections: the right-hand one in the figure is 28 mm thick while the left-hand is 42 mm thick. The middle section, where the highest stresses are reached, is 45 mm wide while the front and the back side are 64 mm thick for clamping during the fatigue tests. The sample was machined from a plate as the next picture shows:

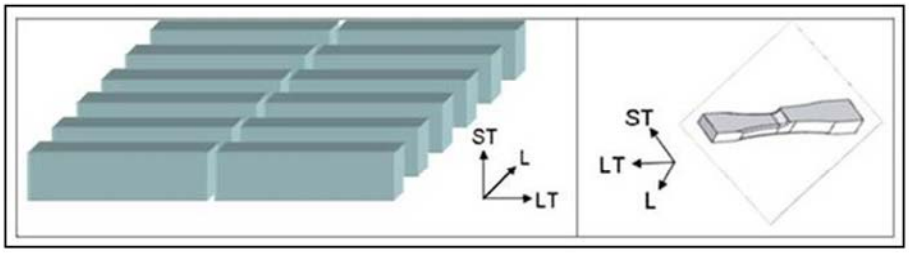

Fig. 3.2 Machining process for the stepped coupon

As can be seen in Fig. 3.2, the stepped coupon was machined from a larger plate with the direction of rolling (L) aligned with the thickness of the sample. Due to this process, grains elongated in this direction are expected. To confirm this hypothesis, a metallographic analysis at the round edge was carried out on a spare sample used previously for contour method measurements and reported here [1]. The procedure followed was suggested by [2]. The following picture shows the sample for the metallographic analysis:

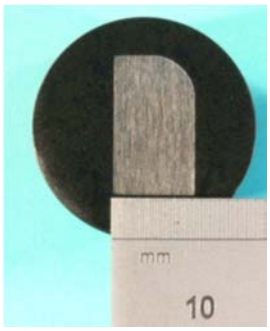

Fig. 3.3 Curved edge sample enclosed in the resin support

First an optical microscope was used in order to obtain a visualization of the grains distribution and elongation. The result can be seen in the next picture:

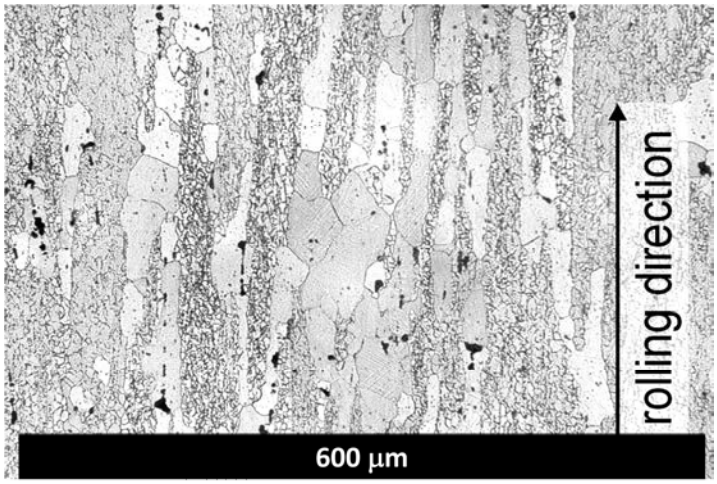

Fig. 3.4 Grains alignment close to the round edge of the Stepped Coupon

From the metallographic analysis it was possible to conclude that the grains are orientated in the same direction of rolling direction. It is also possible to see that the grain structure is composed of very small grains (2 µm) and a small amount of larger grains (150 µm). A further investigation of the grain structure was made by Scanning Elector Microscope (SEM), that was used on a sample which was first polished and then etched with Keller's reagent in order to understand if the smaller grains were generated by cracking of larger grains.

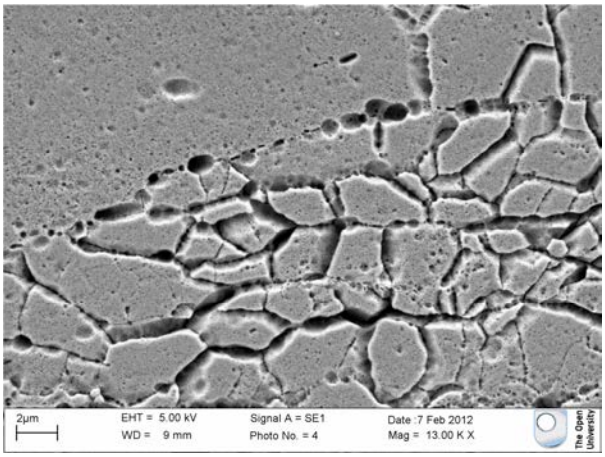

Fig. 3.5 Image obtained with SEM of the smaller grains of the Stepped Coupon

The sample was subject to laser peening by Metal Improvement Company base Earby, UK. The pattern of the laser process can be seen in the following picture:

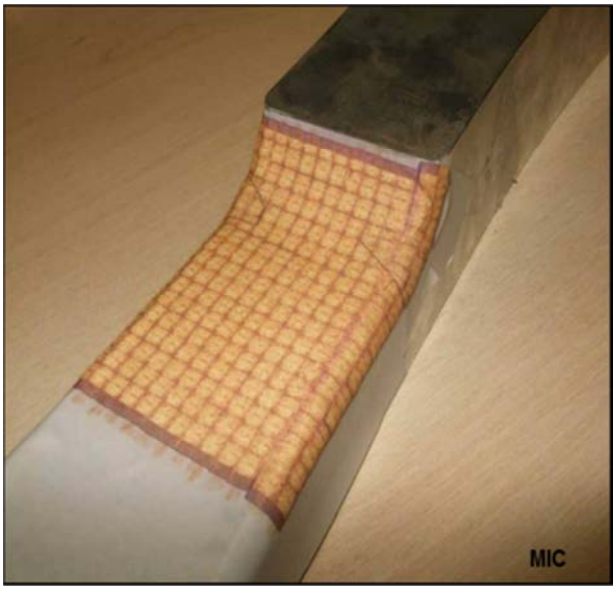

Fig. 3.6 Pattern of the LSP process for the first layer of treatment

The laser treatment parameters used were 4 GW/cm^2 as power density, 18 ns pulse length and 3 layers of treatment with a geometric shift of 33% between each layer to homogenize the compressive stresses on the top surface as described in chapter 2; the spot was square with an edge of 4 mm. This particular set of parameters was demonstrated to be the one which improved most the fatigue life [3]. The stepped coupon was extensively fatigue tested and the results are reported in [4].

The stepped coupon was the subject of several residual stress measurements and they are reported in chapter 6.

3.2.2 Single Edge Notch – SEN(T)

A second sample made of AA7050-T7451 used during this research is a Single Edge Notch Tension (SENT) configuration. A picture of the sample and the Finite Element Modelling 2D linear analysis run with ABAQUS software are here shown:

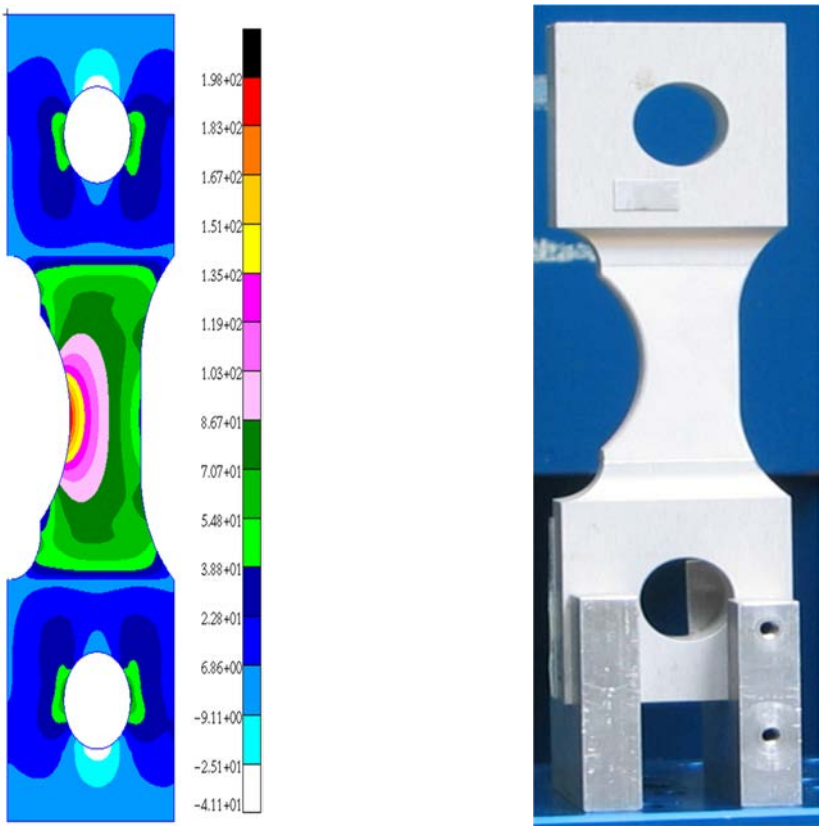

a) b)

Fig. 3.7 a) Distribution of the stresses during a tensile test; b) Iicture of the sample

The SEN was designed for studying the fatigue life of samples subject to both LSP and SP. The sample is 245 mm long, and the middle section is 10 mm thick. It is possible to see in Fig. 3.7 that the sample was designed in order to increase the stress concentration factor at the notch where the crack was supposed to start, i.e. during a tensile test the stresses will be higher at the notch due to the low section. In order to get a stress concentration factor of 2 at the notch, during the tensile loading the sample is subjected to

both tension deriving from the applied load and tension deriving from bending. The latter was possible to be obtained by the two holes for clamping having their centres 7 mm away from the vertical axis of symmetry.

The sample was subjected to both LSP and SP in the middle section. The LSP parameters involved were: 2 GW/cm^2, 18 ns pulse length and 4 layers. These parameters were chosen by EADS in order to reduce as much as possible the deformation and furthermore the samples treated with these laser parameters have been demonstrated to have the best fatigue life performance [5]. The LSP pattern can be seen in the following pictures:

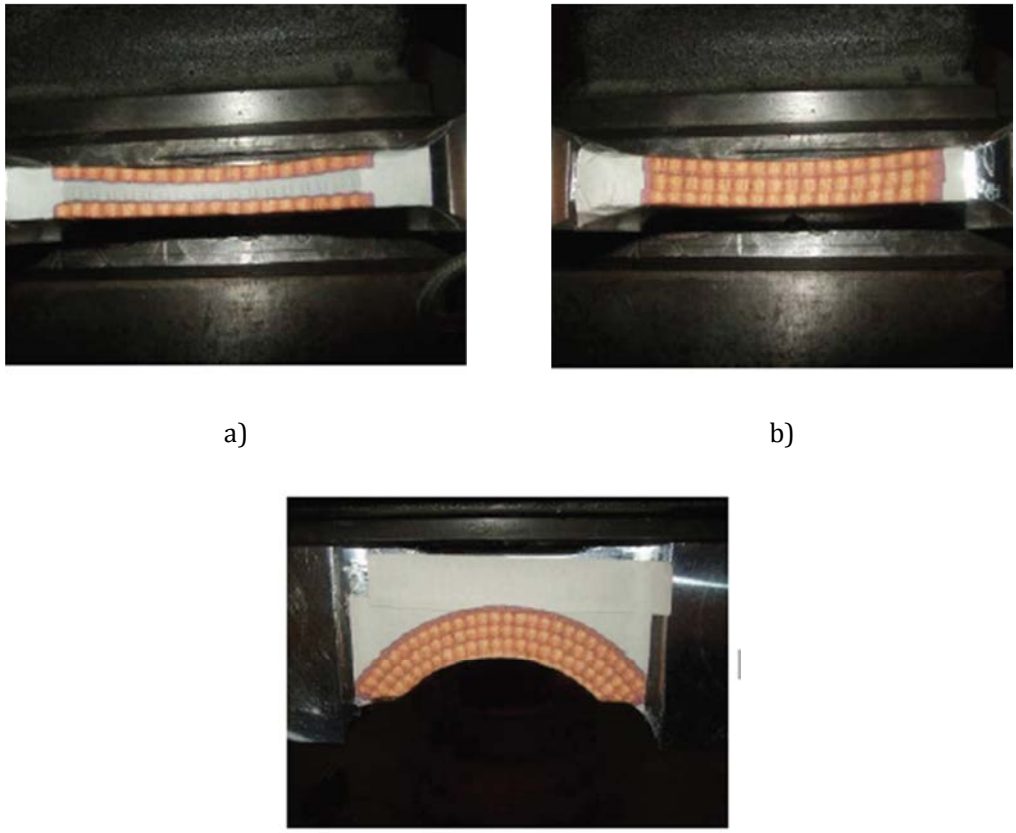

a) b)

c)

Fig. 3.8 LSP at a) the radius, b) the notch) the lateral side

The sample was then subjected to SP all around the mid-section. It was not possible to carry out any metallographic analysis due to the fatigue test purpose of the sample, i.e. the sample had to be intact.

3.3 AA2024-T351

Besides the thick samples described previously, the LSP and the subsequent RS measurements were carried out also on thin samples supplied by EADS and treated with LSP by two different laser suppliers as described in chapter 2: Universidad Politécnica de Madrid (UPM) and Toshiba Corporation, Japan. In both cases the aluminium alloy used was AA2024-T351 typical of aerospace structures applications. The main chemical composition is reported in the following table while some minor alloy elements were not reported:

Table 3.2

Element	Al	Cu	Mg	Mn	Zr
Weight %	89.0	4.5	1.3	0.6	0.5

The T351 temper treatment is a solution heat treatment at 493°C followed by a subsequent cold work to straighten. The samples were all clad, i.e. they have a 0.2 mm layer of pure aluminium on both faces in order to protect the AA2024 from corrosion. Twelve samples were supplied by UPM, all of them 2 mm thick, 100 mm wide and 160 mm long. Six samples were subjected to a single LSP treatment of one stripe 10 mm wide and 100 mm long, while the remaining six samples were double-peened which means the same LSP treatment was repeated on the back surface, with the treatment of the front surface. For all the samples a laser energy of 4.8 J/pulse was used. A picture of the sample can be seen in Fig. 3.9:

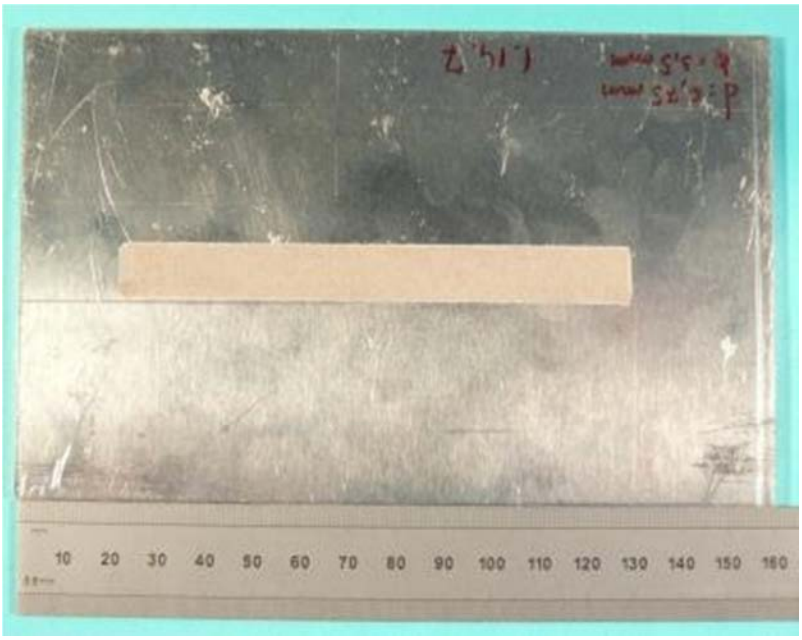

Fig. 3.9 Picture of the sample LSP'ed by UPM

The list of samples is seen in the following table:

Table 3.3 List of samples supplied by UPM

Aluminium Alloy AA2024-T351					
Specimen number	Overlapping distance d (mm)	Pulses/cm^2	Spot diameter (mm)	Peened surfaces	Power Density GW/cm^2
1.15.4	0.75	178	2.0	Single	8.92
1.15.3	0.90	124	2.0	Single	8.92
1.15.6	0.75	178	2.5	Single	5.71
1.15.8	0.90	124	2.5	Single	5.71
1.13.2	0.75	178	3.5	Single	2.91
1.13.6	0.90	124	3.5	Single	2.91
1.13.4	0.75	178	2.0	Double	8.92
1.14.1	0.90	124	2.0	Double	8.92
1.14.3	0.75	178	2.5	Double	5.71
1.14.4	0.90	124	2.5	Double	5.71
1.14.7	0.75	178	3.5	Double	2.91
1.16.1	0.90	124	3.5	Double	2.91

The metallographic analysis results are reported in [1] while the analysis by SEM was carried out by EADS before and after the LSP treatment and pictures are shown in Fig. 3.10:

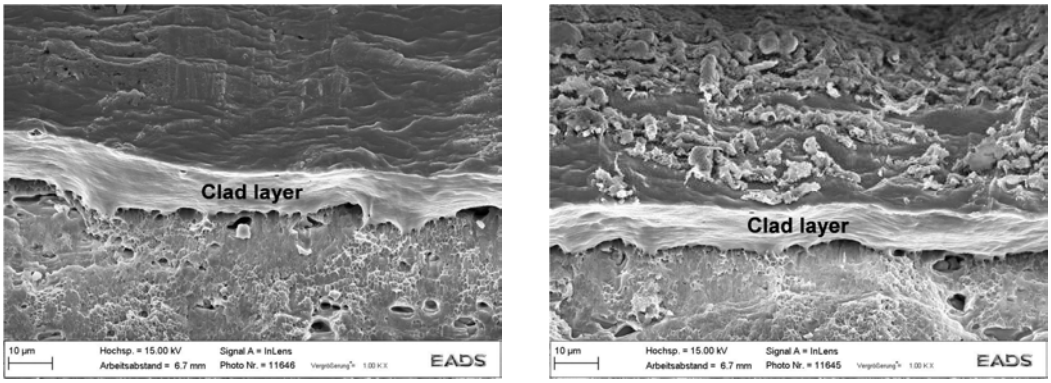

a) b)

Fig. 3.10 The surface of the sample a) before LSP and b) after LSP both obtained by internal reports

It is possible to see in Fig. 3.10 a) and b), that LSP seems to not have melted locally the clad layer.

The sample supplied by Toshiba was LSP'ed as well on both faces. The peened area was 10 mm wide and 40 mm long. A power density of 1.99 GW/cm^2 was used. The sample is shown in Fig. 3.11:

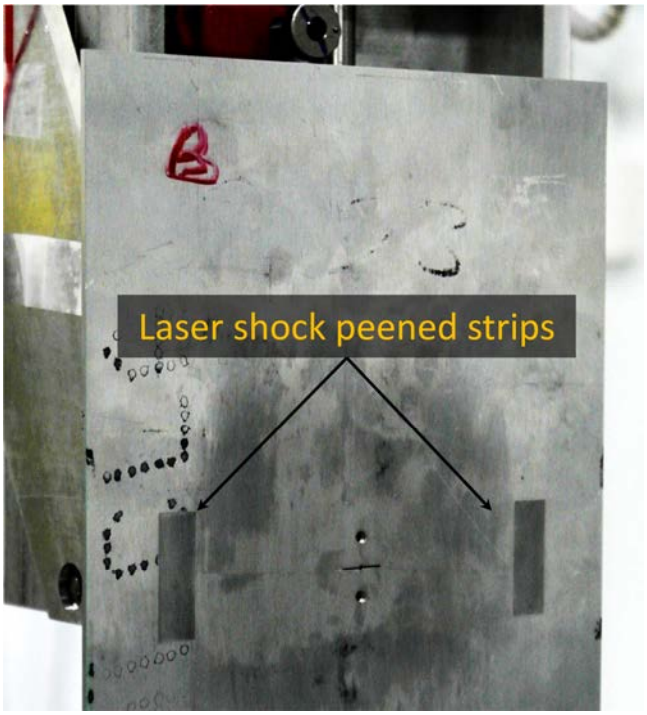

Fig. 3.11 sample supplied by Toshiba

Two samples were available for residual stress measurements but due to lack of time at the beamline, only one sample was able to be tested and the results are reported in chapter 9.

3.4 Conclusions

In this chapter a list of the samples used during this research program and some metallographic analysis were reported. All the described samples were measured with different residual stress measurements techniques as it will be described in chapter 4 and the results are reported in chapters 6 for the stepped coupon, 7 for the SEN, 8 for the thin single laser shock peened samples and 9 for the double peened ones. In particular the thick samples were used in this thesis in order to study the application of Eigenstrain on both more complex geometries and to study the possibility to predict the RS field when both LSP and SP are applied on the sample surface. The thin samples instead were used in order to understand the distribution of the RS field after a single and a double peen treatment.

Reference

[1] M. B. Toparli, "Analysis of Residual Stress Fields in Aerospace Materials After Laser Peening," PhD Thesis, The Open University, Milton Keynes, 2012.

[2] H. E. Hu, L. Zhen, B. Y. Zhang, L. Yang, and J. Z. Chen, "Microstructure characterization of 7050 aluminum alloy during dynamic recrystallization and dynamic recovery," *Mater. Charact.*, vol. 59, no. 9, pp. 1185–1189, Sep. 2008.

[3] H. Luong and M. R. Hill, "The effects of laser peening and shot peening on high cycle fatigue in 7050-T7451 aluminum alloy," *Mater. Sci. Eng. A*, vol. 527, no. 3, pp. 699–707, 2010.

[4] U. C. Heckenberger, V. Holzinger, W. von Bestenbostel, and E. Hombergsmeier, "Laser shock peening to improve the fatigue resistance of AA7050 components," *Int. J. Struct. Integr.*, vol. 2, no. 1, pp. 22–33, 2011.

[5] U. C. Heckenberger, E. Hombergsmeier, and D. Furfari, “Residual stress fields in LSP and SP treated aluminium specimens after fatigue testing,” in *4th International Conference on Laser Peening and Related Phenomena;* 2013, unpublished research.

4 Residual Stress Measurements

In this chapter all the residual stress measurement techniques used for the experiments described in this dissertation will be discussed. For each of them, a detailed explanation of the technique principles will be given. Then, a description of each experiment will be included. In particular, here can be found: Incremental Hole-Drilling technique and the description of the measurements for the thin plates; Synchrotron X-ray and Neutron diffraction techniques with the details of the experiments for all the sample used. Since the latter techniques are available only in large-scale facilities, a brief description of them will be given as well.

4.1 Hole-drilling

Incremental Hole-Drilling (ICHD) is one of the most common used, cheapest and reliable techniques available for measuring the RS. It is considered to be a destructive technique since it's based on material removal and subsequent stress relaxation. However, since the drilled holes can be small enough to not compromise the structural integrity of the tested specimen, within certain limits ICHD can be considered to be a semi-destructive technique.

ICHD made its first appearance in 1934 when Mathar [1] published a paper describing the technique which can be summarized in these three steps:

1. Drilling of a small hole in order to let the stress relax;
2. Recording of the strain relaxation;
3. Computing the strain to calculate the stresses present before the drilling process.

Even if the technique philosophy hasn't been changed, the drilling process has been improved as well as the displacement recording techniques. The experiments carried out

in this project are based on the standard method described in the ASTM Standard E837 [2], and the NPL Measurement Good Practice Guide No. 53 [3].

The drilling process consists of removing, with successive steps, thin layers of material in order to let the surrounding material relax. As it was studied by Nau *et al.* [4], this process has better results when an orbital milling is adopted. In this way, the applied forces and the heat generated are smaller than the drilling process without the orbital movement and all these factors result in more stable strain readings. The other two important parameters to take into account during the drilling process are the final diameter of the drilled hole and its total depth. Generally speaking, larger final hole diameters are preferred in most cases in order to have more removed material, and so larger displacements. Regarding the final depth of the hole, it is suggested to not be deeper than the half of the final hole diameter in order to allow the strain recording sensor to detect the displacements of the material even when they are not close to the surface.

The displacement recording process is probably the most diversified aspect of this technique. There are several sensors that can be used to detect the displacements which occur after the material removal. The most known and used sensors are strain gauges and the ASTM Standard Test Method E837 was introduced to be used as reference for this process: more details about it can be found in the next section. More recently, optical methods like Moiré [5], and Digital Image Correlation [6], [7] were developed as well as Electronic Speckle Pattern Interferometry (ESPI) which will be described in more detail in section 4.1.2.

The last step during the hole-drilling process consists of calculating the residual stress profile from the detected displacements. For this purpose the ASTM E837 standard reports all the coefficients (G_{ij}) needed to apply the Integral Method which was proposed by Schajer [8], [9] and is considered to be the most accurate method for non-uniform

residual stress profiles. This method is based on change of the stiffness due to the drilling process. In Fig. 4.1 the importance of the calculation of the coefficients G_{ij} is shown. It is possible to see that every further drilling increment allows the relaxation of the residual stress in the entire section but at the same time the stiffness of the sample changes as well. Considering for example the first drilling step, a coefficient G_{11} is calculated which takes into account the stiffness of the sample when the first hole is drilled. After three more steps of drilling, still residual stress relaxation occurs close to the edge but, due to the change of the stiffness, this relaxation cannot be modelled with the same coefficient calculated at the first step (G_{11}) even though the position is the same. A new coefficient is needed: G_{41}. All these coefficients were calculated through Finite Element Analysis (FEA) and reported in ASTM E837 in order to calculate easily the residual stresses during the measurements without the need of further modelling.

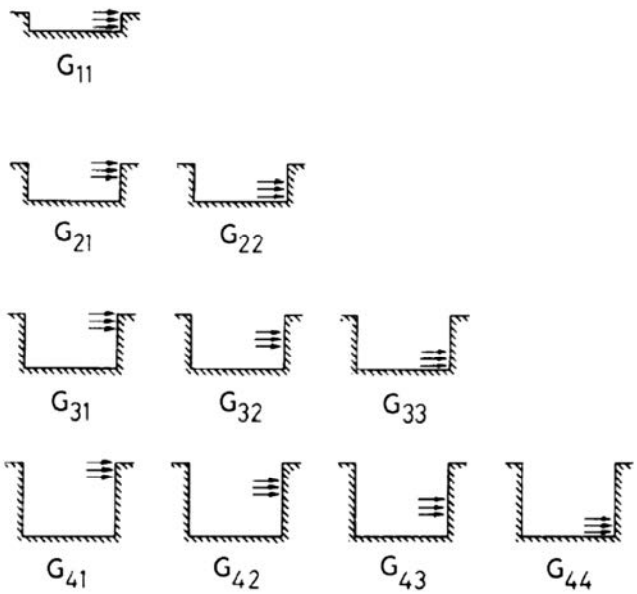

Fig. 4.1 Schematic representation of the calculated coefficients through FE modelling.

The hole-drilling technique has been used in this research for two different RS measurements: to measure the RS profile in thin aluminium alloy samples, and in a 5 mm curved edge of a 28 mm thick stepped coupon. For the first purpose, strain gauges were

used to measure the displacement during the stress relaxation while for the second purpose, the Electronic Speckle Pattern Interferometry technique was used with the collaboration of the Helmholtz-Zentrum in Geestacht, Germany. In the next two sections both experiments are described and the measurement details are reported.

4.1.1 Application of Strain Gauges on thin aluminium alloy samples

ICHD coupled with strain gauges is most probably the most used residual stress measurement technique due to its reliability, cost and availability. Previously hole-drilling was used to measure the residual stress profile generated by shot peening [10] and further studies demonstrated good agreement with the X-ray diffraction technique [11] and the neutron diffraction technique [12]. For this reason the technique was chosen to get a first estimation of the residual stress profiles generated by different laser peening settings in thin aluminium alloy samples and the results were published by Dorman et al. [13]. The same technique was used for several samples by Toparli and data were presented in [14]. Since the samples are 2 mm thick, the same approach described by Toparli was used: a thick epoxy resin support was installed first on the back of the samples in order to allow deeper measurements than is admitted by the standard. Toparli demonstrated not only that coefficient corrections were not needed because of the presence of this support, but also that the reliability of the data close to 1.4 mm from the surface of the sample (which is more than half of the sample) was still good. The strain gauges were them applied to the surface.

The strain gauge is a device used to measure the elastic strain in a component. It is usually formed by a thin constantan alloy foil attached to a polymer substrate to allow easy handling of the foil and to attach it to the specimen surface through suitable glues. When the sample is subjected to an elastic deformation, this will elastically modify the length of the foil pattern which becomes narrower and longer in case of a tensile load and

broader and shorter in case of a compressive load. These changes in dimensions change the electric conductance of the gauge from which it's possible to infer the total strain change.

The process of the sample surface preparation to stick the strain gauges to the sample is described in the ASTM standard E837 and in [3]. Generally speaking the process involves the following steps:

- Preparation of the metallic surface by grinding it to get as flat a surface as possible;
- Degreasing the surface to eliminate any contamination;
- Treating the surface with conditioner to remove all the remaining dirt;
- Neutralizing the surface to eliminate any residual of the conditioner in order to return the surface to an optimum neutrality of pH 7;
- Gluing the strain gauge on to sample surface.

According to [15], grinding the surface of a metallic sample can introduce further residual stresses up to the 80% of the material yield stress into a depth of 60 μm underneath the surface. Since our aim was to measure the residual stress profile at the surface of the sample (which is considered to be the most important area, as said in chapter 2), the grinding process was avoided and the sample was first degreased and then directly conditioned, neutralized and the sensor was finally applied. The strain gauges used are shown in Fig. 4.2 and they are produced by Vishay, UK.

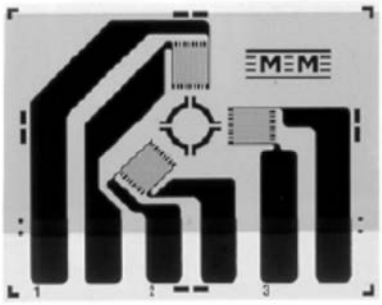

Fig. 4.2 Picture of the strain gauge used for all the RS measurements

These hole-drilling measurements were carried out with the set-up of Stresscraft, UK. The system, which can be seen in Fig. 4.3, allows the alignment of the sample to the drilling axes through a magnifier.

Fig. 4.3 Hole-Drilling system [14]

The samples were then fixed to the table with Blu-Tack. The drill tip diameter was 1.2 mm and the eccentricity was 300% (with a total nominal final hole of 3.6 mm). The drilling steps were so divided: 4 steps of 32 μm each, 8 steps of 64 μm each and 8 steps of 128 μm each. The final nominal depth resulted to be 1408 μm. As the strain gauge remains at the surface of the sample for the entire experiment, it loses sensitivity as the drilling depth increases. In order to be able to still record the strain changes even when the depth of the hole is larger, the amount of the removed material has to increase. Finally the strains are

calculated by the Stresscraft RS INT software version 5.1.3 which gives in output the normal stress in the two directions of alignment of the strain gauge, the shear stress and the principal stress components. All these calculations are based on the Integral Method proposed by Schajer [8], [9].

In a different experiment with a stepped coupon sample, we wanted to measure the residual stress profile after the laser peening treatment on a curved edge of 5 mm radius. Due to the geometry, the strain gauge application was not preferred and a different approach was necessary. For this reason, an optical system has been used at the Helholtz-Zentrum, Geestacht, Germany.

4.1.2 Electronic Speckle Pattern Interferometer

In the system employed in this work, an electronic speckle pattern interferometer (ESPI) [16] replaces the strain gauges. This allows a fast, non-contact and easy measurement, avoiding the procedure of strain gauge application. In the case of a dull surface, no specific preparation of the sample is required for this technique. If the surface of the sample is too shiny, a spray paint must be used in order to avoid reflection of the laser beam and this was the case in the presented experiment. To avoid any reflection, first a layer of paint was sprayed onto the surface of the sample then, to hide the most reflective area surrounding the hole, a paper tape layer was applied all around the area where the hole was going to be drilled.

The ESPI hole-drilling measurements were conducted at Helmholtz-Zentrum-Geesthacht, using a Stresstech PRISM system as shown in Fig. 4.4.

Fig. 4.4 Setup of the ESPI incremental hole-drilling system [17]

As shown in Fig. 4.4, the light from a coherent laser source is split into two parts. One part illuminates the object, which is imaged by a Charge-Coupled Device (CCD) camera. The second light (called the reference light) passes through an optical fibre directly to the camera. The two parts of the laser light interfere on the CCD surface to form a speckle pattern. The phase at each pixel of the camera is determined by taking images at four phase angle steps. Deformations of the object surface, caused by the hole-drilling, change the relative path lengths of the illumination and reference beams and hence the measured phases. Subtraction of the pixel phases measured before and after hole-drilling gives the surface displacements, from which the in-plane residual stresses can be calculated. Details of this technique can be found in [16], [18], [19].

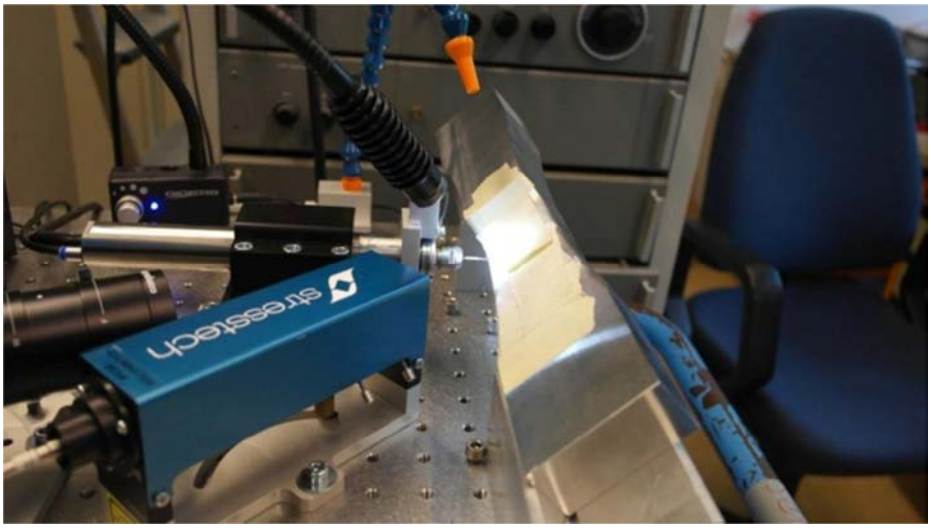

Fig. 4.5 The set-up of the measurement for the experiment. On the left the blue box is the illumination laser while the black camera behind it is the CCD camera. The drill tip is set-up in order to be perpendicular at the curved surface

In Fig. 4.5 the experiment set-up is shown. Since the measured line was normal to the surface of the curved edge, the sample was laid on two clamps to allow the measurement line to be co-axial to the drill bit axis. The drill steps chosen were alternatively 0.03 mm and 0.02 mm so that the sequence of the depths drilled through the thickness was 0.03 mm, 0.05 mm, 0.08 mm, 0.10 mm and so on up to 0.3 mm where the steps were changed and were fixed to 0.05 mm each up to 0.7 mm. The process was totally automatic and when the strain measurements were finished, the software PRISM gave the output of the residual stress profile.

4.2 Bragg's Law

X-rays and neutrons share several physical properties which make them suitable for the investigation of residual stresses. Both of them have wavelengths in the order of atomic distances in conventional metallic materials and they can penetrate without interacting from some μm to cm. On the other hand a distinction between the two must be made: X-rays interact strongly with the surrounding matter due to the Coulomb

interaction and for this reason laboratory X-rays are used for surface measurements (weak X-rays) or, at synchrotron facilities, they have enough energy to penetrate several mm of material; neutrons are small particles without charge and for this reason their interaction with the surrounding matter is weaker and this allows their use when the thickness of the sample is of several cm. Generally speaking, when a beam made of photons or neutrons interacts with matter, scattering phenomena may occur in particular conditions. Considering the figure below:

Fig. 4.6 Schemata of the diffraction phenomena [20]

It is possible to see from Fig. 4.6 that the scattering which occurs at atom P and K has the same path length (1-1' and 1a-1a') and can be calculated as:

$$QK = PR = PK\cos\theta$$

Equation 4.1

Similarly, when atoms from different planes are scattering the X-rays, e.g. K and L, the path length (2-2') will be different due to the longer distance the X-rays have to travel to reach deeper atoms. This difference can be formulated as:

$$ML + LN = 2d\sin\theta$$

Equation 4.2

In order to obtain constructive interference for X-rays 1 and 2, the difference in path length should be equal to an integer (n) multiple of the X-ray wavelength (λ).

This linear relationship was formulated for the first time in 1912 by W. L. Bragg and it is expressed as:

$$n\lambda = 2\,d\,sin\theta$$

Equation 4.3

Which is the basic equation to derive all the equations needed for different techniques that are going to be presented in the this chapter.

During the experiments the diffraction pattern is formed by a flux of particles which before diffraction is called the incoming beam and after diffraction is called the outgoing beam. The 3D space where the two beams encounter is called the gauge volume. The gauge volume is the portion of the samples where the diffraction phenomenon takes place and the size of it is a key element during the experiments because it defines the spatial resolution for the residual stress measurements. The picture below shows the definition of the gauge volume:

Fig. 4.7 In grey shade the gauge volume is highlighted [21]

In Fig. 4.7 is possible to see how the gauge volume is formed. On the left the incoming beam dimension is tailored by a slit so it is possible to fix the height and width of the beamline. After the sample, the second slit defines the length of the final gauge volume.

4.3 X-ray diffraction

As said in the introduction, X-ray diffraction is a phenomenon generated by the interaction between photons and matter. Depending on the energy of the photons, they are able to penetrate from some millimeters to some centimeters of matter. For this reason there are two different ways to produce photons for the residual stress measurements purpose: either by producing and accelerating electrons inside a vacuum tube and then rapidly stopping them, or by using the phenomena of synchrotron radiation. The first method is cheaper and it is the one used for laboratory-based surface X-ray diffraction; while the second method (sometimes called hard X-rays due to the higher energy level) needs large-scale facilities (synchrotron sources) to accelerate and deviate the electron beam, and it allows the measuring of residual stresses up to several centimeters through a sample thickness. In this dissertation both methods will be explained in detail: surface X-ray diffraction will be described in section 4.3.1, while diffraction by synchrotron radiation will be explained more in section 4.3.2.

4.3.1 Surface X-ray method

As said before, Bragg's law is considered the most important equation in the diffraction methods. In order to calculate the stress, the strains must be calculated first. By recalling the definition of the strain given in chapter 2: "normalized measure of the deformation relative to a reference length", it is possible to conclude that the strain in the residual stress measurement can be defined in this way:

$$\varepsilon = \frac{d - d_0}{d_0}$$

Equation 4.4

Where d is the distance between two atom layers while d_0 is the unstressed lattice parameter that must be used as a reference length. One of the most common methods to calculate the stresses is the $sin^2\psi$ method. Considering Fig. 4.8:

Fig. 4.8 Schematic of surface XRD showing the interplanar spacing measured and principal stress directions [20]

The previous figure shows a generic distribution of three principal stress components and the generic lattice distance (d and $d_{\phi\psi}$). The perpendicular strain components can be written exactly like Equation 4.4, while a generic strain component $\varepsilon_{\phi\psi}$ can be written as:

$$\varepsilon_{\phi\psi} = \frac{d_{\phi\psi} - d_0}{d_0} = \varepsilon_{11}\cos^2\phi\sin^2\psi + \varepsilon_{12}\sin 2\phi\sin^2\psi + \varepsilon_{22}\sin^2\phi\sin^2\psi + \varepsilon_{33}\cos^2\phi + \varepsilon_{13}\,\mathrm{com}\,\phi\sin 2\psi + \varepsilon_{23}\sin\phi\sin 2\psi$$

Equation 4.5

With Equation 4.5 is possible to calculate the plane stress components. Furthermore, it is possible to affirm that when the measurement of the strains are close to the surface, the component of the stress perpendicular to this surface (σ_{33}) is 0, even if that doesn't mean the component of the strain in the same direction is 0. As stated before, the energy of the X-ray produced by a vacuum tube is small enough to not allow a large penetration of the photons within the sample. Usually, the maximum penetration in depth achieved with this

technique is aluminium alloy is 17 μm when a Cr-α tube is used according to [20]. For this reason, the measurement of the residual stress does not take into account the out-of-plane component. Thus, stating that σ_{33}=0, it is possible to calculate the following equation by using Equation 4.4 and Equation 2.8 section 2.1.2:

$$\varepsilon_{33} = \varepsilon_{\perp} = \frac{\mathrm{d}_{\perp} - \mathrm{d}_0}{\mathrm{d}_0} = -\frac{\nu}{E}(\sigma_1 + \sigma_2)$$

Equation 4.6

By using Equation 4.6 and Equation 4.5 we can obtain the following equation:

$$\varepsilon_{\phi\psi} = \frac{\mathrm{d}_{\phi\psi} - \mathrm{d}_0}{\mathrm{d}_0} = \frac{1+\nu}{E}\sigma_{\phi}\sin^2\psi - \frac{\nu}{E}(\sigma_1 + \sigma_2)$$

Equation 4.7

where $\sigma_{\phi} = \sigma_1 \cos^2\phi + \sigma_2 \sin^2\psi$.

Finally, by rearranging Equation 4.7 it is possible to obtain the following equation for the $\mathrm{d}_{\phi\psi}$ measurement:

$$\mathrm{d}_{\phi\psi} = \left(\left(\frac{1+\nu}{E}\right)\mathrm{d}_0\sigma_{\phi}\right)\sin^2\psi - \left(\frac{\nu}{E}\right)(\sigma_1 + \sigma_2)\mathrm{d}_0 + \mathrm{d}_0$$

Equation 4.8

Equation 4.8 describes the fundamental relationship between the lattice spacing ($\mathrm{d}_{\phi\psi}$) and the biaxial stress state of the component surface and it is worth noting that there is a linear dependency between $\mathrm{d}_{\phi\psi}$ and $sin^2\psi$. For this reason, the residual stress can be calculated for different ψ angles and for each of them a point in a plot $\mathrm{d}_{\phi\psi}$ vs. $\sin^2\psi$ can be obtained like the one in Fig. 4.9. The slope of the plot gives the values of the σ_{ϕ}, the elastic

constant E and ν are usually known or can be calculated experimentally. This method is the so-called *sin²ψ* method.

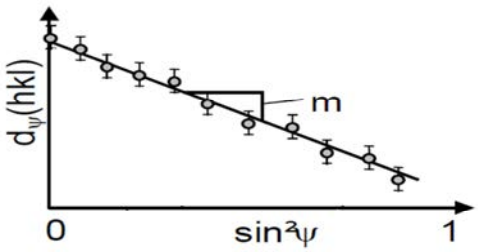

Fig. 4.9 $d_{\phi\psi}$ vs. $\sin^2\psi$ plot

Regarding the d_0 the following consideration must be done [22]: by considering the Equation 4.8 calculated when $\sin^2\psi=0$ we obtained the following equation:

$$d_{\phi 0} = d_0 \left[1 - \left(\frac{\nu}{E}\right)(\sigma_1 + \sigma_2)\right]$$

Equation 4.9

Equation 4.9 described the relationship between d_0 and $d_{\phi 0}$.

Since generally $E \gg (\sigma_1 + \sigma_2)$ the value of d_0 and $d_{\phi 0\ differs}$ only by ±1% i.e. they can be considered the same. At the same time we can calculate the slope of the plot:

$$\frac{\partial d_{\phi\psi}}{\partial \sin^2\psi} = \left(\frac{1+\nu}{E}\right) d_0 \sigma_\phi$$

Equation 4.10

And by rearranging Equation 4.10 for the stress σ_ϕ we obtain the following equation:

$$\sigma_\phi = \left(\frac{E}{1+\nu}\right)\frac{1}{d_0}\left(\frac{\partial d_{\phi\psi}}{\partial \sin^2\psi}\right) = \left(\frac{E}{1+\nu}\right)\frac{1}{d_{\phi 0}}\left(\frac{\partial d_{\phi\psi}}{\partial \sin^2\psi}\right)$$

Equation 4.11

In this way the problem becomes a differential technique and the measurement of d_0 is not required anymore. Beside the $sin^2\psi$ method there are also the single-angle and the two-angle methods which are briefly described and referenced in [22].

One last important aspect must be considered in this section: it has been said previously that there is a linear relationship between $d_{\phi\psi}$ and $sin^2\psi$ but this is not always the case. In particular, if the residual stress state on the examined sample presents a components of shear stress, the lines of the $d_{\phi\psi}$ vs. $\sin^2\psi$ plot might split. A further different behaviour of the plot might occur when the sample presents a strong texture, e.g. when a thin sample is laminated. In this scenario, the resulting plot is an oscillating line. To avoid the problem some precautions can be taken like rocking the detector of the X-ray during the measurements in order to include a higher number of grains and reduce the effect of the preferential direction of elongation. All the three cases shown in [14] from where Fig. 4.10 is taken:

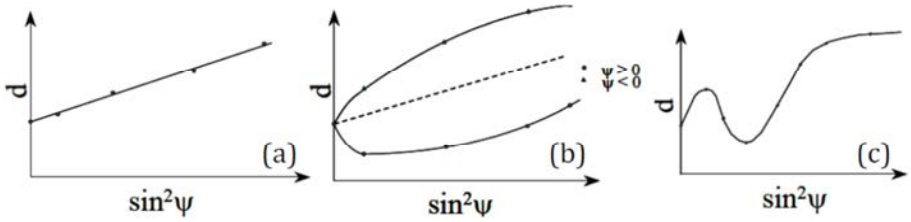

Fig. 4.10 Different $d_{\phi\psi}$ vs. $\sin^2\psi$ plot: (a) linear, (b) split due to the shear stress and (c) oscillating line due to textured structure.

4.3.1.1 Surface X-ray technique for thin aluminium samples

Surface XRD experiments were carried out with a Stresstech X3000 diffractometer equipped with a G2 goniometer. The measurements were carried out according to the NPL Good Practice Guide No. 52 [20]. A Chrome anode was used in order to obtain diffraction peaks generated by the 311 lattice plane which, according to the same reference, reflects the macroscopic behaviour of the aluminium more closely than any other lattice plane and

has a high multiplicity (24) which means that it is preferred for highly textured sample. For this reason the detectors were set with an angle of 139.9°. Tests were carried out with two different collimators: 1 mm and 2 mm in diameter. Since the sample was highly textured and there was a preferential direction of the elongation of the grains due to the lamination process, the 2 mm collimator was chosen for all the tests in order to include more grains during each measurement. As stated previously, d_0 measurement is not requested in this type of analysis, however, the machine requires a calibration which was carried out with a powder aluminium sample. For the residual stress measurement test, the ψ angle was set to ±40°. An additional rocking angle of ± 5° was added during the measurements. This rocking movement allows the introduction of more diffracting grains inside the gauge volume, i.e. it reduces problems related to the texture. Once the diffracted peaks were fitted, the $sin^2\psi$ method is applied to calculate the residual stress. Generally, the residual stresses measured with a surface XRD are considered to be measured at a depth of 40 μm from the surface and the gauge volume is as big as the collimator diameter.

Thin aluminium alloy AA2024-T351 samples, both single and double-side laser shock peened, were the subject of RS measurements with this technique. The aim of the measurements was to get the RS values close to the surface in order to compare them with the results obtained with the hole-drilling technique. The following scheme shows the path of measurements for the XRD technique:

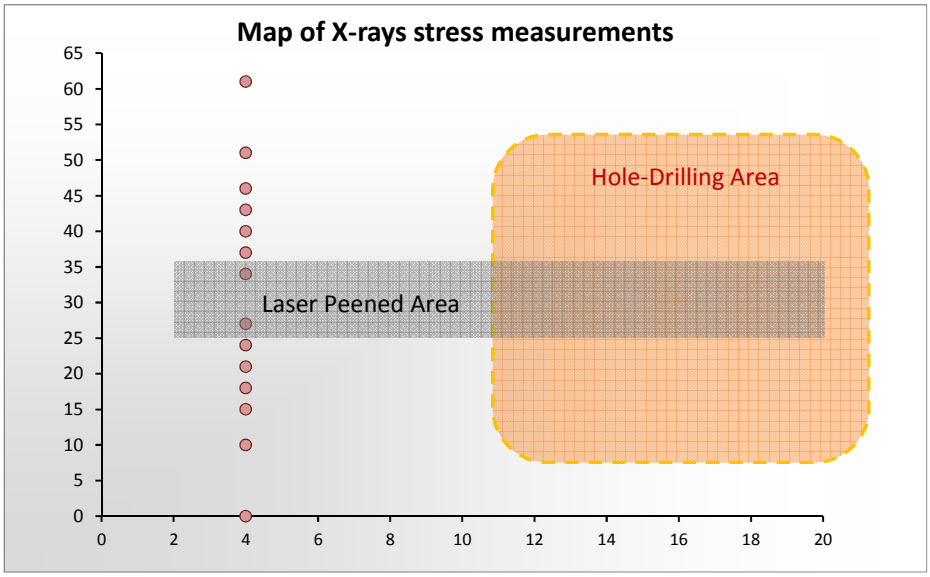

Fig. 4.11 Distribution of measurement points used for the laser peened plates

In Fig. 4.11 the distribution of the measurement points is shown. Four rows made of 14 measurement points were taken, one outside the laser peened area and three inside of it. The rows were aligned to the coordinate system of the laboratory X-ray instrument so the (0;0) point of the plate coincides with the centre of the instrument coordinate system.

4.3.2 Synchrotron Radiation

Synchrotron Radiation (SR) consists of a controlled emission of electromagnetic radiation (photons) due to the acceleration (or deceleration) of charged particles like electrons. SR possesses several interesting properties and among which we can list the following [23]:

- Continuous spectrum of energy;
- High intensity;
- Small beam dimension.

The continuous spectrum energy allows tuning the energy of the X-rays to the required energy level, which due to Bragg's Law, will highlight the desired diffraction peaks during analysis; the high intensity allows a deeper penetration depth than the laboratory X-rays so it is possible to measure the residual stresses up to several centimetres depth; finally

the small beam dimension allows a high spatial resolution, better than neutrons as will be described in paragraph 4.4. SR is produced in large-scale synchrotron facilities and a general sketch can be found in the following picture:

Fig. 4.12 Sketch of the SOLEIL synchrotron radiation storage ring [24]

In Fig. 4.12 is possible to see a sketch of the SOLEIL Synchrotron built in France [24]. The same configuration applies for all the synchrotron sources visited for the experiments reported in this dissertation. In more detail, the synchrotron in general is composed of a booster/injector where the electrons are produced, then they are accelerated up to 99.99% of the speed of light and increase their energy. Once the desired speed and energy level is reached, the electrons are injected into the main ring. To keep the charged particles in a circular trajectory a force is needed. This force takes its name after H. Lorentz and it originates from the interaction of the charged particle and a magnetic field produced by the bending magnets. Once the charged particles deviate from their circular trajectory, photons are emitted in a trajectory tangential to the photons' direction. In order to increase the intensity of the light (or brilliance) to a factor of 10^6 [25], a linear

insertion device is installed in state-of-the-art synchrotrons. These linear devices are called wigglers and undulators and they are composed of several couples of magnets which rapidly change the trajectory of the particles allowing them to emit more photons. During this process the charged particles lose energy which is compensated in radio-frequency cavities which re-accelerate the particles. All the photons produced are eventually guided through mirrors into the experimental hutch. The photons then will be tailored through slits as large as the chosen beam size and finally directed to the sample (in the case of a monochromatic beam the photon will first cross a crystal to extract the desired wavelength). The diffraction pattern is recorded by a detector placed after the sample at a fixed distance.

With SR the strains can be measured with two different approaches:

1. **Angle Dispersive XRD**: the strains are related to the shifting of the diffracted peak. The beam must be monochromatic and the diffraction plane peaks obtained are depending on the slits used;
2. **Energy Dispersive XRD**: the beamline is kept polychromatic which means photons with different energy levels are present at the same time. In this configuration it is possible to have photons diffracted by different planes at diverse penetration depths [26].

In the present dissertation both techniques were used for the experiments. In the following sections, the beamlines used will be described and the experimental details will be discussed. In particular, for the angle dispersive technique, measurements on 2 mm thick aluminium alloy double-peened samples were performed at Argonne Photon Source, USA, and for the 28 mm thick aluminium sample experiments were performed both at PETRA III, Germany, and Diamond Light Source, UK. For the energy dispersive approach, experiments were performed at Berliner Elektronenspeicherring-Gesellschaft für Synchrotronstrahlung (BESSY-II), Germany.

4.3.2.1 Conical slits

When a polycrystalline sample is exposed to a photon or neutron flux, the Debye-Scherrer cones are produced due to the diffraction phenomena and the section of these cones can be recorded through a detector as shown in Fig. 4.13.

Fig. 4.13 Debye-Scherrer rings with apex aperture of $2\theta_1$ and $2\theta_2$ generated by the scattered photons [27]

Each cone is generated by a different diffraction plane and their apex angle is the scattering angle 2θ and, as said before, this angle can be related to the $2\theta_0$ generated by the unstressed lattice parameter and by the shift of the peaks' positions is possible to calculate the strain. If no slits were put between the sample and the detector, the information given by the cones would be averaged all through the thickness, which is not scientifically relevant to study the residual stress profile generated by a surface treatment. The slits allow us to limit the length of the generated gauge volume in order to achieve a better spatial resolution along the longitudinal axis, i.e. the beam axis. The Single Triangulation Slit allows measurement of only a portion of one Debye-Scherrer's ring , thus only one diffraction plane per measurement can be detected; the Spiral Slit allows measurement of several portions of the Debye-Scherrer's rings but not the entire cone section; the Conical Slit was recently introduced and it allows measuring the complete section of one or more Debye-Scherrer's rings (depending on the alignment) in order to

get two strain components in one measurement for a given depth and their set-up can be seen in Fig. 4.14:

Fig. 4.14 Set-up for the conical slits for strain measurements [28]

In [29] descriptions for both the conical and spiral slits are reported but a brief description of the former only will be given since it was used in two separate experiments in this thesis. As reported in [30], the conical slits consist of a 4 mm thick tungsten-carbide plate with six different apertures of 25 μm each produced by Electro Discharge Machining (EDM). This configuration is useful for any fcc material. Furthermore, a centre hole is produced to let the undiffracted beam go through the slit and be stopped before reaching the detector. In Fig. 4.15 a picture of the section of the conical slit is shown:

Fig. 4.15 Section of the conical slits [31]

In Table 4.1 all the radius of the slits and the relative diffraction angles for aluminium are listed for each lattice plane used in the Argonne Photon Source for a given wavelength:

Table 4.1

Ring	Diffraction Plane	Radius (mm)	2θ (rad)
1	[1 1 1]	4.8378	0.0965
2	[2 0 0]	5.5927	0.1114
3	[2 1 1]	6.8657	0.1365
4	[2 2 0]	7.9465	0.1576
5	[2 2 2]	9.7787	0.1931
6	[3 3 1]	12.4080	0.2432
7	[4 2 2]	14.0300	0.2736

4.3.2.2 Argonne Photon Source

A synchrotron X-ray diffraction experiment was conducted at the Argonne Photon Source (APS), at beamline 1-ID, useful for powder diffraction experiments. The main characteristics of the beamline can be found in [32]. The experiments conducted at APS consisted of through-thickness measurements for thin aluminium alloy AA2024-T351

samples which were laser shock peened on both faces. The results and discussion are reported in paragraph 9.3. A previous experiment on Nickel alloy samples was reported in [33] and was used as baseline.

The monochromatic beam was obtained from the polychromatic main beamline with a Si{111} crystal. Considering the Planck-Einstein equation:

$$\boldsymbol{E = \frac{hc}{\lambda}}$$

Equation 4.12

where E is the energy of the photons, h is the Planck constant, c the speed of light and λ the wavelength of the photons, it's possible to calculate the latter once the energy is fixed. During this experiment, the energy was tuned at 54.5 keV which gives a wavelength λ=0.227Å. The experiment set-up and a picture of the used conical slits can be seen in the following pictures:

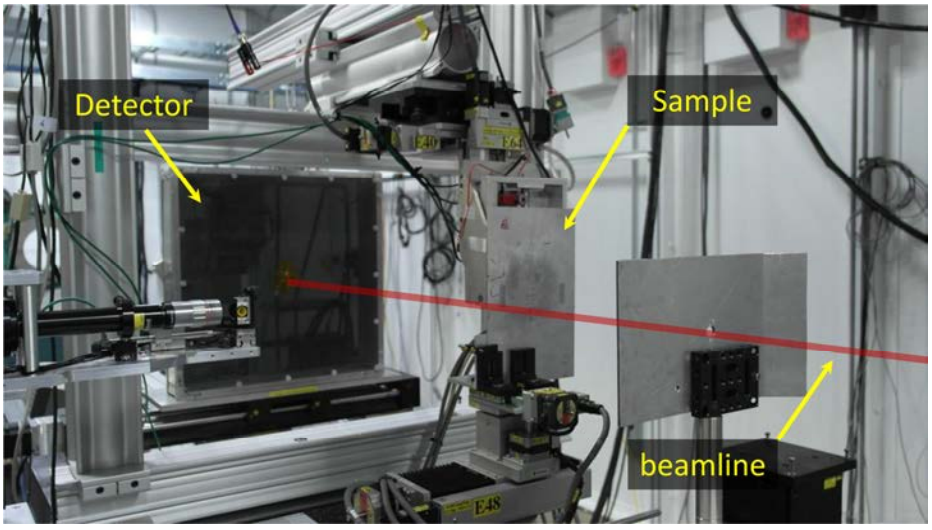

Fig. 4.16 Experiment set-up: the beamline comes from the right and it crosses an aluminium plate with a hole for alignment purposes only. Once the beamline hits the samples, the Debye-Scherrer cones are generated and they are recorded with the detector

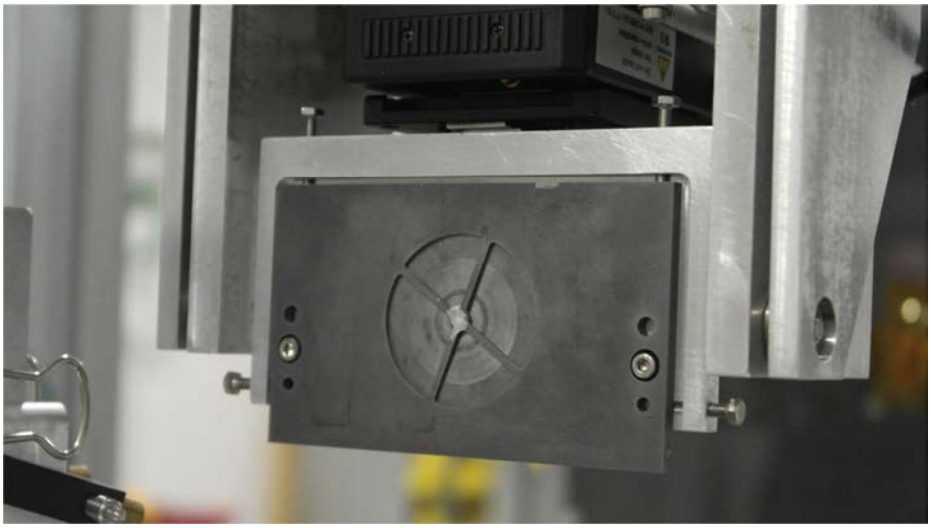

Fig. 4.17 Conical slits used for the experiment at APS

With this set-up, five different diffraction planes were able to be recorded by the detector but not all of them with the same intensity: {111} {200} {220} {311} {222}. In order to know the inter-planar atomic spacing (d) for each of the diffraction planes, the following equation can be used:

$$d_{hkl} = \frac{a}{\sqrt{h^2 + k^2 + l^2}}$$

Equation 4.13

where a is the lattice parameter and for aluminium is 4.049 Å while h, k and l are the indices of the lattice planes. By combining Equation 4.13 with Equation 4.3 (Bragg's Law) it's possible to obtain the following equation which is valid for fcc cubic structure only:

$$\left(\frac{\lambda}{2a}\right)^2 = \frac{\sin^2\theta}{h^2 + k^2 + l^2}$$

Equation 4.14

Equation 4.14 can be easily used to calculate the diffraction angles for each peak.

The following table shows the diffraction angles (2θ) for the five available planes:

Table 4.2

lattice plane	2θ (°)
{111}	5.57
{200}	6.43
{220}	9.09
{311}	10.67
{222}	11.14

Even though the NPL Good Practice Guide [20] suggests to use the {311} plane due to its higher multiplicity, the only available peak for all measurements was the {111} that eventually was chosen to calculate the strains. According to Clausen et al. [34] and Lorentzen [35], the Young's modulus calculated for the {111} is around 73 GPa which is very close to the one calculated experimentally on our samples (72 GPa). Since the difference between the two of them can be considered negligible, no further corrections were made during the calculation of the strains.

As said before, the experiment carried out at APS was intended to measure the residual stress inside thin samples which were double peened. Since the samples were 2 mm thick, good spatial resolution along the beam direction was necessary. For this reason, the size of the beam was set to 50 µm × 50 µm from which the length of the gauge volume was calculated to be around 200 µm. This gave us the possibility to measure the residual strain through the thickness with a step as small as the gauge volume length while the lateral spatial resolution was the width of the beamline, 50 µm. Due to the spatial resolution achievable and to low time required for each measurement, a 2D map of the residual strains was possible through the thickness, where both the surface of the samples were laser peened, and outside of it. To improve the reliability of the data close to the surface, the measurements were taken starting outside the sample surface and introducing the

sample into the gauge volume step by step. Further details about this technique can be found later in this section. The following picture shows the measurement points:

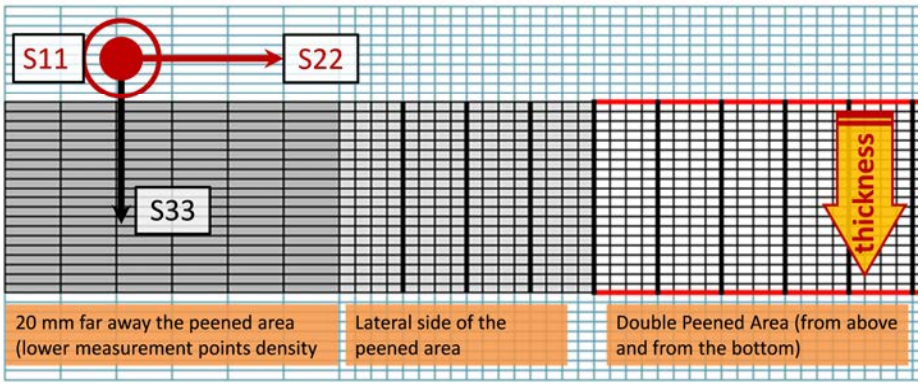

Fig. 4.18 View of the section of the thin sample. The measurement points are the points of the grid: denser through the thickness of the laser peened areas and less dense 10 mm away from it

For each measurement point, an image from the germanium detector was obtained. The pictures collected by the detector are sections of the Debye-Scherrer cones, i.e. rings. All of them are concentric and each ring is produced by a different lattice plane. All these pictures were then analysed with FIT2D software [36]. The following picture shows a generic image collected with the detector:

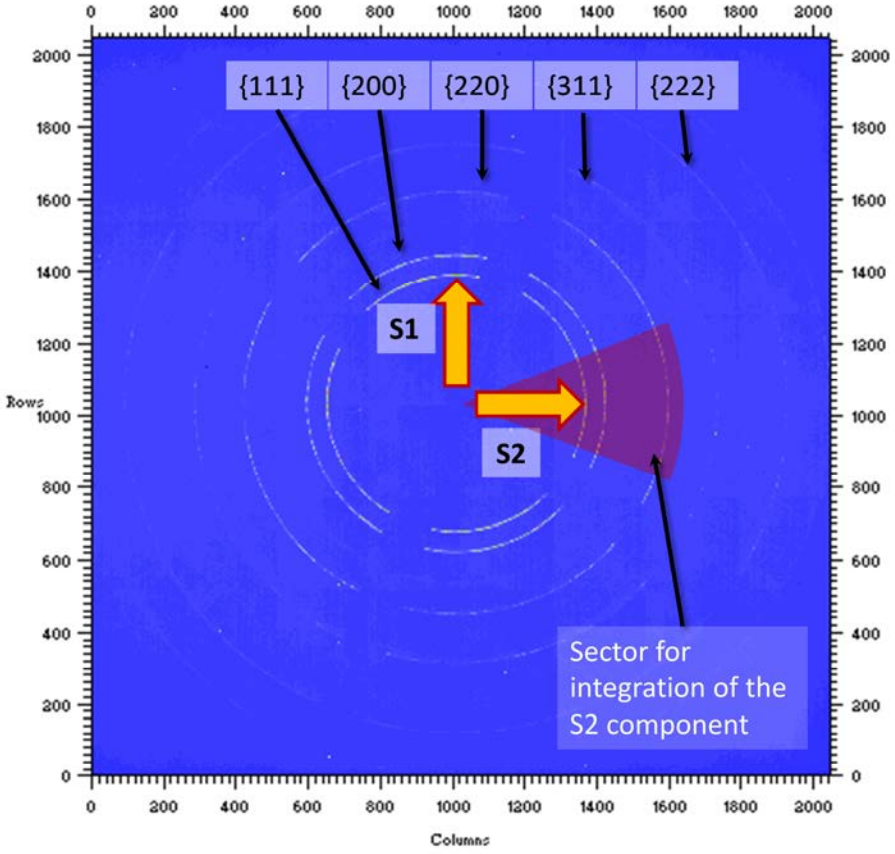

Fig. 4.19 Picture taken from the detector showing the rings of the conical slits. The more intense are the line the more photons were diffracted from that plane.

The analysis is divided into two different sets: first the parameters of the beam alignment are calculated by using a cerium oxide sample picture as calibrant; subsequently, all the collected images are integrated by sector of ±10° horizontally for the S2 stress component and vertically for the S1 components as shown in Fig. 4.19. Thus the angular position of each peak is found. The S3 component, which is directed perpendicular to the plane formed by components S1 and S2, was not possible to be measured with this configuration. However, it is worth noting that this component is considered to be 0 due to the low thickness of the sample, and, as a consequence, the distribution of the residual stresses was considered to be plane-stress. Once the angular position of the unstressed lattice parameter d_0 is known, this following equation can be applied to calculate the strains:

$$\boldsymbol{\varepsilon = -\cot\theta(\theta - \theta_0)}$$

Equation 4.15

According to Equation 2.12 in Chapter 2, the generic σ_i stress component can be easily calculated from the strains with the following equation:

$$\sigma_i = \frac{E_{hkl}}{1 - \nu_{hkl}^2}(\varepsilon_i + \nu_{hkl}\varepsilon_j)$$

Equation 4.16

where E is the Young's modulus and ν is the Poisson's ratio for the considered *hkl* lattice plane while ε_i and ε_j are the measured strains components.

As said previously, in order to get a better estimation of the surface positioning (which during the set-up is aligned to the beam centre through a laser only), the measurements were started outside the sample (where no diffraction peaks were recorded) and step-by-step the sample was introduced inside the gauge volume. The following picture shows the intensity of the detected signal during this process:

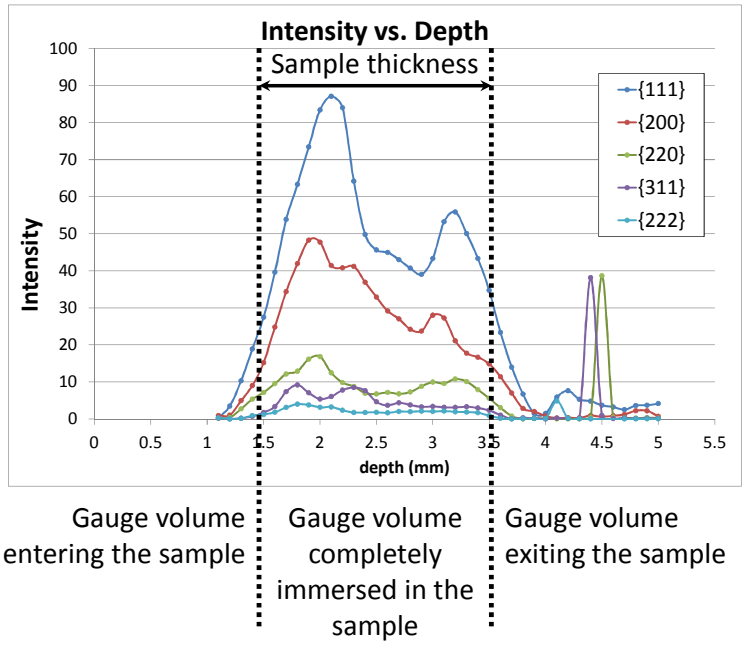

Fig. 4.20 Intensity vs. sample position

Fig. 4.20 reports the intensity vs. sample position. It is possible to see how the intensity increases as the gauge volume is introduced inside the sample[*]. When the intensity reached the highest level it means the gauge volume is completely inside the sample. During this process the gauge volume is partially filled with air and partially filled with the sample. This set-up generates fictitious strains generally called pseudo-strain. Pseudo-strains contain both the real strains of the sample close to the surface and "false" strains generated by diffraction from the non-immersed gauge volume. A further error introduced by the half-immersed gauge volume is the positioning of the centre of the gauge volume. When the gauge volume is completely immersed inside the sample, the geometric centre of it coincides with the centre of the scattering volume. When the gauge volume is not completely immersed, the scattering volume is positioned in the centre of the immersed portion only. By knowing the relative potion of the gauge volume immersed inside the sample, it is possible to calculate where the scattering volume is positioned and hence is possible to calculate the exact location of the measured strains. On the other hand, the pseudo-strain treatment is slightly more complicated. Webster et al. [37] reported that pseudo-strains can be generated (among the others) because of a geometric effect which are reported in the following picture:

[*] In reality the gauge volume position is set by the position of the conical slits and this doesn't move during the whole experiment, i.e. the gauge volume doesn't move either. What actually is moving is the sample which is mounted on a motor or hexapod. Since the movements are relative, it's easier to talk in terms of gauge volume movements rather than sample movements.

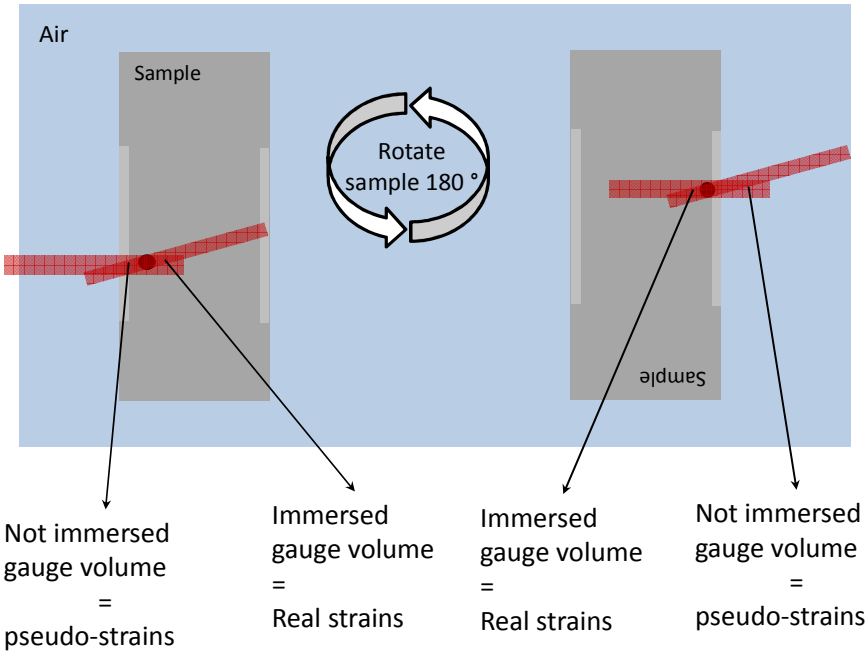

Fig. 4.21 Schematic of the geometric effect and the folding technique

In Fig. 4.21 the geometric effect is shown. The diffracted beam in the first case has to cross all the sample thickness to reach the detector while in the second case this happens to the incoming beam. To eliminate the pseudo-strains, the folding technique is applied. This technique consists of both measuring the same point (which is marked with a black spot) twice by rotating the sample of 180° as reported in Fig. 4.21. In this way the obtained strains plot looks like the following picture:

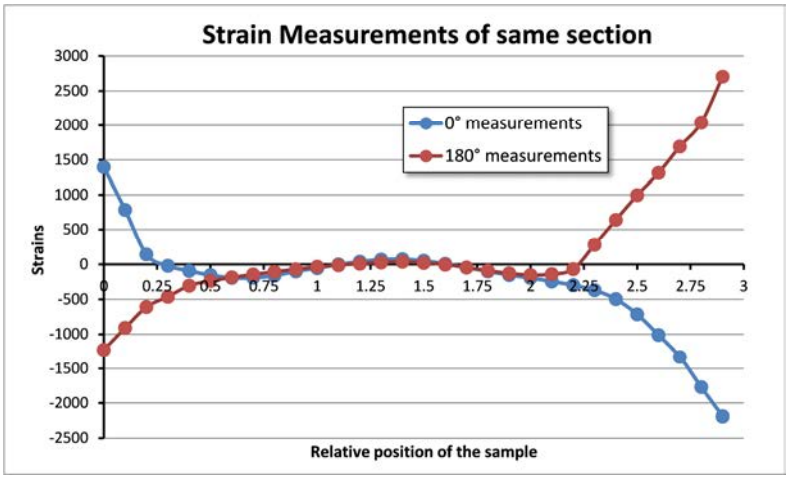

Fig. 4.22 Strain profiles with the presence of pseudo strains.

As it is possible to see in Fig. 4.22, by measuring the same sample before after a 180° rotation, the residual strain profiles through the thickness are similar while the pseudo-strains are opposite. As shown in Fig. 4.21, by a simple algebraic summation of the peak generated before and after the rotation, it is possible to finally obtain the total peak which can be easily integrated with a Gaussian function and the peaks' centres can be easily calculated as was done previously. During the rotation of the sample for the second set of measurements, a misalignment of the samples occurred. This was easily noted by the intensity vs. position graph which is here reported:

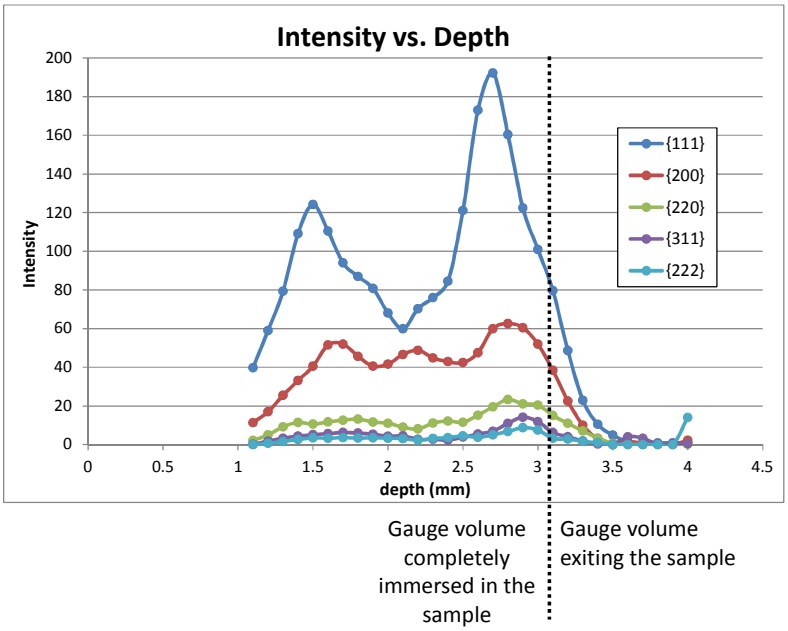

Fig. 4.23 Intensity vs. position graph once the sample was rotated of 180°

After the rotation of the sample, the gauge volume was again moved step-by-step inside the sample but, as reported in Fig. 4.23, the intensity of the first points was higher than 0 which indicates the possibility that the gauge volume was already inside the sample at the start of the acquisition. Since the alignment of the sample didn't change during the rotation process, the only reasonable explanation for this misalignment is the bending of the sample. Thin samples can present a gentle bending (in the order of millimetres or smaller) due to the laser peening process, as it was reported in [14]. In Chapter 9 the

complete 2D map of the double peened samples is presented as a comparison with hole-drilling results and how the latter can be used to correct the former.

4.3.2.3 BESSY II

Laser shock peened thin samples were also measured at the Energy Dispersive DIffraction (EDDI) beamline at BESSY-II, Germany. The characteristics of the beamline can be found in [38]. Since the beamline uses the energy dispersive technique, it is still possible to measure the residual strains through the $sin^2\psi$ method but with this technique the 2θ angle is fixed and the lattice parameter can be linked to the photon energy by combining Equation 4.3 and Equation 4.12 obtaining:

$$d(hkl) = \frac{hc}{2sin\theta}\frac{1}{E(hkl)} = cost\frac{1}{E(hkl)}$$

Equation 4.17

where h is Planck's constant, c the speed of light. Finally by combining Equation 4.4 and Equation 4.17 it is possible to calculate the strain directly from the energy of each lattice plane:

$$\varepsilon_{\phi\psi} = \frac{E_0(hkl)}{E_{\phi\psi}(hkl)} - 1$$

Equation 4.18

where $E_0(hkl)$ is the energy that corresponds to the strain-free lattice parameter $d_0(hkl)$.

It's implicit that the beamline is polychromatic in order to have photons at different energy levels, usually between 10-80 keV. Only the photons which satisfy the Bragg's equation will be diffracted from a lattice plane, depending on their energy level. This allowed us to get a residual stress profile up to 500 μm through the thickness.

At the EDDI beamline we measured the residual stresses on thin aluminium samples which were laser shock peened. The samples were supplied by the Universidad Politécnica de Madrid and they are 2 mm thick aluminium alloy AA2024-T351 clad samples. A better description of them can be found in chapter 3 while the results can be found in chapter 9.

The layout of the beam can be seen in the next figures:

Fig. 4.24 Beamline layout [38]

The polychromatic beamline is tailored through the slit S1 and S2 in order to get a beam cross section of 0.5 x 0.5 mm^2. The length of the gauge volume is defined by the slit S3 and S4 which were respectively 0.03 and 8 mm. The 2θ angle was fixed at 10°. The sample was positioned on a movable platform which is able to rotate around the beam axis to change the ψ angle. This angle was changed between 0 and 88° with a step of 4° both clockwise and anticlockwise. With this set-up we were able to record 10 different lattice planes which were: {111}, {200}, {220}, {311}, {222}, {400}, {420}, {331} and {422}. In the picture below the set-up of the experiment is shown:

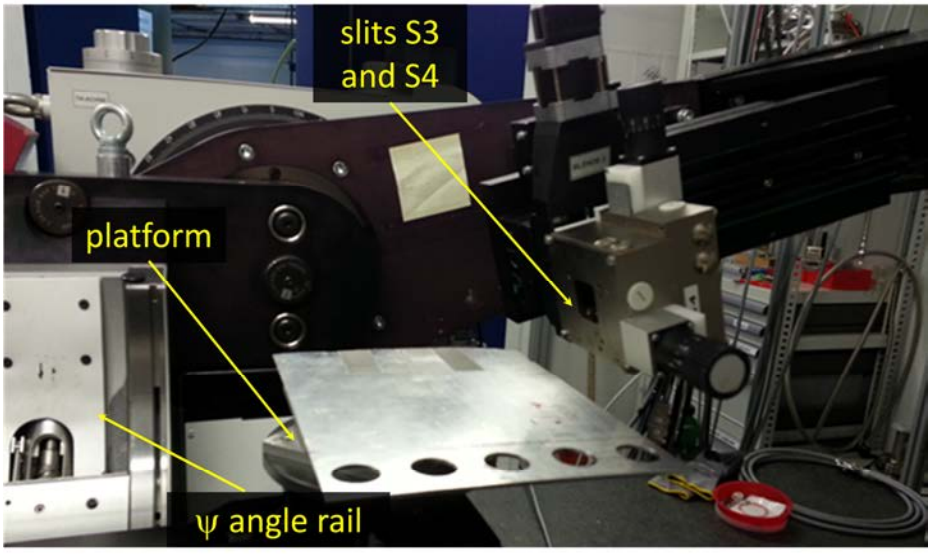

Fig. 4.25 Experiment set-up. On the left the ψ angle rail where the sample can rotate around the ψ angle as indicated in Fig. 4.24. Slits S3 and S4 indicate the apertures where the diffracted beam goes through before hitting the detector.

Once the energy vs. intensity plot is obtained, the peaks were fitted with a Pseudo-Voigt function to find the peak centre and the residual stress was calculated automatically by the software available at EDDI as explained in section 4.3.1.1.

4.3.2.4 PETRA III

A thick aluminium alloy AA7050-T451 sample was measured at the High Energy Materials Science (HEMS) beamline inside the PETRA III Synchrotron in Helmholtz Zentrum, Hamburg, Germany. A full description of the sample can be found in chapter 3. The layout of the beamline is described in detail in [39]. As in the APS experiment (section 4.3.2.2), a conical slit was used to obtain a consistent depth profile resolution. The conical slits had been already used at HEMS and results were reported in [40]. For this experiment the energy was tuned to 74.5 keV in order to obtain a wavelength of 1.16 Å; with this set-up the strongest reflecting plane was {311}. The incoming beam had a cross-section of 50 × 50 μm^2, and the gauge volume length was approximately 1.2 mm. A layout of the experiment room can be seen in the next picture:

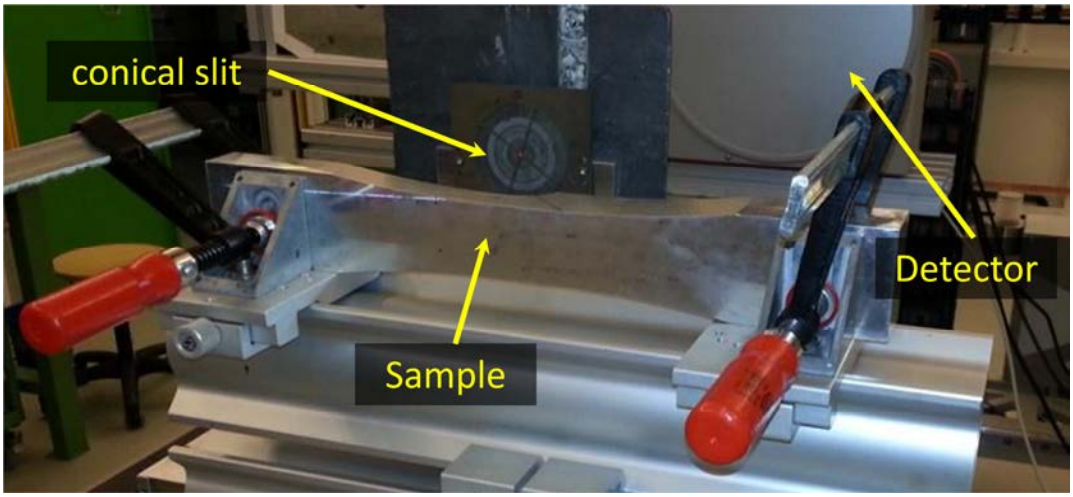

Fig. 4.26 layout of the experiment. The beamline hits the sample and the Debye-Scherrer cones are generated. These cones are recorded by the detector behind the conical slits.

Since the section of the interest in the sample was 28 mm thick and 45 mm wide, a plane-stress approximation was not possible and the sample had to be measured in two different positions to have three strain components. In the following pictures the section of interest and the positions of the measurements are presented:

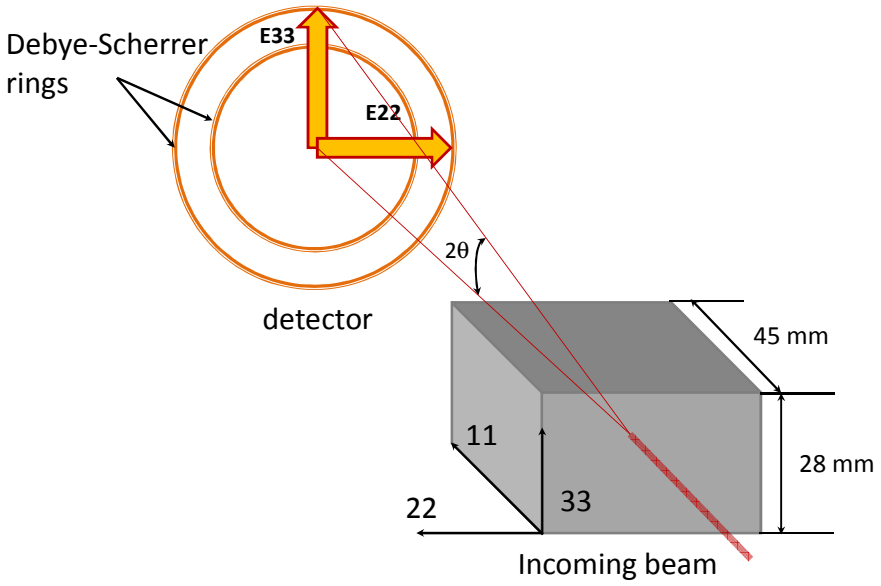

Fig. 4.27 Experiment set-up to measure both E22 and E33 strain components

The coordinate system used to measure both E22 and E33 components is reported in Fig. 4.27 as are the dimensions of the sample. As said before, with a conical slit is possible

to measure two* strain components at the same time: to measure the E22 and the E33 strain components, the beam has to be aligned along the E11 component which means it must be perpendicular to the shorter edge (28 mm). However, in this configuration the E11 component could not be measured. To obtain this component, the sample has to be rotated by 90°, as shown in Fig. 4.28.

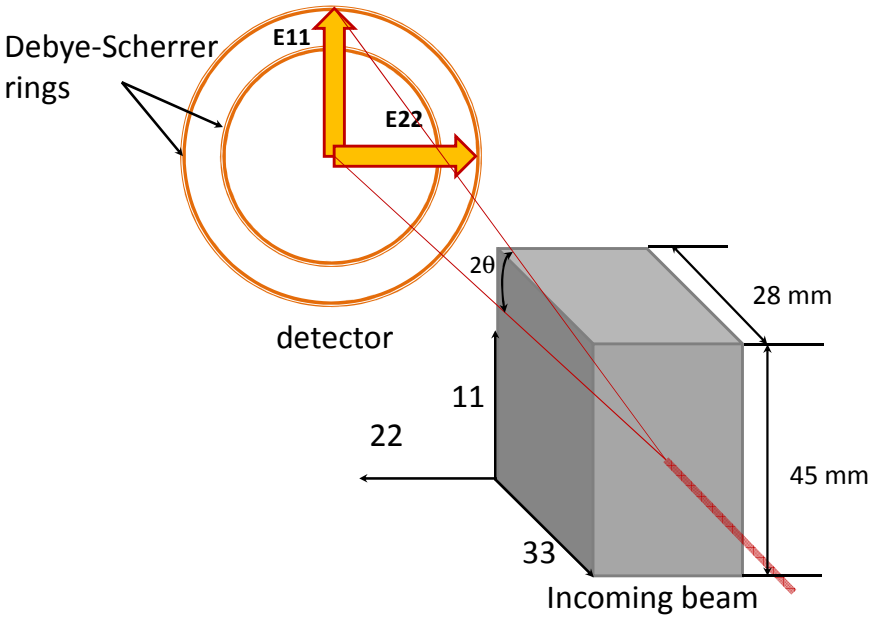

Fig. 4.28 Experiment set-up to measure both E11 and E22 strain components

In this way, the beam is aligned to the E33 component (which can't be measured this time but is was measured with the previous set-up) and the E11 and E22 components were measured. During the post-processing of the data both the E22 components measured during the two different set-ups were averaged to obtain better statistics.

The post-processing of the data was made through FIT2D software provided by A. Hammersley at the European Synchrotron Radiation Facility [36]. Since only one reflection plane was used to calculate the stress from the measured strains, a specific Young's

* In theory, according to Fig. 4.19, by integrating the sector at 45° it's possible to calculate the shear strain E12 but the coordinate system used is believed to be orientated as the ideal stress components.

modulus should be used. However, Lorentzen reported in [35] that for the {311} reflection the Young's Modulus based on the Kroner modelling scheme is equal to 70.2 GPa instead of 72 GPa measured with a tensile test. Since the difference is essentially around 2%, it can be considered negligible and a value of 72 GPa was kept for these calculations as well.

Unfortunately due to lack of time during the experiment, measurements to eliminate the pseudo strains were not possible. For this reason, the strains between 0 and 0.6 mm were not taken into account.

4.3.2.5 Diamond Light Source - JEEP

A second experiment on the same thick aluminium alloy stepped coupon was carried out at the Diamond Light source (DLS), UK, using the beamline I12: Joint Engineering, Environmental, and Processing (JEEP) [41], a polychromatic X-ray beamline. The experiment carried out at DLS aimed to measure the residual stresses at the curved edge on the sample. The gauge volume was diamond-shaped with a cross section of 50 × 50 μm^2, while the length was fixed at 2 mm. With this set-up, the closest measurement point at the surface was taken at 200 μm and measurements were taken up to 5 mm depth. A "horseshoe" 23-element solid state detector is used at JEEP and it allows simultaneous collection of strain measurements from 23 scattering vectors. The post-processing of the data was carried out with DAWN software [42]. During the post-processing, only the {311} plane reflection was taken into consideration and the peak-fitting was made with a Gaussian curve.

The following picture shows the experiment set-up:

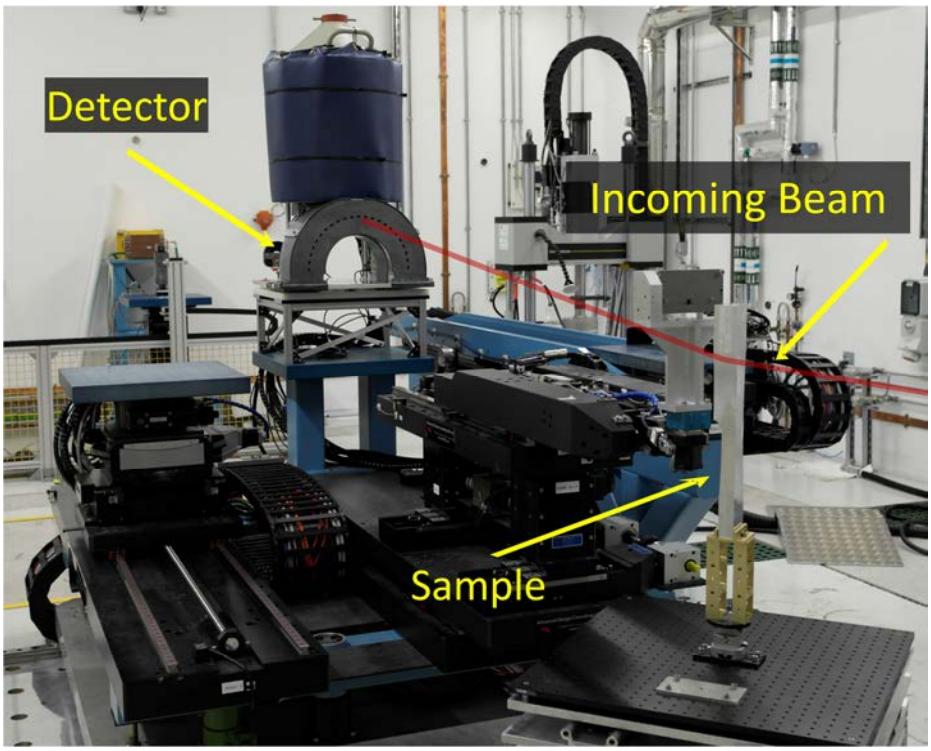

Fig. 4.29 Experiment set-up at JEEP (the sample is outside in the beam path). The incoming beam hits the sample and it is diffracted. The diffracted beam is recorded by the horse-shoe detector.

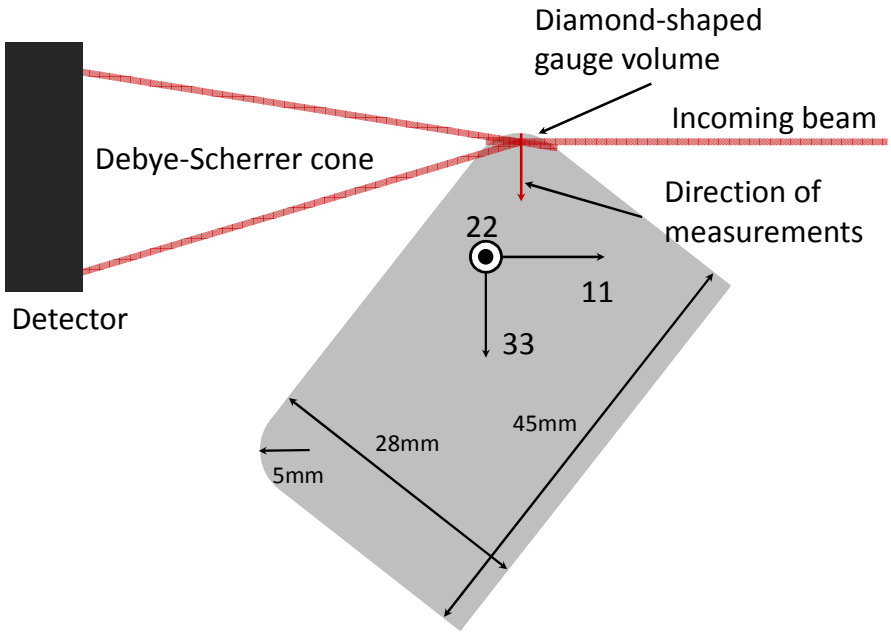

Fig. 4.30 View from above: measurements line (red arrow) and stress directions

In the configuration shown in Fig. 4.29, it was possible to measure the E22 and E33 strain components according to the coordinate system and set-up shown in Fig. 4.30. The measurements were taken along the red line shown in Fig. 4.30 thus the spatial resolution is of the same order as the gauge volume width. As said in section 3.3.2.4, the strain component parallel to the beam, i.e. E11, cannot be measured. To calculate the E11 component the beam has to be parallel to the sample length which is 420 mm. In this configuration, the photons would not have enough energy to cross undisturbed the large amount of aluminium. To overcome this problem, the central part of the sample was cut in order to keep enough material to not modify the residual stress field in the area of measurement. The final set-up can be seen in the following pictures:

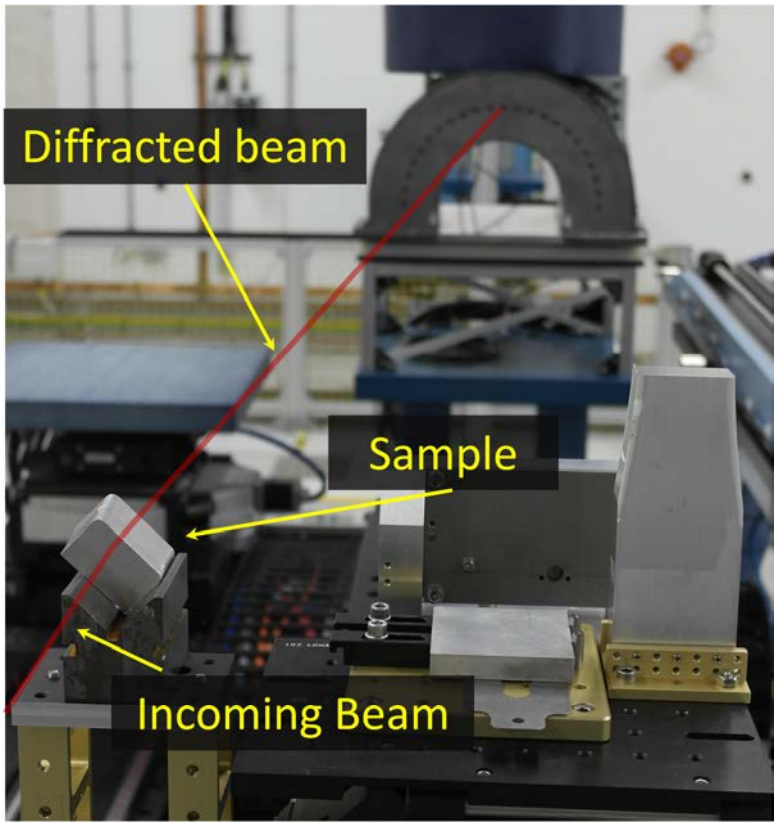

Fig. 4.31 Set-up for the experiment in order to measure the E11 component. The interested sample is on the left of the picture, on a 45° clamp

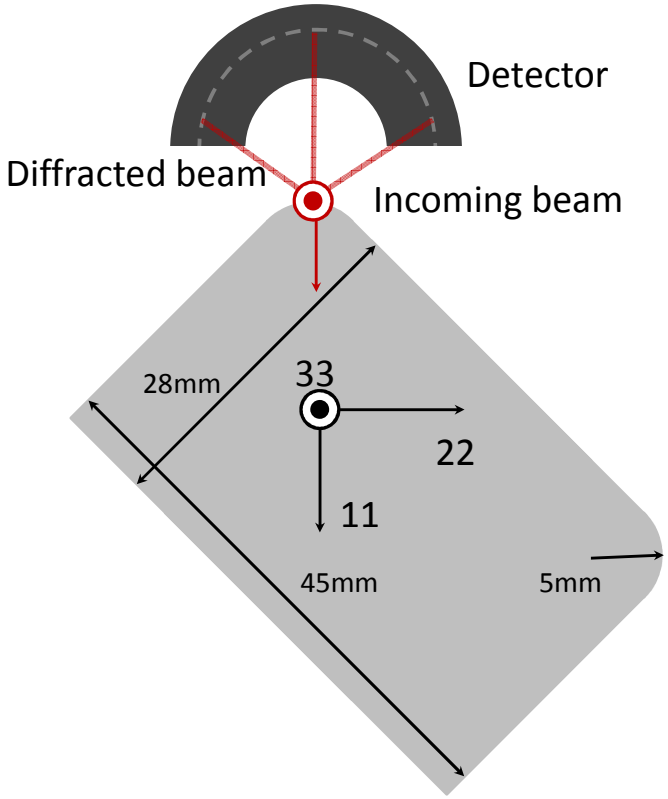

Fig. 4.32 Configuration to measure the E11 and E22 components

The final sample is shown in Fig. 4.31 on the left, clamped at 45°. The experiment set-up is shown in Fig. 4.32. In this configuration, the beam is parallel to the 33 direction which means the E33 component cannot be measured. With this configuration, both E11 and E22 strain components can be measured with the same spatial resolution as the previous measurements, thus the measurements were taken with a step of 50 μm along the 11 direction (red arrow).

4.4 Neutron Diffraction

Neutron diffraction is another technique to calculate the residual strains based on Bragg's law. As stated before, neutrons are particles bigger than electrons and they tend to interact less with the surrounding matter. This allows a higher penetration through the material, reaching a depth of several centimetres. On the other hand, the gauge volume

required by neutrons is generally larger than the one required by using photons with a general loss of spatial resolution. Furthermore, the measurement time required using neutrons is generally longer than the time required for the same measurements made using photons (even if several parameters have to be taken into account like the material of the specimen and its thickness).

Neutrons can be produced in two different ways:

- **Nuclear Reactor**: the neutrons are produced by the nuclear fission process. During the fission of uranium or plutonium, several neutrons are produced, some of them with a high energy level. To reduce their energy level a moderator is interposed between the reactor and the final target;
- **Spallation source**: the neutron are generated by the evaporation from a target material which is bombed with protons; since the incident protons beam is pulsed, the neutrons are produced in sharp pulses in a range between 10 and 50 Hz.

The two techniques allow two different approaches for measuring the residual strains in a component [43][44]:

- **Constant wavelength**: similarly to what was described previously for the synchrotron X-rays, the neutrons produced in a nuclear reactor are guided toward a crystal which makes the beam monochromatic, in this way the neutrons all have the same wavelength. With this technique it is possible to get an intensity vs. 2θ plot, i.e. it's possible to calculate the strains by the shifting of the 2θ angle once the $2\theta_0$ is known; as said already in this dissertation, the wavelength of the neutron has to be tuned accordingly to the desired lattice plane;
- **Time-of-flight (TOF)**: neutrons are produced in different pulses so they have different random wavelengths which means they have different times-of-flight which can measured and they are used to calculate their respective wavelengths. With this technique is possible to get the diffracted neutrons from

several angles, i.e. it is possible to measure the strains from several lattice planes.

In this dissertation, experiments were carried out in both nuclear reactors and spallation sources. In particular, the nuclear reactors used were the Forschungs Neutronenquelle Heinz Maier-Leibnitz (FRM II), beamline Stress-Spec in Germany, Institute Laue-Langevin (ILL), SALSA instrument, France and the Canadian Neutron Beam Centre (CNBC), L3 beamline, Canada; the TOF source used was instead the Paul Scherrer Institute (PSI), POLDI beamline, Switzerland.

4.4.1 CNBC - L3

In the L3 beamline, the residual strains of a Single Edge Notch (SEN) sample both shot and laser peened were measured. More details of the sample are reported in chapter 3. Since the sample was both shot and laser peened over all three faces, our target was to characterize the residual stress profile to determine where the tensile stresses are highest, their average magnitude and their depth from the surface. For this reason we needed to measure the residual stresses from the notch side to the opposite side along the three main specimen directions. The primary and secondary slits were set to a relative angle of 90° in order to get a gauge volume with a square section. In consultation with the local contact and according with Fig. 4.33 we selected a gauge volume of 1 × 1 × 5 mm^3 for the in-plane lattice strain components (S22 and S33). For the third component, a slightly smaller gauge volume of 1.5 × 1.5 × 2 mm^3 was used because the spatial resolution along the measurement line is determined by the height of the gauge volume. The measurements within the thickness started 0.5 mm beneath the surface and a step size of 1.5 mm was used.

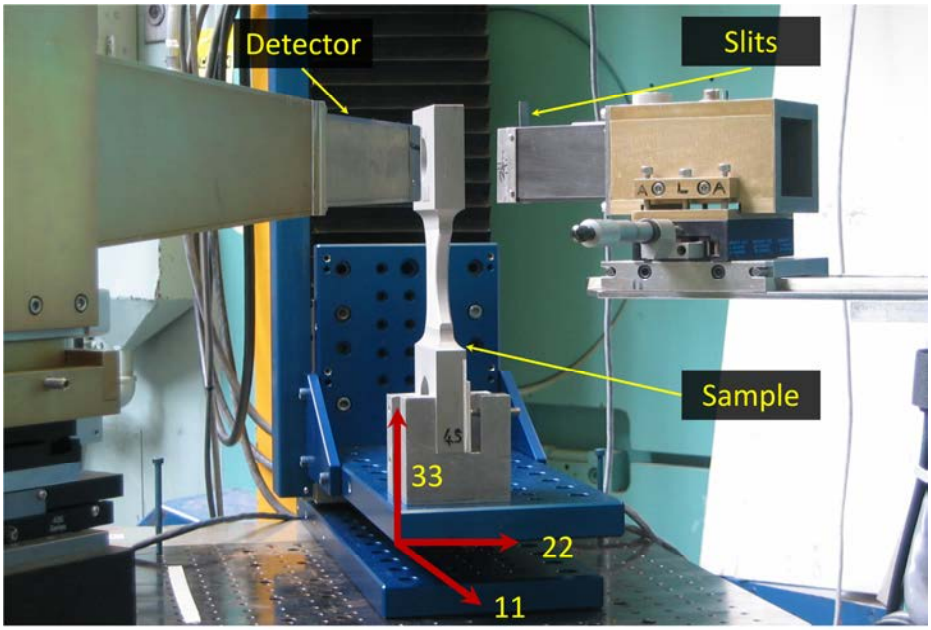

Fig. 4.33 Experiment layout at L3 beamline

Further measurements were made along the narrower side of the notch and at the surface of the lateral side, as Fig. 4.34 below shows:

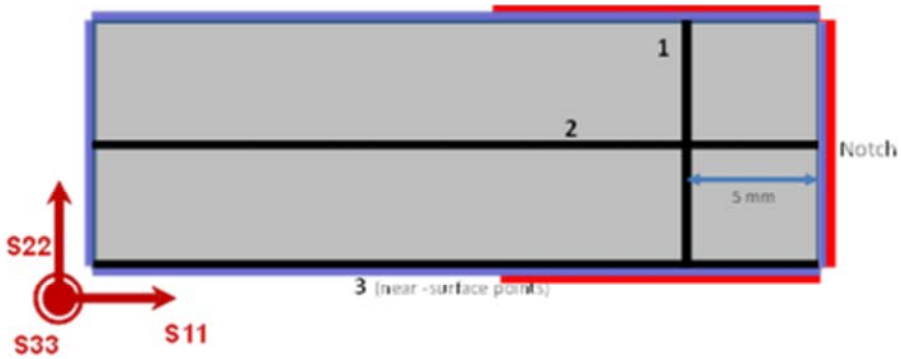

Fig. 4.34 Central section of the SEN. The black lines are the directions of measurements: line 1 goes from side to side along the shorter edge of the section; line 2 goes from the notch to the shoulder of the sample and line 3 follow the same direction of line 2 but at the surface on the central section

In particular, for the measurements close to the surface, the geometric centre of the gauge volume was positioned at the surface of the sample in order to have half gauge volume immersed in the sample. The pseudo-strains (PS) generated by the non-immersed gauge volume were subsequently corrected through the following technique: the gauge

volume was positioned in a region which was supposed to be stress-free in the same configuration of the measurements close to the surface (so half immersed and half non-immersed). By knowing the unstressed lattice parameter d_0, the d_0+PS obtained from this latter configuration and the *d(hkl)*+PS obtained during the measurements close to the surface, it's possible to algebraically subtract the PS generated by the non-immersed side of the gauge volume. The actual position of the diffraction vector was finally calculated by considering the geometric centre of the immersed-only gauge volume.

4.4.2 FRM II – Stress-Spec

Stress-Spec is powerful neutron diffraction facility that allows the measurement of both texture and residual strains. The experiment carried out at Stress-Spec involved three samples. The three samples were simple parallelepipeds with a squared base, with the edges around 45 mm and thickness of 10 mm. They were made of AA7050-T7451, cut from a bigger block through EDM cutting to avoid any further residual stress. One was only shot peened on one of the wider surfaces, the second sample was laser shock peened only, with a laser power density of 2 GW/cm^2, 18 ns shot time length and 4 different layers of treatment to get a more homogenized stress profile at the surface. The last sample was treated with both techniques.

The experiment was carried out at the Stress-Spec instrument at FRM II. The primary and secondary slits were set in order to get a gauge volume of $2 \times 2 \times 10$ mm^3. The unstressed lattice parameters d_0 was measured from another sample of the same batch of the treated ones, assumed to be stress-free.

4.4.3 ILL – SALSA

The stepped coupon sample which has been already described in the previous sections, was tested also at the neutron facility Institut Laue-Langevin (ILL), using the instrument SALSA [45]. The neutron facility is a nuclear reactor, the beamline is monochromatic

thanks to the presence of an Si crystal. The scope of this experiment was to measure the residual stress profile through thickness starting from the surface of the 5 mm curved (exactly like the experiment at Diamond Light Source but with a different radiation source). The primary and secondary slits were set with an angle around 90°. The sample was placed on a hexapod as the Fig. 4.35 shows:

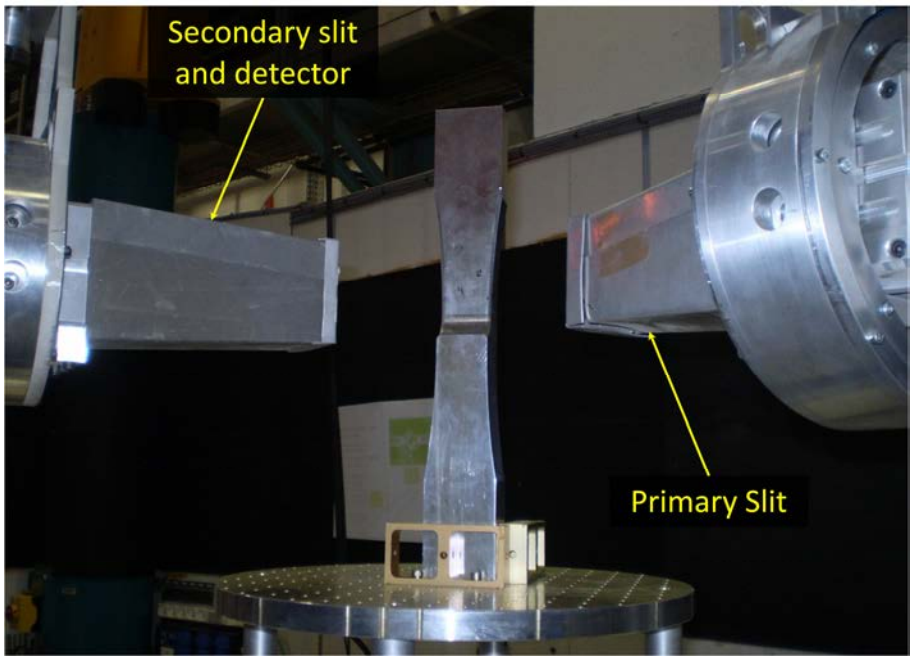

Fig. 4.35 Set-up of experiment at SALSA. The incoming beam comes from the primary slits and hits the sample forming an angle of 90°. The diffracted beam enters inside the secondary slit where the detector is located

Due to the curvature of the round corner, a small gauge volume was chosen in order to fully immerse it inside the sample. The primary and secondary slits were set in order to have the gauge volume $0.6 \times 0.6 \times 2$ mm^3. The measurements were taken as Fig. 4.36 shows:

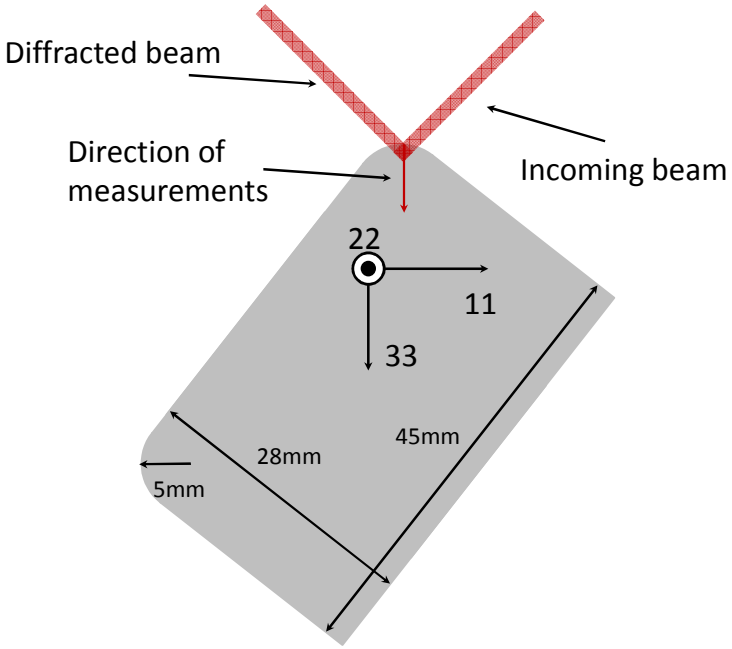

Fig. 4.36 The measurement were taken along the red arrows according with the shown coordinate system

Due to the shut-down of the facility during the last part of the experiment, it was not possible to measure the corrections for the pseudo-strains generated close to the surface where the gauge volume was half-immersed. The picture below shows a 2D graph of the intensity vs. position:

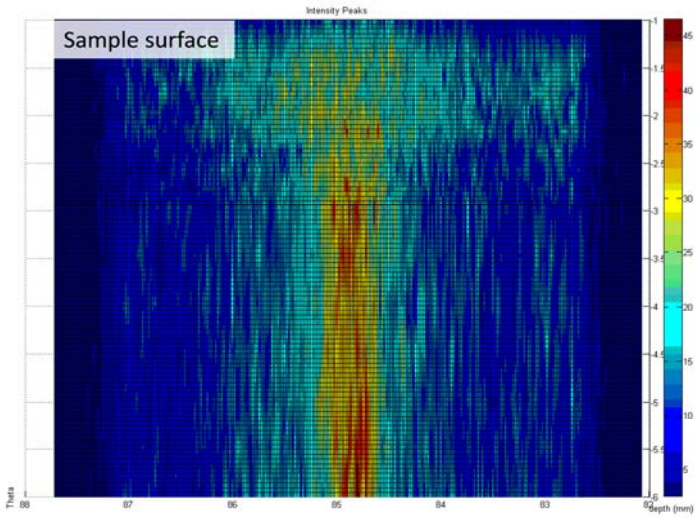

Fig. 4.37 Intensity vs. Vertical position plot. Y axis indicated the vertical position of the gauge volume is respect of the sample surface. When the gauge volume is only partially immersed inside the sample the intensity drops.

It is possible to see in Fig. 4.37 that the intensity tends to decrease as the gauge volume approaches the surface of the sample. When the gauge volume starts being partially outside the sample, the intensity of peaks decrease in intensity since less material is diffracting the neutrons: the peaks become broader and of the same order of magnitude of the noise.

4.4.4 PSI – POLDI

An experiment was performed at the Paul Scherrer Institute, Switzerland, which includes a spallation neutron source. The beamline used was POLDI (Pulse-Overlap DIffractometer), a time-of-flight thermal neutron diffractometer, dedicated to materials science applications [46], [47]. In these facilities the TOF is the fundamental parameter which is measured to calculate the strains. By considering the de Broglie equation it is possible to relate the wavelength with the speed of a particle:

$$\lambda = \frac{h}{mv}$$

Equation 4.19

Where λ is the wavelength, h is Planck's constant, m in the mass of the particle and v its speed. Considering that the speed $v=L/t$ where L in the path length and t in the time to cover this length, and by considering Bragg's Law we can obtain:

$$\frac{ht}{mL} = 2\,\mathrm{d}\sin\theta$$

Equation 4.20

By rearranging Equation 4.20 it's possible to conclude that strains can be measured by measuring the time that the particles cover a certain path, i.e. the time-of-flight:

$$\varepsilon = \frac{t - t_0}{t_0}$$

Equation 4.21

where t_0 is the TOF for the unstressed sample. This theory is generally applicable to all the TOF facilities. Usually the beam is generated by pulsed neutrons. Each pulse is emitted after a time long enough in order to not allow the fastest neutron of the second pulse to catch up with the slowest neutrons of the previous pulse. POLDI is different since it is based on the principle of multiple pulse overlap. In this way several neutrons coming from different pulses can reach the detector at the same time. In order to recognize which neutron is coming from different pulses, a third parameter is introduced in the analysis which is the angular dependence of the TOF spectra. To analysis the data, a graph like the following is generally produced:

Fig. 4.38 Intensity vs. Angular scattering vs. time plot [46]

In Fig. 4.38 it's possible to see a generic plot generated after an analysis with the POLDI instrument: lines with different slopes correspond to different Bragg reflections; parallel lines correspond to the same Bragg reflection but originated from different pulses.

With POLDI the residual strains along the thickness of the stepped coupon were measured. The following picture shows the direction of measurements:

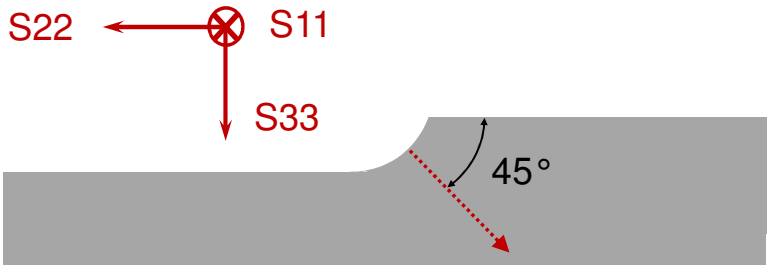

Fig. 4.39 The red dot line shows the direction of the measurements

In Fig. 4.39 the direction of the measurements is shown and the strains were measured according to the coordinate system in the same picture. The residual stress in the curved blend area between the ends of the sample was measured to investigate the applicability of the Eigenstrain approach when the thickness is changed. Measurements were taken from the centre of the blend, normal to the sample surface. The unstressed lattice parameter d_0 was measured far away from the laser peened away and close to the surface in order to decrease the possibility of measuring any pre-stress field. The problem of the pseudo-strain generation was solved with the approach already explained previously. The results of the experiment can be found in chapter 7.

During the measurements a gauge volume with a section of 2×2 mm^2 was used; the length of the gauge volume was set to 7 mm in the 1 direction according with the coordinate system in Fig. 4.40, both to decrease the amount of time per measurement and to include as many diffracting grains as possible to improve statistics.

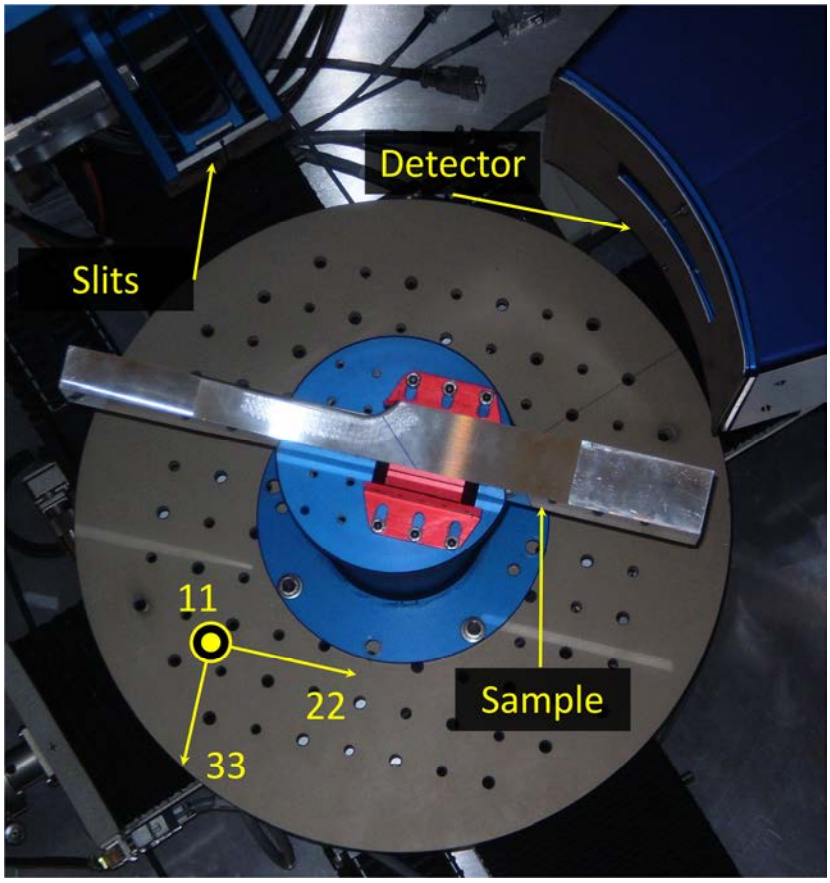

Fig. 4.40 layout of the experiment at POLDI instrument. The incoming beam comes from the primary slits and it is diffracted by the sample. The diffracted beam enters the secondary beam where the detector is located. The coordinate systems shows the strain directions.

4.5 Conclusions

In this chapter the residual stress measurement techniques via various diffraction methods were discussed. All the experiments carried out in different facilities have been outlined and discussed. To assess the reliability of a single measurement technique, more than one measurement with different techniques of the same sample were carried out. The results of the experiments can be found in chapter 6 for the stepped coupon, in chapter 7 for the Single Edge notch, in chapter 8 for the single peened thin aluminium alloy samples and in chapter 9 for the same sample with a double-side laser treatment.

References

[1] J. Mathar, "Determination of Initial Stresses by Measuring the Deformation Around Drilled Holes," *Trans. ASME*, vol. 56, no. 4, pp. 249–254, 1934.

[2] ASTM E837 - 13a, "Standard Test Method for Determining Residual Stresses by the Hole Drilling Strain Gauge Method," vol. 03.01, 2009.

[3] P. V. Grant, J. D. Lord, and P. S. Whitehead, "The measurement of residual stresses by the incremental hole drilling technique," NPL, *Meas. Good Pract. Guid.*, vol. 53, Issue 2, 2006.

[4] A. Nau and B. Scholtes, "Evaluation of the High-Speed Drilling Technique for the Incremental Hole-Drilling Method," *Exp. Mech.*, vol. 53, no. 4, pp. 531–542, 2013.

[5] J. Chen, Y. Peng, and S. Zhao, "Hole-drilling method using grating rosette and Moiré interferometry," *Acta Mech. Sin.*, vol. 25, no. 3, pp. 389–394, Jan. 2009.

[6] J. D. Lord, D. Penn, and P. Whitehead, "The Application of Digital Image Correlation for Measuring Residual Stress by Incremental Hole Drilling," in *Applied Mechanics and Materials*, 2008, vol. 13–14, pp. 65–73.

[7] D. V. Nelson, A. Makino, and T. Schmidt, "Residual Stress Determination Using Hole Drilling and 3D Image Correlation," *Exp. Mech.*, vol. 46, no. 1, pp. 31–38, Feb. 2006.

[8] G. S. Schajer, "Measurement of Non-Uniform Residual Stresses Using the Hole-Drilling Method. Part I—Stress Calculation Procedures," *J. Eng. Mater. Technol.*, vol. 110, no. 4, p. 338, Oct. 1988.

[9] G. S. Schajer, "Measurement of Non-Uniform Residual Stresses Using the Hole-Drilling Method. Part II—Practical Application of the Integral Method," *J. Eng. Mater. Technol.*, vol. 110, no. 4, p. 344, Oct. 1988.

[10] E. Valentini, M. Beghini, L. Bertini, C. Santus, and M. Benedetti, "Procedure to Perform a Validated Incremental Hole Drilling Measurement: Application to Shot Peening Residual Stresses," *Strain*, vol. 47, pp. e605–e618, Jun. 2011.

[11] V. Fontanari, F. Frendo, T. Bortolamedi, and P. Scardi, "Comparison of the hole-drilling and X-ray diffraction methods for measuring the residual stresses in shot-peened aluminium alloys," *J. Strain Anal. Eng. Des.* , vol. 40 , no. 2 , pp. 199–209, Jan. 2005.

[12] A. T. Fry and J. D. Lord, "Measuring the Variation of Residual Stress with Depth: A Validation Exercise for Fine Incremental Hole Drilling," in *Materials Science Forum*, 2006, vol. 524–525, pp. 531–537.

[13] M. Dorman, N. Smyth, A. Cini, M. E. Fitzpatrick, P. E. Irving, and M. B. Toparli, "Effect of laser shock peening on residual stress and fatigue life of clad 2024 aluminium sheet containing scribe defects," *Mater. Sci. Eng. A*, vol. 548, no. 30, pp. 142–151, 2012.

[14] M. B. Toparli, "Analysis of Residual Stress Fields in Aerospace Materials After Laser Peening," PhD Thesis, The Open University, 2012.

[15] P. S. Prevey, "Residual-stress distributions produced by strain-gauge surface preparation," *Exp. Mech.*, vol. 28, no. 1, pp. 92–97, Mar. 1988.

[16] G. S. Schajer, "Advances in Hole-Drilling Residual Stress Measurements," *Exp. Mech.*, vol. 50, no. 2, pp. 159–168, 2010.

[17] M. Steinzig and E. Ponslet, "Residual stress measurement using the hole drilling method and laser speckle interferometry: Part I," *Exp. Tech.*, vol. 27, no. 3, pp. 43–46, May 2003.

[18] P. Jacquot, "Speckle interferometry: A review of the principal methods in use for experimental mechanics applications," *13th International Conference on Experimental Mechanics*, vol. 44. Wiley-Blackwell, Alexandroupolis, pp. 57–69, 2008.

[19] D. V Nelson, "Residual Stress Determination by Hole Drilling Combined with Optical Methods," *Exp. Mech.*, vol. 50, no. 2, pp. 145–158, 2010.

[20] M. E. Fitzpatrick, A. T. Fry, P. Holdway, F. A. Kandil, J. Shackleton, and L. Suominen, "Determination of residual stresses by X-ray diffraction," NPL, *Meas. Good Pract. Guid.*, Issue 2, 2005.

[21] P. J. Withers, "Use of synchrotron X-ray radiation for stress measurement," in *Analysis of residual stress by diffraction using neutron and synchrotron radiation*, M. E. Fitzpatrick and A. Lodini, Eds. London: Taylor & Francis, 2003, pp. 170–189.

[22] P. S. Prevéy, "X-ray diffraction residual stress techniques," *Met. Handb.*, vol. 10, pp. 380–392, 1986.

[23] W. Knop, P. K. Pranzas, and P. Schreiner, "Radiation Source," in *Neutrons and Synchrotron Radiation in Engineering Materials Science*, W. Reimers, A. R. Pyzalla, A. Schreyer, and H. Clemens, Eds. Weinheim: WILEY-VCH Verlag GmbH & Co. KGaA, 2008, pp. 91–112.

[24] "Synchrotron SOLEIL," 2014. [Online]. Available: http://www.synchrotron-soleil.fr/. [Accessed: 04-Aug-2014].

[25] C. Riekel, "The use of synchrotron radiation for materials research," in *Analysis of Residual Stress by Diffraction using Neutron and Synchrotron Radiation*, M. E. Fitzpatrick and A. Lodini, Eds. London: Taylor & Francis, 2003, pp. 28–44.

[26] C. Genzel, "Formalism for the evaluation of strongly non-linear surface stress fields by X-ray diffraction performed in the scattering vector mode," *Phys. Status Solidi*, vol. 146, no. 2, pp. 629–637, Dec. 1994.

[27] K.-D. Liss, A. Bartels, A. Schreyer, and H. Clemens, "High-Energy X-Rays: A tool for Advanced Bulk Investigations in Materials Science and Physics," *Textures Microstruct.*, vol. 35, no. 3–4, pp. 219–252, 2003.

[28] P. Staron, T. Fischer, J. Keckes, S. Schratter, T. Hatzenbichler, N. Schell, M. Müller, and A. Schreyer, "Depth-Resolved Residual Stress Analysis with High-Energy Synchrotron X-Rays Using a Conical Slit Cell," in *Materials Science Forum*, 2014, vol. 768–769, pp. 72–75.

[29] R. V. Martins, "Residual Stress Analysis by Monochromatic High-Energy X-rays," in *Neutrons and Synchrotron Radiation in Engineering Materials Science*, W. Reimers, A. R. Pyzalla, A. Schreyer, and H. Clemens, Eds. Weinheim: WILEY-VCH Verlag GmbH & Co. KGaA, 2008, pp. 177–194.

[30] S. F. Nielsen, A. Wolf, H. F. Poulsen, M. Ohler, U. Lienert, and R. A. Owen, "A conical slit for three-dimensional XRD mapping.," *J. Synchrotron Radiat.*, vol. 7, no. Pt 2, pp. 103–9, Mar. 2000.

[31] U. Lienert, "Specification of a Conical Slit Cell." [Online]. Available: www.risoe.dk/Research/sustainable_energy/new_energy_technologies/projects/synchrotron/~/media/risoe_dk/research/synchrotron/documents/conicalspecsalfe1.ashx+&cd=2&hl=en&ct=clnk. [Accessed: 30-Sep-2014].

[32] D. R. Haeffner, J. D. Almer, and U. Lienert, "The use of high energy X-rays from the Advanced Photon Source to study stresses in materials," *Mater. Sci. Eng. A*, vol. 399, no. 1–2, pp. 120–127, Jun. 2005.

[33] A. S. Gill, Z. Zhou, U. Lienert, J. Almer, D. F. Lahrman, S. R. Mannava, D. Qian, and V. K. Vasudevan, "High spatial resolution, high energy synchrotron x-ray diffraction characterization of residual strains and stresses in laser shock peened Inconel 718SPF alloy," *J. Appl. Phys.*, vol. 111, no. 8, pp. 84904–84912, 2012.

[34] B. Clausen, T. Lorentzen, and T. Leffers, "Self-consistent modelling of the plastic deformation of f.c.c. polycrystals and its implications for diffraction measurements of internal stresses," *Acta Mater.*, vol. 46, no. 9, pp. 3087–3098, May 1998.

[35] T. Lorentzen, "Anisotropy of lattice strain response," in *Analysis of residual stress by diffraction using neutron and synchrotron radiation*, M. Fitzpatrick and A. Lodini, Eds. Taylor & Francis, 2003, pp. 114–130.

[36] A. Hammersley, "The FIT2D homepage," 2004. [Online]. Available: http://www.esrf.eu/computing/scientific/FIT2D/.

[37] M. G. Webster P. J. Wang X. D., Kang W. K. and Holden T. M., "Impediments to efficient through-surface strain scanning," *J. Neutron Res.*, vol. 3, 1996.

[38] C. Genzel, I. A. Denks, J. Gibmeier, M. Klaus, and G. Wagener, "The materials science synchrotron beamline EDDI for energy-dispersive diffraction analysis," *Nucl. Instruments Methods Phys. Res. Sect. A Accel. Spectrometers, Detect. Assoc. Equip.*, vol. 578, no. 1, pp. 23–33, Jul. 2007.

[39] N. Schell, A. King, F. Beckmann, T. Fischer, M. Müller, and A. Schreyer, "The High Energy Materials Science Beamline (HEMS) at PETRA III," *Mater. Sci. Forum*, vol. 772, no. 57, pp. 57–61, 2013.

[40] P. Staron, T. Fischer, E. H. Eims, S. Frömbgen, N. Schell, S. Daneshpour, R. V. Martins, M. Müller, and A. Schreyer, "Depth-Resolved Residual Stress Analysis with Conical Slits for High-Energy X-Rays," in *Materials Science Forum*, 2014, vol. 772, pp. 3–7.

[41] M. Drakopoulos, T. Connolley, C. Reinhard, R. C. Atwood, L. Connor, M. Hart, B. Humphreys, U. Pedersen, and M. Basham, "I12: The Joint Engineering, Enviromental & Processing (JEEP) beamline at Diamond Light Source," *J. Sychrotron Radiat.*, 2014.

[42] M. Gerring, "DAWN Science," 2014. [Online]. Available: http://confluence.diamond.ac.uk/display/DAWN/DAWN+Science. [Accessed: 06-Jun-2014].

[43] L. Pintschovius, "Neutron diffraction using constant wavelenght," in *Analysis of residual stress by diffraction using neutron and synchrotron radiation*, M. Fitzpatrick and A. Lodini, Eds. London: Taylor & Francis, 2003, pp. 133–145.

[44] M. W. Johnson and M. R. Daymond, "Neutron pusled source instrumentation," in *Analysis of residual stress by diffraction using neutron and synchrotron radiation*, M. Fitzpatrick and A. Lodini, Eds. London: Taylor & Francis, 2003, pp. 146–158.

[45] T. Pirling, G. Bruno, and P. J. Withers, "SALSA: Advances in Residual Stress Measurement at ILL," in *Materials Science Forum*, 2006, vol. 524–525, pp. 217–222.

[46] U. Stuhr, "Time-of-flight diffraction with multiple pulse overlap. Part I: The concept," *Nucl. Instruments Methods Phys. Res. Sect. A Accel. Spectrometers, Detect. Assoc. Equip.*, vol. 545, no. 1–2, pp. 319–329, 2005.

[47] U. Stuhr, H. Spitzer, J. Egger, A. Hofer, P. Rasmussen, D. Graf, A. Bollhalder, M. Schild, G. Bauer, and W. Wagner, "Time-of-flight diffraction with multiple frame overlap Part II: The strain scanner POLDI at PSI," *Nucl. Instruments Methods Phys. Res. Sect. A Accel. Spectrometers, Detect. Assoc. Equip.*, vol. 545, no. 1–2, pp. 330–338, 2005.

5 Eigenstrain: Theory and Applications

In this section the Eigenstrain definition, theory and approach in presented. Even though the initial concept of the Eigenstrain was introduced in 1931, a complete mathematical treatment was not written until more than 50 years later. Since the latter approach is quite difficult to understand and with few real engineering applications, the Eigenstrain approach was considered for years a complex mathematical approach for simple problems. The arrival of Finite Element Methods (FEM) reinvigorated interest in the Eigenstrain approach and several studies have demonstrated their versatility. In this chapter, the history of the Eigenstrain approach is briefly presented while more attention is focused on the application of the Eigenstrain theory to predict the residual stress field within the samples studied during the PhD program.

5.1 Introduction

Although the term Eigenstrain was introduced by Mura [1] only in 1987, the very first concept of the Eigenstrain (or *inelastic strains* as the author defined them) which generate residual stresses was introduced in 1931 by Reissner [2]. During the late 1950s Eshelby referred to Eigenstrain with the term *equivalent strain* and mathematically determined the elastic field of an ellipsoidal inclusion in a surrounding material [3], [4]. Ueda [5] called the Eigenstrain the *inherent strain*. Generally speaking, a more informal but clearer definition of the Eigenstrain can be given by the fact that the term Eigenstrain refers to all the strains within a body which are not purely elastic. In this ensemble can be included strains coming from different mechanical processes like thermal strains, plastic strains, phase transformation strains, chemical change strains and so on. By knowing a particular mechanical treatment it is possible to understand which of these strains will be present

inside the component after the treatment but, since a strain keeps no track of its origins, it is impossible to understand which treatment generates a particular set of strains.

The major interest in the Eigenstrain approach resides in the fact that, knowing a limited set of residual stress data, it is possible with the Eigenstrain approach to calculate the entire self-consistent RS field within a component. From a mathematical point of view, the entire Eigenstrain approach was solved by Mura [1] but, as summarized by Luzin [6], although it was demonstrated that the Eigenstrain can be used to predict the residual stress field for one, two and three different stress components, the final mathematical solution can be easily found only when basic geometries are used like a flat surface, a sphere and a cylinder which usually have few real-world engineering applications. Before Mura, in 1970 Fujimoto [7] proposed a method to calculate the residual stress field once the Eigenstrain values are known but without proposing a method to calculate the latter. But most important, he was the first researcher who assumed that the Eigenstrain field was generated only where a mechanical treatment occurs (in this case a welding process), i.e. the Eigenstrains are generated only within the treated area while the remaining material has to balance the new misfit by generating elastic stresses automatically. Only in 1975 Ueda [5] proposed a simplified method to calculate the Eigenstrain field based on the finite element method (FEM). In particular the following equations summarize Ueda's approach:

$$\{\varepsilon\} = [H^*]\{\varepsilon^*\}$$

Equation 5.1

$$\{\sigma\} = [D]\{\varepsilon\} = [D][H^*]\{\varepsilon^*\}$$

Equation 5.2

It is possible to see how Ueda linked the Eigenstrain value $\{\varepsilon^*\}$ to the elastic field $\{\varepsilon\}$ via the elastic response matrix $[H^*]$, and the so-calculated elastic field can be used to

calculate the stress field $\{\sigma\}$ via the elasticity matrix $[D]$. Once the problem was formulated, a series of residual stress field calculations for welded structures were presented and can be found in [8]–[10]. In order to mitigate Ueda's drawback, Hill [11] proposed a different method to obtain the three axial residual stress field in long welded joints but the method is suitable only for welded joints of simple geometry samples. In parallel, through the use of computer-aided FEM, the Eigenstrains have been demonstrated to predict the residual stress field in friction stir welding [12] and shot peening [13]. In 2005 Korsunsky [14] proposed the SIMple TRIangle method (SIMTRI) to easily implement the Eigenstrains through FE modelling and demonstrated its versatility on a variety of problems [12], [15]. A complete treatment of the SIMTRI method can be found in [16].

As laser shock peening is quite a young technology, only during the last 20 years have researchers tried to implement the Eigenstrain approach to predict the residual stress field generated by this surface treatment. The first application was published by Hill in 1996 [17] with the only scope to demonstrate that, as previously done, by knowing a series of residual stress measurements it was possible to obtain the full RS field within a body after the LSP treatment. In 2008, DeWald *et al.* [18] proposed a different method that will be explained in the next sections and that was used during this research to predict the residual stress inside complex geometry components.

5.2 Eigenstrain Approach

The Eigenstrain approach used in this dissertation is based on the model proposed by DeWald [18], [19]. In particular, the proposed method aims not only to know the full RS field within a component when few RS measurements are known, but was also used to

predict the RS field generated within a more complex geometry via FEA only. In particular, the application of the Eigenstrain approach is divided into three different steps:

1. laser shock peening a simple geometry sample and measuring the RS field;
2. calculate the Eigenstrains;
3. impose the Eigenstrain to a different and more complex geometry sample via FE in order to predict the RS that this sample will generate if it is LSP with the same laser parameters as the simple geometry sample.

It is easy to understand how important a similar approach could be in predicting the RS field in more complex geometries only through FEM instead of measuring the real sample, particularly if a parametric study is required.

As stated before, the Eigenstrains can have a different nature depending on the treatment which generated them. It has been said in chapter 2 that LSP is not a thermal treatment due to the fact that the short length of time in which the metal is exposed to the laser heat is not enough to actually heat the metal surface (but only the ablative layer). Similarly, the LSP is not a creep-based treatment and, so far, no phase transformations have been detected during the analysis after the treatment. It is possible to conclude then, that in the case of LSP the only Eigenstrains are purely plastic strains. In spite of this conclusion, some important assumptions must be made in order to apply correctly the Eigenstrain approach:

- ✓ The Eigenstrains can be treated as thermal strains instead of purely plastic strains due to the fact that the actual FE software does not give the possibility to the user to introduce directly plasticity into the model;
- ✓ The Eigenstrains are geometry and thickness independent.

All these assumption have led to formulate the *Principle of Transferability of Eigenstrain* which, paraphrased, indicates that there is the possibility to calculate the Eigenstrain from a simple geometry sample and then *transfer* them on to a more complex geometry to predict the RS field generated by the LSP. In more details, since the RS are strictly depending on the elastic properties of the materials, the Eigenstrain can be measured from a sample and *transferred* into a more complex one via FEM to a sample made of the same material; for the same reason, a certain set of Eigenstrains is produced for a set of given LSP parameters, i.e. imposing the Eigenstrain to another sample via FEM is like laser peening the sample with the same laser parameters. Furthermore, since the analysis through the Eigenstrain approach is completely elastic, the computational cost is extremely low when compared to the direct method simulation of the LSP process, as briefly described in chapter 2.

In the next paragraphs each step will be explained in more details.

5.2.1 Residual Stress profile Measurement

First, a stress-free simple geometry sample like the one in Fig. 5.1 is laser shock peened over the wider top surface to assure that the tensile stress distribution is confined underneath the surface (when multiple layer treatment is done this hypothesis is confirmed) and, furthermore, a plane stress configuration in the x and z directions is generated since no stress in the *y* direction is expected due to the characteristics of the treatment. The residual stress profile through the thickness is then measured. The final result will not be dependent on the technique used to measure the residual stress profile but at the same time the entire RS profile is needed, thus the contour method and neutron diffraction are the most useful technique to achieve this target due to their applicability in determining RS field through the thickness.

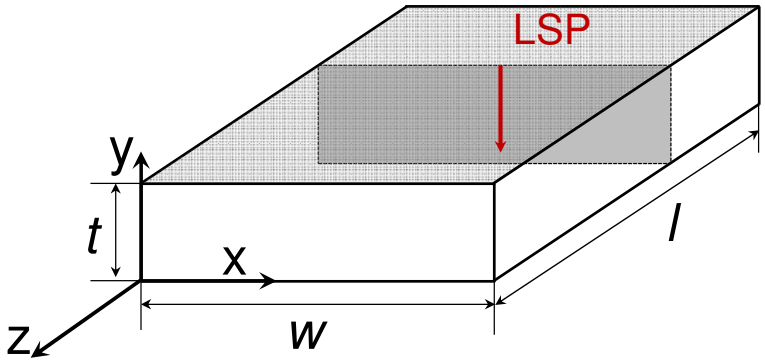

Fig. 5.1 simple geometry sample

Thus, the only non-zero stress components are the ones along *x* and *z*. Furthermore, assuming that the width *w* and the length *l* of the sample are of the same dimensions, it is possible to assume that the stress components along *x* and *z* are the same. Having said that, effectively only one component can be measured saving time during the RS measurements. Both using the neutron diffraction technique and the contour method, the final RS profile will undergo a smoothing process to avoid possible artefacts due to the limitations of these techniques (scattering due to large grains in the case of neutron diffraction or inaccuracies of the RS profile due to the cutting process in case of the contour method. The final profile will look like the one shown in Fig. 5.2 in red and is called σ_{TOT} to indicate the total residual stress profile measured along the *y* direction in the *x* (or *z*) component.

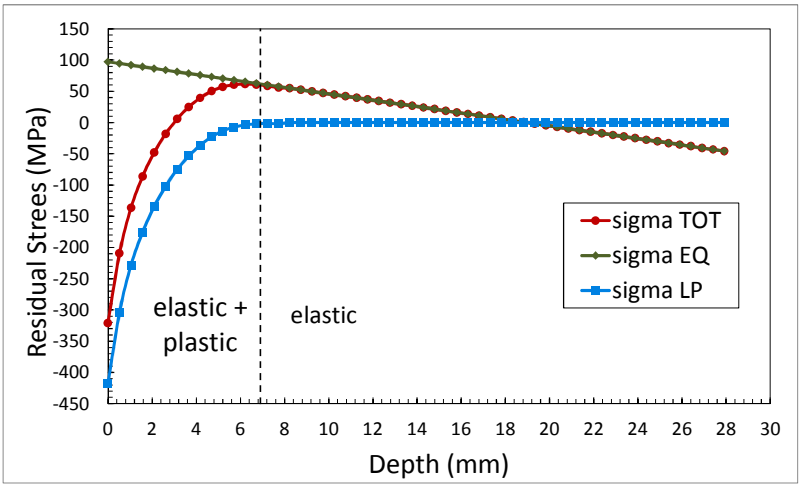

Fig. 5.2 separation of stress components

5.2.2 Eigenstrain calculation

Considering the total RS profile, it is possible to divide it into two stress profiles: the *Laser Peening* induced RS (σ_{LSP}) and the RS generated automatically by the material to balance the externally induced component, formally called *EQuilibrium* residual stress (σ_{EQ}). The first depends only on laser peening parameters [20] and the assumption is that it is geometry independent while the latter is geometry dependent. Mathematically this can be seen as a superposition as expressed in Equation 5.3 (referring to the *z* component of the stress):

$$\sigma_{TOT_{zz}}(y) = \sigma_{LP_{zz}}(y) + \sigma_{EQ_{zz}}(y)$$

Equation 5.3

The equilibrium residual stress component can be visually identified after a certain depth called the laser peening affected depth since beyond which the total residual stress profile is completely linear as can be seen in Fig. 5.2. While in [18], [19] this was only an assumption, later it was verified by Achintha *et al.* [21] that the plasticity generated by the laser peening process occurred up to the predicted laser peening affected depth. In other words, the LSP process induces plasticity up to some millimetres underneath the surface

and the misfit induced by it (i.e. Eigenstrain) must be balanced by the material's elastic response.

By extrapolating the equilibrium stress component up to the surface, it is possible to obtain a straight line which can be visualized in green in Fig. 5.2. In order to get the σ_{LSP} component Equation 5.3 must be rearranged to obtain the Equation 5.4:

$$\sigma_{LP_{zz}}(y) = \sigma_{TOT_{zz}}(y) - \sigma_{EQ_{zz}}(y)$$

Equation 5.4

As reported in [18] and by using Equation 5.1 and Equation 5.2, the Eigenstrains can be considered an elastic strain distribution that produces the post process residual stress field, and it is possible to easily calculate them from the σ_{LSP} using the following linear system:

$$\underline{\varepsilon^*}_{LP_{xx}}(y) = \begin{Bmatrix} \varepsilon^*_{LP_{xx}}(y) \\ \varepsilon^*_{LP_{yy}}(y) \\ \varepsilon^*_{LP_{zz}}(y) \end{Bmatrix} = -\frac{1}{E}\begin{bmatrix} 1 & -\nu & -\nu \\ -\nu & 1 & -\nu \\ -\nu & -\nu & 1 \end{bmatrix}\begin{Bmatrix} \sigma_{LP}(y) \\ 0 \\ \sigma_{LP}(y) \end{Bmatrix}$$

Equation 5.5

We get three Eigenstrain components for each *y* location. It is worth here noting that the minimum distance between two consecutive *y* position calculations, is the scientist's choice. Based on the author's experience, this distance should be small enough to allow a smooth residual stress profile but at the same time large enough to not increase significantly the number of FE elements during the meshing operation (removing in this way all the benefits of the Eigenstrain approach). In this study the Eigenstrains were calculated with a step of 0.5 mm. Since during the measurements of the residual stress this step is not always available (for example in case of the contour method it depends on the mesh of the model used), an interpolation process is necessary to find the best curve that fits all the points of the σ_{LSP} curve. This simple operation is easily solved by calculating a

polynomial through MATLAB. Once the equation of the polynomial is known, it is easier to calculate the σ_{LSP} value at a fixed distance and then the Eigenstrain using Equation 5.5.

For illustrative purposes only, Table 5.1 shows the values of the Eigenstrains of the stepped coupon calculated with a fixed step of 0.5 mm.

Table 5.1

		Eigenstrain		
		εxx	εyy	εzz
1	0	-0.00383	0.003892	0.003892
2	0.5	-0.00283	0.002869	0.002869
3	1	-0.00214	0.002174	0.002174
4	1.5	-0.00166	0.001682	0.001682
5	2	-0.00129	0.001311	0.001311
6	2.5	-0.001	0.001013	0.001013
7	3	-0.00075	0.000765	0.000765
8	3.5	-0.00055	0.000556	0.000556
9	4	-0.00038	0.000385	0.000385
10	4.5	-0.00025	0.000252	0.000252
11	5	-0.00015	0.000155	0.000155
12	5.5	-8.8E-05	8.95E-05	8.95E-05
13	6	-4.8E-05	4.91E-05	4.91E-05
14	6.5	-2.5E-05	2.52E-05	2.52E-05
15	7	-1.1E-05	1.17E-05	1.17E-05
16	7.5	-1E-05	1.02E-05	1.02E-05

5.2.3 Eigenstrain simulation

The final step regards the design of the FE model and the solving for equilibrium to generate the residual stress profile in the new geometry. Once the external geometry is set, as many sections as the number of y positions have to be created, e.g. 16 if we consider the Table 5.1. Each section must have the same thickness as the y distance previously chosen (thus 0.5 mm). As many materials as the created sections have to be created. Each material has two different properties:

- the elastic one, which contains the elastic behaviour of the material, i.e. the Young's modulus and the Poisson's ratio;

- the thermal one, which contains the information about the Eigenstrain;

For the last assignment each material will be assigned three thermal expansion coefficients (one for each direction) which are exactly the calculated values of the Eigenstrain for a given *y* position. So for example, according to Table 5.1, the 5th section of the sample will be designed at a depth of 2 mm from the surface and the three sets of thermal coefficients will be $\varepsilon_{xx} = -0.00383$, $\varepsilon_{yy} = 0.003892$ and $\varepsilon_{zz} = 0.003892$: Finally to activate these coefficients, the sample is subjected to a change of 1° in temperature and solved for equilibrium. According to the following equation:

$$\sigma_{ij} = E\alpha_{ij}\Delta T$$

Equation 5.6

the stress σ generated in the ij direction is directly proportional to the thermal coefficient (i.e. Eigenstrain) α along the same ij direction. These stresses are the so-called σ_{LSP}, and they are generated where the real sample is supposed to be peened. The elastic properties of the sample will restore the residual stresses within the sample in order to auto-balance the total stress.

To conclude this chapter, it is worth noting that since the theory used in the Eigenstrain approach is totally linear and elastic, in the FE post-analysis neither qualitative nor quantitative information about the plasticity are available: the final sample will result with no plasticity in it. This is one of the limitations of the Eigenstrain approach, other limitations need more comprehensive explanations and can be found in the next section.

5.3 Limitations of the Eigenstrain Approach

Before showing how the Eigenstrains were calculated and applied in order to predict the RS field within real samples, a detailed study about the limitations of the Eigenstrain

approach was carried out during this research. Following the basic theory, three different FE approaches are shown: the superposition of the Eigenstrain used to simulate a double treatment; the superposition of the Eigenstrain at a sharp corner; and the use of the Eigenstrain approach on a round edge.

For this particular research, the Eigenstrains were calculate from a stepped coupon made from aluminium alloy AA7050-T7451, typical for aerospace applications, machined by Airbus Group Innovations. According to MatWeb [22], the tensile yield strength for this alloy is 469 MPa at room temperature. The sample was laser peened by Metal Improvement Company with a power density of 4 GW/cm^2, the time length of a single shot was 18 ns and the number of peening treatments with the same laser settings was three.

5.3.1 Superposition of Eigenstrain to simulate double treatment

It has been demonstrated that Laser Shock Peening technology can increase in magnitude the compressive residual stress by increasing the number of surface treatments from 1 to 3 [23]. For this reason we used the Eigenstrain approach to simulate what happens when the same set of Eigenstrain is applied twice on the same sample. A block that was 30 mm thick and 50×50 mm^2 wide and long was taken into consideration. The sample was meshed along the thickness with elements 0.5 mm thick. The Eigenstrains were applied all over one of the wider surfaces and the model was then solved for equilibrium. The final residual stress profile was then used again as an input to apply a second time the same Eigenstrain set in the same position, thus simulating a second set of treatment made by three layers of laser peening (six layers of treatment were then simulated in two different steps). The final residual stress profiles taken in the centre of the sample to avoid any edge effect are shown in Fig. 5.3.

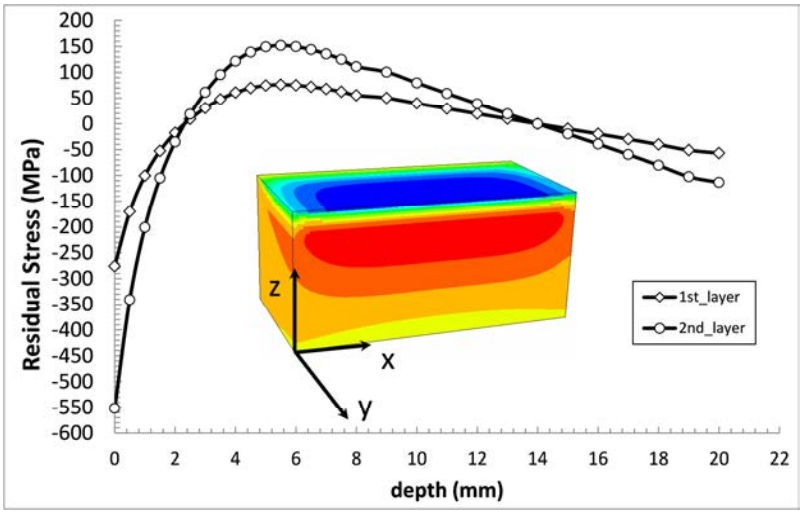

Fig. 5.3 Comparison between the residual stress profiles with one application and two application of Eigenstrains. The FEM picture gives a qualitative view of the distribution of the RS: blues indicates compression and red indicates tension.

As it is possible to see in Fig. 5.3, after the first application of Eigenstrain, the residual stress profile starts from –275 MPa and reaches a peak in tensile of 76 MPa. To simulate a second treatment with the Eigenstrain approach, a second layer of Eigenstrain was introduced in exactly the same position and the model was solved again for the equilibrium using as input the residual stress profile generated by the first application of Eigenstrain. As expected, since the theory is purely elastic, the new RS profile obtained after the second analysis shows a RS peak in compression equal to –550 MPa and a peak in tensile equal to 155 MPa. Both these values are the exact double of the values obtained with the first application of the Eigenstrain. The latter application of the Eigenstrain can be seen as the treatment was repeated for a further three layers with the same laser parameters. Heckenberger [24] carried out RS measurements on the same sample for both the configurations with three layers and the configuration with six layers of treatment. Since all the residual stress measurements were carried out with both lab X-ray diffraction and Incremental-Hole-Drilling (ICHD), it is not possible to know the entire residual stress profile through the thickness but at least it is possible to understand what happens within the first mm from the treated surface. According to the ICHD

measurements, by increasing the number of layers, the residual stress at the surface tends to increase when the number of layers are increased but they reach a value of –350MPa only, instead of –550MPa as calculated from the Eigenstrain prediction. A similar study conducted by Luong *et al.* [25] with a sample made by the aluminium alloy AA7085 demonstrates that by doubling the layers of treatment, the lowest value of compressive residual stress doesn't change, while the tensile stresses slightly increase but not proportionally to the number of layers. Furthermore, by increasing the number of layers of treatment, the residual stresses tend to stay in compression up to a higher depth. This effect is not simulated by the Eigenstrain where with both three or six layers the residual stresses become tensile at the same depth.

In conclusion, the Eigenstrain approach cannot simulate the application of a multitude of layers simply by superposition of them in the same area. In other words, Eigenstrain calculated from (for example) a single layer of treatment cannot be applied three times on the same area to simulated an LSP process of three layers. This happens because by increasing the number of layers the material reaches the yield stress where the behaviour is not linear anymore, while the Eigenstrain approach is totally linear and does not account for the plastic behaviour.

5.3.2 Use of Eigenstrain to simulate residual stresses in a sharp edge

A further application where the Eigenstrain can show limitations is at a sharp corner. Usually a sharp corner is not used in engineering since it can act as a stress concentration factor and cracks can easily start from this edge. However, some engineering components have an edge with a radius of 0.2-0.3 mm which can be considered similar to a sharp edge. In these particular locations the interest of using the LSP technology to introduce compressive residual stresses it aimed at retarding the crack initiation.

For this particular study, the same block of the preceding section was used. The block presented a sharp edge to keep the geometry as simple as possible for the meshing process. This time, the upper, lower and lateral surfaces where subjected to the Eigenstrain approach with subsequent generation of residual stresses. The Eigenstrains were applied in three different steps simulating what a real laser treatment would do. In particular, the mesh was first optimized to apply the Eigenstrain to the upper surface. Once the residual stresses were generated, the sample was re-meshed to have several layers of mesh 0.5 mm thick on the lateral side. The Eigenstrains were then applied to the lateral surface and at the same time the previous residual stresses were introduced as input. Since the analysis is perfectly elastic, the final residual stress profile is given by the summation of the residual stress profile generated during the first step and the residual stresses generated with the second step. For the lower surface the same procedure was used.

The following pictures show the application of the Eigenstrain and the subsequent generation of the residual stresses:

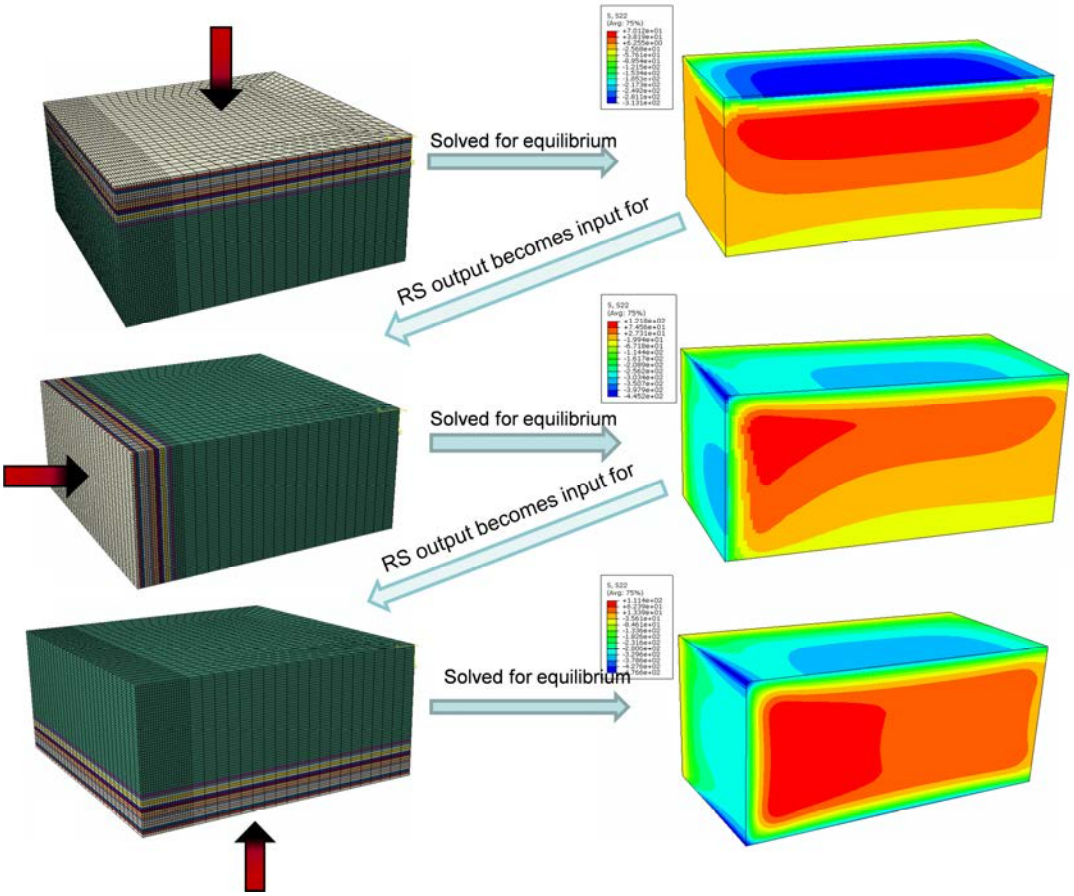

Fig. 5.4 The steps to apply the Eigenstrain on the same sample in three different location are shown

As it is possible to see from the scheme in Fig. 5.4, at the end of the process at the two sharp edges the compressive residual stresses reach the highest value within the sample (easily spotted by the deep blue colour). As reported in [26] a sample with the same geometry and same laser peening pattern was the subject of the residual stress mapping and it was found that the residual stresses tend to decrease when approaching the edge of the sample rather than increase as is predicted by the Eigenstrain approach.

To overcome this problem the following approach was taken: instead of applying the Eigenstrain on the top and side surface with an overlap, the Eigenstrain layers were shifted from the edge by 0.5 mm as shown in Fig. 5.5.

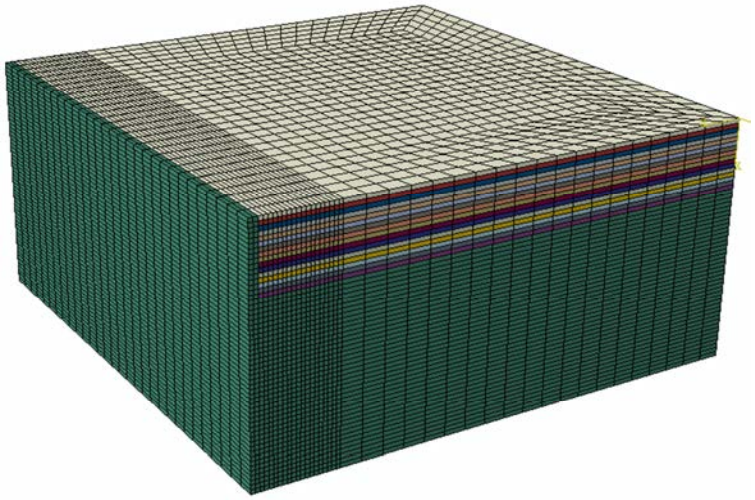

Fig. 5.5 The parallelepiped used during the analysis with the Eigenstrain layers (the coloured ones) shifted towards right

In this way there was no overlapping between the Eigenstrains applied to the top and the side at the sharp edge. The final result is shown in Fig. 5.6:

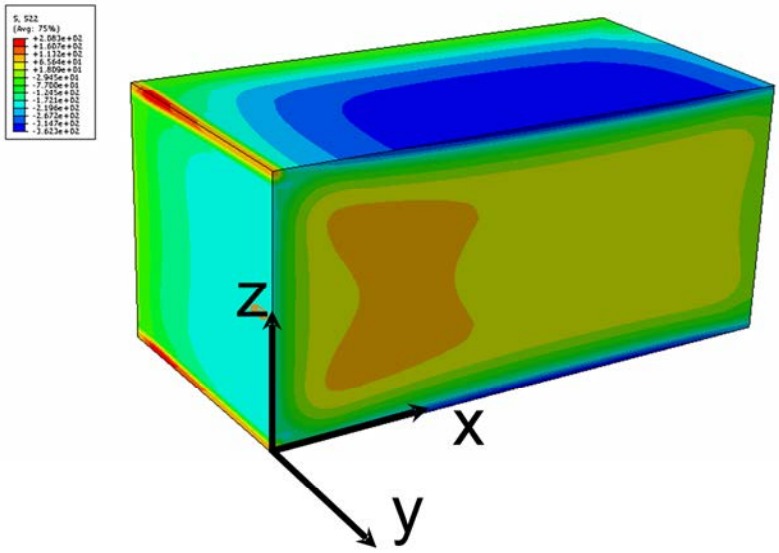

Fig. 5.6 The final result of the application of the Eigenstrain with no overlapping at the sharp edge.

The stresses shown are in *y* direction. It is possible to see now that at the edge the stresses are in tension again (red colour), this because some elements were not included in the plasticity process coming from the Eigenstrain application.

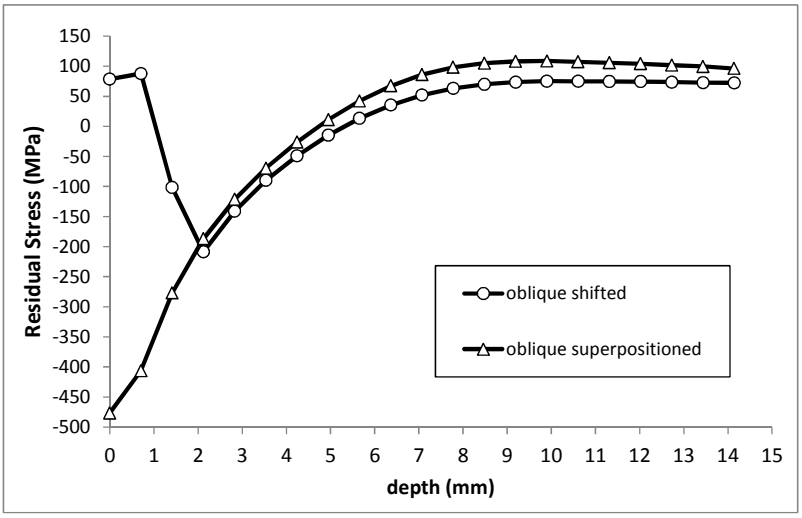

Fig. 5.7 Comparison between the residual stresses with and without of the Eigenstrains

In particular the stresses at the corner when the overlapping is present reached a value of −476 MPa while when this overlapping is avoided, the stresses at the corner become tensile and the value reached is approximately 80 MPa. Even this latter value seems to overestimate the real stress values close to a corner since as shown in [26], approaching the edge the residual stress tend to decrease in magnitude but they are still in compression. From a practical point of view, to avoid the generation of tensile residual stress at a *quasi*-sharp corner, a shot inclined at 45° directly on-top of the corner is made. This is the case of the Single Edge Notch (SEN) sample which is the subject of the RS measurements and prediction reported in chapter 7. The characteristics of the LSP treatment will be reported in more details in chapter 3 but for the purpose of the Eigenstrain application some information will be given here. The sample has a middle section 10 mm thick and it was laser peened around the three surfaces of the notch. In order to estimate the final RS field with the Eigenstrain, the simulation regarded first the application of the Eigenstrain at one of the wider surfaces and then the application at the corner. The following pictures show how the Eigenstrain were distributed:

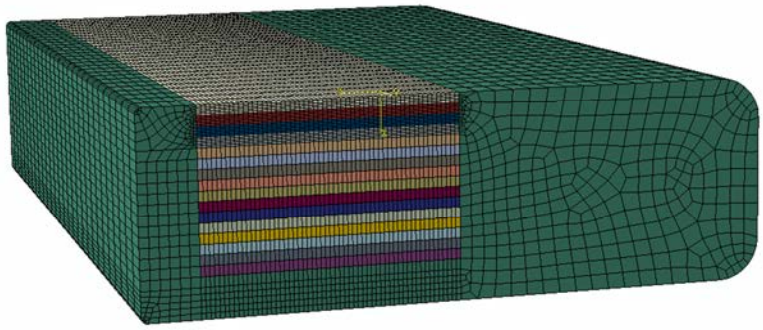

Fig. 5.8 Distribution of the Eigenstrain for the wider surface peening simulation

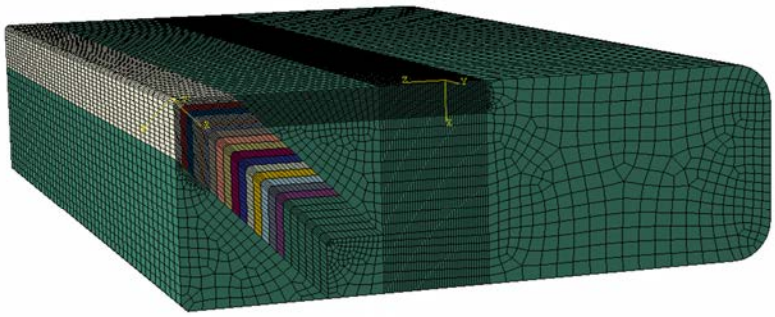

Fig. 5.9 Application of the Eigenstrain at the rounded corner

According to Fig. 5.8 and Fig. 5.9, the application of the Eigenstrain was made similarly to the application of the LSP treatment. However, after a preliminary analysis, the partial result was as shown in the next picture:

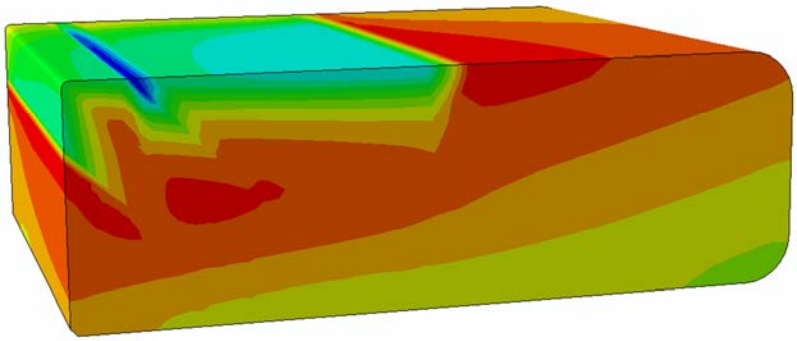

Fig. 5.10 Partial results of the application of the Eigenstrain for the two consecutive steps shown in Fig. 5.8 and Fig. 5.9

It is possible to see in Fig. 5.10 that the distribution of the residual stresses at the surface of the sample is not homogeneous, in particular a darker blue area is present as deeper compressive RS after the second treatment. The RS measurement of the SEN reported in

[27] shows an homogeneous distribution of the RS at the surface up to the edge where the RS tend to decrease. The increase of the compressive RS was due again to the superposition of the Eigenstrain. To avoid it, a different distribution of Eigenstrain was introduced as the following pictures indicates:

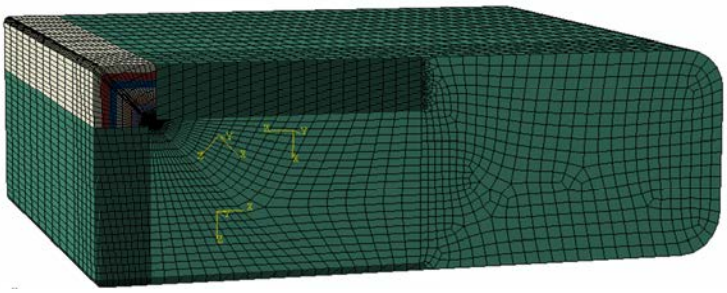

Fig. 5.11 New distribution of Eigenstrain

In Fig. 5.11 the new approach is shown. In this case the Eigenstrains were not overlapped and the final RS distribution result was more homogeneous. The final results can be seen in the following picture:

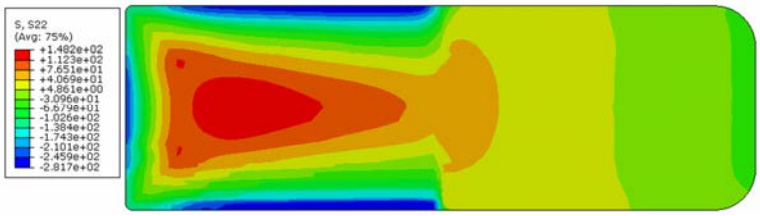

Fig. 5.12 Final RS distribution after the new Eigenstrain approach

From a qualitative point of view, the RS distribution shown in Fig. 5.12 is closer to reality. The compressive residual stresses are concentrated where the area is flat, while, getting closer to the edge, the RS tend to decrease their value. Tensile stress is confined within the LSP region.

5.3.3 Use of Eigenstrain to predict residual stress at a round edge

One last example is given by the application of the Eigenstrain theory to predict the residual stress profile where a round edge is present. A round edge with a 5 mm radius was chosen. Usually when these geometries are subjected to laser peening, the laser pattern follows the curvature of the radius. For this reason also the Eigenstrain application has to follow the same pattern. To obtain a complete residual stress map in one step, particular attention must be paid to the application of the Eigenstrain. In particular, as said before, one of the key elements for a correct application of the Eigenstrains resides in the correct thickness of the mesh elements created in the FEM environment that must be as thick as the distance the Eigenstrain were previously calculated, i.e. if the Eigenstrains were calculated every 0.5 mm through the thickness, the mesh elements have to be 0.5 mm thick. In the following picture the arrows indicate the sections where the Eigenstrain were applied with a step of 0.5 mm for a total length of 5 mm:

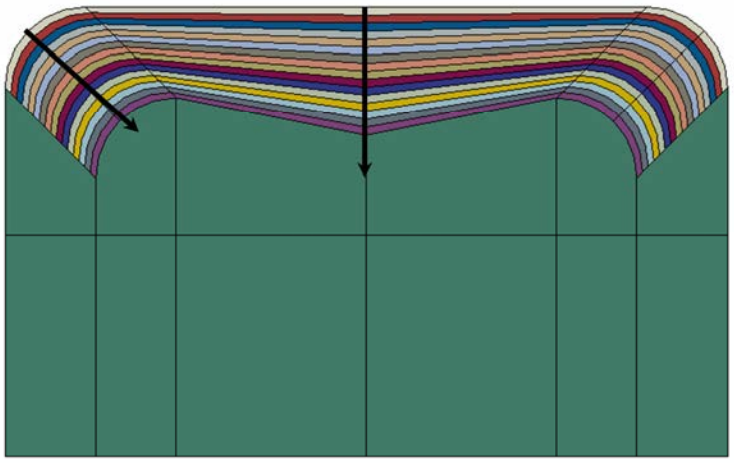

Fig. 5.13 2D section of a sample with two round edge with a 5mm radius. Different colours indicate different Eigenstrain layers

The sample has an infinite length and Fig. 5.13 shows a 2D section. It is possible to see the different coloured sections which indicate different Eigenstrain layers. Another important aspect to keep into consideration when the Eigenstrain theory is used is the correct use of the coordinate system. As said before, the Eigenstrains are applied to the

new geometry as orthotropic thermal expansion coefficients since for each *y* location three of them are calculated, one per each direction x, y and z. The coordinate system must be then consistent with the direction of action of the Eigenstrain. As reported in [28] and [29] we have to distinguish two different effects of the laser when the treatment is made with a certain inclination: on one hand even if the laser direction is not perpendicular to the surface, the shock wave propagation direction and the subsequent generation of plasticity are still perpendicular to the surface; but on the other hand, due to the non-perpendicularity of the process, the energy is seriously reduced since an inclination of the laser implies a wider area of treatment thus a lower power density. For these reasons, two different coordinate systems were taken into account for the Eigenstrain:

Plasticity point of view: a cylindrical coordinate system was chosen for this case so the Eigenstrains were reproducing the effect of a small single spot of laser peening with the same power of the one used, acting perpendicular to each point of the surface of the round edge; in this way the geometry and the Eigenstrain alignment are the same, Fig. 5.14;

Energy point of view: considering that the round edge is formed by an arc of 90°, the coordinate system is rectangular and it is aligned with the bisecting of this arc, thus is inclined at 45°. In this way the Eigenstrain will generate a residual stress field which is inversely proportional to the angle between the mesh element direction and the coordinate system, i.e. the greater the angle the less the residual stress generated. In this way both the inclination of the laser and the fact that the laser spot is as wide as the round edge was taken into account, Fig. 5.15.

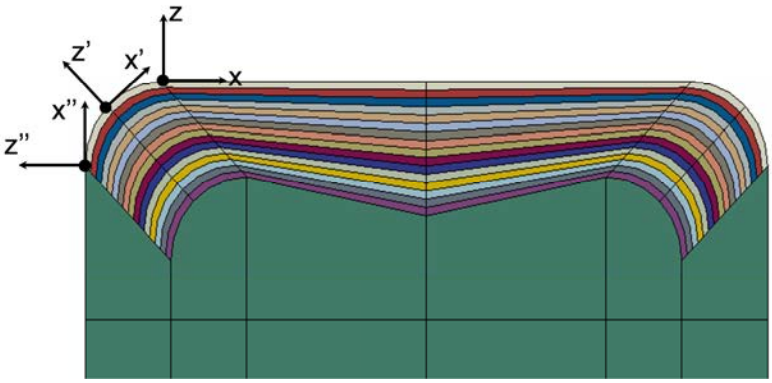

Fig. 5.14 The coordinate system parallel to the laser direction was used in order to get plasticity perpendicular to each point of the round edge surface. The *y* component is out of the plane

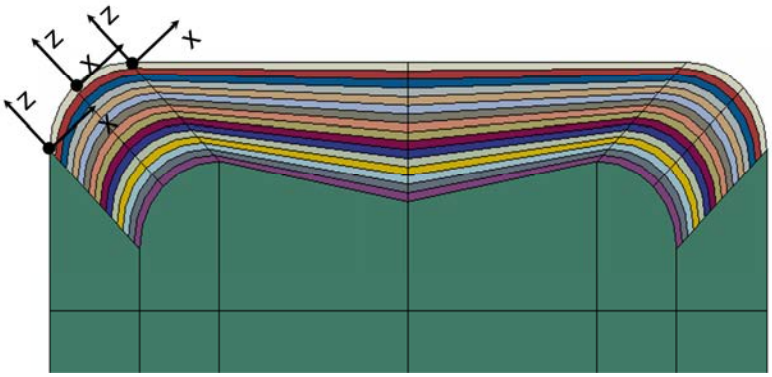

Fig. 5.15 45° inclined coordinate system was used; the *y* component is out of the plane.

The results of the two different approaches are reported in the following graph:

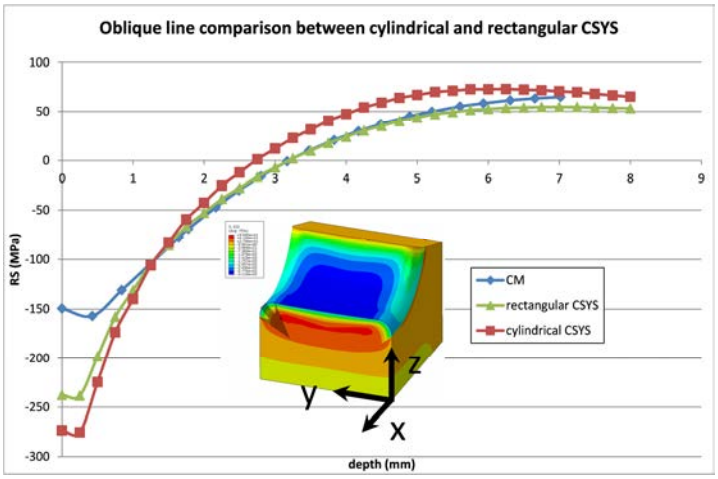

Fig. 5.16 Differences between the use of the cylindrical coordinate system and the rectangular one. The stress component is in the *x* direction.

In Fig. 5.16 the blue line shows the residual stress measured with the contour method [30] while the green and the red lines show the residual stresses with two the different coordinate systems used. It is possible to see that even if none of the approaches can predict correctly the residual stresses close to the surface, the model with the rectangular coordinate system has a good agreement with the measured data (the residual stress difference is below 5 MPa). In the author's opinion the main reason for this behaviour is that the cylindrical coordinate system effectively models the Eigenstrain acting as though the laser peening treatment was perpendicular to each single point of the surface, which it was not. What actually was perpendicular, as said before, is the generation of the shock waves and the plasticity but since the laser spot was as large as the entire round edge, the laser was distributed on the round edge surface. This led to a distribution of the laser energy on a wider area with a subsequent reduction of the laser power density. This effect is taken into account only by the use of a rectangular coordinate system.

5.4 Conclusions

In this chapter the Eigenstrain theory has been explained and some historical background has been given. It has been shown in the chapter, that the approach given by DeWald and Hill does not necessitate a complicated mathematical background since all the theory is based on linear analysis and, being as low computational-cost as any other linear analysis, puts the Eigenstrain application in direct competition with the direct FE modelling of LSP. However, since no information about plasticity can be obtained by the Eigenstrain approach, it is the author's opinion that the Eigenstrain theory cannot take the place of full LSP simulation but it will rather work alongside it to reach faster similar results concerning the RS distribution only.

References

[1] T. Mura, *Micromechanics of Defects in Solids (Mechanics of Elastic and Inelastic Solids)*. Martinus Nijhoff Publiesher, 1987.

[2] T. Reissner, "Eigenspannungen und Euigenpannungensquellen," *J. Appl. Math. Mech.*, vol. I, no. I, pp. 1–8, 1931.

[3] J. D. Eshelby, "The Determination of the Elastic Field of an Ellipsoidal Inclusion, and Related Problems," *Proc. R. Soc. London. Ser. A. Math. Phys. Sci.*, vol. 241, no. 1226, pp. 376–396, 1957.

[4] J. D. Eshelby, "The Elastic Field Outside an Ellipsoidal Inclusion," *Proc. R. Soc. London. Ser. A. Math. Phys. Sci.*, vol. 252, no. 1271, pp. 561–569, 1959.

[5] Y. Ueda, K. Fukuda, K. Nakacho, and S. Endo, "A New Measuring Method of Residual Stresses with the Aid of Finite Element Method and Reliability of Estimated Values," *Trans. JWRI*, vol. 4, no. 2, pp. 123–131, Oct. 1975.

[6] V. Luzin, "Use of the Eigenstrain Concept for Residual Stress Analysis," in *Materials Science Forum*, 2014, vol. 768–769, pp. 193–200.

[7] T. Fujimoto, "A method for analysis of residual welding stresses and deformations based on the inherent strain : A theoretical study of residual welding stresses and deformations (Report 1)," *J. Japan Weld. Soc.*, vol. 39, no. 4, pp. 236–252, Apr. 1970.

[8] Y. Ueda, Y. C. Kim, and M. G. Yuan, "A Predicting Method of Welding Residual Stress Using Source of Residual Stress (Report I) : Characteristics of Inherent Strain (Source of Residual Stress)(Mechanics, Strength & Structural Design)," *Trans. JWRI*, vol. 18, no. 1, pp. 135–141, Jun. 1989.

[9] Y. Ueda and M. G. Yuan, "A Predicting Method of Welding Residual stress Using Source of Residual Stress (Report II) : Determination of Standard Inherent Strain(Mechanics, Strength & Structural Design)," *Trans. JWRI*, vol. 18, no. 1, pp. 143–150, Jun. 1989.

[10] Y. Ueda and M. G. Yuan, "A Predicting Method of Welding Residual Stress Using Source of Residual Stress (Report III) : Prediction of Residual Stresses in T- and I-joints Using Inherent Strains(Mechanics, Strength & Structural Design)," *Trans. JWRI*, vol. 22, no. 1, pp. 157–168, Aug. 1993.

[11] M. R. Hill and D. V. Nelson, "The inherent strain method for residual stress determination and its application to a long welded joint," in *ASME*, 1995, vol. 318, pp. 343–352.

[12] H. T. Luckhoo, T. S. Jun, and A. M. Korsunsky, "Inverse Eigenstrain analysis of residual stresses in friction stir welds," *Procedia Eng.*, vol. 1, no. 1, pp. 213–216, 2009.

[13] X. Song, W. C. Liu, J. P. Belnoue, J. Dong, G. H. Wu, W. J. Ding, S. A. J. Kimber, T. Buslaps, A. J. G. Lunt, and A. M. Korsunsky, "An Eigenstrain-based finite element model and the

evolution of shot peening residual stresses during fatigue of GW103 magnesium alloy," *Int. J. Fatigue*, vol. 42, pp. 284–295, Sep. 2012.

[14] A. M. Korsunsky, "On the modelling of residual stresses due to surface peening using Eigenstrain distributions," *J. Strain Anal.*, vol. 40, pp. 817–824, 2005.

[15] T.-S. Jun, A. M. Venter, and A. M. Korsunsky, "Inverse Eigenstrain Analysis of the Effect of Non-uniform Sample Shape on the Residual Stress Due to Shot Peening," *Exp. Mech.*, vol. 51, no. 2, pp. 165–174, Apr. 2010.

[16] J. Tea-Sung, "Determination of the Eigenstrain Reconstruction Method for the Interpretation of Diffraction Stress Measurements in Engineering Components," PhD Thesis, Oxford University, Oxford, UK, 2009.

[17] M. Hill, "Determination of Residual Stress Based on the Estimation of Eigenstrain," PhD Thesis, Stanford University, 1996.

[18] A. T. DeWald and M. R. Hil, "Eigenstrain-based model for prediction of laser peen ingresidual stresses in arbitrary three-dimensional bodies. Part 1 and Part 2," *J. Strain Anal.*, vol. 44, no. Special Issue Paper, pp. 1–27, 2008.

[19] A. T. DeWald and M. R. Hill, "Eigenstrain-based model for prediction of laser peening residual stresses in arbitrary three-dimensional bodies. Part 2: model verification," *J. Strain Anal.*, vol. 44, 2008.

[20] R. Fabbro, P. Peyre, L. Berthe, and X. Scherpereel, "Physics and applications of laser-shock processing," *J. Laser Appl.*, vol. 10, no. 6, pp. 265–279, 1998.

[21] M. Achintha, D. Nowell, K. Shapiro, and P. J. Withers, "Eigenstrain modelling of residual stress generated by arrays of laser shock peening shots and determination of the complete stress field using limited strain measurements," *Surf. Coatings Technol.*, vol. 216, no. 0, pp. 68–77, 2013.

[22] "MatWeb-Material Property Data," 2014. [Online]. Available: www.matweb.com. [Accessed: 28-Jun-2014].

[23] P. Peyre, R. Fabbro, P. Merrien, and H. P. Lieurade, "Laser shock processing of aluminium alloys. Application to high cycle fatigue behaviour," *Mater. Sci. Eng. A*, vol. 210, no. 1–2, pp. 102–113, Jun. 1996.

[24] U. C. Heckenberger, V. Holzinger, W. von Bestenbostel, and E. Hombergsmeier, "Laser shock peening to improve the fatigue resistance of AA7050 components," *Int. J. Struct. Integr.*, vol. 2, no. 1, pp. 22–33, 2011.

[25] H. Luong and M. R. Hill, "The effects of laser peening on high-cycle fatigue in 7085-T7651 aluminum alloy," *Mater. Sci. Eng. A*, vol. 477, no. 1–2, pp. 208–216, Mar. 2008.

[26] U. C. Heckenberger, E. Hombergsmeier, and D. Furfari, "Residual stress fields in LSP and SP treated aluminium specimens after fatigue testing," in *4th International Conference on Laser Peening and Related Phenomena;*, 2013.

[27] E. Hombergsmeier, V. Holzinger, and U. C. Heckenberger, “Fatigue Crack Retardation in LSP and Sp Treated Aluminium Specimens,” in *Advanced Materials Research*, 2014, vol. 891–892, pp. 986–991.

[28] M. R. Hill, A. T. DeWald, A. G. Demma, L. A. Hackel, H.-L. Chen, D. Brent, R. C. Specht, and F. B. Harris, “Laser peening technology,” *Adv. Mater. Process.*, vol. 161, no. 8, pp. 65–67, 2003.

[29] Evans, A. D., King, A., Pirling, T., Bruno, G., & Withers, P. J. (2003). Near Surface Residual Stress Determination of Laser Shock Peening by Neutron Diffraction. *Journal of Neutron Research*, *11*(4), 229–233.

[30] M. B. Toparli, “Analysis of Residual Stress Fields in Aerospace Materials After Laser Peening,” PhD Thesis, The Open University, 2012.

6 Measurements of residual stress profiles within a stepped coupon AA7050-T7451 and comparison with the Eigenstrain approach

In this chapter the Laser Shock Peened AA7050-T7451 stepped sample will be discussed. Through-thickness residual stress profiles in different locations within the sample were measured in different neutron and Synchrotron X-ray diffraction facilities. A contour method measurement carried out by Dr M. B. Toparli will be used as comparison as well. All these data will be compared with the residual stress profiles obtained with the Eigenstrain method approach.

6.1 Introduction

As said in chapter 5, the Eigenstrains can be calculated from a simple geometry sample and applied in different geometries to predict the final residual stress profiles when the surface treatment and materials are the same. This approach can be interesting when complex geometries are involved since it is computationally intensive to predict through the direct simulation of the laser peening the final distribution of the residual stress and at the same time can be expensive to conduct several trial and error tests to find the best laser setting for the desired residual stress profiles within a particular sample. In order to understand the potentials and the limits of the Eigenstrain approach, an aluminium alloy stepped coupon with a complex geometry is the subject of this study. In particular, the Eigenstrains were calculated from a flat area of the stepped coupon and they were subsequently applied through an FE model in the same areas where the real sample was

laser peened. The real sample was then the subject of several residual stress measurements in different locations and the obtained residual stress profiles were then compared to the ones obtained from the FE model. The RS tests made were:

- Contour method – The Open University, Milton Keynes;
- Electronic Speckle Pattern Interferometry Hole-drilling – Helmholtz Zentrum, Geestacht;
- X-ray diffraction strain measurements – JEEP instrument, Diamond Light Source Synchrotron, Oxford;
- Neutron Diffraction strain measurements – SALSA instrument, ILL, Grenoble;
- Neutron Diffraction strain measurements – POLDI instrument, SINQ, Zurich;

Some publications already showed the limits of the Eigenstrain theory at curved surfaces. In particular DeWald [1] showed that the Eigenstrain approach tends to overestimate the residual stresses through the thickness of a blended curved surface while Vasu [2] studied the distribution of the residual stresses around curved edges from a computational point of view with all the limitations this approach can have for a such a complex technique.

6.2 Stepped Coupon

The sample studied is a stepped coupon made of aluminium alloy AA7050-T7451, milled from a rolled plate by EADS Innovation Works for fatigue testing. The material composition is listed in (Table 1, Chapter 5). The sample is shown in Fig. 6.1. A complete description of all the samples involved in the broader research programme can be found in [3]. Two samples with the same geometry were laser shock peened by Metal Improvement Company (MIC), Earby, UK, with the same laser parameters, and their description can be found in chapter 3. The following laser parameters were chosen to keep the distortions as low as possible: the power density was 4GW/cm^2; the duration of each shot was 18ns; and three successive layers of treatment were done with a 33% geometrical shift from each other. This level of coverage was expected to produce a homogeneous distribution of residual stress at the surface of the sample: low levels of coverage have previously been

shown to introduce oscillatory stress fields [4]. The laser used a square spot size of 4×4 mm^2.

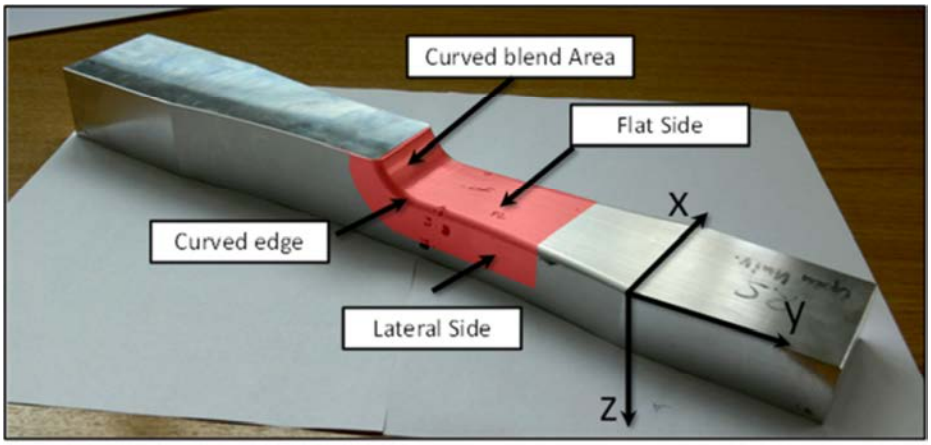

Fig. 6.1 The stepped coupon sample, with the axis system used

The sample provided three different areas for study: the central planar area from where the Eigenstrains were derived; the curved edges at the extremes in the *x*-direction, where the effect of geometry change could be studied; and the curved blend between the two ends of the sample along the *y*-direction where the effect of thickness change could be studied.

6.3 Residual Stress Results

In this section all the residual stress results and the comparison with the Eigenstrain FE analysis obtained residual stress profiles are presented.

6.3.1 Residual Stress in the Plane Area

An initial comparison was made between the measured residual stress in the central planar area and the residual stresses derived from the Eigenstrain FE model. This gives verification that the Eigenstrains were implemented correctly inside the ABAQUS environment, as they should reconstruct the measured residual stress. The measurements

were taken from the planar area through the thickness, with the σ_{yy} component of stress obtained from the contour method. It is possible to see, in Fig. 6.2, that the peak compressive and tensile stresses match extremely well, within an error of ±5 MPa that is within any technique sensitivity. The two curves should overlap perfectly in principle, since the Eigenstrains were derived from the residual stress profile measured in the same position. However, there is smoothing applied to the data which accounts for the small differences observed between the two profiles. This first check confirmed the correct derivation of the Eigenstrains and their application within the FE model.

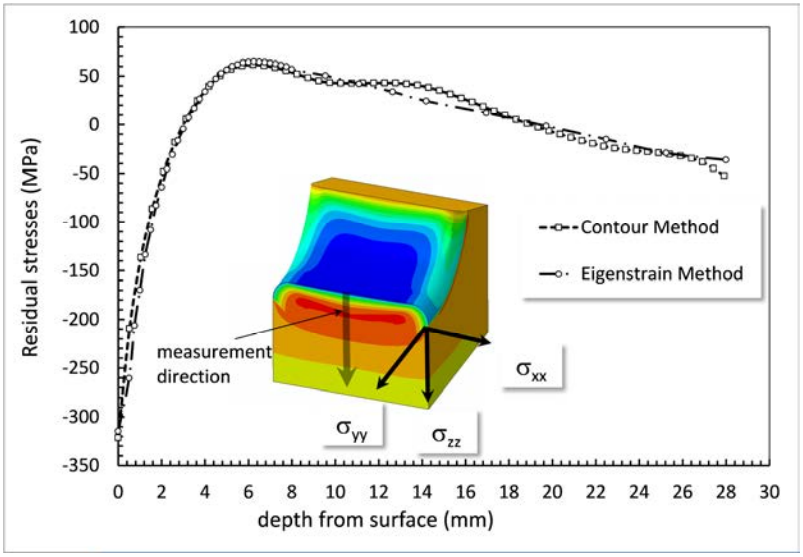

Fig. 6.2 Comparison between the Contour method results and the Eigenstrain approach results for the σ_{yy} residual stresses component. The colours show the distribution of the RS, in particular blue indicates the presence of compression and red indicated the highest tension present within the component

6.3.2 Residual stresses at the Curved Edges

The derived Eigenstrains were used to calculate the stresses normal to the curved edges of the sample. Fig. 6.3 shows the results of the Eigenstrain calculation using the Eigenstrains (derived from the planar region of the sample) compared to the measured results from the contour method. There is good agreement, within ±20MPa, from a depth of 1.5 mm from the surface. However, there is significant discrepancy within the first 1.5 mm from the surface where the gap is up to 85 MPa.

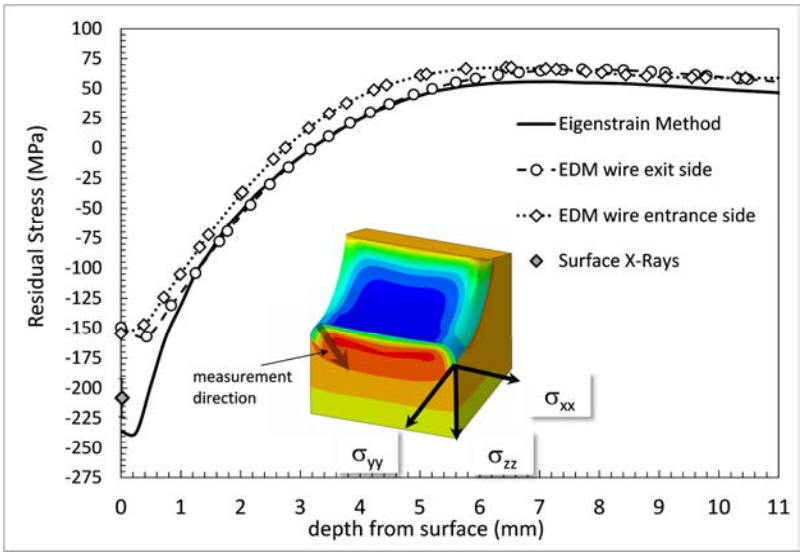

Fig. 6.3 Comparison between the Contour method results and the Eigenstrain approach results for the σ_{yy} residual stresses component.

The contour method is not reliable very close to a surface as a consequence of near-surface cutting artefacts and limitations in the data fitting [5]. Since it was impossible to establish *a priori* if either the contour method or Eigenstrain approach were respectively underestimating or overestimating the residual stress values, the incremental hole drilling technique was used for its higher reliability close to the surface. Four measurements were obtained at the curved edge to increase the reliability of the collected data, and we believe that this is the first time that incremental hole drilling has been used to determine residual stress from a curved surface after laser peening. The four different residual stress profiles were averaged. In Fig. 6.4 all these data are presented.

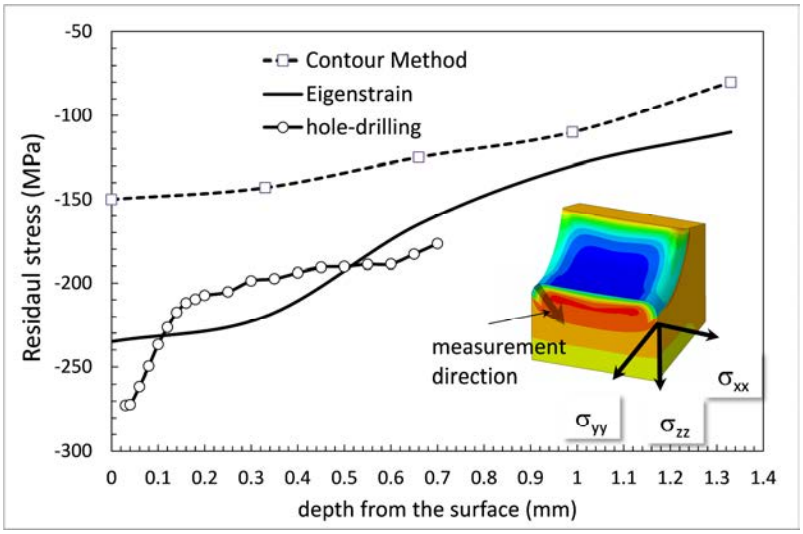

Fig. 6.4 Comparison between the Contour method results, the Eigenstrain approach results and the hole-drilling results for the σ_{yy} residual stress component.

Fig. 6.4 shows that the measurements taken at the round edge by incremental hole drilling lay between the Eigenstrain prediction and the contour method measurements between 0.2 mm and 0.7 mm depth, while between 0 and 0.2 mm the data were more compressive than either method. Generally speaking, the residual stress profile of laser shock peened component tends to be smoother very close to the surface owing to the reverse yielding effect. The ESPI hole-drilling technique suggests a residual stress profile that tends to be steeper close to the surface, which looks unrealistic. This trend may be due to the fact that during the drilling the material very close to the surface was not removed homogeneously so the data may not be completely reliable. The system used performs simple drilling of the hole, and it is known that orbital milling produces more accurate results [6].

The analysis method of the deformed area with the ESPI technique requires certain assumptions. One of the assumptions states that the surface of the sample is flat before drilling the hole, out to at least about 5 diameters from the centre of the hole [7]. The ESPI measurement technique interprets the deformation as if the surface were flat. In the presented measurements, the authors did not account for the curved surface. This could

be a further explanation of the steeper trend of the curve near the surface. In consequence, the results from the hole-drilling are not reliable near the surface, but can be taken to be acceptable after 0.1 mm depth; and since these data are closer to the Eigenstrain approach than to the contour method, this may indicate that the peak magnitude of near-surface compression was not adequately captured by the original contour method measurements from the central planar area. The difference may alternatively be a consequence of a change in material response to the peening at the curved edge. The laser spot was 4 × 4 mm^2 which is of the same order as the radius of the curved edge. This may have led to a different generation of shock waves and their interaction within the sample, and consequently a different distribution of residual stresses.

The residual stresses at the curved edge were then measured with both neutron and X-ray diffraction. The chosen beamline for the first experiment was the SALSA beamline at the Institue Laue-Langevin (ILL) in France. The facility details and the experiment procedures can be found in chapter 4. The following graph shows the comparison between the measured residual stresses and the ones obtained with the Eigenstrain approach.

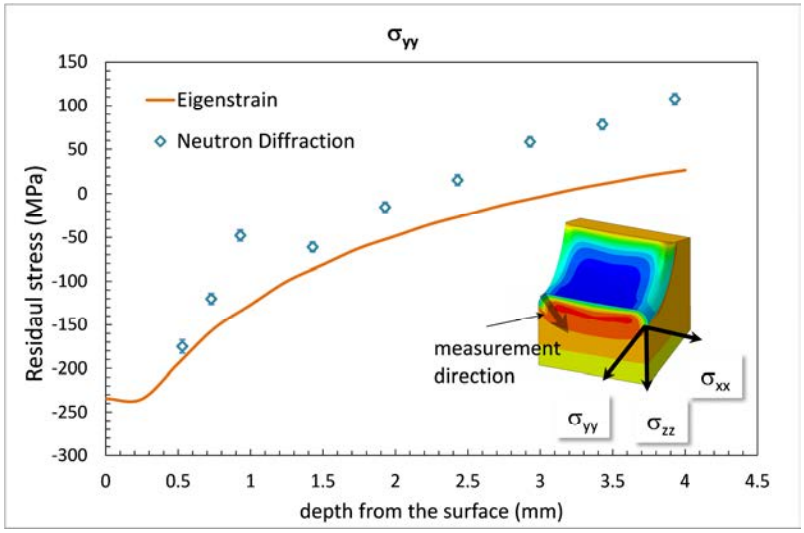

Fig. 6.5 The graph shows the comparison between the distribution of the σ_{yy} stress components obtained through the neutron diffraction method and the Eigenstrain predicted ones

As it is possible to see from Fig. 6.5, even if the trend of both the residual stress profiles are very similar, there is a gap between the measured and the predicted ones, which is approximately 10 MPa at 0.5 mm from the surface and then it increases up to 70 MPa close to 4 mm from the surface. By studying the distribution of the strains rather than the stresses, it' s possible to see that the ε_{zz} component is not matching well the distribution of strains predicted by the Eigenstrain approach.

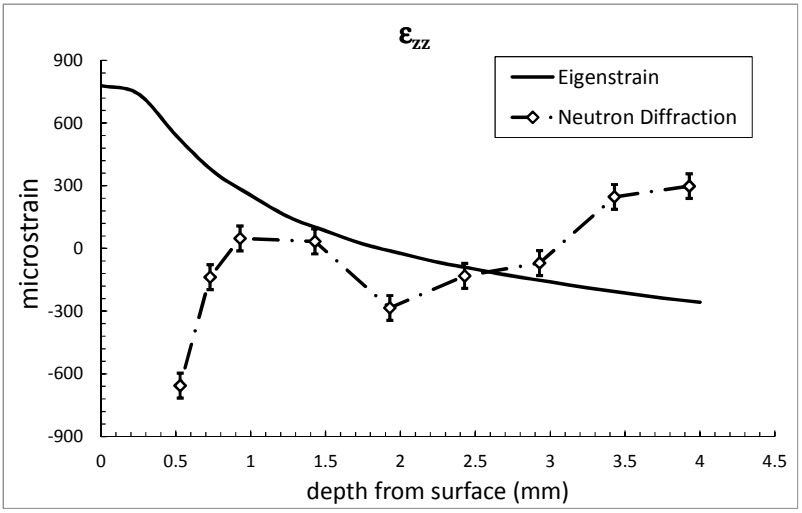

Fig. 6.6 The graph shows the difference between the strains predicted by the Eigenstrain approach and the strains calculated with the neutron diffraction method

As was said in chapter 3, the stepped coupon was rolled from a plate in the z-direction of the sample so all the grains are elongated in this same direction. By using a small gauge volume section, as in this experiment, on highly textured samples, the grains included in the single point measurement could be insufficient to get an average value of the strain in a single point and this could lead to scatter in the strain values. In order to overcome this limitation a further experiment was carried out with X-ray synchrotron diffraction method.

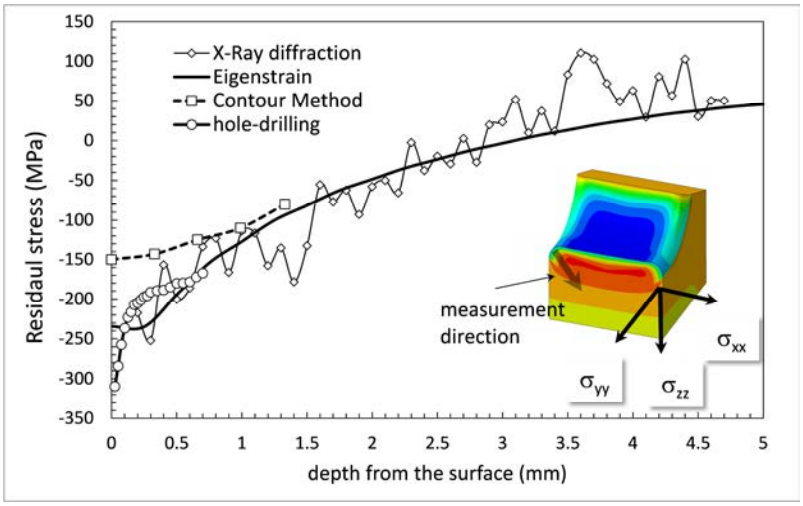

Fig. 6.7 Comparison between residual stress measurements along the direction indicated in the picture. The stress components is σ_{yy}.

Fig. 6.7 shows the comparison between the Eigenstrain prediction and the measured residual stresses in the σ_{yy} component along the direction indicated in the figure with all the three techniques used. Regarding the X-ray diffraction data, the agreement is very good for the entire set of data from 0.2 mm from the surface up to 5 mm within the sample. Since the diamond-shaped gauge volume was very narrow and elongated in the same direction of the elongation of the grains, data scatter is more evident. This is particularly noticeable around 1.5 mm from the surface and 3.7 mm from the surface.

6.3.3 Curved blend Area

A final experiment was carried out with neuron diffraction using the POLDI instrument at PSI, Switzerland. The residual stress in the blend area between the thicknesses at each end of the sample was measured to investigate the applicability of the Eigenstrain approach when the thickness is changed. Measurements were taken from the centre of the blend, normal to the sample's surface (Fig. 6.8). Fig. 6.8 b), c) and d) show the results for the three stress components along with the coordinate system shown in Fig. 6.8 a):

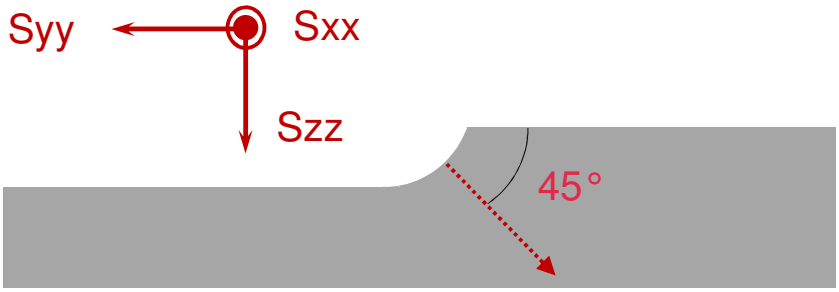
Syy
Sxx
Szz
45°

a)

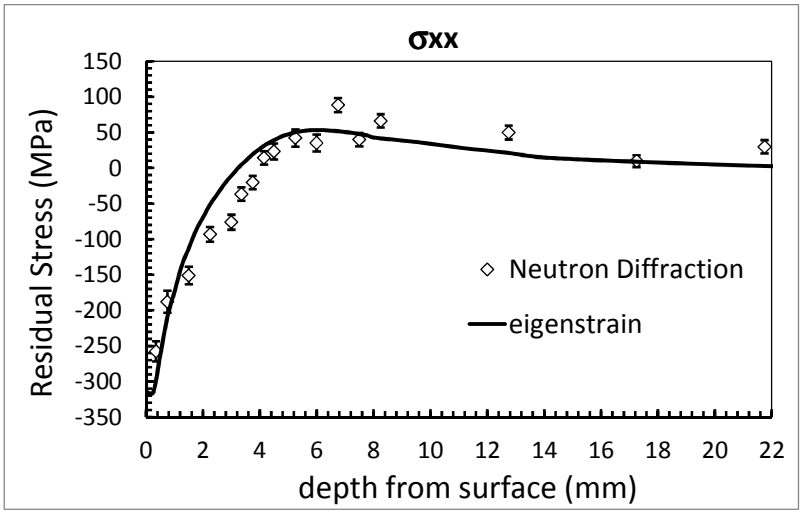
σxx
Residual Stress (MPa)
150
100
50
0
-50
-100
-150
-200
-250
-300
-350
0
2
4
6
8
10
12
14
16
18
20
22
depth from surface (mm)
Neutron Diffraction
eigenstrain

b)

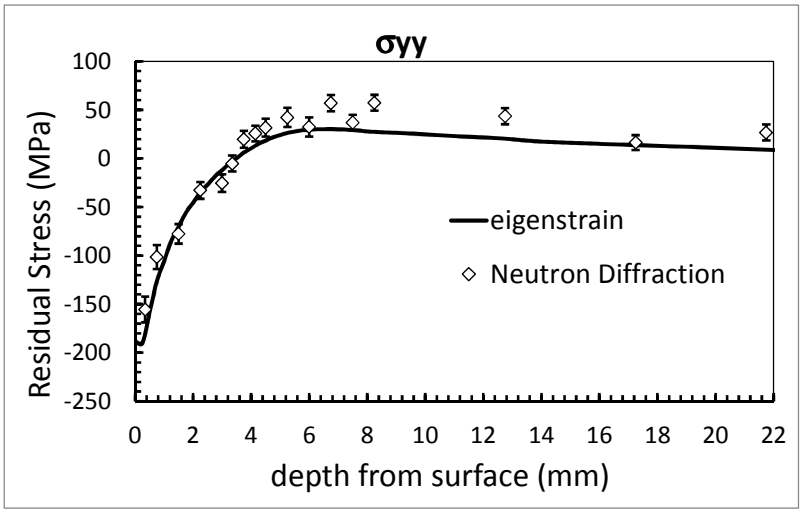
σyy
Residual Stress (MPa)
100
50
0
-50
-100
-150
-200
-250
0
2
4
6
8
10
12
14
16
18
20
22
depth from surface (mm)
eigenstrain
Neutron Diffraction

c)

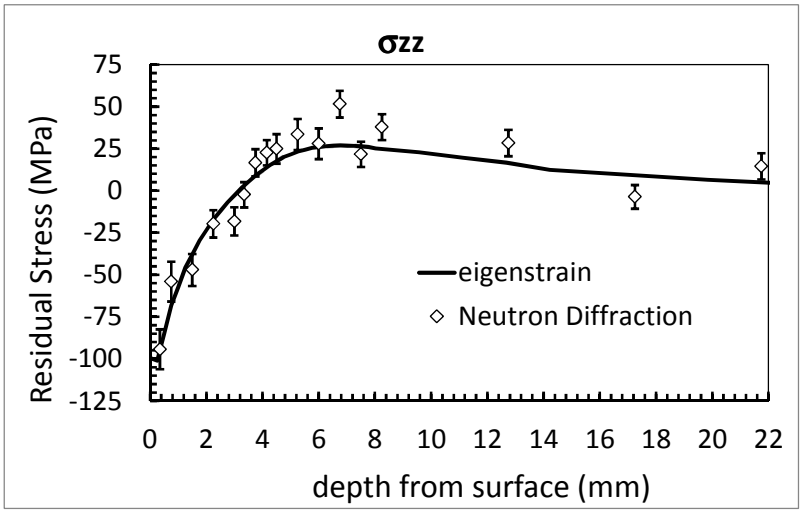

d)

Fig. 6.8 a) Direction of the measurements and coordinate system; b) σ_{xx} stress component; c) σ_{yy} stress component; d) σ_{zz} stress component

Fig. 6.8 shows that the agreement between the Eigenstrain prediction and the data from POLDI are within the measurement errors for most of the points in directions σ_{yy} and σ_{zz}. For the σ_{xx} component there are some differences between the neutron measurements and the data from the Eigenstrain prediction at around 2-5 mm depth. Close to the surface some pseudo-strain corrections were made as described previously in this paper, and the corrected results match the Eigenstrain predictions within the error band.

6.3.4 Lateral Side

The residual stress measurements from the surface of the lateral side (according to Fig. 6.1) along the y direction were made at the PETRA III synchrotron source, using the beamline P07 for strain measurement. A conical slit arrangement was used to reach a depth of 7 mm into the thickness. In Fig. 6.9 the comparisons between the Eigenstrain approach, the three measured stress components with Synchrotron X-ray and with lab X-ray are shown:

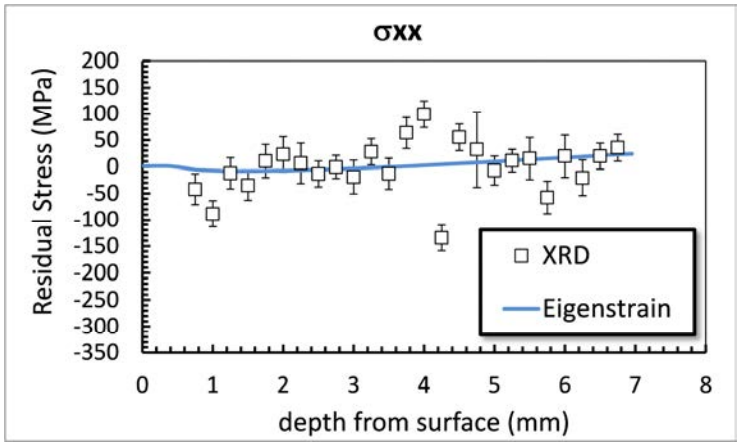

a)

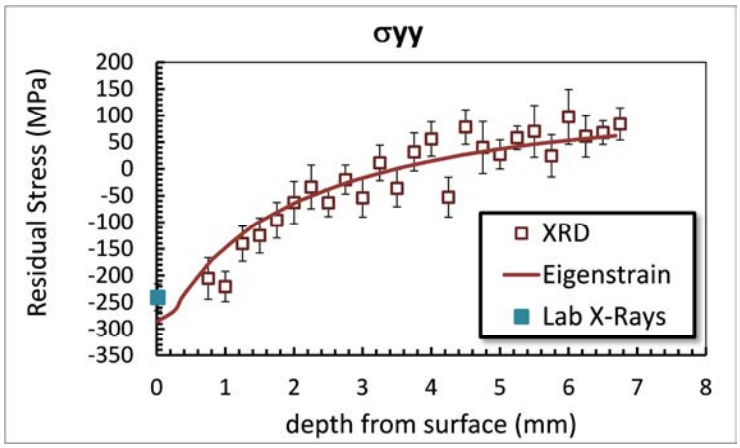

b)

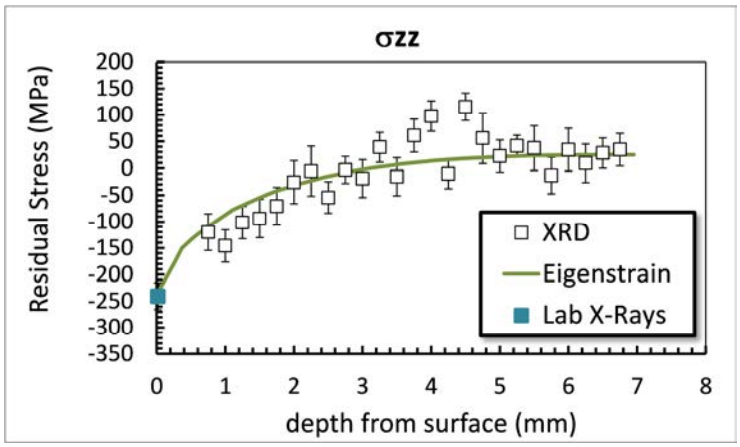

c)

Fig. 6.9 a), b) and c) the comparisons between the Eigenstrain distribution and the calculated stresses.

Fig. 6.9 shows that the residual stresses predicted with the Eigenstrain approach lie within the error bands for most of the measured data. The data from within the first 0.5 mm from the surface were removed because they were affected by pseudo-strains and no corrections were made. The unstressed lattice parameter was measured for the σ_{yy} and σ_{zz} component only, owing to time constraints. The d_0 value for the σ_{zz} components was calculated based on the fact that the σ_{zz} components must be 0 at the surface. Furthermore, it's possible to see that at 4.5 mm depth there is some scattering in the measured residual stresses. This could derive from the presence of a large grain or grains which occupied a large portion of the gauge volume.

6.4 Conclusions

1. In this study the application of the Eigenstrain theory was investigated on a laser-shock-peened aluminium alloy sample containing changes in geometry. Specifically, laser peening was applied to a flat, planar surface, and to curved surfaces with both convex and concave radii. Residual stresses in the sample were measured by a combination of the contour method, neutron diffraction, synchrotron X-ray diffraction and incremental hole drilling.
2. Eigenstrains for the plasticity induced by the laser peening were calculated from the planar section of the sample. Introducing the Eigenstrains into an FE model accurately re-created the original residual stress field.
3. Where the thickness of the sample increased, on the concave surface with low curvature radius compared to the laser peen spot size, the Eigenstrain approach accurately predicts the trend of the residual stress profile in the three components of the stress.
4. Where the geometry changed significantly relative to the planar section, on the convex curved edges of the sample, the Eigenstrain theory shows discrepancies

relative to the experimental measurements. Some of the discrepancies may arise from limitations of the raw contour data used to calculate the Eigenstrain field, as the contour method has various sources of inaccuracy when determining near-surface residual stress.

5. We can summarize that the Eigenstrain theory is a conceptually-simple and time-efficient approach for the prediction of residual stress. However, attention has to be paid in the derivation of the Eigenstrains, and caution taken if the geometry of the sample changes significantly from that from which the Eigenstrains are derived.
6. Using different techniques allowed collecting several data in different positions of the sample. During the experiment plan it is fundamental to understand the limits of the used technique and how this technique can be used in a certain position of the sample. Usually a preliminary investigation of the RS can be conducted with either the ICHD technique in case it is possible to locally destroy the sample or with surface X-ray technique. Both of them area easily available inside research centres or universities. In order to obtain a RS field through thickness, the contour method can give a full 2D RS map in a relatively small amount of time (strictly dependent of the experience of the experimenter) even if the contour method is considered a full destructive technique. In case the sample cannot be destroyed or a second set of data is needed to increase the reliability of them, neutron diffraction are suggested where geometries are smooth and thickness are larger than 4-5 mm and the RS field changes with a rate of 50 MPa per mm. Otherwise the synchrotron X-ray are the only way to get the data due to relatively small gauge volume and a higher speed of measurement.

References

[1] A. T. DeWald and M. R. Hill, "Eigenstrain-based model for prediction of laser peening residual stresses in arbitrary three-dimensional bodies. Part 2: model verification," *J. Strain Anal.*, vol. 44, 2008.

[2] A. Vasu and R. V. Grandhi, "Effects of curved geometry on residual stress in laser peening," *Surf. Coatings Technol.*, vol. 218, pp. 71–79, Mar. 2013.

[3] U. C. Heckenberger, V. Holzinger, W. von Bestenbostel, and E. Hombergsmeier, "Laser shock peening to improve the fatigue resistance of AA7050 components," *Int. J. Struct. Integr.*, vol. 2, no. 1, pp. 22–33, 2011.

[4] M. Dorman, N. Smyth, A. Cini, M. E. Fitzpatrick, P. E. Irving, and M. B. Toparli, "Effect of laser shock peening on residual stress and fatigue life of clad 2024 aluminium sheet containing scribe defects," *Mater. Sci. Eng. A*, vol. 548, no. 30, pp. 142–151, 2012.

[5] F. Hosseinzadeh, P. J. Bouchard, and P. Ledgard, "Controlling the Cut in Contour Residual Stress Measurements of Electron Beam Welded Ti-6Al-4VAlloy Plates," *Exp. Mech.*, vol. 53, pp. 829–839, 2012.

[6] A. Nau and B. Scholtes, "Evaluation of the High-Speed Drilling Technique for the Incremental Hole-Drilling Method," *Exp. Mech.*, vol. 53, no. 4, pp. 531–542, 2013.

[7] M. Steinzig and E. Ponslet, "Residual stress measurement using the hole drilling method and laser speckle interferometry: Part I," *Exp. Tech.*, May 2003.

7 Measurements of residual stress profiles within a Single Edge Notch AA7050-T7451 specimen and comparison with the Eigenstrain approach

The aim of the study was to fully understand the distribution of the residual stresses after two separate surface treatments: laser shock peening and shot peening on an aluminium alloy component. A Single Edge Notch sample is the subject of this preliminary study. Some residual stress surface measurements were made by EADS in order to understand how the residual stresses are distributed in samples with only LSP treatment and both LSP and SP treatments. In order to better understand where and how the tensile stress is distributed inside the component, residual stress measurements were carried out at the Chalk River Laboratories in Canada. Furthermore, the Eigenstrain approach was used in order to predict the RS field of the sample and some preliminary results are presented at the end of this chapter.

7.1 Introduction

Both Laser Shock Peening (LSP) and Shot Peening (SP) have been described in chapter 2 to be capable of introducing compressive RS inside a metallic component and thus enhancing its fatigue life. In particular, it has been demonstrated how LSP can increase the fatigue life of AA7050-T451 [1], [2], and better results of the SP treatment are obtained [3] in terms of fatigue life even if in fretting fatigue SP seems be more beneficial than LSP [4]. In 2003 a preliminary study of coupling both treatments on AA2024-T351 was presented

[5] and it was demonstrated that both the LSP treatment and the coupling of LSP and SP noticeably improved the fatigue life of the component. EADS (now Airbus Innovation Group) recently started research about the possibility to improve the fatigue life of an AA7050 sample by coupling the two surface treatments. The sample involved is a Single Edge Notch specimen, it was described in chapter 3 and here a brief description is reported.

7.2 Single Edge Notch

The Single Edge Notch (SEN) sample is made from AA7050-T7451 and was milled by EADS Innovation Work for fatigue tests. The next picture shows the SEN:

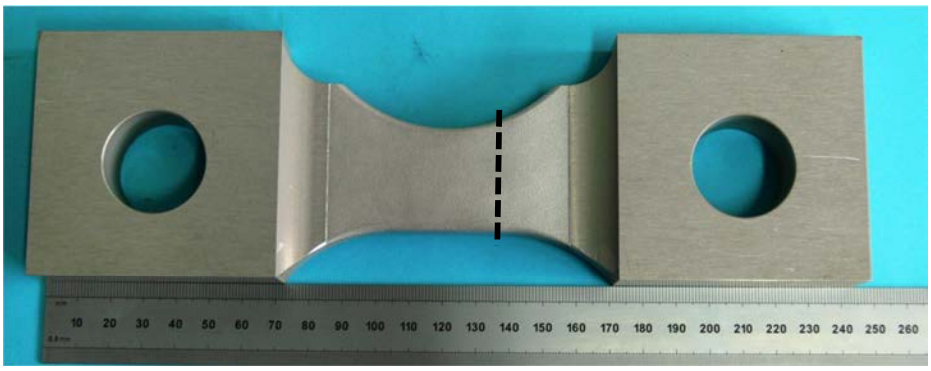

Fig. 7.1 Picture of the SEN(T)

A first set of samples were laser shock peened only, with different laser parameters and the RS measurements were performed as well as the fatigue tests. Contour method RS mapping was carried out by Toparli [6] in the section of the sample indicated by the dotted line shown in Fig. 7.1. The results of the fatigue test and RS measurements are published in [7] and it was demonstrated that the sample treated with a power density of 2 GW/cm^2, 18 ns pulse length and 4 layers reached a fatigue life 300% higher than the as-machined sample. This laser set-up was chosen for further investigation. In particular, a new SEN was treated with the same laser parameters and subsequently was shot peened.

The treatment was described in chapter 3. With this new combined treatment, new RS measurements were performed at the surface and some preliminary results are shown in [8]. In order to know the distribution of the RS within the sample, the neutron diffraction technique was chosen. Experimental details and techniques can be found in paragraph 3.4.1.

7.3 Residual Stress Measurements Results

The RS measurements were performed at beamline L3 at the Chalk River Laboratories, Canada. The measured area is the mid-section where the tensile stresses are expected to be stored. The following picture shows the measurement lines in the mid-section of the SEN which is the section of the sample at the dotted line in Fig. 7.1:

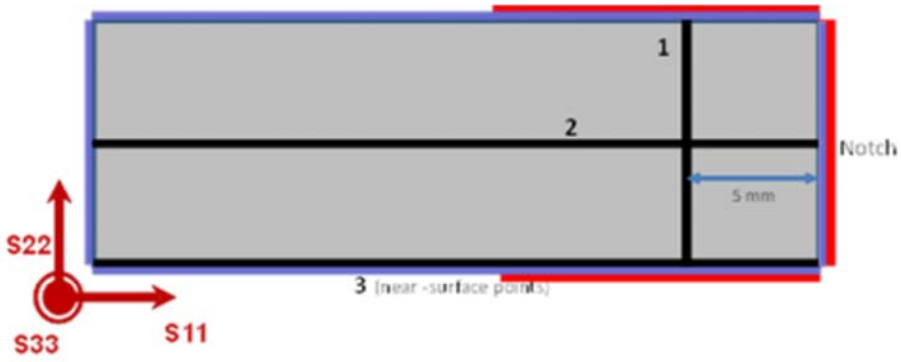

Fig. 7.2 Central section of the SEN. The black lines are the lines of measurements

In Fig. 7.2 the rectangular section of the sample is shown. The red lines on the right side represent the LSP treatment around the notch while the violet lines represent the SP treatment and, as it can be seen, it was made all around the middle section.

As it is shown in Fig. 7.2, three different lines of measurement were made in order to have a clear distribution of the residual stress within the sample thickness and close to the surface. In particular the line 1 is taken from side-to-side of the section along its thickness

(10 mm), line 2 is taken in the middle of the section, from the notch to the other side of the sample, line 3 is taken close to the surface in order to measure the RS at 0.6 mm circa from the surface.

Starting from line 1, the Fig. 7.3 shows the RS distribution obtained according to the coordinate system showed in Fig. 7.2:

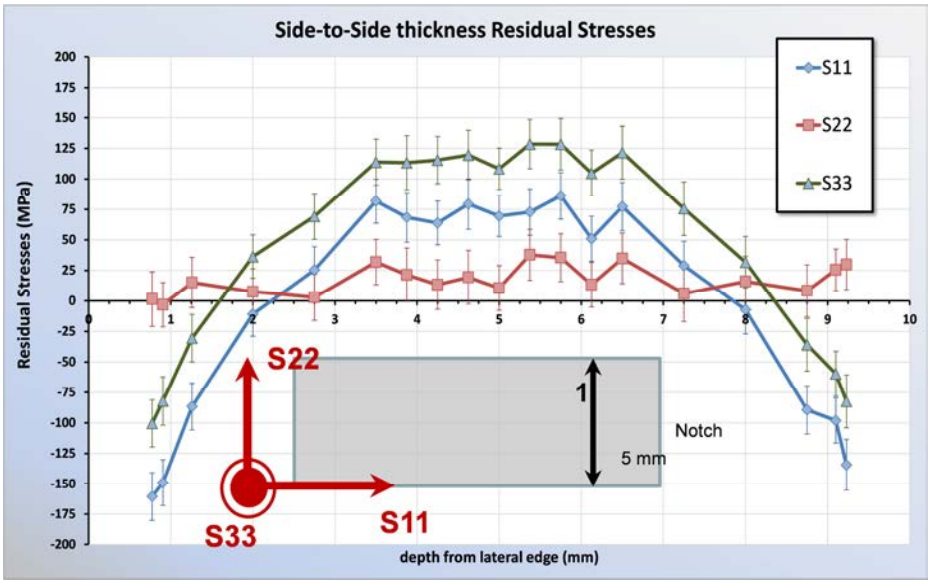

Fig. 7.3 RS distribution of three stress components along line 1

In Fig. 7.3 the distribution of the RS along line 1 is shown. It is possible to see that both S11 and S33 components follow the same RS trend, thus they start in compression up to 1.5 mm from the surface for S33 and 2 mm for S11 and then they reach the tension region where both reach a constant value: around 115 MPa for S33 and around 75 MPa for S11. This indicates the presence of constant tension between 3.5 and 6.5 mm from the surface. The S22 component is between 0 and 25 MPa. Due to the treatment this component is expected to be 0 at the surface (because of plane-stress) and also through the thickness since both LSP and SP introduce plasticity perpendicular to the treated surface, i.e. along the S11 and S33 components.

The following graph shows the distribution of the RS along line 2 (according to Fig. 7.2) starting from the notch:

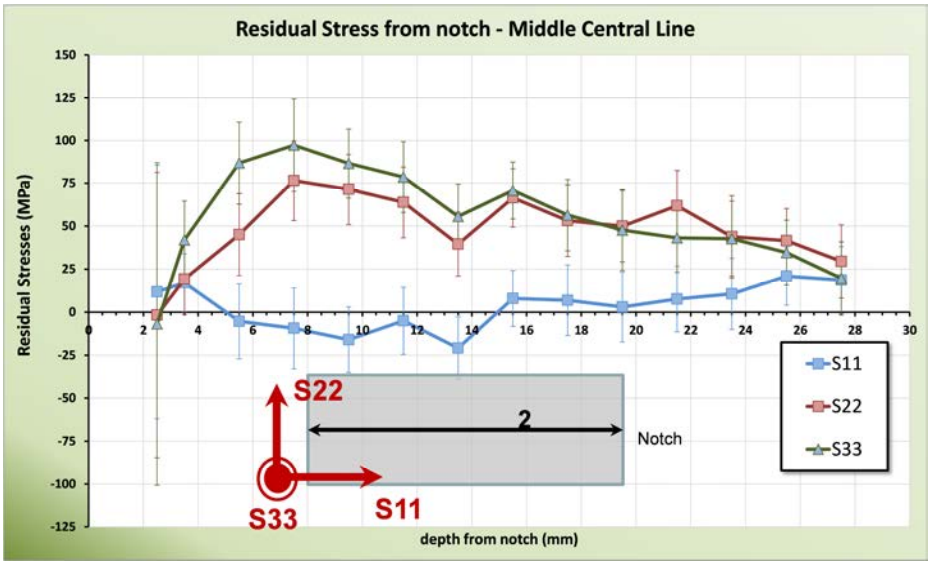

Fig. 7.4 distribution of the RS along the central line

When the measurements for the S11 component were made, the gauge volume was introduced inside the sample at a distance of 2 mm from the surface in order to avoid any pseudo-strains and measurements were taken with a step of 2 mm. As it is possible to see in Fig. 7.4 both the stress components S22 and S33 show a similar RS distribution, completely in tension. A peak around 100 MPa is reached by S33 while S22 reaches a peak of 75 MPa. After circa 10 mm, both profiles show a linear decay till the end of the section. The S11 component is the one perpendicular to the notch surface, thus is supposed to be 0 MPa. The distribution of the RS for this component is 0±20 MPa. Opposite to the notch, this component is supposed to be 0 but it is around 25 MPa. This might be due to the fact that the measurements of the unstressed lattice parameter d_0 were made in a position of the sample where some previous stresses were present even if this area was far away from the LSP treated area, in the clamping area. The presence of stresses might also come from the machining process.

The third measured line, number 3, was taken at the surface of the sample, in the same section of the notch, as shown in Fig. 7.2. The following graph shows the three stress component distributions:

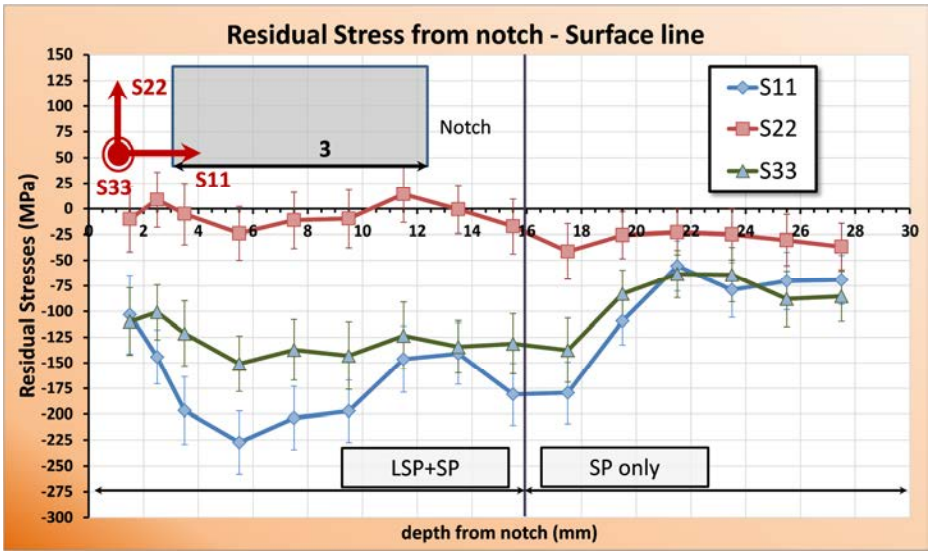

Fig. 7.5 Stress distributions along the surface, line 3

In Fig. 7.5 the distribution of the stresses at 0.6 mm from the surface is shown. The neutron diffraction measurements were performed at the surface (where the geometric centre of the gauge volume was positioned) but the real centre of the measurements was calculated to be at 0.6 mm from the surface. On the graph it is also indicated where the coupling of the treatments ended and where only SP was performed. From Fig. 7.5 it is possible to see that the components of the stresses perpendicular to the surface (S11 and S33) have a similar distribution. In particular close to the notch the RS are approximately around –100 MPa and then they drop to –225 MPa for the S11 and –150 MPa for the S33. After the LSP'ed area, the RS decrease in magnitude their value up to –75 MPa which is kept constant. The S22 component lies around 0 MPa as expected.

The following picture shows the distribution of the RS at the lateral surface of the middle section (line 3 according with Fig. 7.3) that were measured by EADS with surface X-ray diffraction:

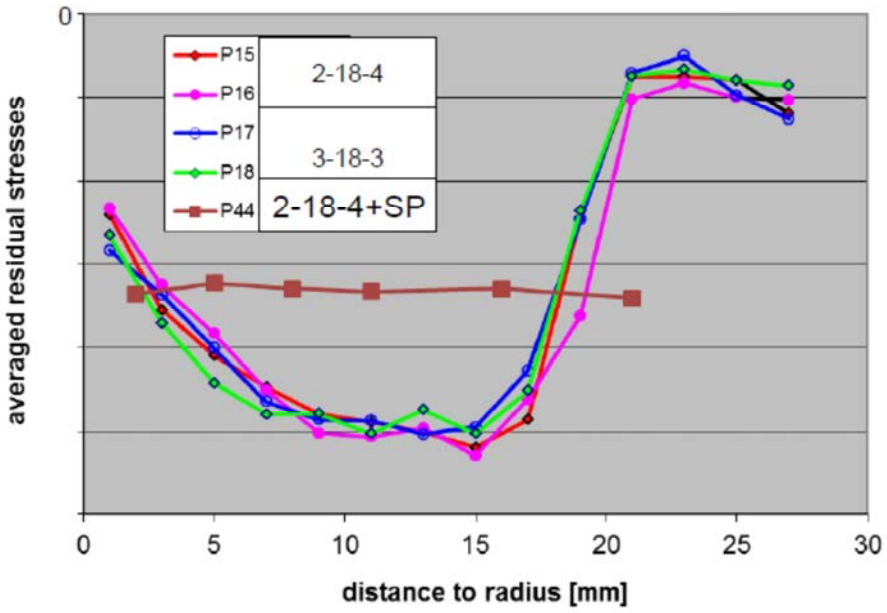

Fig. 7.6 RS distribution along line 3 made by EADS

As shown in Fig. 7.6, the RS distributions of the samples that were LSP only are in compression all along the line of measurement and where the LSP treatment was done (up to 16 mm) the compression is even higher. After the SP treatment, the RS are flattened to an average value and they are constant along line 3. As shown in Fig. 7.6, the SP modifies the RS distribution at the surface only. Where the SP effect terminates (usually around 0.2 mm underneath the surface), only the RS introduced by the LSP are left and the distribution of the RS at 0.6 mm looks similar to those at the surface shown in Fig. 7.6.

7.4 Eigenstrain Prediction

In order to predict the RS introduced by the LSP and SP via FEA, the Eigenstrain approach was used. As was explained in chapter 5, the Eigenstrains have to be measured in a simple geometry sample and then applied via FE modelling to a more complex geometry. In this study, two samples with a square base of 50 mm and a thickness of 10 mm were treated on one of their wider surfaces. Both of them were subject to laser

peening treatment with the same laser parameters used for the SEN (2-18-4). Only one of them was subsequently subjected to shot peening on the same surface, with the same parameters as the SEN. As was shown in chapter 5, the entire RS profile is needed in order to calculate the three components of the stress: the linear (or elastic) component, the LSP components and the total component, which is the one measured. Among the techniques available, the neutron diffraction method was chosen. The experiment was performed at the Stress-Spec instrument at FRM II, Munich and the experiment details are reported in paragraph 3.4.2.

The results of the neutron diffraction measurements are reported in the following pictures:

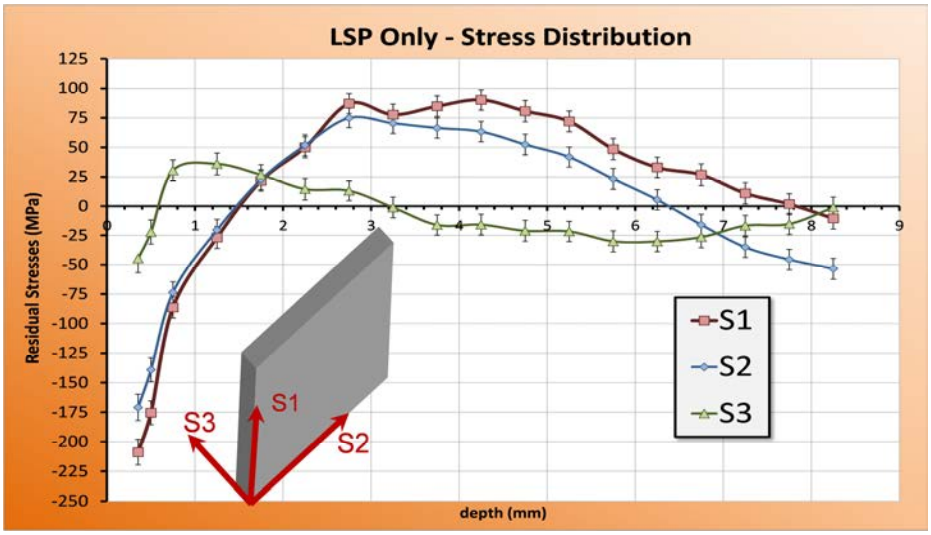

Fig. 7.7 Stress distribution through the thickness of the sample

As Fig. 7.7 shows, the in-plane stress components are very similar as expected. In particular both S1 and S2 start in compression, around –200 MPa and after 1.4 mm depth they become tensile. The maximum peak reached in tension is 85 MPa and this value is kept almost constant (especially for the S1 component) between 2 and 4.8 mm depth before linearly decaying up to 0 MPa. The S3 component is expected to be 0 MPa and the measurements show that it tends to remain between ±25 MPa.

The same experiment was performed in the sample that was subjected to both LSP and SP and the results are shown in the next graph:

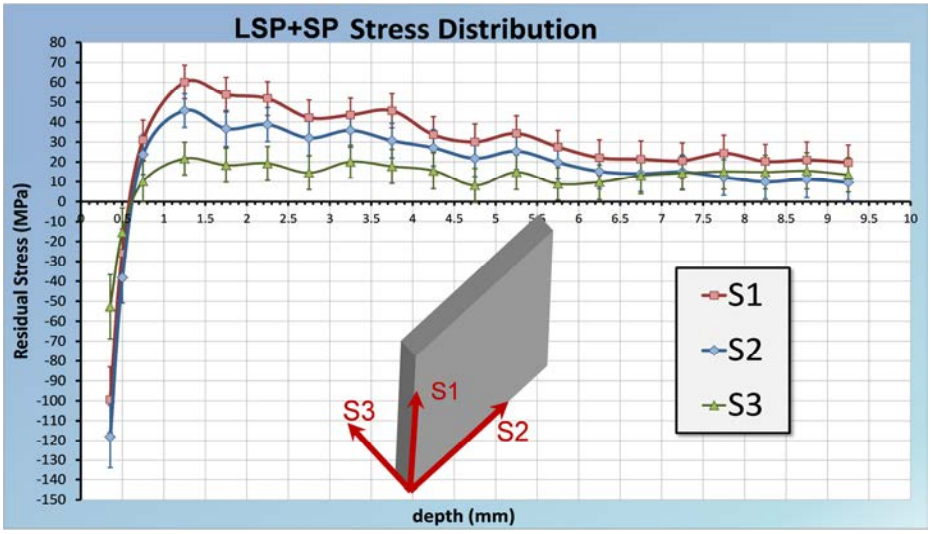

Fig. 7.8 Stress distribution in LSP+SP sample

As can be seen in Fig. 7.8 after the SP treatment the distribution of the RS is different from that measured in the LSP'ed only sample. The in-plane stress components (S1 and S2) show a very similar RS trend, starting in compression, around –110 MPa. The tensile region is reached at 0.6 mm from the surface and the tensile peak is reached at 1.3 mm from the surface: its value is around 60 MPa for the S1 component. Both S1 and S2 show a linear decay of the RS after 1.5 mm. At the end of the thickness these two components should be 0 but they are stabilized at a level of circa 20 MPa. As was said before, this is probably due to the presence of RS where the unstressed lattice parameters measurement was performed. This hypothesis is confirmed by the fact the S3 component, which is supposed to be constantly 0 through the thickness, assumes a value around 10 MPa through the thickness.

The Eigenstrain values were calculated with the procedure shown in chapter 5 for both the RS distributions (LSP only and LSP+SP) and they were subsequently applied to an FEM model on the central section of the SEN. The following graphs show the comparison

between the Eigenstrain approach and the FEA prediction considering the Eigenstrain calculated with the LSP only:

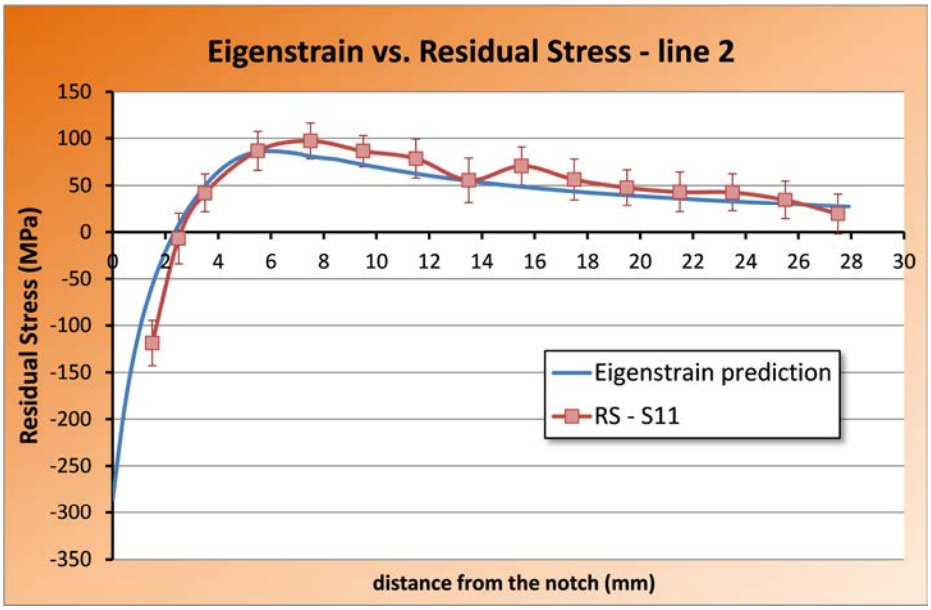

Fig. 7.9 Comparison between the RS measurements and the Eigenstrain prediction – line 2

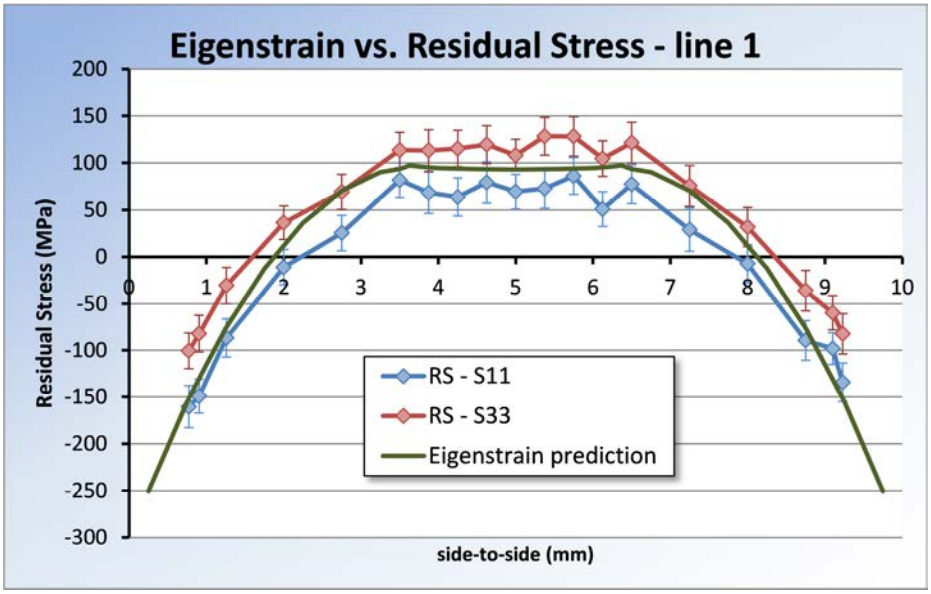

Fig. 7.10 Comparison between the RS measurements and the Eigenstrain prediction – line 1

In Fig. 7.9 the comparison between the Eigenstrain and the RS measurements is shown for the line 2 (according with Fig. 7.2). As can be seen the Eigenstrain prediction lies within the error bands of the RS measurements for most of the points (which is on

average ±20 MPa). Fig. 7.10 shows the comparison between the Eigenstrain prediction and the RS measurements along line 1 (Fig. 7.2). In this case both the S11 and S33 components were reported to show that the Eigenstrain prediction lies between the two measured RS (in case of the Eigenstrain, S11 and S33 stress distribution are identical. Due to the treatment, an identical RS profile for both S11 and S33 components was expected too.

The following graphs show the application of the Eigenstrain calculated from the sample that was LSP'ed and SP'ed:

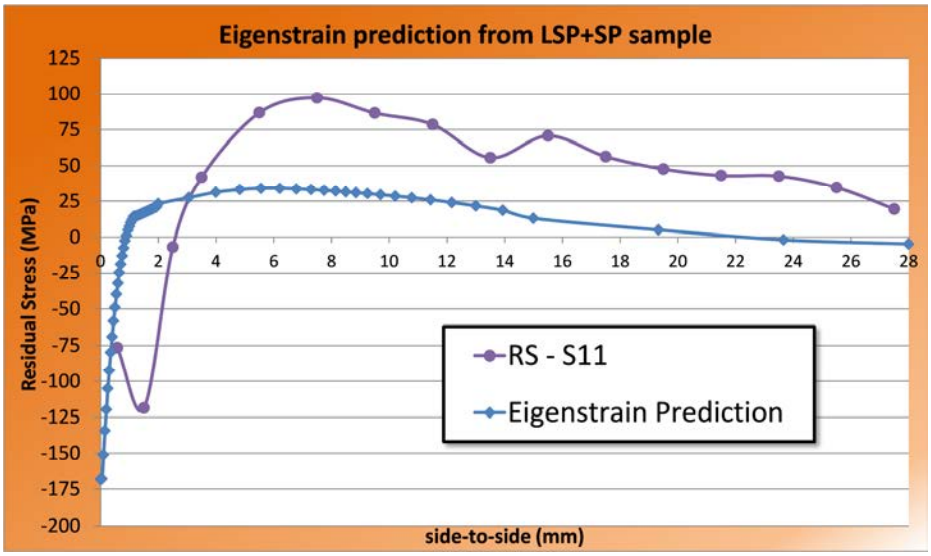

Fig. 7.11 Comparison between the RS measurements and the Eigenstrain prediction – line 2

It is possible to see in Fig. 7.11 how the RS profile changes once the Eigenstrain values are changed. In this case, the Eigenstrain values were expected to predict better the distribution of the RS measured due to the fact that the treatment of the simple geometry samples and SEN were the same, i.e. same Eigenstrains. But apparently it is not so. The shot peening after the LSP treatment seems to have localized the residual stresses closer to the surface (as it can be seen in Fig. 7.8) but in the SEN this didn't happen.

7.5 Conclusions

As mentioned in the introduction to this chapter, the application of the Eigenstrain analysis on this sample was just a preliminary study and no previous publications have been found made on the application of Eigenstrain in sample that was double treated. The internal distribution of the RS seems to remain unchanged after the SP treatment and this could explain why the Eigenstrain values calculated by the LSP'ed only sample are predicting better the RS distribution of the SEN both line 1 and along the line in the middle of the section. It is hypothesized that the SP treatment changes the RS distribution only within a tenth of millimetre from the surface and this cannot be detected by the neutron diffraction method. More investigations are needed to better understand how the RS underneath the surface are distributed.

Reference

[1] X. D. Ren, Y. K. Zhang, H. F. Yongzhuo, L. Ruan, D. W. Jiang, T. Zhang, and K. M. Chen, "Effect of laser shock processing on the fatigue crack initiation and propagation of 7050-T7451 aluminum alloy," *Mater. Sci. Eng. A*, vol. 528, no. 6, pp. 2899–2903, Mar. 2011.

[2] Y. K. Gao, "Improvement of fatigue property in 7050–T7451 aluminum alloy by laser peening and shot peening," *Mater. Sci. Eng. A*, vol. 528, pp. 3823–3828, 2011.

[3] H. Luong and M. R. Hill, "The effects of laser peening and shot peening on high cycle fatigue in 7050-T7451 aluminum alloy," *Mater. Sci. Eng. A*, vol. 527, no. 3, pp. 699–707, 2010.

[4] J. Vázquez, C. Navarro, and J. Domínguez, "Experimental results in fretting fatigue with shot and laser peened Al 7075-T651 specimens," *Int. J. Fatigue*, vol. 40, pp. 143–153, Jul. 2012.

[5] C. A. Rodopoulos, J. S. Romero, S. A. Curtis, E. R. de los Rios, and D. P. Peyre, "Effect of Controlled Shot Peening and Laser Shock Peening on the Fatigue Performance of 2024-T351 Aluminum Alloy," *J. Mater. Eng. Perform.*, vol. 12, no. 4, pp. 414–419, Aug. 2003.

[6] M. B. Toparli, "Analysis of Residual Stress Fields in Aerospace Materials After Laser Peening," PhD Thesis, The Open University, 2012.

[7] U. C. Heckenberger, V. Holzinger, W. von Bestenbostel, and E. Hombergsmeier, "Laser shock peening to improve the fatigue resistance of AA7050 components," *Int. J. Struct. Integr.*, vol. 2, no. 1, pp. 22–33, 2011.

[8] E. Hombergsmeier, V. Holzinger, and U. C. Heckenberger, "Fatigue Crack Retardation in LSP and Sp Treated Aluminium Specimens," in *Advanced Materials Research*, 2014, vol. 891–892, pp. 986–991.

8 Measurements of residual stress profiles within single-peened thin samples of aluminium AA2024-T351

In the previous chapters thick samples with different laser peening parameters were presented. In the next two chapters, the RS measurements of the single and double-peened thin samples are presented. In particular, two different laser peening techniques were taken into account: the one delivered by TOSHIBA Company and the one delivered by the Unversidad Politécninca de Madrid (UPM). The samples taken into consideration are 2.0 mm thick samples made of aluminium AA2024-T351, typical for aerospace applications. The presence of a clad layer on both surfaces of the sample plays a fundamental role in terms of distribution of RS , surface roughness etc. All the RS measurements presented here were either carried out with Incremental Hole-Drilling or with X-ray diffraction.

8.1 Introduction

Thin samples are extremely important for research in the aerospace field. Most aerospace structures are designed on the principles of shell theory, where every single panel of the fuselage or the wing skin takes part actively in the distribution of the aerodynamic loads. LSP on thin samples, as mentioned in chapter 2, can improve the fatigue life of the structures. Specifying the LSP of thin samples can be very challenging for the following reasons:

- first of all due to the low thickness, the shock waves generated by the LSP travel within the thickness generating RS but once they reached the back face of the sample, they bounce backwards and interact again with the early-generated RS field;

- secondly, in case of low thickness with a peening strip, the compressive residual stresses are balanced aside the laser peened area while in the thick component most of the balancing tension is stored underneath the compression area. Furthermore as Toparli has verified [1], by changing the laser supplier and the laser setting, the RS distribution can be totally different.

Some important tests were carried out to fully understand the role of the LSP in the case of an open-hole, a typical aerospace problem for riveted thick structures. In 2000 the first publication about the LSP process on a thin sample was published [2] and it was shown how LSP can improve the fatigue performance. The only limitation is that in this experiment the plate 2.5 mm thick was laser peened from both sides but often in real service this option is not available. A similar study was carried out by Ivetic *et al.* [3] where it was found that the sequence of laser peening and then drilling the hole improves the fatigue life but the other way around deteriorates the fatigue life.

Due to the limited information from studies in this field, at Cranfield University some FE simulations were carried out to understand the exact role of the RS and the fatigue life in terms of compressive peak value and its depth. As reported by Toparli [4], from this research, two important results can be highlighted:

- ✓ to greatly improve the fatigue life of a component, a RS value higher than 120 MPa must be achieved;
- ✓ the peak of the compressive RS must be at least at 250 μm under the surface to significantly improve the fatigue life;

These two main conclusions led our research to find the best laser setting parameters in order to take into consideration the conclusions written above. In the light of these, Toparli *et. al* carried out some research about the distribution of the residual stress after laser peening in thin samples as reported in [4]–[6]. Several samples and three different laser peening suppliers were taken into account. In the final conclusion Toparli stated that the LSP process can effectively increase the fatigue life of the thin samples but the laser

parameters have to be decided carefully in order to avoid any local surface melting and to keep distortions as low as possible.

A continuation of Toparli's work will be presented in this dissertation. Similar samples were laser peened with different laser setting parameters and they were subsequently the object of RS measurements. To increase statistics of the measured residual stress data, two different RS techniques were used: Incremental Hole-Drilling (ICHD) and surface X-ray. The description of the techniques and the experiment details can be found in chapter 4.

8.2 Samples

Twelve aluminium alloy AA2024-T351 samples, 2.0 mm thick with one layer (on each face) of pure aluminium cladding were available for the tests. All the samples are 160 × 100 mm^2 in length and width. The samples were LSP'ed with different parameters: six of them with only one stripe of peening and the other six with two stripes of peening, one on each face. The results and discussions of the six double-peened samples can be found in chapter 9. In Fig. 8.1 a sample is shown.

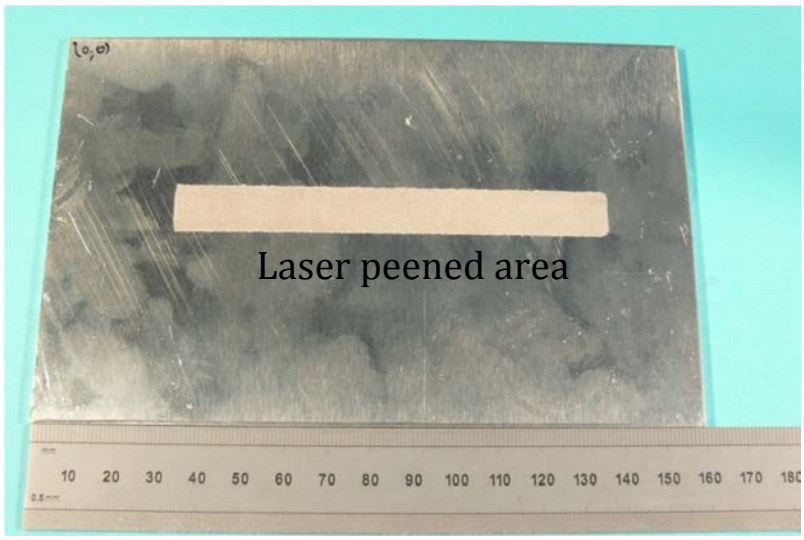

Fig. 8.1 a generic LSP'ed thin aluminum sample

Table 8.1 shows the spot diameter and the overlapping distances (which is defined as the distance between the centres of two circular spots) used for the six single-peened samples and the calculated power density:

Table 8.1 List of samples LSP'ed on one side only

Aluminium Alloy AA2024-T351					
Specimen number	Overlapping distance d (mm)	Pulses/cm^2	Spot diameter (mm)	Peened surfaces	Power Density GW/cm^2
1.15.4	0.75	178	2.0	Single	8.92
1.15.3	0.90	124	2.0	Single	8.92
1.15.6	0.75	178	2.5	Single	5.71
1.15.8	0.90	124	2.5	Single	5.71
1.13.2	0.75	178	3.5	Single	2.91
1.13.6	0.90	124	3.5	Single	2.91
1.13.4	0.75	178	2.0	Double	8.92
1.14.1	0.90	124	2.0	Double	8.92
1.14.3	0.75	178	2.5	Double	5.71
1.14.4	0.90	124	2.5	Double	5.71
1.14.7	0.75	178	3.5	Double	2.91
1.16.1	0.90	124	3.5	Double	2.91

The overlapping distance d is the distance between the centre of the circular spots in two consecutive shots. As it's possible to see from Table 8.1, on the samples LSP'ed on both sides, the same laser parameters setting used for the single-peened specimens were used. This approach aimed to find how the RS distributions changed when only the number of peened surfaces was changed and no other parameters. Regarding the laser treatment, two important parameters were changed: the spot diameter size and the overlapping distance. The circular spot was used in three different diameter sizes: 2.0, 2.5 and 3.5 mm. The overlapping distance, which is the distance between the centres of two circular laser spots, was used with two different values: 0.75 mm and 0.90 mm. By increasing this distance (which means the actual overlapped area decreases) the number of pulses per cm^2 is decreased and vice versa. According to the supplier, the energy involved for each shot was 2.8 J and the time duration of each pulse was 10 ns. As

mentioned in chapter 2, the parameter generally used to compare different LSP treatments is the power density, so this was calculated and is reported in Table 8.1.

All the samples were subjected to RS measurements with ICHD and some of them were measured with X-ray diffraction and for this reason the samples were divided in two different areas. As reported in chapter 4, since the ICHD is a semi-destructive RS measurement technique, after the drilling process the RS field is changed around the hole. In order to make a second measurement far enough from the hole, in an area where the RS field is assumed to be not modified by the drilling process, a minimum distance of 10 mm between two drilled holes was chosen. The following map shows a schematic of the sample with a strip of laser peening. The grid was used to choose the exact location of each drilling point, far enough from the others.

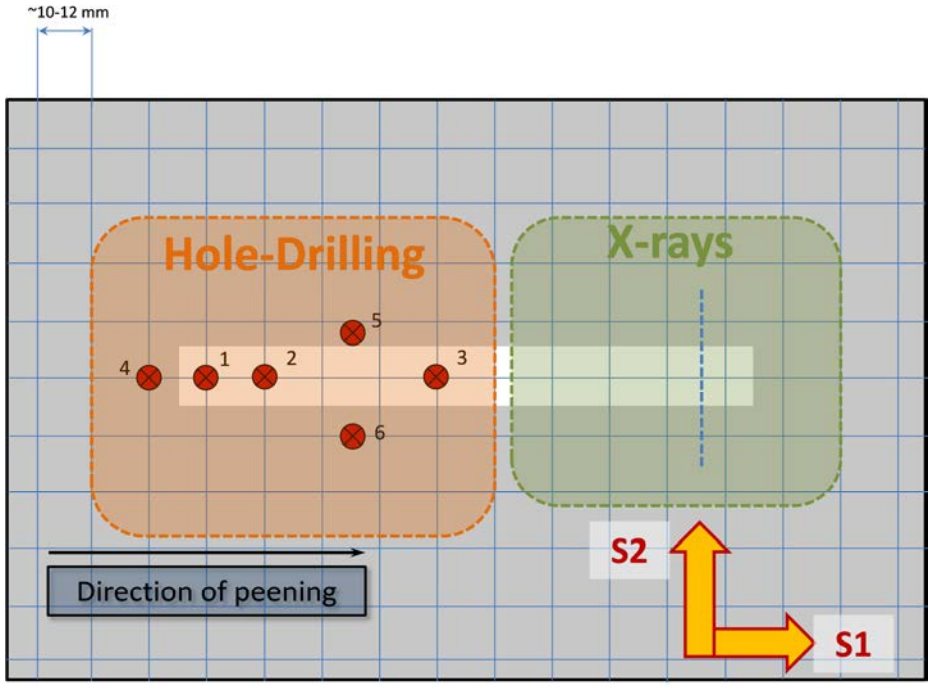

Fig. 8.2 Scheme of the sample with the choice of the drilling measurement regions and the X-ray measurement regions.

On the other side of the sample, no further holes were drilled, in order to measure the surface RS with X-ray.

Since the samples have two dimensions an order of magnitude larger than the remaining one, the plane stress assumption was made. In this way, the only RS components we were interested in are (according with Fig. 8.2): S1, along the direction of peening and S2, perpendicular to the direction of peening, while S3 (which would be perpendicular to the plate) is assumed to be 0.

8.3 Residual Stress Measurements with ICHD

In the following paragraphs the ICHD measurements results will be presented for the single-peened samples only. The double-peened samples and comparison between the two are reported in chapter 9.

Only the measurements of three points out of six will be shown, in particular points 2, 4 and 5. This is because points 1,2 and 3 presented very similar RS profiles and the same happened for points 5 and 6.

8.3.1 Overlapping of 0.75 mm - 178 pulses/cm²

In this paragraph the samples with an overlapping distance of 0.75 mm between each spot are presented:

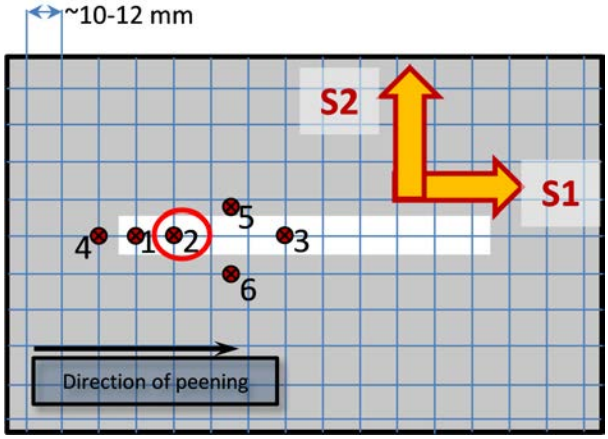

Fig. 8.3 position of the hole drilling

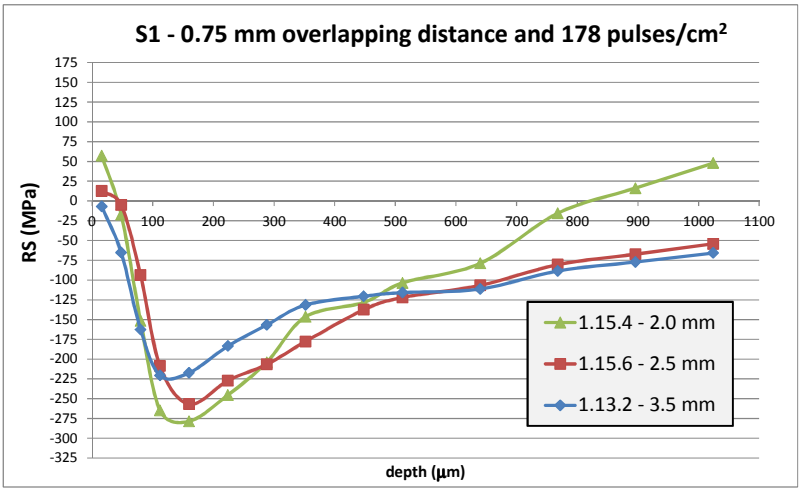

Fig. 8.4 Comparison between three samples with different spot sizes – S1 direction

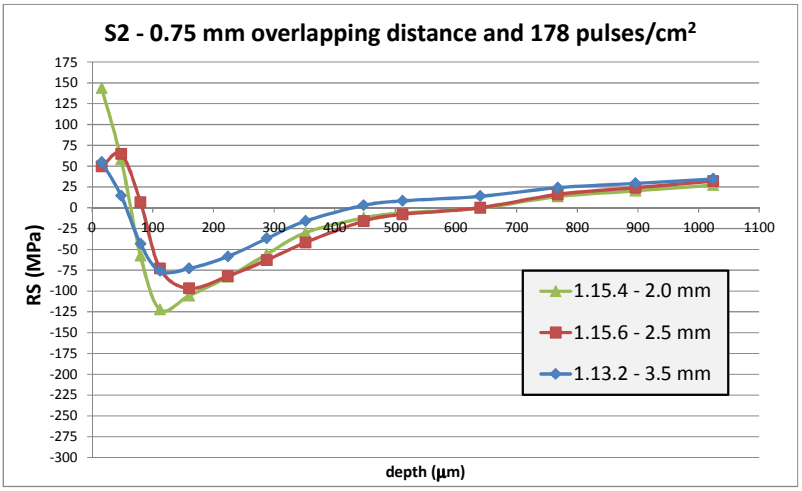

Fig. 8.5 Comparison between three samples with different spot sizes – S2 direction

In Fig. 8.4 and Fig. 8.5, the comparison between the RS profiles of three samples, all drilled in the same position (point 2 as shown in Fig. 8.3) are shown. All the samples were peened with constant parameters apart from the size of the spot diameter. Referring to both graphs it's possible to see that with the smallest spot diameter (2.0 mm) it is possible to get higher compressive RS in the depth but at the same time the tensile stresses at the surface are increased. In particular, the compressive RS reaches a value of –275 MPa at 100 µm in the S1 direction and –125 MPa at 150 µm in the S2 direction in the sample that was LSP'ed with the smallest laser spot.. At the same time though, the same sample shows

the highest tensile RS at the surface: around 55 MPa in the S1 direction and around 150 MPa in the S2 direction. This is probably due to higher power density (8.92 GW/cm^2) and this could lead to a local melting of the clad metal which leads to a generation of tensile stress as reported by Peyre in [7]. In fact, the sample 1.13.2 which was peened with the largest spot size, shows a smaller peak in both compression and tension. Eventually it is worth noting that the ICHD technique is reliable up to 1 mm through the thickness and the RS up to this depth are still compressive in S1 direction.

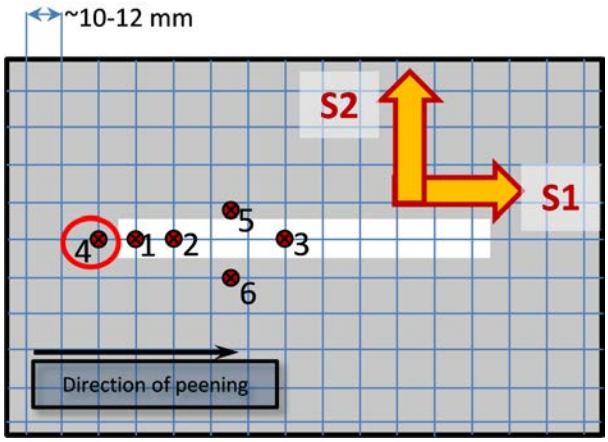

Fig. 8.6 Position of the hole-drilling

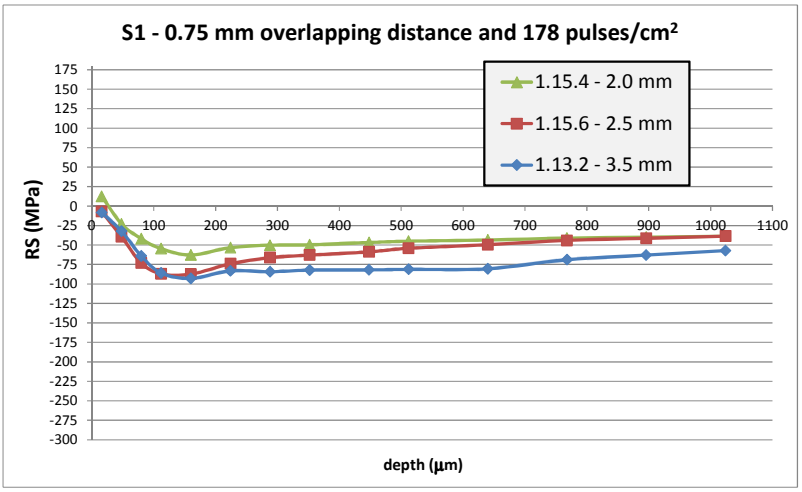

Fig. 8.7 Comparison between three samples with different spot sizes – S1 direction at point 4

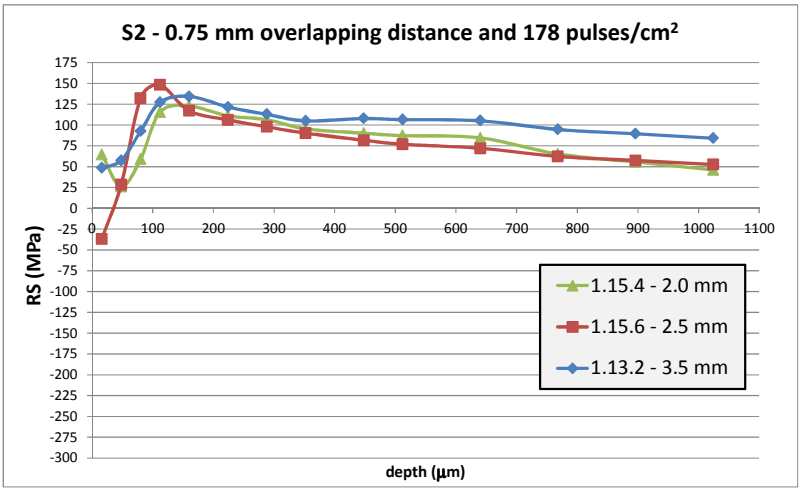

Fig. 8.8 Comparison between three samples with different spot sizes – S2 direction at point 4

Both Fig. 8.7 and Fig. 8.8 show the RS results of point 4. This point is outside the laser peening area. In this position, the stresses in the S1 direction are still compressive but the RS values are lower (in magnitude). Fig. 8.7 shows that the lowest value of compressive RS was measured within the sample peened with the largest spot size, in particular a value of –93 MPa is reached at 160 µm depth; at the same time the only sample which has tensile stress at the surface is 1.15.4, with the smallest spot size. Along the S2 direction the distribution of the RS is totally different: only tensile stresses are present. In this case the sample with a spot diameter of 2.5 mm shows the highest tensile peak of 148 MPa at 112 µm depth. The other two samples present a similar RS profile, with a peak around 125 MPa reached at 160 µm depth.

A final comparison was made between the same samples in point 5, as the following figure shows:

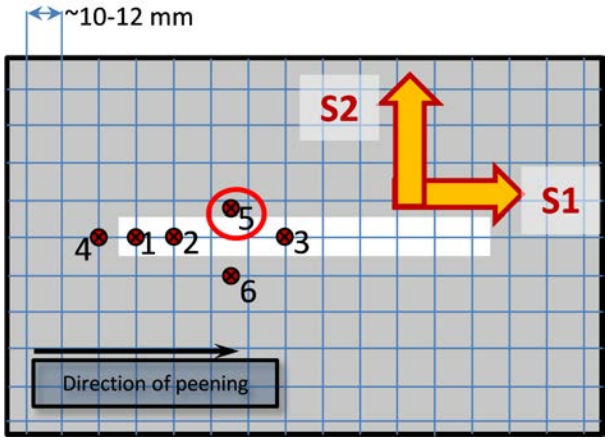

Fig. 8.9 Position of point 5

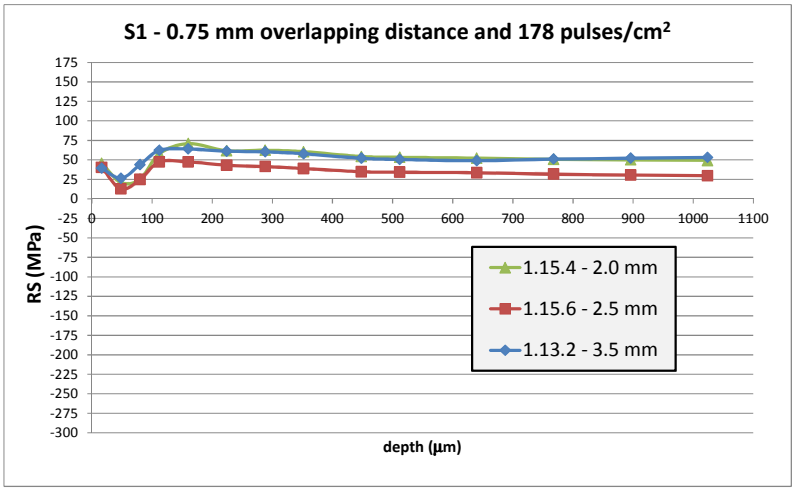

Fig. 8.10 Comparison between three samples with different spot sizes – S1 direction at point 5

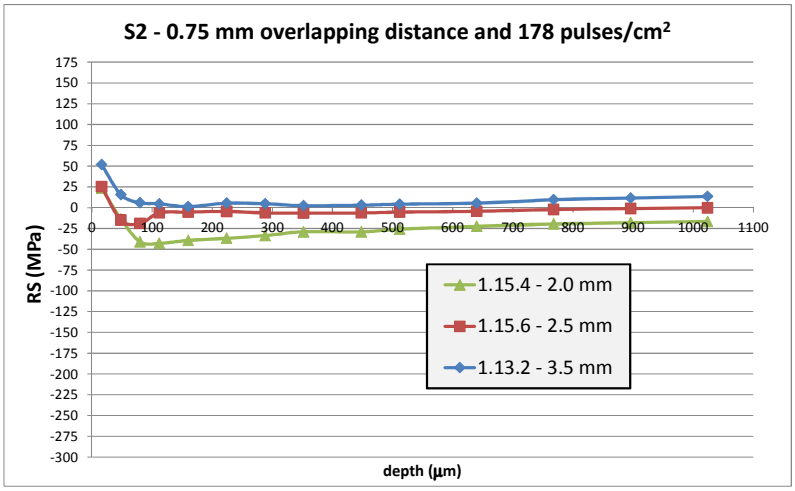

Fig. 8.11 Comparison between three samples with different spot sizes – S2 direction at point 5

Fig. 8.10 and Fig. 8.11 show the RS trend measured at point 5 which is lateral the LSP'ed strip. As it possible to see, the RS trends of the stresses in direction S1 and the S2 are reversed compared to the RS profiles collected in point 4. In point 5, the RS in the S1 direction are in the tensile region for the entire depth profile while the RS in the S2 direction are both tensile and compressive, depending on the spot diameter. Along S1 both samples with 2.0 mm and 3.5 mm spot size present a similar RS trend, with a peak value at 160 µm depth of 71 and 64 MPa respectively. The sample with a laser spot of 2.5 mm presents a lower tensile peak at the same depth: 47 MPa. The profile in the S2 direction is probably more interesting. Fig. 8.11 shows that there is a relation between the spot size and the distribution of stresses along this direction. In more detail, when the spot is 3.5 MPa, the RS tend to be in the tensile region, even if the average value is very low, always between 0 and 10 MPa. By decreasing the spot size (thus increasing the power density), the values of the RS tend to be in the compressive region and when the spot is the smallest one, the RS are within a range of –20 to –40 MPa. They reach a peak of –43 MPa at 112 µm depth.

8.3.2 Overlapping of 0.90 mm - 124 pulses/cm^2

The same approach was used for the three samples with a lower overlapped area, i.e. lower number of pulses per cm^2. The drilling was made in the same positions as shown in Fig. 8.3.

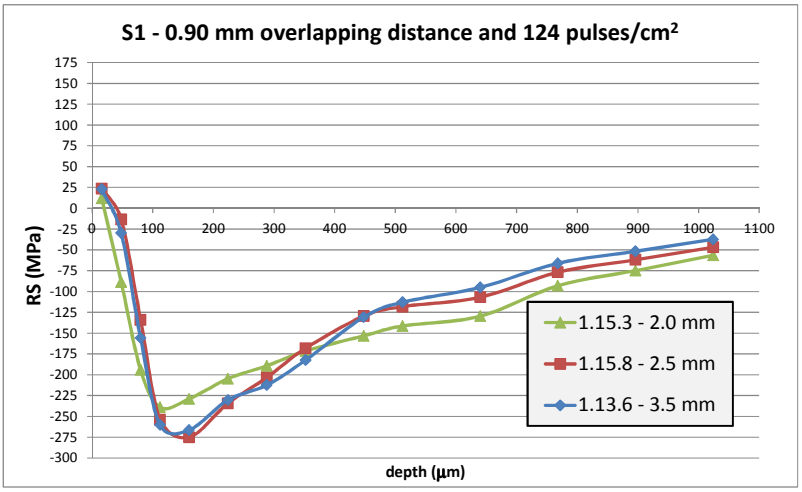

Fig. 8.12 Comparison between three samples with different spot sizes – S1 direction at point 2

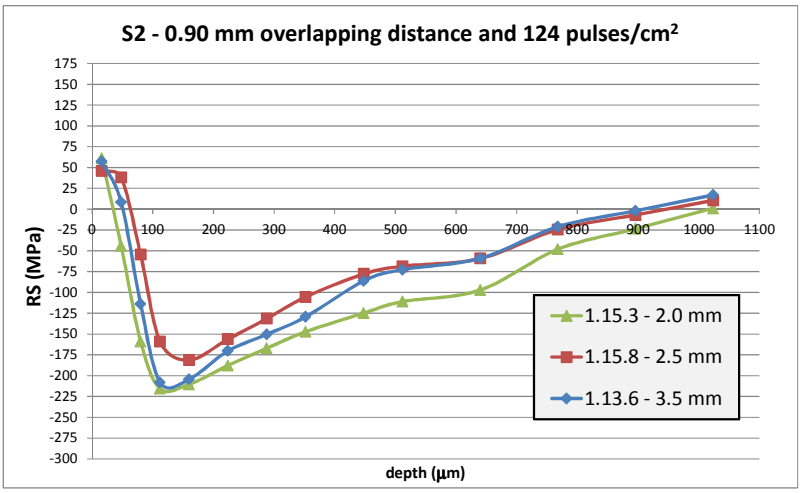

Fig. 8.13 Comparison between three samples with different spot sizes – S2 direction at point 2

In both Fig. 8.12 and Fig. 8.13 the RS profiles of point 2 (Fig. 8.3) are reported. In the S1 direction (Fig. 8.12), the RS of all the three samples present the same trend. All of them start in the tensile region, around a value of 20 MPa. The peak in compression is reached at 112 µm depth for the sample with 2.0 mm spot diameter with a value of –261 MPa and 160 µm depth for the other two samples with a value of –260 and –265 MPa for the sample with 2.5 mm and 3.5 mm spot diameter respectively. The RS profiles in the S2

direction have a very similar trend. They start for all the samples in the tensile region, around a value of 50 ± 5 MPa. The peak in compression is reached at 112 µm depth for two of the samples (2.0 and 3.5 mm spot diameter) and it is around –205 MPa for both.

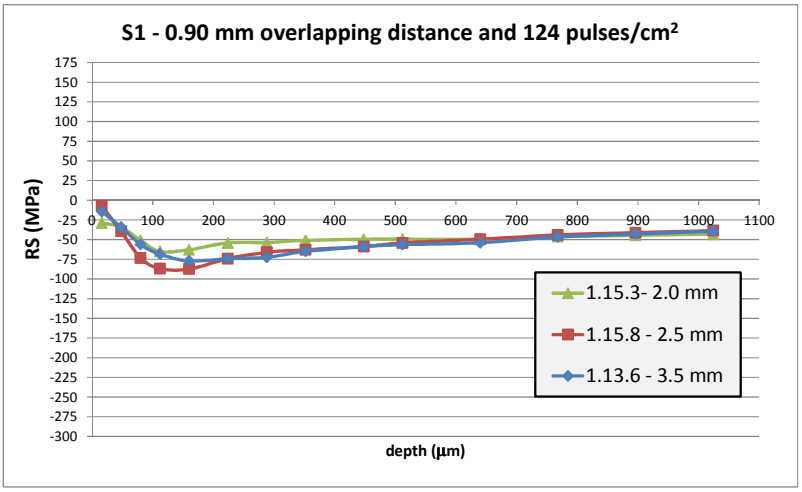

Fig. 8.14 Comparison between three samples with different spot sizes – S1 direction at point 4

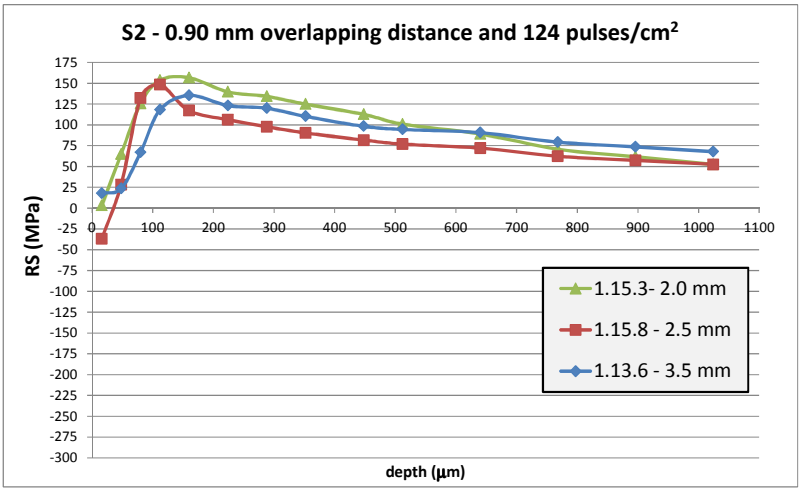

Fig. 8.15 Comparison between three samples with different spot sizes – S2 direction at point 4

In Fig. 8.14 and Fig. 8.15 the RS profiles measured at point 4 (Fig. 8.6) are reported. Again, the RS profile shows a different behaviour depending on the direction of the stress. In the S1 direction the entire profile for all the three spot sizes is always in compression. In the S2 direction, the profiles are completely in the tensile region (apart for the stress

profile of the 2.5 mm spot diameter sample which starts in the compressive region): the reach a peak around 150 MPa at 112µm depth.

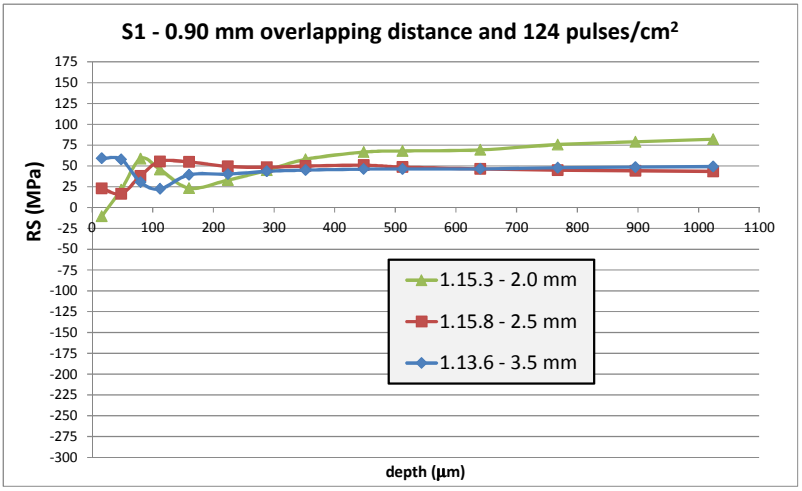

Fig. 8.16 Comparison between three samples with different spot sizes – S1 direction at point 5

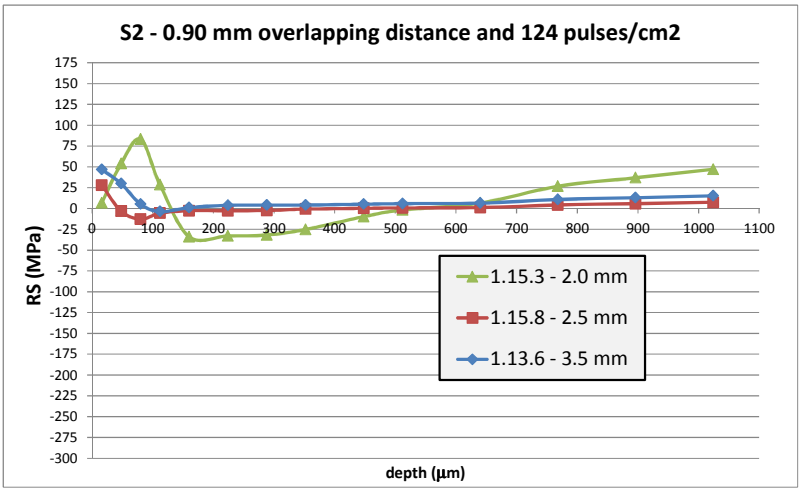

Fig. 8.17 Comparison between three samples with different spot sizes – S2 direction at point 5

As it can be seen from Fig. 8.16, in the S1 direction all the RS profiles are entirely in tension. From the trend it can be seen that by increasing the spot diameter size, the RS peak tends to decrease, while after a depth of 300 µm the RS profiles tend to be more linear. In the S1 direction, the RS profiles in tension are the ones with the 2.0 mm and 3.5 mm spot diameter. The behaviour of the RS in the S2 direction is a bit different. Both the

profiles generated by the 2.0 mm spot and the 3.5 mm spot are in the tensile region while the one generated with the spot of 2.5 mm is completely in compression.

8.3.3 Comparison between constant spot diameters at different overlapping settings

One last comparison which is considered very important, it's the one between different overlapping distance when the spot diameter size is kept constant.

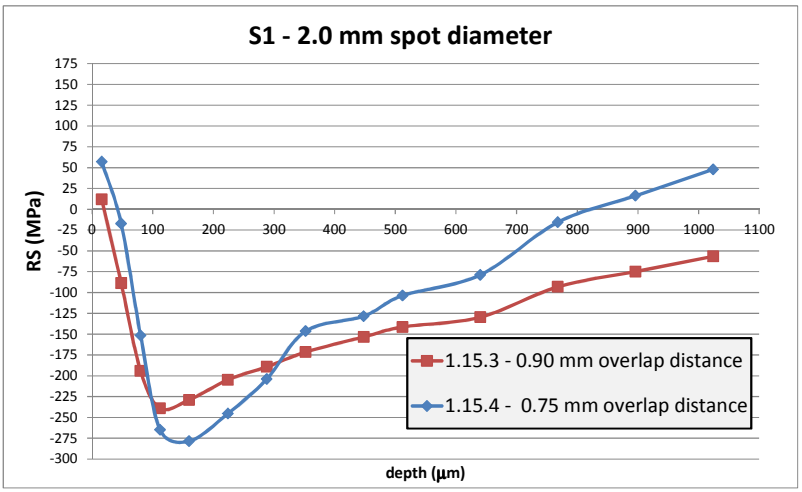

Fig. 8.18 S1 – spot diameter of 2.0 mm is kept constant and the overlapping distance is changing

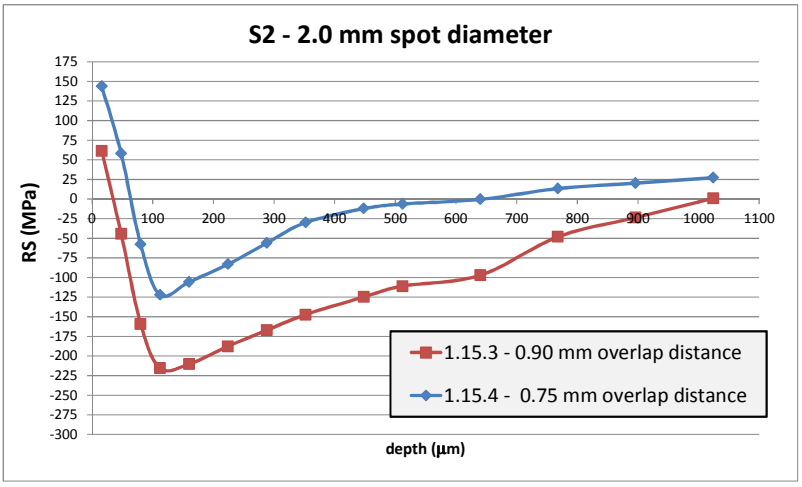

Fig. 8.19 S2 – spot diameter of 2.0 mm is kept constant and the overlapping distance is changing

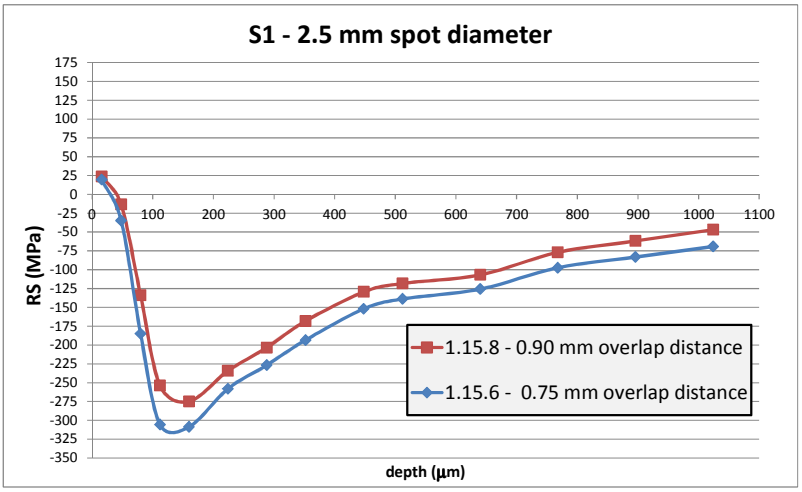

Fig. 8.20 S1 – spot diameter of 2.5 mm is kept constant and the overlapping distance is changing

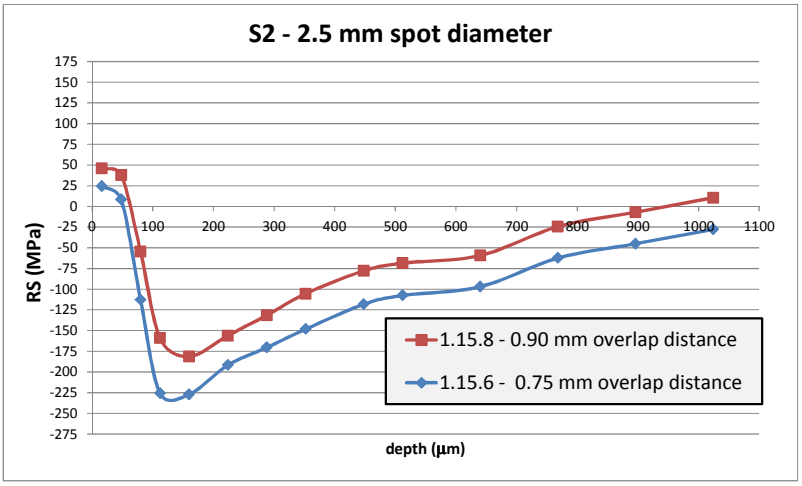

Fig. 8.21 S2 - spot diameter of 2.5 mm is kept constant and the overlapping distance is changing

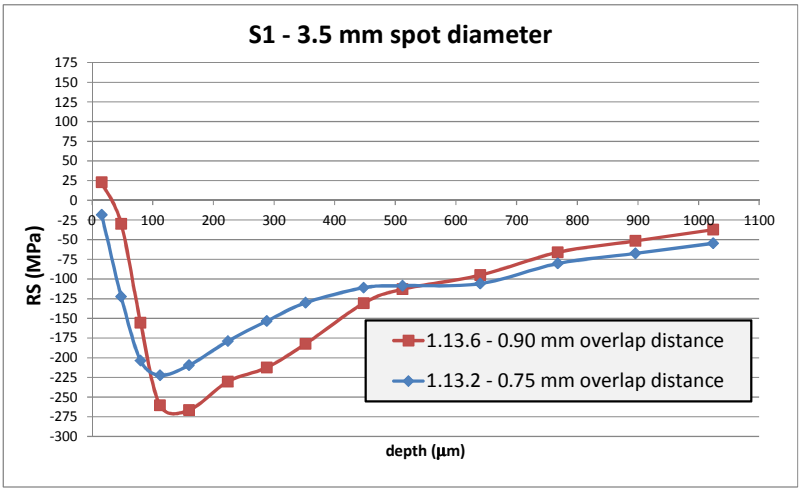

Fig. 8.22 S1 - spot diameter of 3.5 mm is kept constant and the overlapping distance is changing

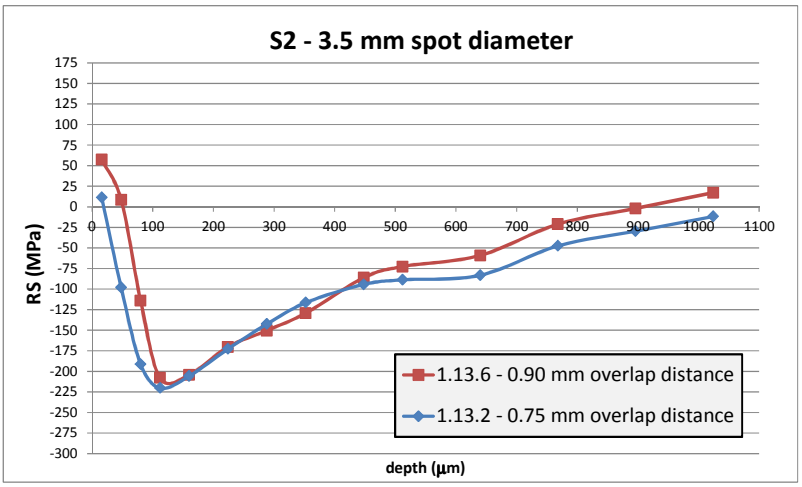

Fig. 8.23 S2 - spot diameter of 3.5 mm is kept constant and the overlapping distance is changing

From Fig. 8.18 to Fig. 8.23, six different comparison graphs are shown. All of them are referred to measurements made at point 2 in the sample (Fig. 8.3). Considering the profiles in the S1 direction only, all of them start from the tensile region, which, as said before, is probably due to local melting of the surface. The maximum peak reached is –309 MPa in sample 1.15.6 with 2.5 mm of spot diameter size (Fig. 8.21). A very similar value is reached by the sample 1.15.4 (2.0 mm spot size and 0.75 overlapping -Fig. 8.19) and sample 1.13.6 (3.5 mm spot size, 0.90 mm overlapping - Fig. 8.23). Similarly, the starting point of the RS profile of the sample with same overlapping tends to decrease by

increasing the spot size. When the spot size is 3.5 mm and the overlapping is 0.75 mm the RS at the surface are compressive (sample 1.13.2). In the S2 direction, the compression peak reached by all the profiles is lower than the ones in the S1 direction with a maximum of –221 MPa reached by sample 1.15.6 (the same sample which presented the lowest compressive RS in the S1 direction). Finally, sample 1.15.4 presents a RS profile in the S2 direction which has a very high peak in tension at the surface and furthermore, the compressive residual stresses terminate at a depth of around 600 µm.

Considering that when the spot diameter size is small, the energy is focused on a smaller area and the power density necessarily increases, this leads to local melting of the surface, generating tensile stress. If the overlapped area between two spots is high, this effect is even larger. Contrarily, when the spot size is larger and the overlapping area is smaller, the residual stresses tend to be slightly lower (in magnitude) and at the surface the stresses are closer to 0 MPa, or even in compression.

The same comparison was made also for point number 4 (according to Fig. 8.2) where, as was shown before, the behaviour of the stress S1 and S2 components are different.

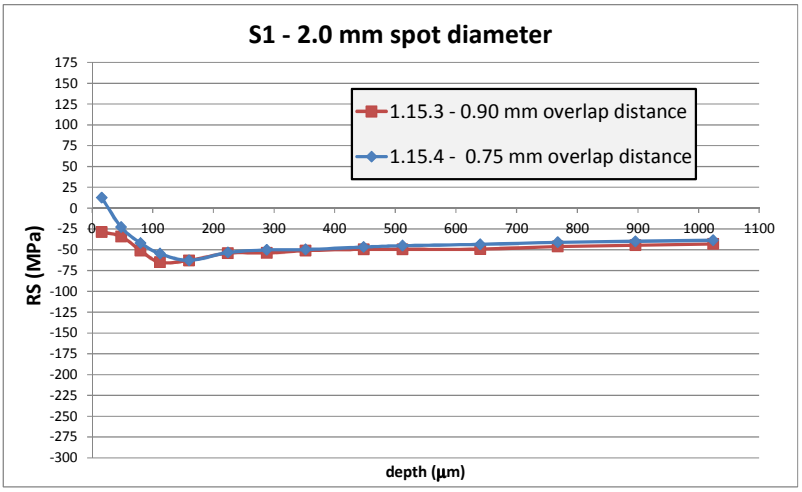

Fig. 8.24 S1 – spot diameter of 2.0 mm is kept constant and the overlapping distance is changing

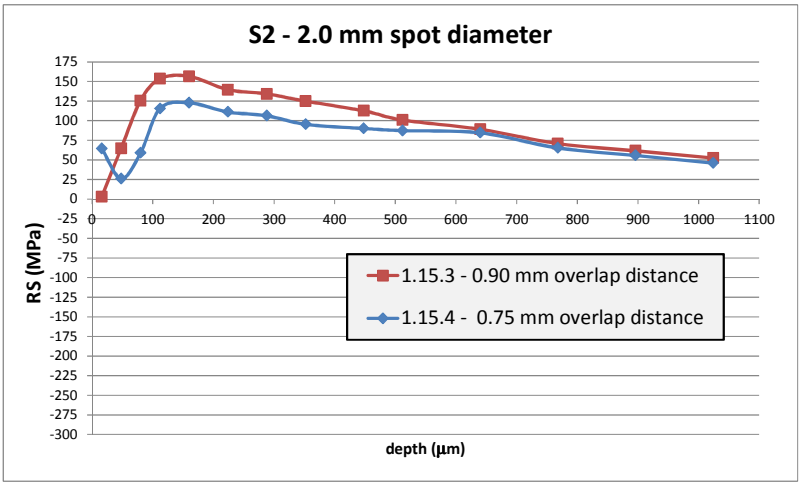

Fig. 8.25 S2 – spot diameter of 2.0 mm is kept constant and the overlapping distance is changing

As shown in Fig. 8.24 and Fig. 8.25, sample 1.15.4, which has the smaller overlapping distance (0.75 mm), shows a higher tensile stress at the surface in the S1 direction while sample 1.15.3 shows compressive residual stress at the surface. In the S2 direction sample 1.15.4 has still tensile stress at the surface while at the surface of sample 1.15.3 the residual stress is almost 0 MPa. Sample 1.15.3 reaches the highest tensile peak, around 160 MPa at 180 µm depth. After a depth of 500 µm both the samples show the same linear decay of the residual stress.

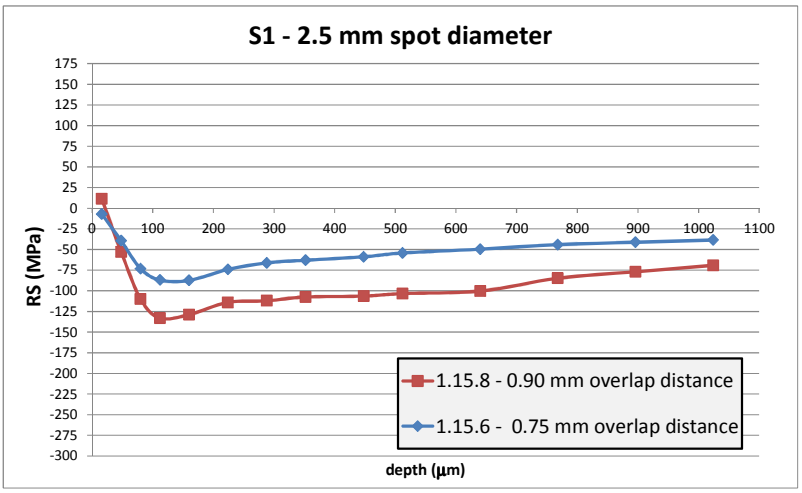

Fig. 8.26 S1 – spot diameter of 2.5 mm is kept constant and the overlapping distance is changing

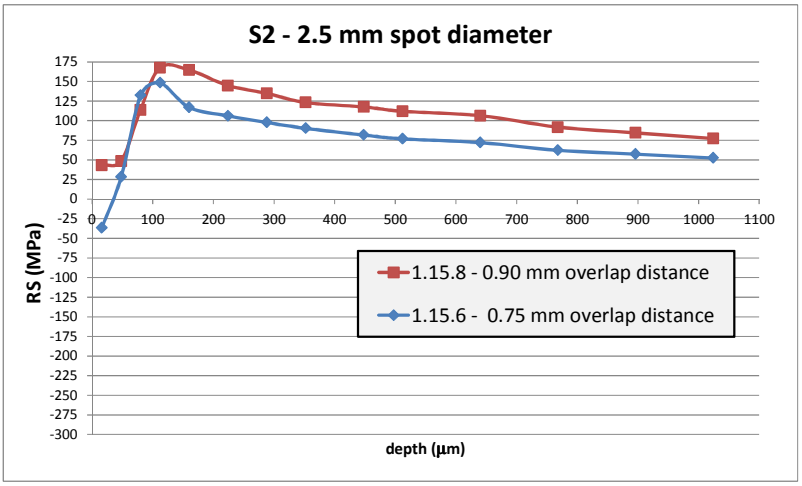

Fig. 8.27 S2 – spot diameter of 2.5 mm is kept constant and the overlapping distance is changing

In Fig. 8.26 and Fig. 8.27 the graphs from the spot with 2.5 mm diameter are shown. Still, the samples with the higher overlapping distance present higher stresses in both directions. In more detail, sample 1.15.8 has a compressive peak in the S1 direction of –133 MPa while it presents a tensile peak in the S2 direction of 168 MPa

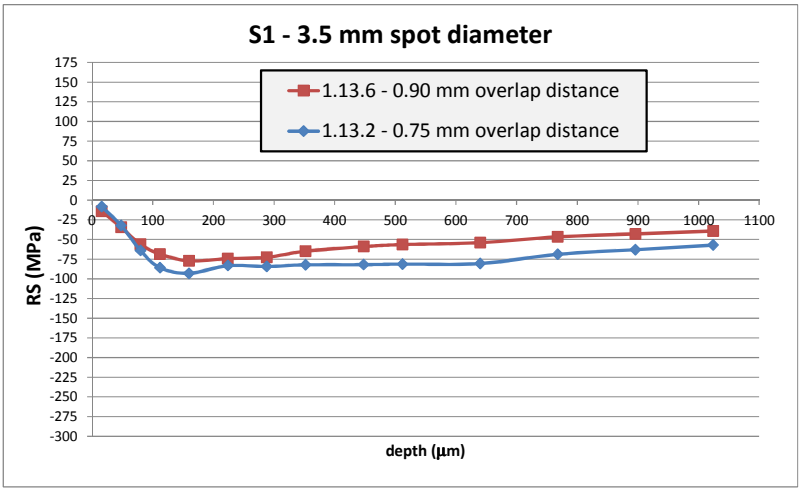

Fig. 8.28 S1 – spot diameter of 3.5 mm is kept constant and the overlapping distance is changing

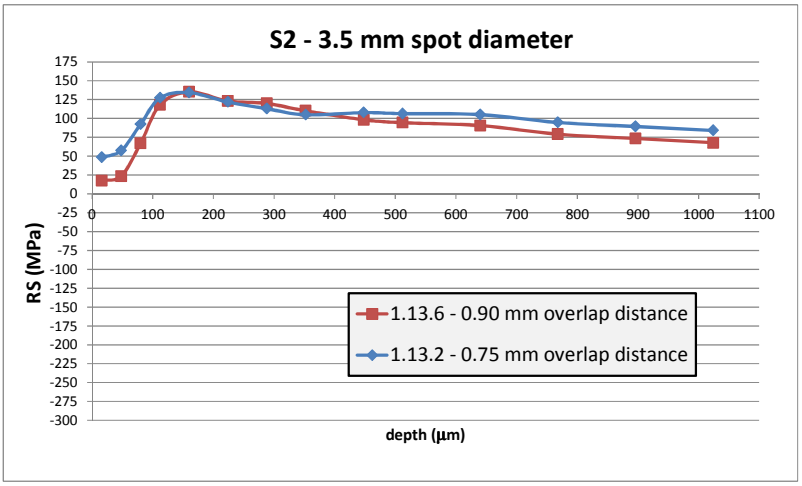

Fig. 8.29 S2 - diameter of 3.5 mm is kept constant and the overlapping distance is changing

In Fig. 8.29 the graphs for the sample with a spot diameter of 3.5 mm are shown. Both the samples present a very similar residual stress profile in both stress directions. In the S1 direction, both of them are completely in the compression region while in S2 they are completely in th the tensile region and the peak point located at 180 µm depth is around 135 MPa for both of them, which is also the lower tensile peak reached for the three different spot sizes.

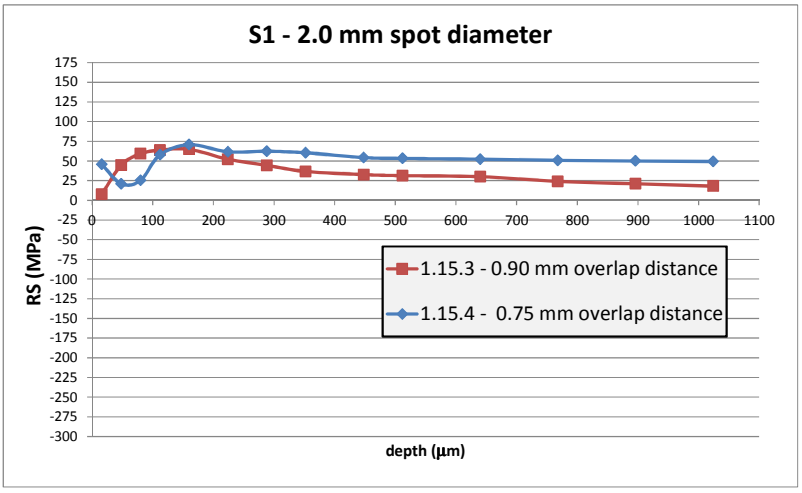

Fig. 8.30 S1 – spot diameter of 2.0 mm is kept constant and the overlapping distance is changing

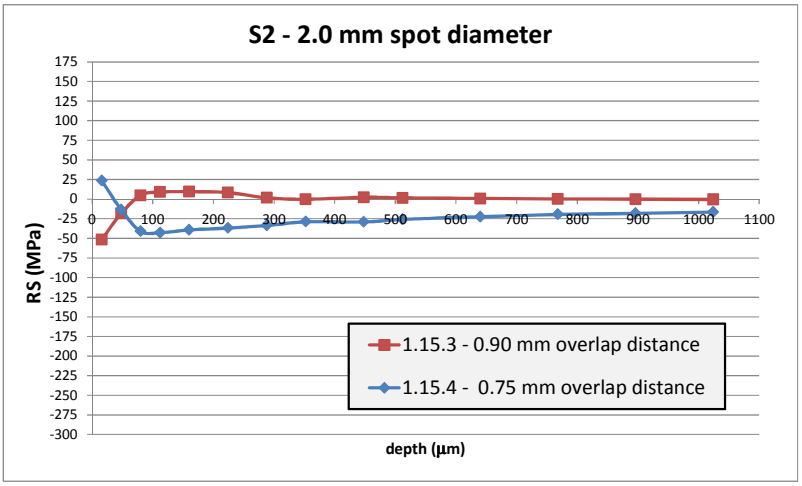

Fig. 8.31 S2 – spot diameter of 2.0 mm is kept constant and the overlapping distance is changing

The last comparison is made between the two different overlapping distances for all of the three different spot sizes at point number 5 which, according to Fig. 8.2, is alongside the LSP'ed strip. Fig. 8.30 and Fig. 8.31 show a different behaviour of the stress profile between the two samples. In particular while in the S1 direction both the stress profiles are in the tension region, in the S2 direction sample 1.15.3 has a value of stresses close to 0 MPa after a peak in compression at the surface of –52 MPa and sample 1.15.4 presents a tensile peak at the surface, with a value 24 MPa and the rest of the stress profile is in compression region.

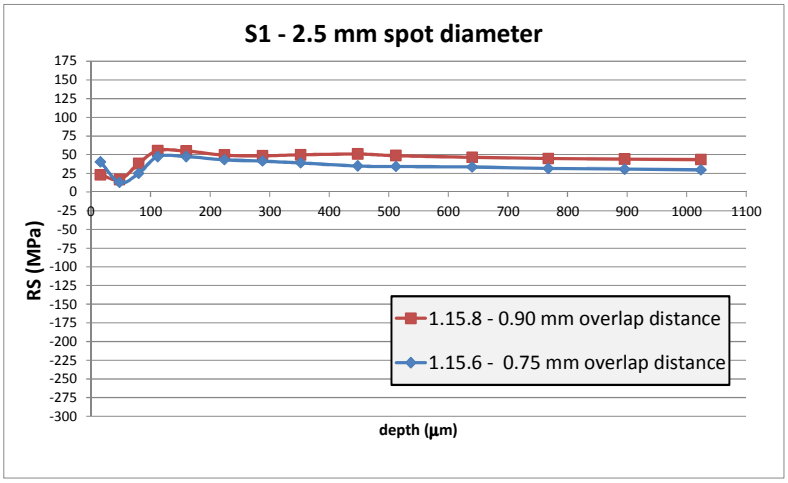

Fig. 8.32 S1 – spot diameter of 2.5 mm is kept constant and the overlapping distance is changing

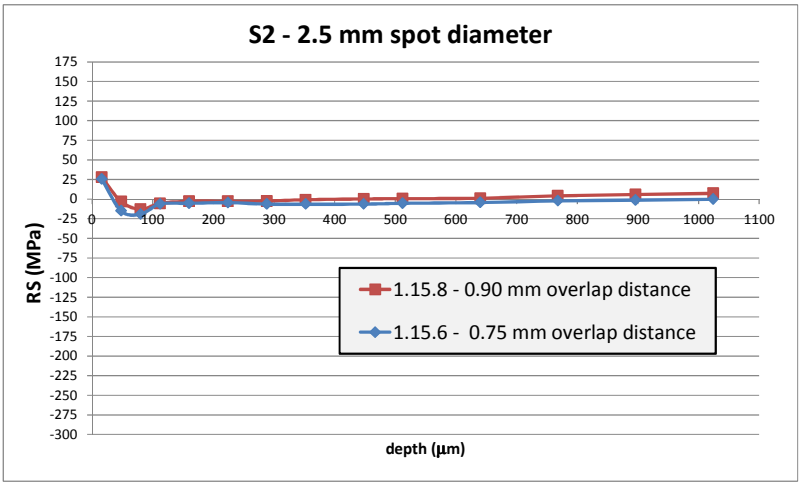

Fig. 8.33 S2 – spot diameter of 2.5 mm is kept constant and the overlapping distance is changing

Fig. 8.32 and Fig. 8.33 show that the residual stress profiles for the two single peened samples with a spot diameter of 2.5 mm are rather similar. Both of them present tensile stress along the S1 direction which is fairly constant through the thickness, with a gentle decay towards 0 MPa. In the S2 direction in contrast, a value around 0 MPa is seen from both samples along the thickness: only at the surface both samples present a tensile stress peak, below 30 MPa.

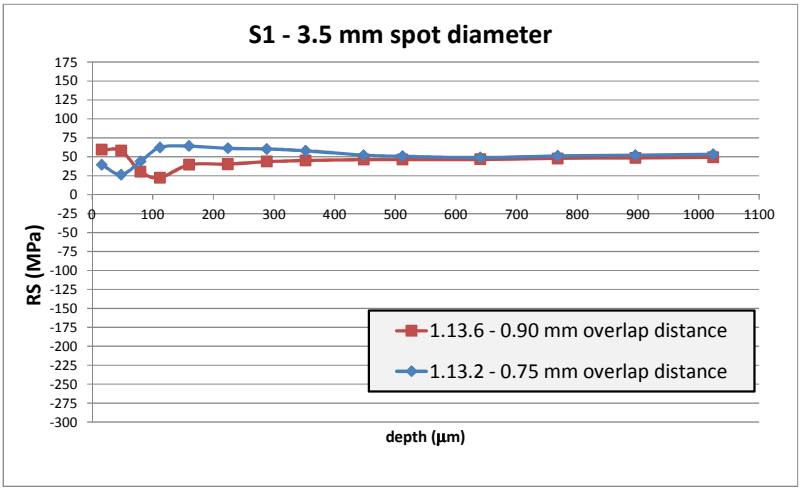

Fig. 8.34 S1 – spot diameter of 3.5 mm is kept constant and the overlapping distance is changing

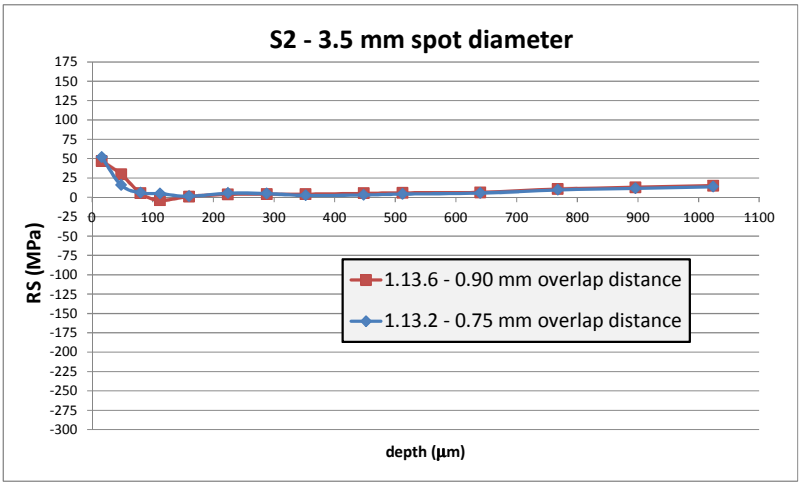

Fig. 8.35 S2 – spot diameter of 3.5 mm is kept constant and the overlapping distance is changing

In Fig. 8.34 and Fig. 8.35 a final comparison between the two samples peened with a 3.5 mm diameter spot is shown. With a similar behaviour of point 4 (Fig. 8.29), both the residual stress profiles have a similar distribution. Along the S1 directions, both the profiles are in tension. Sample 1.13.2 shows a tensile peak of 64 MPa, while sample 1.13.6 has a lower peak in tensile stress of 22 MPa. After a depth of 450 µm both the profiles seem to be equal in value and they stay constant in tension through the thickness. In the S2 direction, both the profiles have a peak in tension around 50 MPa, then after a drop within the first 100 µm through the thickness, the residual stresses lay between 0 and 10 MPa.

8.3.4 Entire Residual Stress profile by ICHD

Finally, with the ICHD it was possible to measure the RS profile from both sides of the samples. For this semi-destructive test only one sample (1.13.2: 0.75 mm spot diameter, 178 pulses/cm^2) was taken into account since the other samples were supposed to be used for X-ray measurements. As described in chapter 4, the samples were prepared with epoxy resin. Once the drilling was carried out also in the back surface the following entire residual stress profile was obtained:

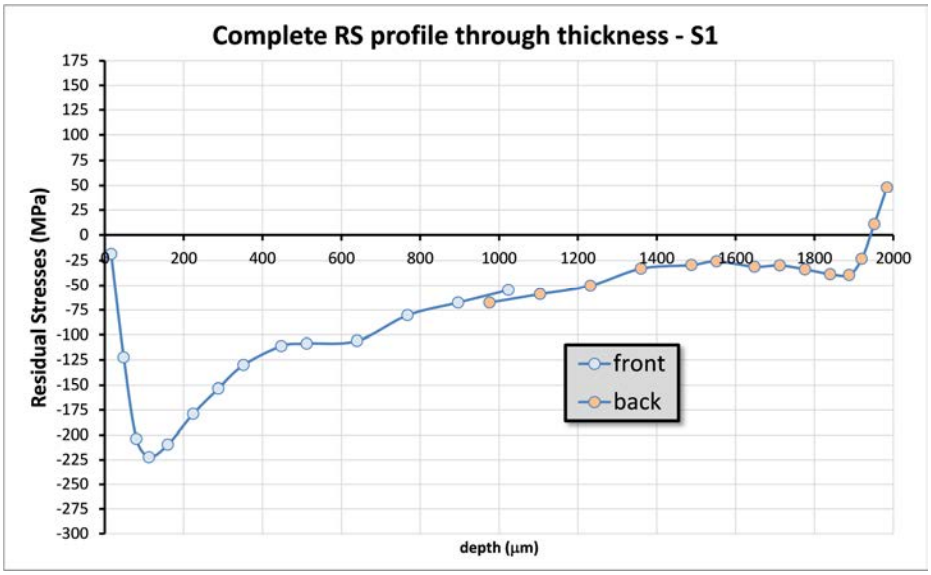

Fig. 8.36 Entire residual stress profile through thickness for a single-peened sample – S1

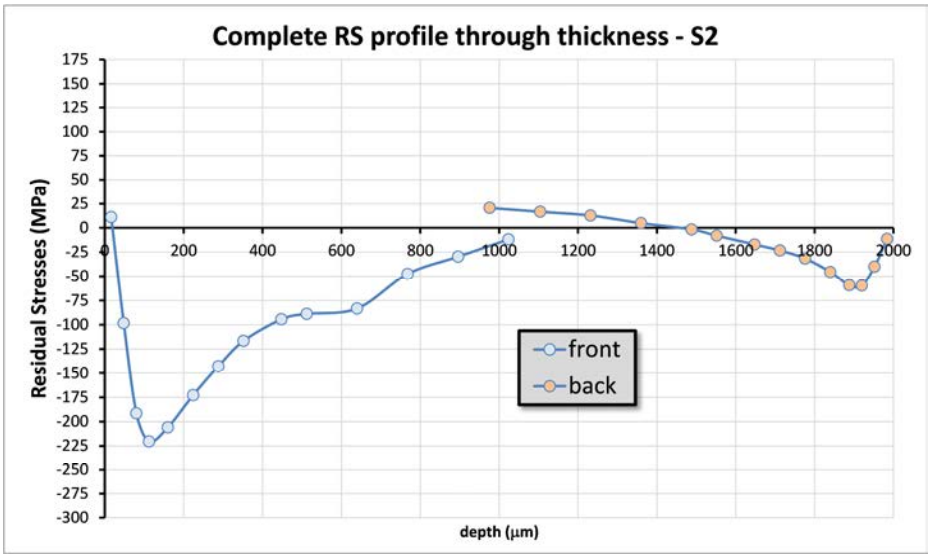

Fig. 8.37 Entire residual stress profile through thickness for a single-peened sample – S2

In Fig. 8.36 and Fig. 8.37 the entire RS profiles for the single peened sample are shown for both S1 and S2 directions. The residual stress profile measured from the back face of the single-peened sample follows the trend of the profile measured from the front face of the sample. The profiles should have the middle point in common but considering that the first RS profile was measured close the starting point of the laser treatment while the

second RS profile was taken close to the ending point of the laser treatment, the difference of 13 MPa of the two points can be considered negligible. What is worth noting in these profiles is that none of them are balanced through the thickness. In the S1 direction, even if the trend shows that the RS are moving toward the tensile region after in compression peak, this region is never reached until the very end of the thickness. A similar trend happens along the S2 direction. The obvious assumption is that the balancing tensile stress is confined outside the peened strip, and since no extra treatments were applied beside the LSP, the balancing tension is expected to be linearly distributed in the untreated sides of the sample.

8.4 Residual Stress Measurement with surface X-ray diffraction and $sin^2\psi$ method

A further residual stress measurement method useful for the these samples is the X-ray diffraction method. The X-ray machine and the $sin^2\psi$ method used to calculate the residual stresses was previously described in chapter 4. The map chosen to measure the residual stresses is the one presented in Fig. 8.2. The measurements were taken with a collimator of 2 mm, from 30 mm before the peened area to 30 mm after the peened area. The step of measurements were different: 10 mm from each measurement far away from the peened area and 2 mm close and inside the peened area as shown in Fig. 3.11 in chapter 4. The results for all the samples are shown in Fig. 8.38 where the grey rectangular shape indicates the peened area.

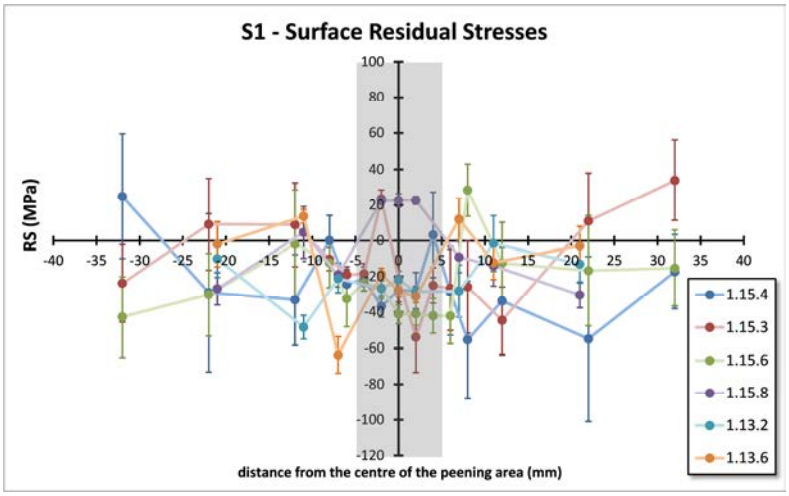

Fig. 8.38 RS profiles of all the single-peened samples centred in the centre of the peened area – S1

While the previous ICHD results presented tensile stress for most of the sample, with the X-ray diffraction technique, most of the samples show compressive residual stress at the surface and nearby to the peened area. In particular, values between -40 and -20 MPa were measured inside the peened area. The only sample who presents tensile residual stress on top the surface is the 1.15.8 (0.90 mm overlapping distance and 2.5 mm spot size) and the values are around 25 MPa which agrees the ones measured with ICHD (see Fig. 8.12).

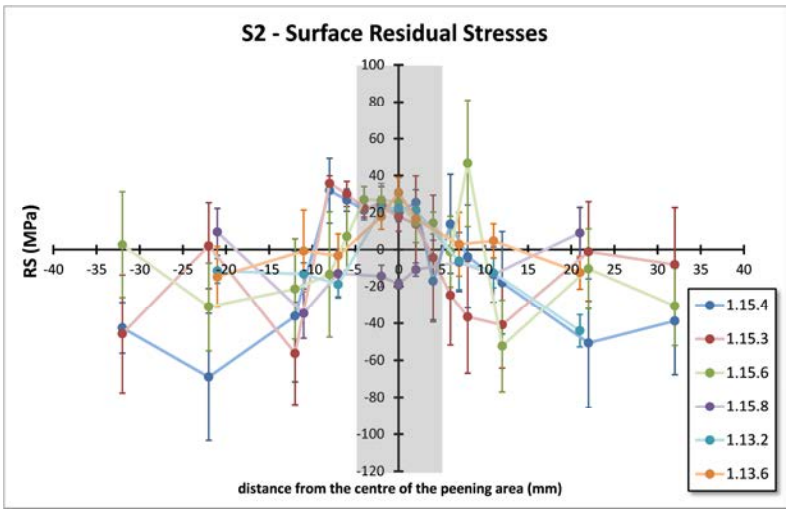

Fig. 8.39 RS profiles of all the single-peened samples centered in the centre of the peened area - S2

In Fig. 8.39 the distribution of the residual stresses in the S2 direction are shown for all the samples. In this case these values seem to match better the values obtained with ICHD. In particular, at the surface of the LSP'ed area the stresses are in tension, around 20 MPa and it is possible to see both in Fig. 8.5 and Fig. 8.13 that the stresses at the surface of the sample are around 50 MPa. Outside the peened area the residual stresses seem to be lower, and most are in compression. The previous ICHD measurements showed that alongside the peened area there is a surface value of the RS around 50 MPa that drops quickly to compression within the first 100 μm from the surface.

8.5 Conclusions

In this chapter the ICHD and surface X-ray results for the single-peened samples were presented. To better understand the distribution of the RS field, several measurements were made. The following conclusions are possible:

1. All the samples present small tensile RS at the surface that is very close to 0 MPa. As stated before, this is probably due to the high power density obtained with the laser setting which leads to local melting of the peened area. Further studies are ongoing; the reason why the ICHD and X-ray measurements are not matching in the S1 direction can probably due to the fact that the X-ray diffraction averages the RS values within a gauge volume which includes the first 20 μm from the surface but the point of highest diffraction is located at 17 μm depth (as said before, this is valid for aluminium and Cr-α tube). Anyway, the difference between the RS values calculated through X-ray diffraction and hole-drilling is around 40 MPa in most of the case which can be considered small considering the high strain rates close to the surface of the peened surface;

2. The measurements carried out at point 2 show that the peak in compression is between −200 and −275 MPa and is usually reached between 150 and 180μm depth. In the S1 direction (peening direction) the profiles always show the same behaviour while the S2 direction is more affected by the laser parameter: a deeper and higher compressive residual stress is obtained when the overlapping distance is higher, i.e. less overlapped area and lover power density;
3. The measurements carried out at point 4 show that in the S1 direction still compressive stresses are present while in the S2 direction the stresses are mostly tensile. The spot diameter size plays a fundamental role: when it's small, the higher overlapping distance generates higher stresses (both in tension and compression); when the spot diameter size increases (and the power density necessarily decreases), the overlapping distance does not greatly affect the RS distribution which tend to be the same with both the overlapping distances studied.
4. The measurements carried out at point 5 show that in the S1 direction tensile stress is present while in the S2 direction the stresses are very small, close to 0 MPa most of the time. Again, when the spot diameter size is small, the stresses generated are higher while, by increasing the spot size the overlapping distance parameter is not affecting anymore the RS distribution; furthermore outside of the peened area is where most of the balancing tensile stress is stored;
5. The entire RS profile shows that for certain conditions of LSP, it's possible to generate a full-compressive RS profile all through the thickness.

At the time of writing this thesis, no publications were made on the measurements of RS in thin samples so it cannot be possible to make a direct comparison with previous results.

References

[1] M. B. Toparli, “Analysis of Residual Stress Fields in Aerospace Materials After Laser Peening,” The Open University, Milton Keynes, 2012.

[2] J.-M. Yang, Y. C. Her, N. Han, and A. Clauer, “Laser shock peening on fatigue behavior of 2024-T3 Al alloy with fastener holes and stopholes,” *Mater. Sci. Eng. A*, vol. 298, no. 1–2, pp. 296–299, Jan. 2001.

[3] G. Ivetic, I. Meneghin, E. Troiani, G. Molinari, J. Ocaña, M. Morales, J. Porro, A. Lanciotti, V. Ristori, C. Polese, J. Plaisier, and A. Lausi, “Fatigue in laser shock peened open-hole thin aluminium specimens,” *Mater. Sci. Eng. A*, vol. 534, pp. 573–579, Feb. 2012.

[4] M. B. Toparli, “Analysis of Residual Stress Fields in Aerospace Materials After Laser Peening,” The Open University, 2012.

[5] M. B. Toparli and M. E. Fitzpatrick, “Residual stresses induced by laser peening of thin aluminium plates,” *Mater. Sci. Forum*, vol. 681, pp. 504–509, 2011.

[6] M. Dorman, N. Smyth, A. Cini, M. E. Fitzpatrick, P. E. Irving, and M. B. Toparli, “Effect of laser shock peening on residual stress and fatigue life of clad 2024 aluminium sheet containing scribe defects,” *Mater. Sci. Eng. A*, vol. 548, no. 30, pp. 142–151, 2012.

[7] P. Peyre, L. Berthe, X. Scherpereel, and R. Fabbro, “Laser-shock processing of aluminum coated 55C1 steel in water-confinement regime, characterization and application to high-cycle fatigue behaviour,” *J. Mater. Sci.*, vol. 33, pp. 1421–1429, 1998.

9 Measurements of residual stress profiles within double-peened thin samples of aluminium alloy AA2024-T351

After presenting all the data collected with the single-peened samples in chapter 8, this chapter presents results from the double-peened samples. The following sections will describe the results in terms of different spot sizes and different overlapping in the same way as for the single-peened samples. A sketch of the position of the drilling point is presented again to facilitate the reader's comprehension. The samples were LSP'ed by two different suppliers: UPM and TOSHIBA. All the samples were measured with ICHD at two different synchrotron facilities: BESSY II and the Argonne Photon Source. The details of the experiments can be found in chapter 4 while a complete description of the samples and the treatment can be found in chapter 3.

9.1 Introduction

The single-peened samples were useful to understand how the different laser parameters affect the distribution of the RS in thin aluminium samples. Similar thin plate samples were then laser peened on both larger surfaces, with the two strips of treatment aligned through-thickness. As said in chapter 2, not many results have been published on two-sided LSP treatment and among the published ones [1]–[3], the main purpose was to reduce the deformation generated by the LSP on thin samples rather than introducing a full compressive residual stress profile through all the thickness. This is mainly due to the fact that LSP technology has been considered so far a technique only for in-service repair

of thin aluminium components rather than a technique exploited during the design process. The laser cannot easily be delivered on both faces of a thin structure after assembly. If the LSP will find its niche along with other techniques that improve the fatigue life like shot peening used during design, it will be possible to use the LSP during the assembly process of the aero structure, thus every component will be easily accessible.

9.2 Samples

In this research, nine different samples were involved: six of them were two-side LSP'ed samples treated by the UPM with the same laser parameters of the single peened samples described in chapter 8; two of them were peened by UPM but with a wider peened area (20 mm instead of 10 mm); one sample was treated by TOSHIBA.

The double-peened samples are of the exact size and material of the single-peened ones. After a first LSP treatment on one of the faces of the samples, they were flipped and a second treatment was done, contrary to what was done by Clauer *et. al* who LSP'ed the samples on both faces at the same time by splitting the laser through an optical system [4]. The two strips were supposed to be exactly one on top of the other but in some samples there is a misalignment of up to 1 mm.

In order to have a complete knowledge of the RS profiles, ICHD was used as initial RS measurement technique for the first six samples while for the sample coming from UPM with a wider LSP'ed area and for the TOSHIBA sample, the measurements were made respectively at BESSY II and APS.

The following table presents the specimens used:

Table 9.1 List of samples laser peened on both sides

Aluminium Alloy AA2024-T351						
Supplier	Specimen	Overlapping	Pulses/cm^2	Spot	Peened	Power
UPM	**1.13.4**	0.75	178	2.0	Double	8.92
	1.14.1	0.90	124	2.0	Double	8.92
	1.14.3	0.75	178	2.5	Double	5.71
	1.14.4	0.90	124	2.5	Double	5.71
	1.14.7	0.75	178	3.5	Double	2.91
	1.16.1	0.90	124	3.5	Double	2.91
	2.7	0.75	178	2.5	Double	5.71
	2.10	0.75	178	2.5	Double	5.71
Toshiba	**T1**		5400	0.4	Double	1.99

It is worth noting how different the parameters of the two suppliers are in terms of spot diameter, spot density and power density.

9.3 Residual Stress Measurements with ICHD

In the next sections, RS measurements will be shown. In particular, as done in chapter 8 for the single-peened samples, comparison will be made between the spot diameters by keeping constant the overlapping distance and then by varying the overlapping distance by keeping constant the spot diameter. Three locations will be taken into consideration and a map of the measurement locations will be introduced to help the reader.

9.3.1 Overlapping of 0.75 mm - 178 pulses/cm²

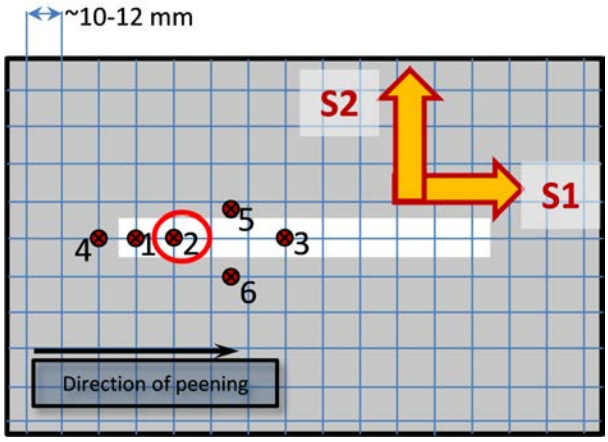

Fig. 9.1 Position of the hole-drilling measurements – point 2

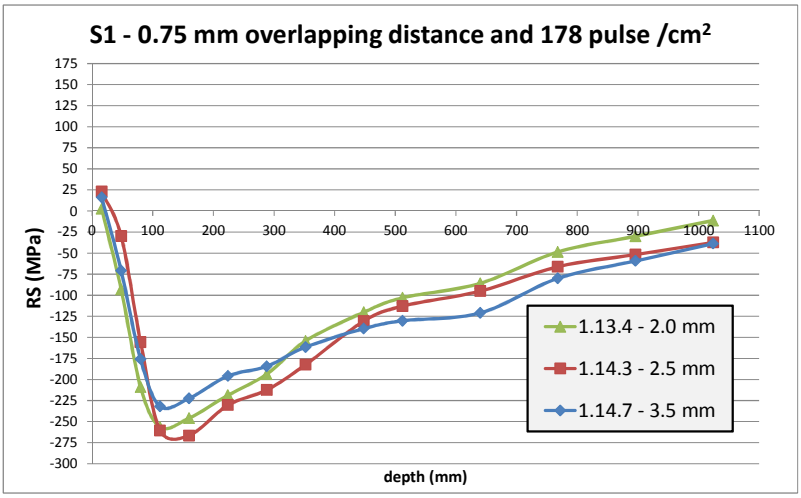

Fig. 9.2 Comparison between three samples with different spot sizes– S1 direction at point 2

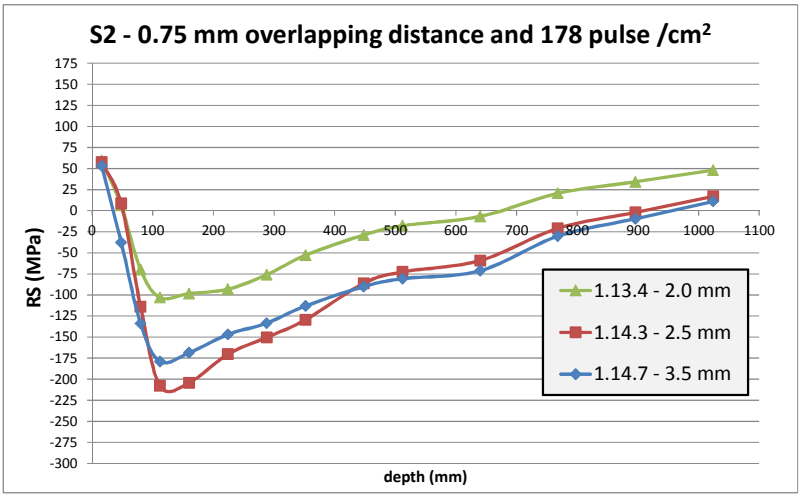

Fig. 9.3 Comparison between three samples with different spot sizes– S2 direction at point 2

In Fig. 9.2 and Fig. 9.3 the RS profiles of three samples with the same overlapping area are shown in both directions S1 and S2 according to Fig. 9.1. In the S1 direction, the three profiles look very similar. All of them present a tensile stress at the surface, the lowest value (3 MPa) was measured at the surface of the sample 1.13.4 (Ø 2.0 mm), while the highest value, 16 MPa, was measured at the surface of the sample 1.14.3 (Ø 2.5 mm). In the compression region, the lowest value is reached by sample 1.14.3 (Ø 2.5 mm) with a value of –267 MPa at 160 µm depth. Sample 1.13.4 (Ø 2.0 mm) has the lowest compression value of –103.1 MPa at 112 µm depth. The same sample RS profile turns into tension in the S2 direction at a depth between 640 and 700 µm while the RS profiles of the other two samples lay in the compression region up to 900 µm.:

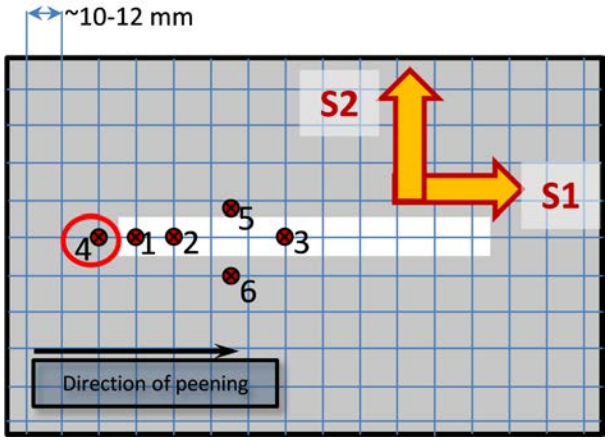

Fig. 9.4 Position of the hole-drilling measurements – point 4

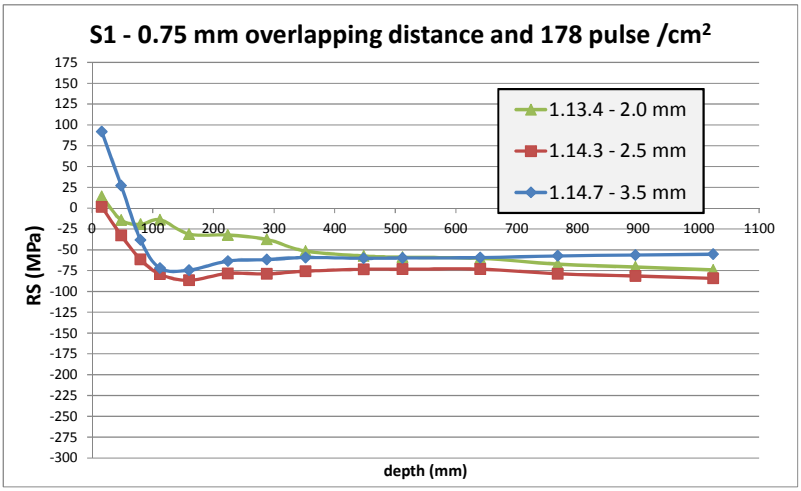

Fig. 9.5 Comparison between three samples with different spot sizes– S1 direction

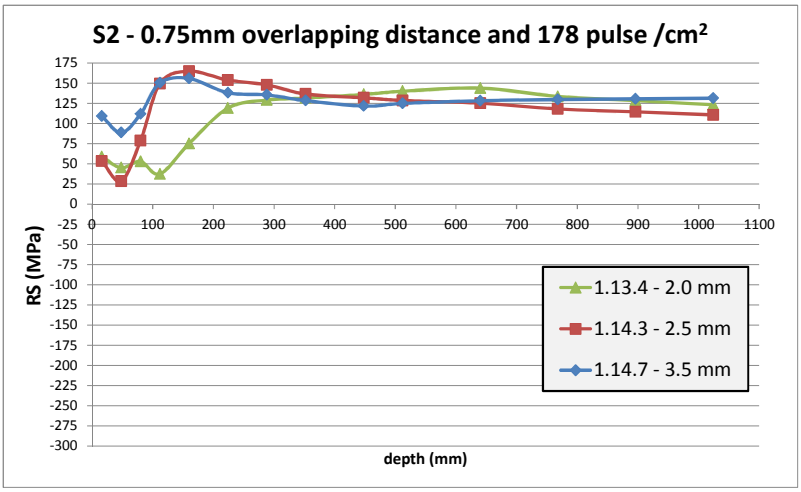

Fig. 9.6 Comparison between three samples with different spot sizes– S2 direction

In Fig. 9.5 and Fig. 9.6 the comparison results of the RS profiles measured at point 4 (Fig. 9.4) are presented. As mentioned already for the single-peened samples, the RS profiles measured outside the peened area, present two different distributions of RS. In the S1 direction, the RS are almost completely in compression and after a depth of 112 µm, the profiles for all the three samples tend to be constant through the depth. At the surface all of the sample show tensile stress with value very close to 0 MPa, apart from sample 1.14.7 (Ø 3.5 mm) which shows a very high tensile stress value, 91.8 MPa. In the S2 direction, as expected the RS profiles are completely tensile. Still sample 1.14.7 shows the highest tensile value at the surface (109 MPa) while the other two samples with the smaller spot diameter size have a value around 55 MPa. Furthermore, samples 1.14.3 (Ø 2.5 mm) and 1.14.7 (Ø 3.5 mm) show a peak in tension at 160 µm while sample 1.13.4 (Ø 3.5 mm) has a smoother RS profile and the peak does not occur until 640 µm.

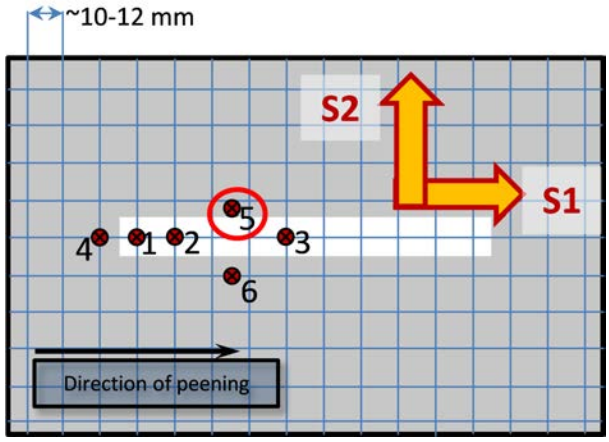

Fig. 9.7 Position of the hole-drilling measurements – point 5

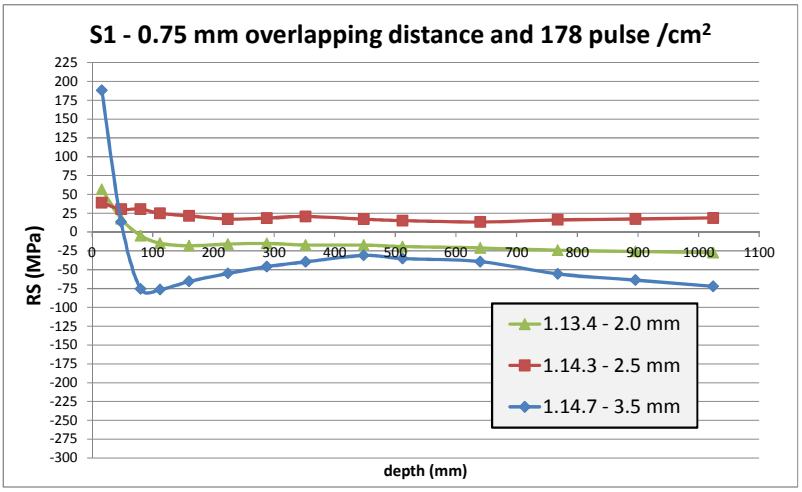

Fig. 9.8 Comparison between three samples with different spot sizes– S1 direction at point 5

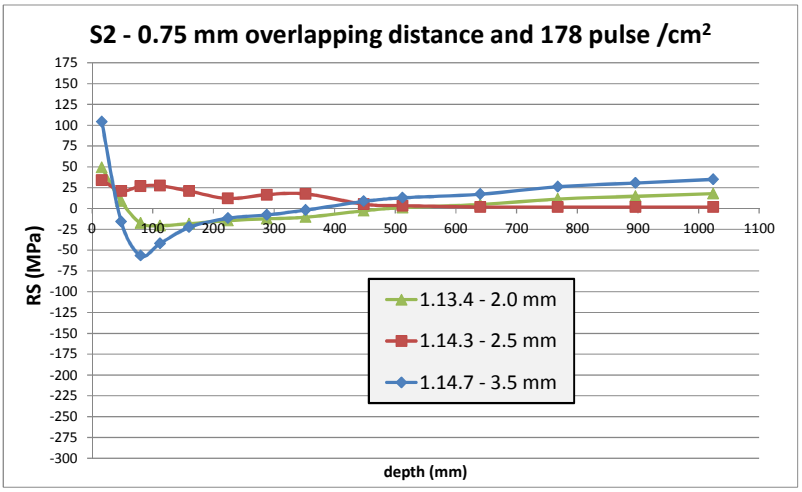

Fig. 9.9 Comparison between three samples with different spot sizes– S2 direction at point 5

In Fig. 9.8 and Fig. 9.9 the RS profiles measured at point 5 (Fig. 9.7) are shown. The trend of the RS is not similar between the three samples. Sample 1.13.4 (Ø 2.0 mm) presents a RS profile which in both directions starts from tension region (57 MPa in S1) but before a depth of 80 µm, the profile turns into compressive; after than the profile is constant in S1 direction while it turns into tension again in S2 at a depth of 500 µm.

Sample 1.14.3 (Ø 2.5 mm) shows a RS profile which lies completely in the tensile region in both directions with a value not higher than 39 MPa, measured at the surface. The profile looks constant for most of the depth, in the S1 direction a value around 0 MPa is reached and maintained after 500 µm depth. Sample 1.14.7 (Ø 3.5 mm) shows a totally different behaviour. At the surface the tensile stress reached is very high in both directions, 188 MPa in S1 and 104 MPa in S2. Furthermore in the S1 direction after a depth of 50 µm, the profile lies completely in the compressive region while in the S2 direction the trend is similar to sample 1.13.4: the profile lays in the compressive region up to a depth of 350 µm and then turns into tension.

9.3.2 Overlapping of 0.90 mm - 124 pulses/cm²

The following data are from the samples double-peened with an overlapping distance of 0.90 mm, e.g. a total of 124 pulses/cm².

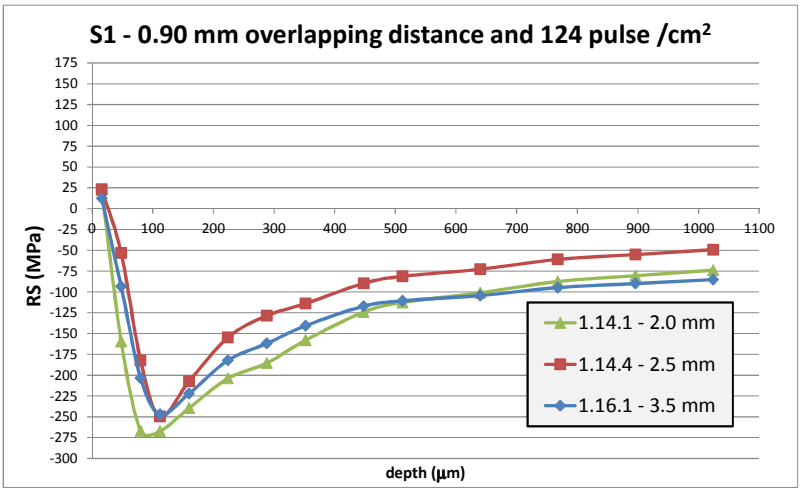

Fig. 9.10 Comparison between three samples with different spot sizes– S1 direction at point 2

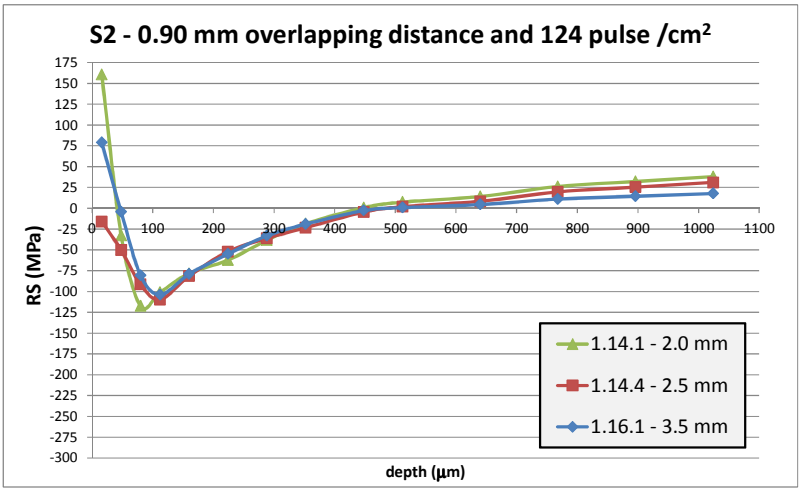

Fig. 9.11 Comparison between three samples with different spot sizes– S2 direction at point 2

In Fig. 9.10 and Fig. 9.11 the RS profiles measured at point 2 (Fig. 9.1) of the double-peened samples are reported. The RS profiles show more commonalities among each other than the previous comparisons made at the same point. In the S1 direction, still the sample with the smallest spot size has the lowest peak RS value, –276 MPa, while the other two samples have a compressive peak at around –250 MPa. For all of them the peak is reached at a depth of 160 µm. Similarly at the surface the profiles show a common value around 20 MPa. The differences are more marked in the S2 direction. At the surface the sample 1.14.1 (Ø 2.0 mm) shows a peak in tension, 161 MPa. This peak is halved with the sample 1.16.1 (Ø 3.5 mm), 79 MPa and, with the sample 1.14.4 (Ø 2.5 mm), it lies in the compressive area with a value of –17 MPa.

The following graphs (Fig. 9.12 and Fig. 9.13) show the RS profiles measured at point 4 (Fig. 9.4).

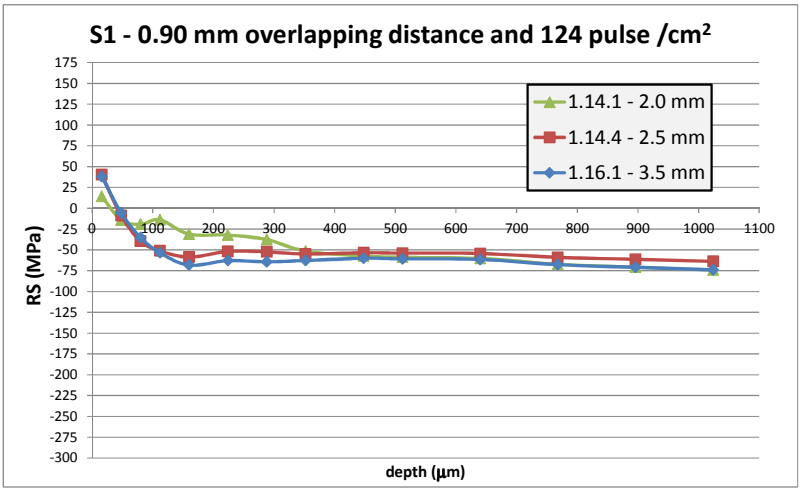

Fig. 9.12 Comparison between three samples with different spot sizes– S1 direction at point 4

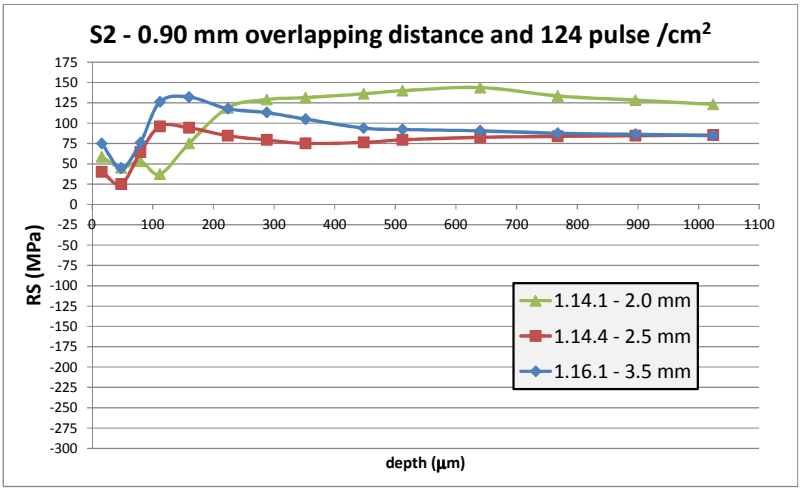

Fig. 9.13 Comparison between three samples with different spot sizes– S2 direction at point 4

At point 4 as expected and already shown by the previous samples, the RS are distributed differently, depending on the direction. In the S1 direction the stresses are mostly in compression but not at the surface. Here the stresses are in tension, with a peak around 40 MPa reached by samples 1.14.4 (Ø 2.5 mm) and 1.16.1 (Ø 3.5 mm). After they turn into compression, they stabilize their value around -60 MPa. In the S2 direction instead, the RS are in the tension region as expected. While samples 1.14.4 (Ø 2.5 mm) and

1.16.1 (Ø 3.5 mm) seems to have a similar trend by reaching of a peak of tension around the same depth (112 and 160 µm respectively), sample 1.14.1 (Ø 2.0 mm) reached a tensile peak only at 640 µm depth.

The final comparison is given for the same three samples at point 5 (Fig. 9.7).

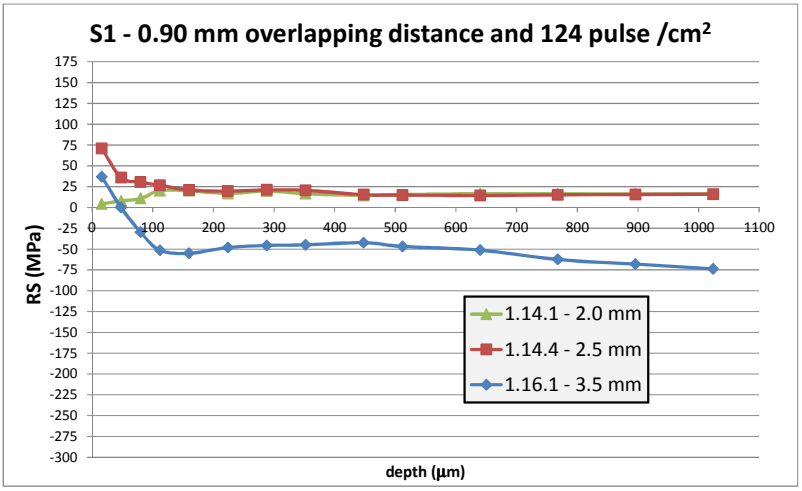

Fig. 9.14 Comparison between three samples with different spot sizes– S1 direction at point 5

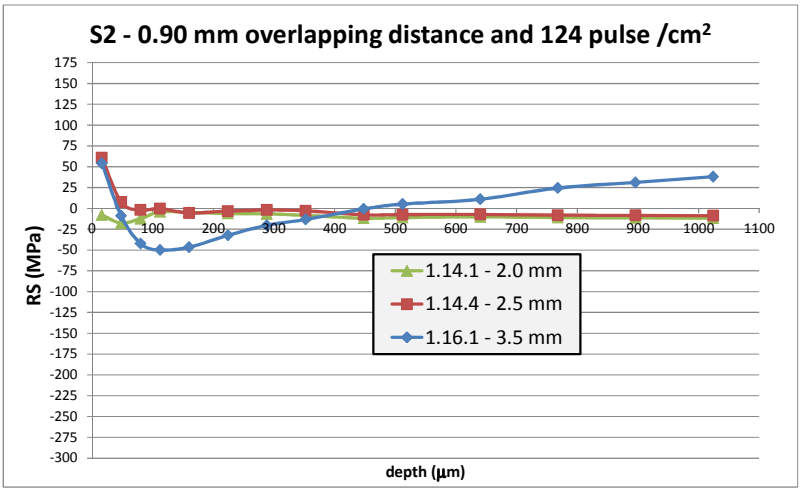

Fig. 9.15 Comparison between three samples with different spot sizes– S2 direction at point 5

In Fig. 9.14 and Fig. 9.15 the RS profiles of point 5 measurements are shown. In the S1 direction all the profiles are in tension and show a peak at the surface which differs for

each sample: the highest one is reached by sample 1.16.1 (Ø 3.5 mm) with a value of 64 MPa. While samples 1.14.1 and 1.16.1 have a RS profile that remains below 20 MPa through the thickness, sample 1.14.4 (Ø 2.5 mm) shows a profile which is higher, around 35 MPa through the thickness. In the S2 direction, at the surface the tension is very high for all three samples with a highest peak of 40 MPa reached by sample 1.14.4 (Ø 2.5 mm). for the rest of the depth all the profiles tend to lie in a region between ± 10 MPa.

9.3.3 Comparison between constant spot diameters at different overlapping settings

In the following section a comparison between the RS profiles with a constant spot diameter size is shown. The comparison was made for all the three points presented previously, starting from point 2:

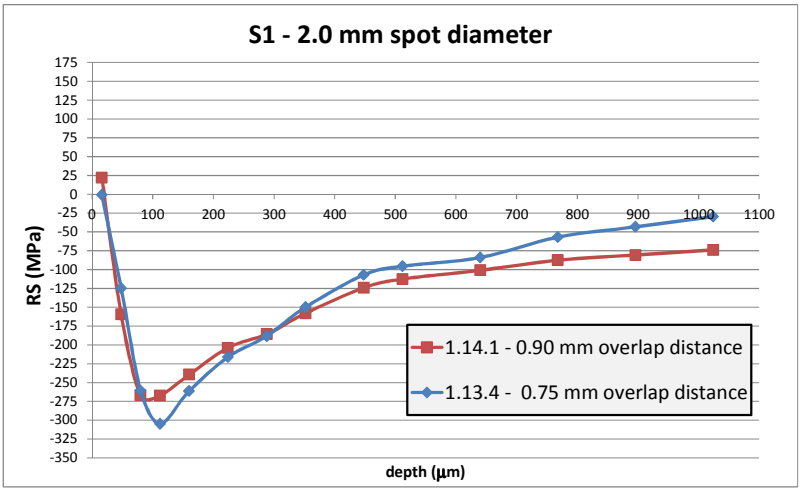

Fig. 9.16 Comparison between 0.75 and 0.90 mm overlapping distance, 2.0 mm spot diameter – S1

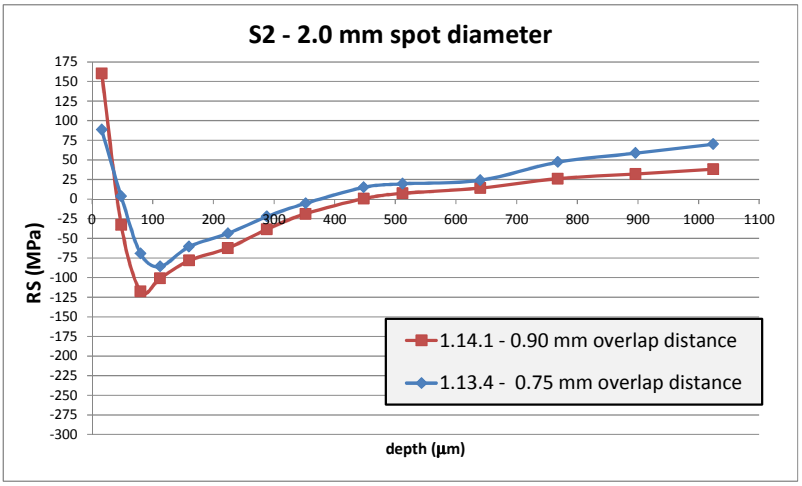

Fig. 9.17 Comparison between 0.75 and 0.90 mm overlapping distance, 2.0 mm spot diameter – S2

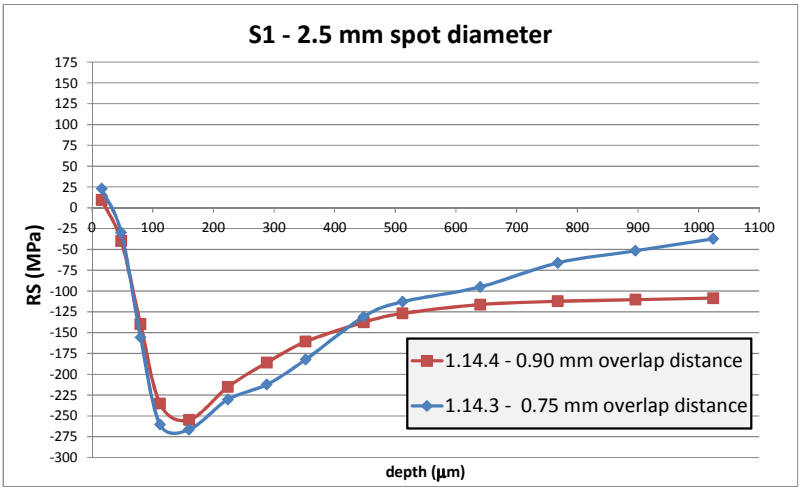

Fig. 9.18 Comparison between 0.75 and 0.90 mm overlapping distance, 2.5 mm spot diameter spot diameter – S1

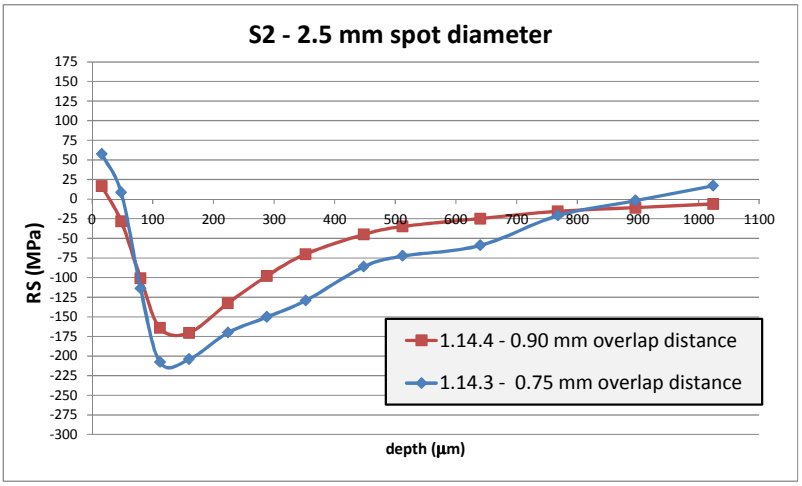

Fig. 9.19 Comparison between 0.75 and 0.90 mm overlapping distance, 2.5 mm spot diameter – S2

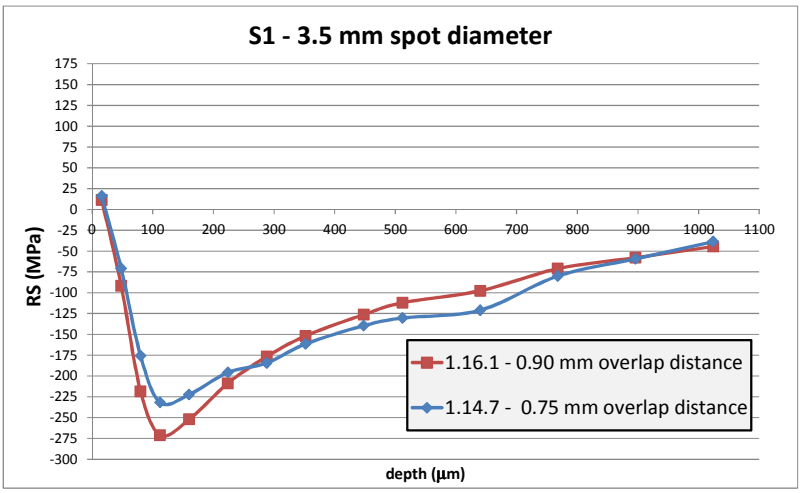

Fig. 9.20 Comparison between 0.75 and 0.90 mm overlapping distance, 3.5 mm spot diameter – S1

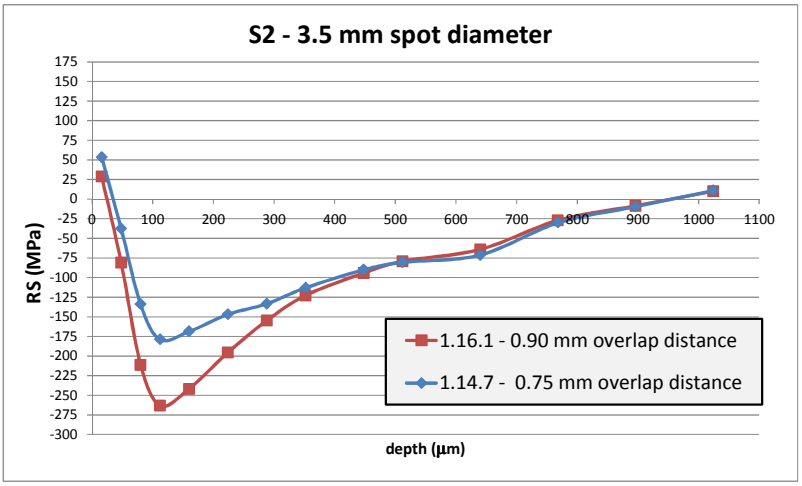

Fig. 9.21 Comparison between 0.75 and 0.90 mm overlapping distance, 3.5 mm spot diameter – S2

All the RS profiles look similar. In particular in both directions, all the profiles start in the tensile region. The peaks in compression seem to be slightly affected by the overlapping distance since with both 0.90 mm and 0.75 mm it reaches a value around –250 MPa in the S1 direction while in the S2 direction it varies depending on the laser spot size, reaching a maximum value of –208 MPa in the sample 1.14.3 (Ø 2.5 mm). What is possible to observe with the six graphs is that what really changes between the two different overlapping distances is the RS trend. In fact, all the RS profiles of the samples with 0.75 mm overlapping distance have a similar trend to the single-peened samples: once the lowest value in compression is reached, the profile tends to increase monotonically in both S1 and S2 directions. For the profiles of the sample with 0.90 mm overlapping distance, they still reach a peak in compression and then they increase monotonically as well but, as seen in Fig. 9.18, they tend to reach a plateau still in compression of the graph (apart from for the sample peened with 2.0 mm spot). Following the trend of these profiles, it is possible to assume that, since that the other side of the sample is peened with the same laser parameters, the RS profile along the whole thickness will never reach the tension region, i.e. the entire thickness of the peened area is in compression.

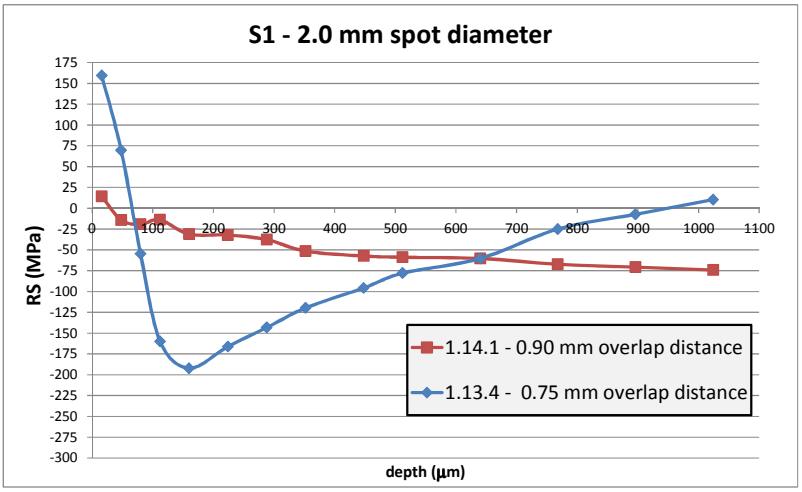

Fig. 9.22 Comparison between 0.75 and 0.90 mm overlapping distance, 2.0 mm spot diameter – S1

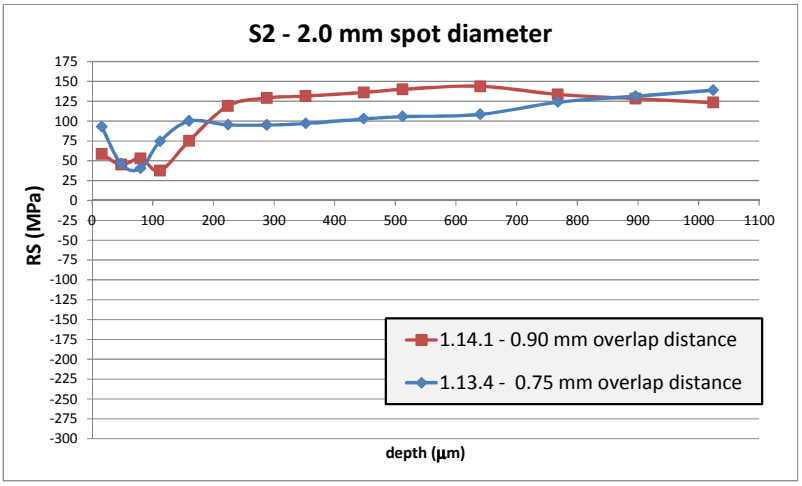

Fig. 9.23 Comparison between 0.75 and 0.90 mm overlapping distance, 2.0 mm spot diameter – S2

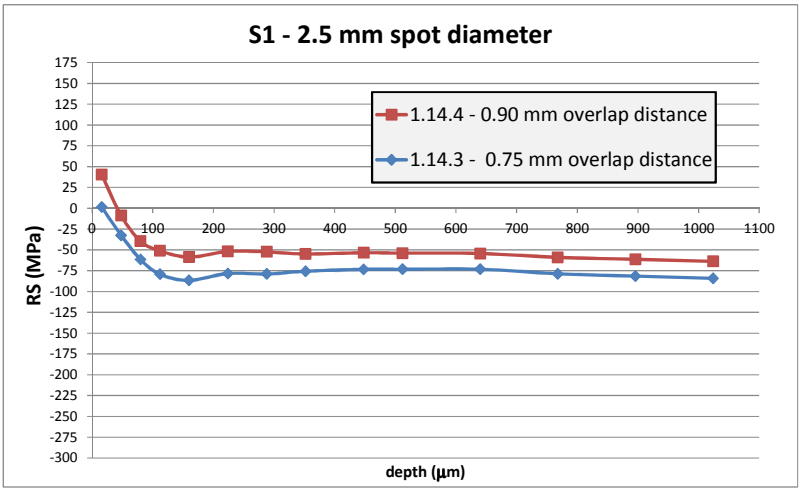

Fig. 9.24 Comparison between 0.75 and 0.90 mm overlapping distance, 2.5 mm spot diameter – S1

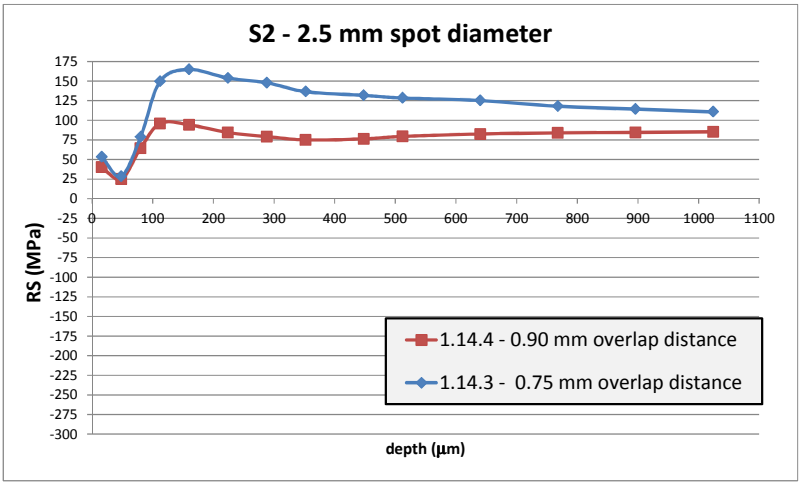

Fig. 9.25 Comparison between 0.75 and 0.90 mm overlapping distance, 2.5 mm spot diameter – S2

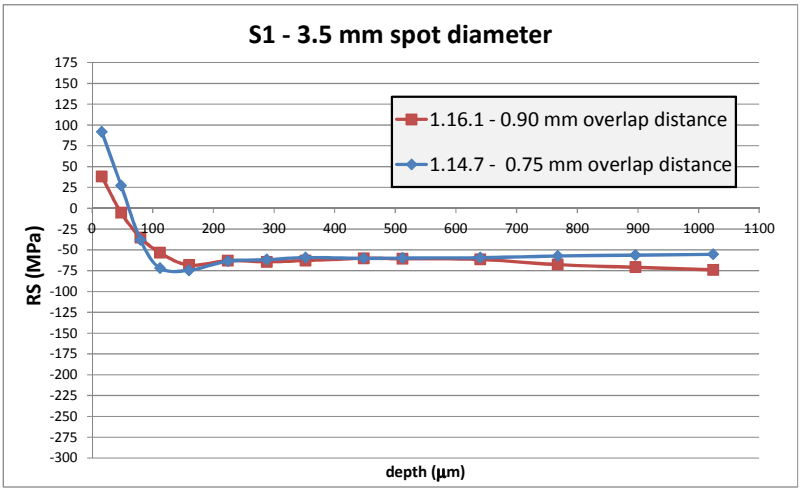

Fig. 9.26 Comparison between 0.75 and 0.90 mm overlapping distance, 3.5 mm spot diameter – S1

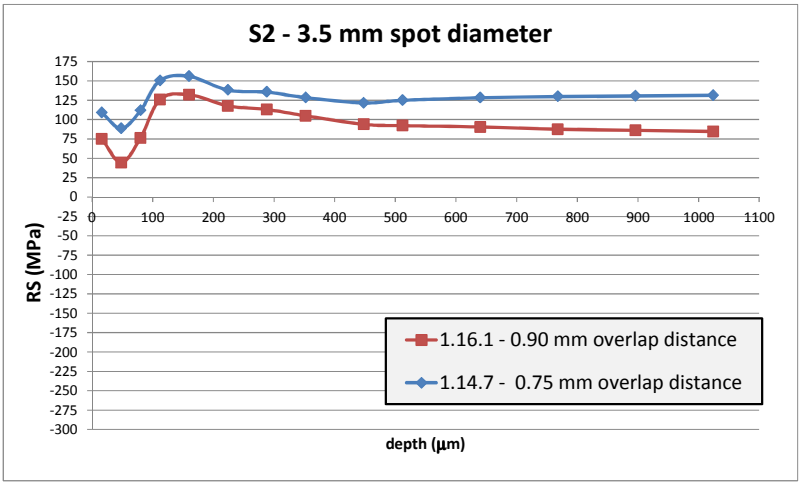

Fig. 9.27 Comparison between 0.75 and 0.90 mm overlapping distance, 3.5 mm spot diameter – S2

From Fig. 9.22 to Fig. 9.27, the comparison between the RS profiles measured at point 4 for samples with same spot diameter and different overlapping distance is shown. The behaviour of the RS in the S1 direction for the samples with 2.0 mm spot size (Fig. 9.22) is different in each case. In particular, the sample with a lower overlap distance, i.e. higher overlapped area between two consecutive spots, shows a RS profile which starts around 160 MPa, then it reaches –192 MPa in compression and then linearly goes back to tension.

Sample 1.14.1 with a 0.90 mm overlapping distance shows a profile which is entirely compressive, besides the RS at the surface which is slightly tensile. When the spot diameter is increased up to 2.5 mm, the RS profiles in both directions tend to assume the same trend. In particular, sample 1.14.4 with a 0.90 mm overlapping distance presents lower RS in magnitude. In the S1 direction the RS are in tension at the surface of the sample but after a depth of 160 μm, the RS are constantly in compression within a value of 55 ± 10 MPa. Sample 1.14.3, with the lower overlapping distance, shows the same trend shifted by −20 MPa. In the S2 directions both samples present a surface stress in tension (40 MPa for the lower overlapping and 53 MPa for the higher one) and the RS values are similar up to 80 μm depth, after which, the trends split and sample 1.14.3 presents a higher RS value, up to 165 MPa vs. 96 MPa for 1.14.4. A further increase in the spot diameter size removes the previous difference between the RS profiles of the two sample. In Fig. 9.20 and Fig. 9.21, it is possible to see how the profiles in the S1 direction are almost identical up to the mid thickness, while at the surface the sample with a higher overlapping distance shows a higher tensile value (92 MPa). Finally in the S2 direction the trends are similar, both RS profiles are in tensile region, and sample 1.14.7 shows slightly higher tensile stresses that lie between 120 and 140 MPa after a peak of 155 MPa. Similarly the sample 1.16.1 RS profile lies between 80 and 100 MPa with a peak of 132 MPa.

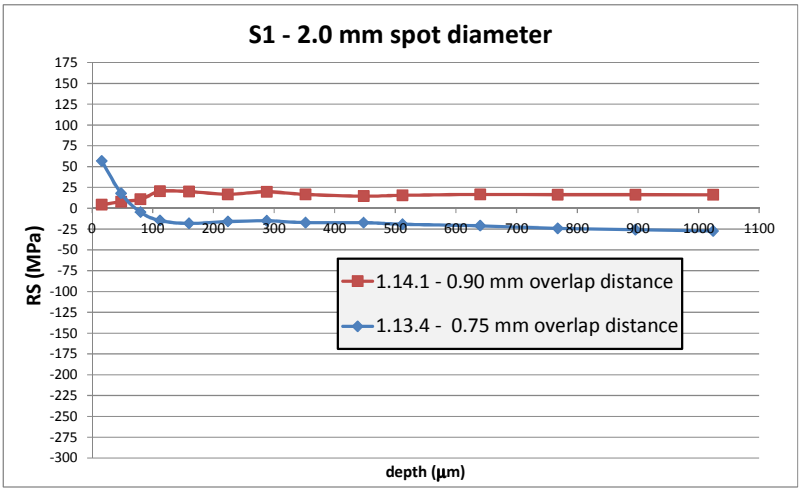

Fig. 9.28 Comparison between 0.75 and 0.90 mm overlapping distance, 2.0 mm spot diameter– S1

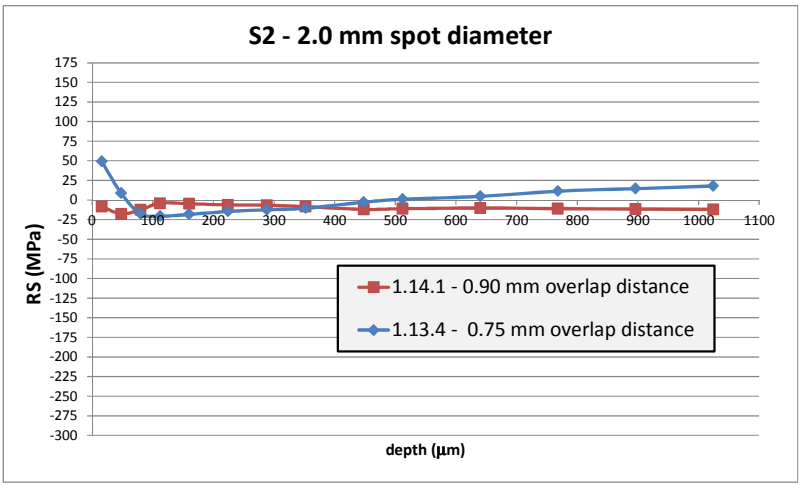

Fig. 9.29 Comparison between 0.75 and 0.90 mm overlapping distance, 2.0 mm spot diameter – S2

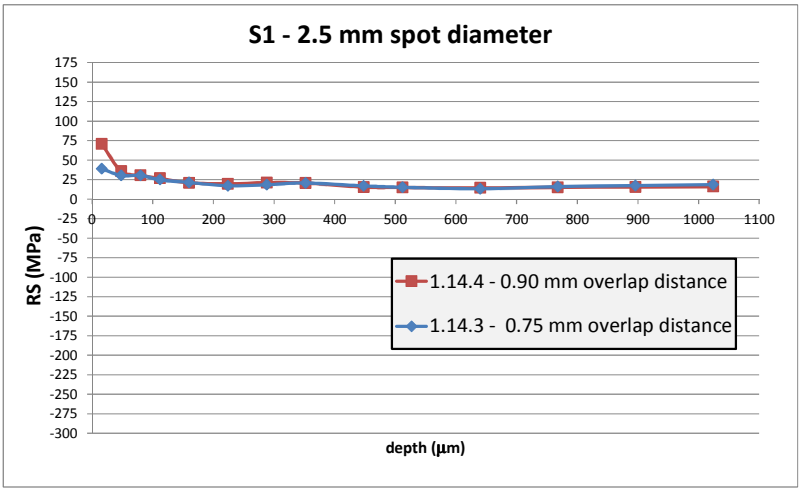

Fig. 9.30 Comparison between 0.75 and 0.90 mm overlapping distance, 2.5 mm spot diameter – S1

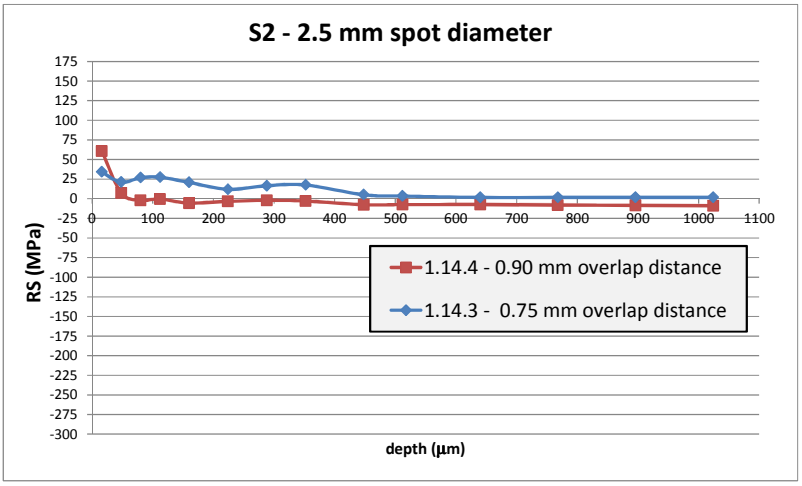

Fig. 9.31 Comparison between 0.75 and 0.90 mm overlapping distance, 2.5 mm spot diameter – S2

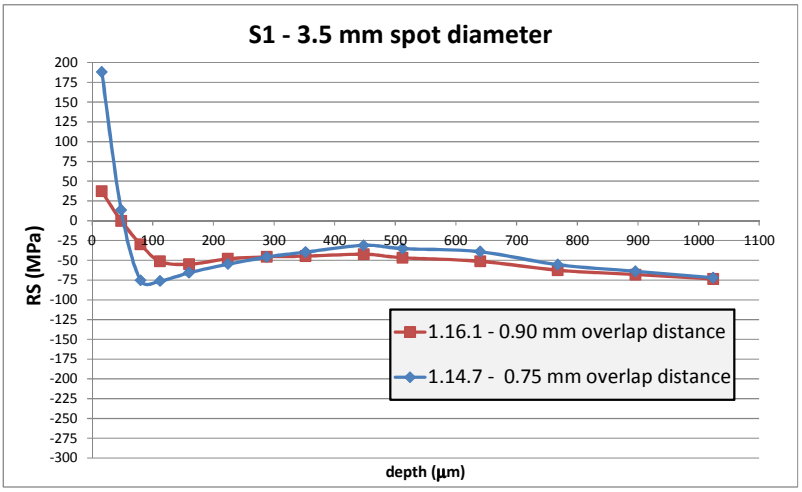

Fig. 9.32 Comparison between 0.75 and 0.90 mm overlapping distance, 3.5 mm spot diameter – S1

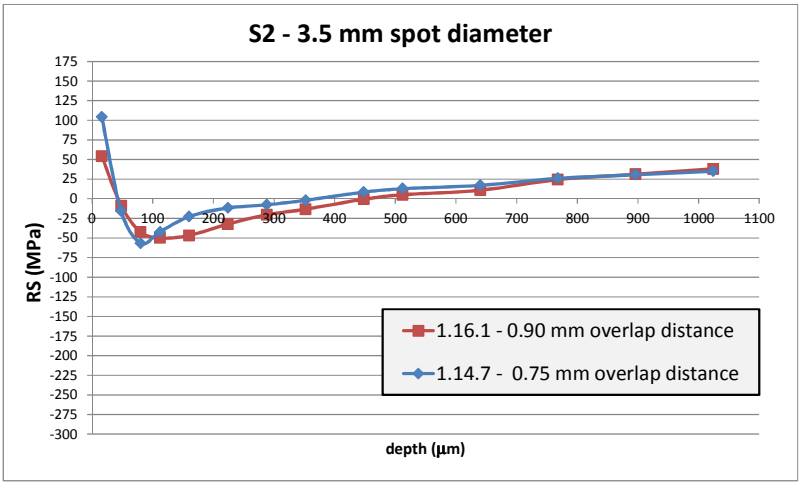

Fig. 9.33 Comparison between 0.75 and 0.90 mm overlapping distance, 3.5 mm spot diameter – S2

From Fig. 9.28 to Fig. 9.33, the RS profiles measured at point 5 are shown. Again, when the spot diameter size is the smallest (2.0 mm) the RS are strongly depending on the overlapping distance and there is no match between the RS profiles of the two samples. When the spot size increases, the RS profiles are matching again but not at the surface where tensile stresses are generated by the surface treatment.

9.3.4 Entire Residual Stress profile by hole-drilling

As it was done previously for the single-peened sample, one double-peened sample (1.16.1) was subjected to a double-drilling process to get an estimation of the RS profile through the thickness. The technique used was previously described in chapter 4.

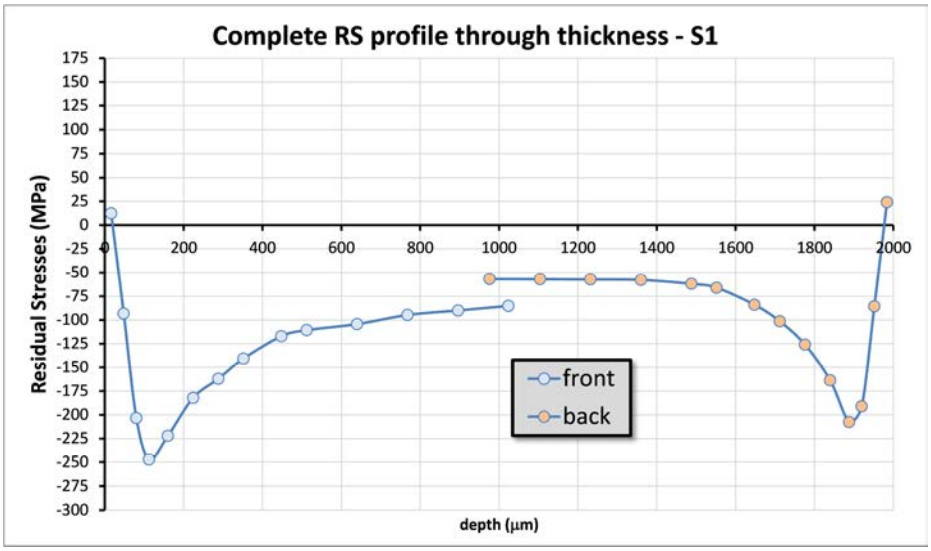

Fig. 9.34 Entire RS profile through thickness for a double-peened sample – S1

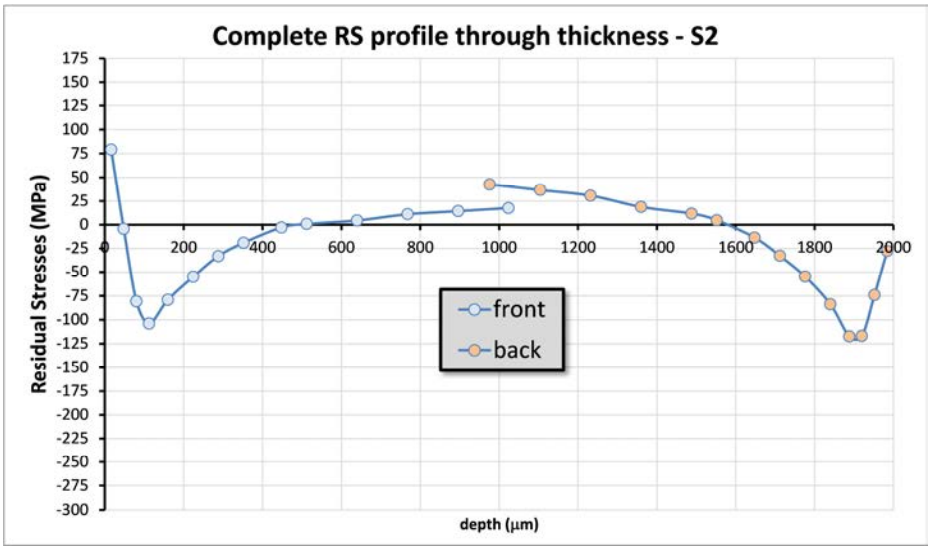

Fig. 9.35 Entire RS profile through thickness for a double-peened sample – S1

The RS profile measured for both faces of the double-peened sample for the S1 direction is shown in Fig. 9.34 and for the S2 direction in Fig. 9.35. As predicted from the measurements made on the front face only, the RS profile is mirrored by the profile obtained from the back face due to the second treatment. Also in this case (as for the case of the single peened samples) the two profiles should match in the middle of the graphs, i.e. in middle of the thickness. It's important to say that even in this case the two RS profiles were not measured in the same position of the sample. Furthermore, it's possible to see that profile measured from the back face starts at a value higher than the profile measured at the front face. It is worth noting that the calibration of this model was not based on the measurements made on thin aluminium samples, but as Toparli showed [5], the corrections of the coefficients used in the integral method for the hole-drilling, do not introduce any significant improvement, i.e. the data can be considered reliable.

9.3.5 Comparison between Single and Double-Peened – Constant Overlap

Now that three distinct points were compared for different parameters, an important comparison has to be done, between the single and double-peened samples RS profiles when the laser peening parameters were the same. The possible comparisons are numerous and only the relevant comparisons will be shown. The following graphs show the comparison between the single and double-peened samples for a given overlapping distance and at a given point. For each graph, all six samples (three single and three double-peened ones) will be shown. A direct comparison between two samples with same parameter but different peened areas is still possible, and this is heLSPed by using similar colours: green for 2.0 mm, red for 2.5 mm and blue for 3.5 mm.

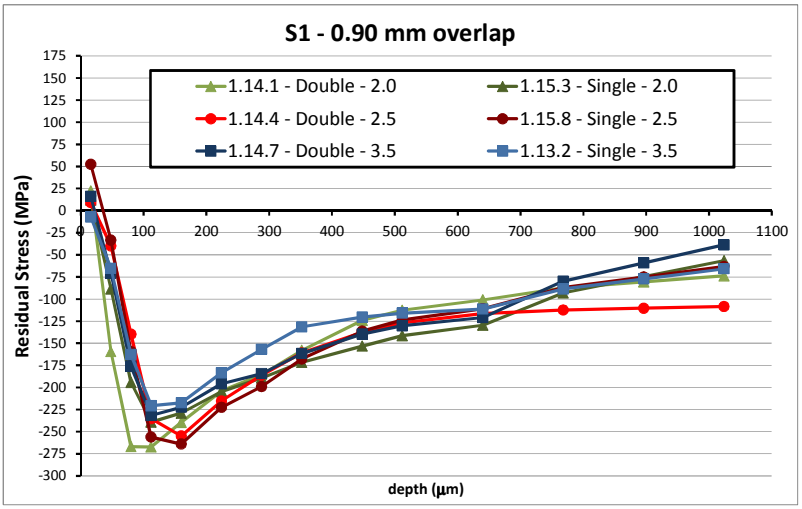

Fig. 9.36 Point 2 - RS profile through thickness for single and double-peened samples with different spot diameters and the same overlapping distance – 0.90 mm – S1

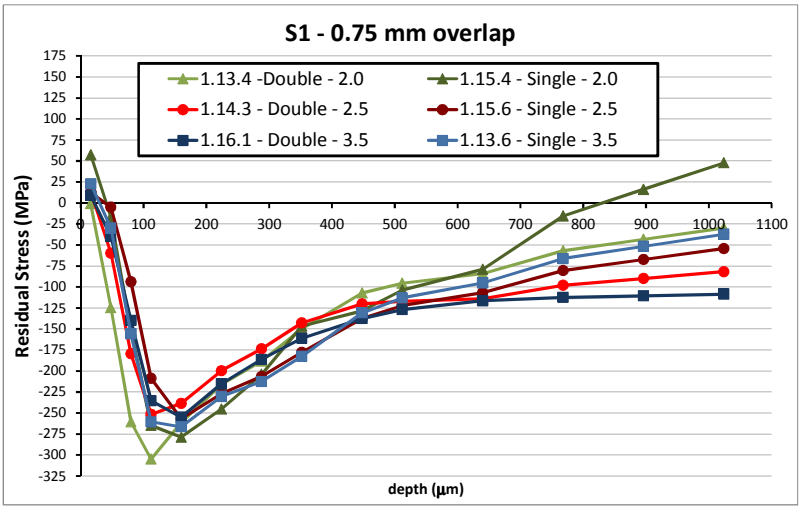

Fig. 9.37 Point 2- RS profile through thickness for single and double-peened samples with different spot diameters and the same overlapping distance – 0.75 mm – S1

Fig. 9.36 and Fig. 9.37 show the comparison of all the samples when the same overlapping distance is used for the S1 direction (the same conclusion can be done for the S2 direction). It is clear that few differences are present up to a depth of 600 µm. All the profiles start in tension and reach a peak in compression at around 180 µm depth with a value of 250 MPa. A difference is seen in the second half of the graph, after a depth of 600 µm. Generally, the double-peened samples tend to have a flat profile toward the middle of the thickness, which means that further compression is expected after a depth of 1000 µm,

which is confirmed as shown in Fig. 9.34. Furthermore, with the increasing of the spot diameter, the "tail" of the profiles tends to be smoother (see samples 1.13.4, 1.14.3 and 1.16.1 in Fig. 9.37). A similar comparison was made for point 4. In this case since the previous results have shown different behaviours between S1 and S2, both the stress directions will be reported:

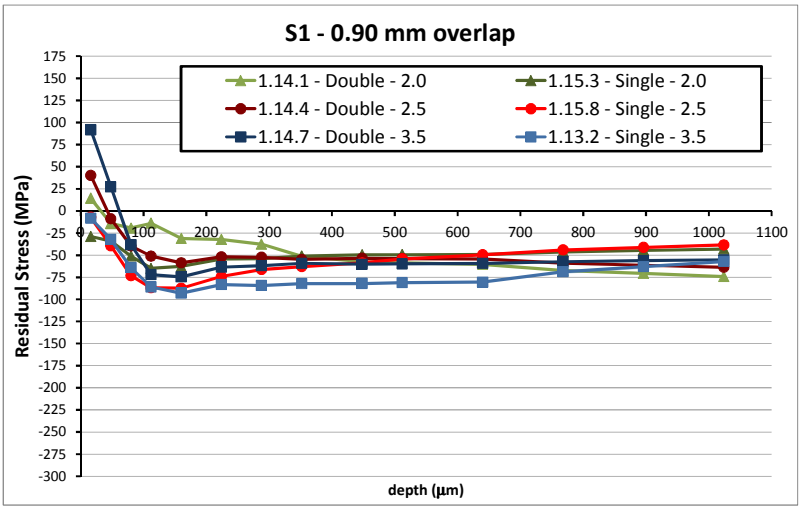

Fig. 9.38 Point 4 – RS profile through thickness for single and double-peened samples with different spot diameters and the same overlapping distance – 0.90 mm – S1

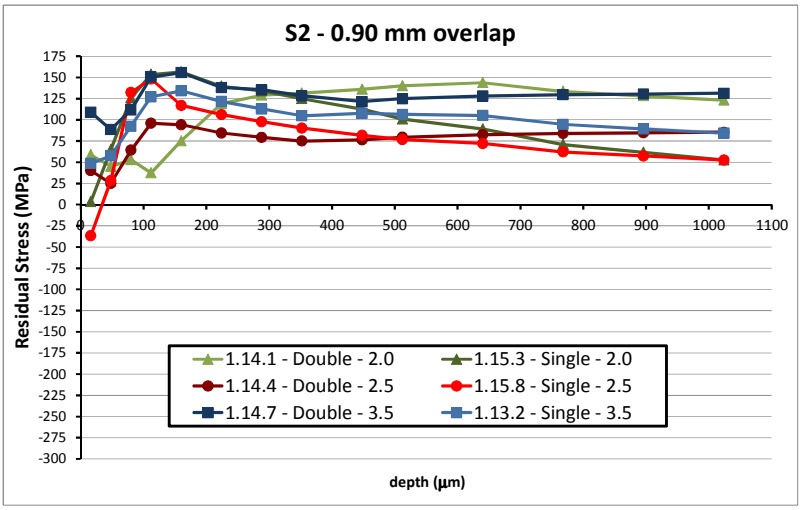

Fig. 9.39 Point 4 – RS profile through thickness for single and double-peened samples with different spot diameters and the same overlapping distance – 0.90 mm – S2

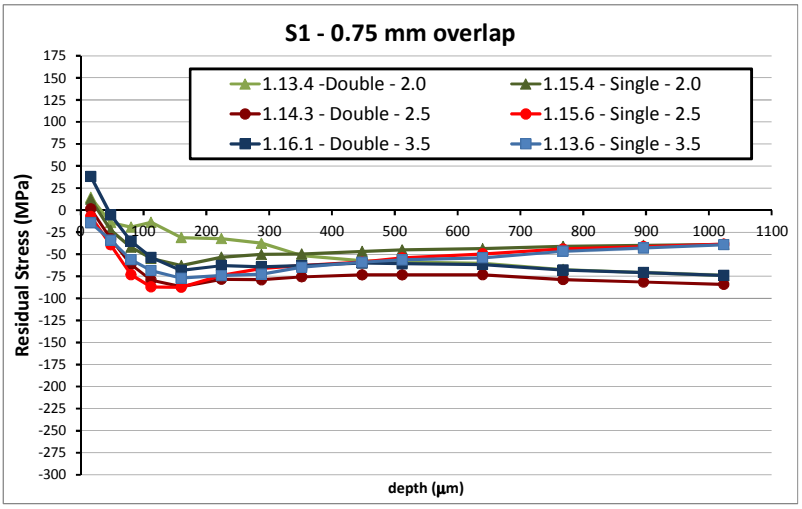

Fig. 9.40 Point 4 - RS profile through thickness for single and double-peened samples with different spot diameters and the same overlapping distance – 0.75 mm – S1

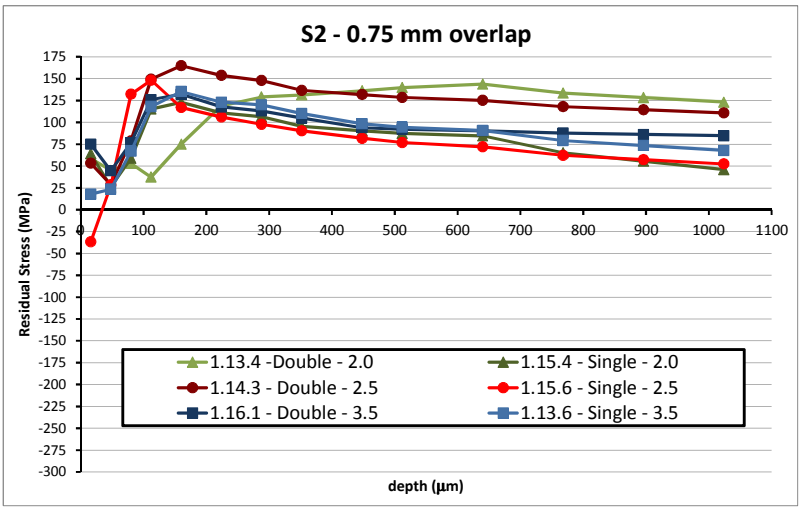

Fig. 9.41 Point 4 - RS profile through thickness for single and double-peened samples with different spot diameters and the same overlapping distance – 0.75 mm – S2

The four previous graphs show interesting elements for discussion. The trend is very similar for all the samples, no matter the size of the laser spot or the use of single or double peening. In general it is possible to see that with the two different overlap settings, the double-peened samples tend to have a tensile peak at the surface in the S1 direction which is higher than the single-peened samples which start in the compression region. Another aspect which highlights the differences between single and double-peened is at the "tails" of the RS profiles: the double-peened samples tend to have a smoother RS

profile in the mid-thickness (particularly visible in Fig. 9.40). In S2 similar conclusions can be valid: the tensile peak at the surface for the single-peened sample is lower than the double-peened and the stresses tend to be steeper in the mid-thickness. Finally, by increasing the spot size (no matter if single or double-peened) the general trend shows that the peaks both in compression (for S1) and in tension (for S2) increase.

The following graphs show the same comparison for point 5:

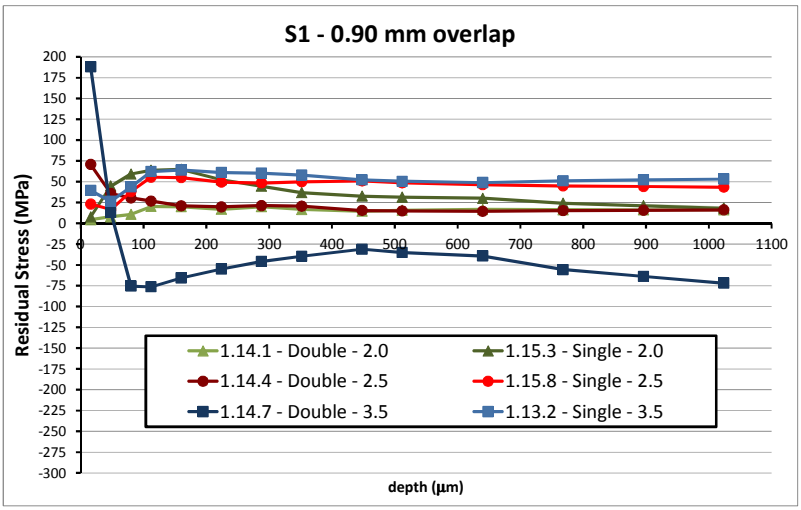

Fig. 9.42 Point 5 - RS profile through thickness for single and double-peened samples with different spot diameters and the same overlapping distance – 0.90 mm – S1

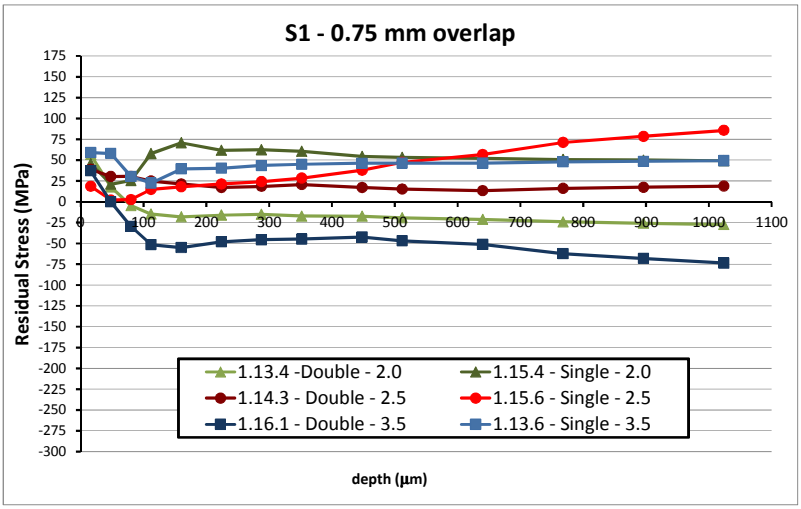

Fig. 9.43 Point 5 - RS profile through thickness for single and double-peened samples with different spot diameters and the same overlapping distance – 0.75 mm – S1

In Fig. 9.42 and Fig. 9.43 both 0.90 and 0.75 mm overlapping are reported for S1 directions only. While with an overlapping of 0.75 mm both the single and double-peened show a constant RS profile in tension, with an overlapping of 0.90 mm the behaviour of the single and the double-peened samples are opposite. While the single-peened samples tend to have a RS profile in the tensile region, the double-peened samples have a RS profile in compression and the values (in magnitude) are similar: around 40-60 MPa.

9.3.6 Comparison between Single and Double-peened – Constant spot diameter size

One last comparison presented in this dissertation is made between different samples with the same spot size and different overlapping distances.

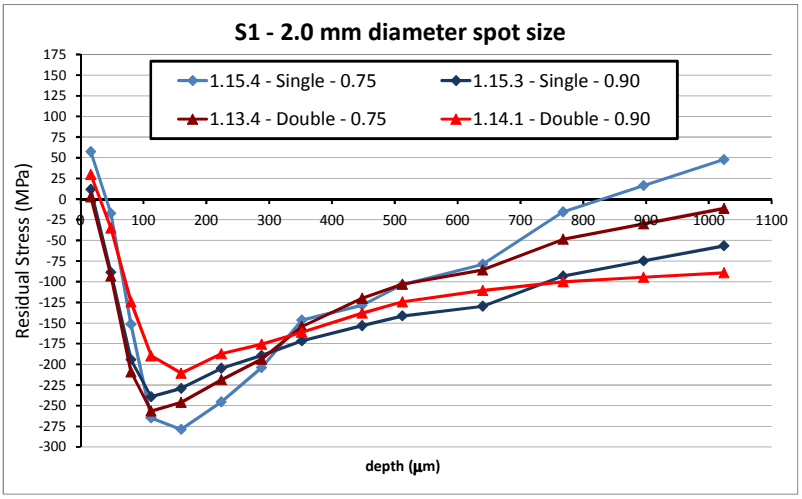

Fig. 9.44 Point 2 – S1 RS profile through thickness for single and double-peened samples with different overlapping distance and same spot diameter – 2.0 mm

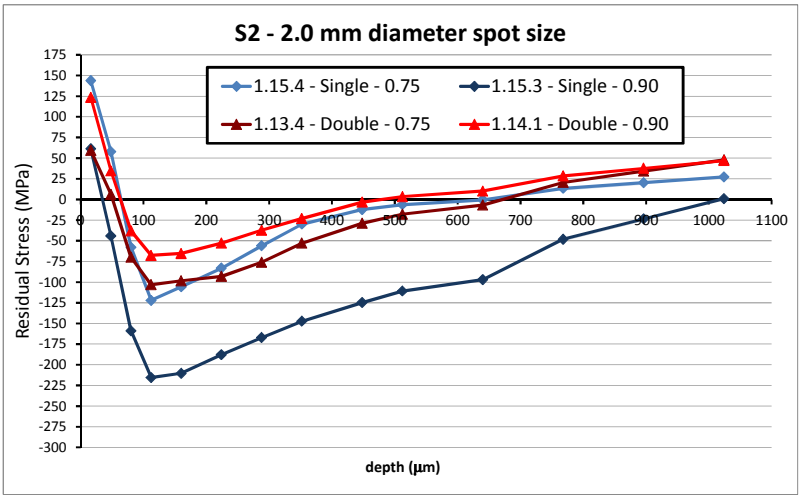

Fig. 9.45 Point 2 – S2 RS profile through thickness for single and double-peened samples with different overlapping distance and same spot diameter – 2.0 mm

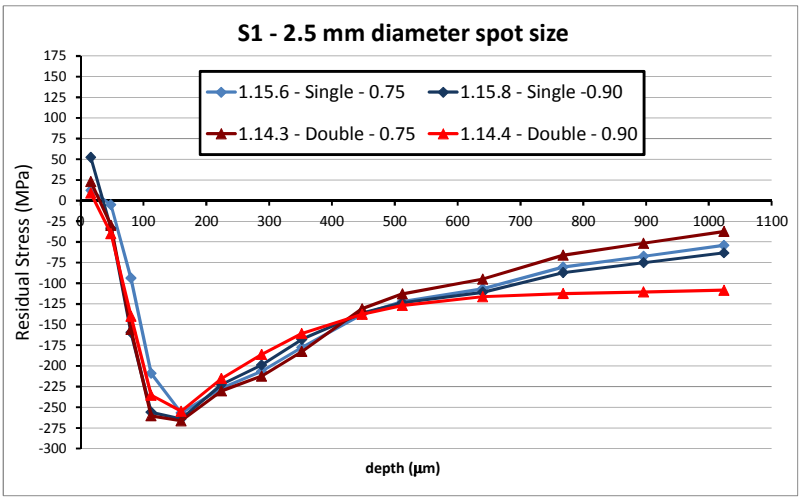

Fig. 9.46 Point 2 – S1 RS profile through thickness for single and double-peened samples with different overlapping distance and same spot diameter – 2.5 mm

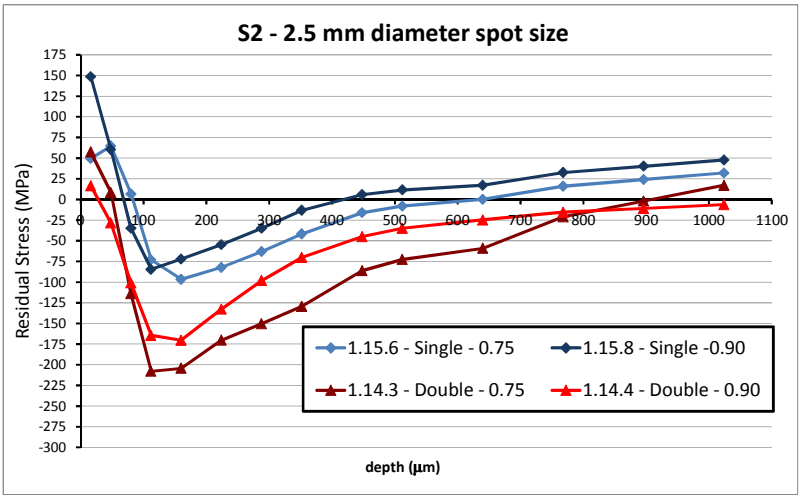

Fig. 9.47 Point 2 – S2 RS profile through thickness for single and double-peened samples with different overlapping distance and same spot diameter – 2.5 mm

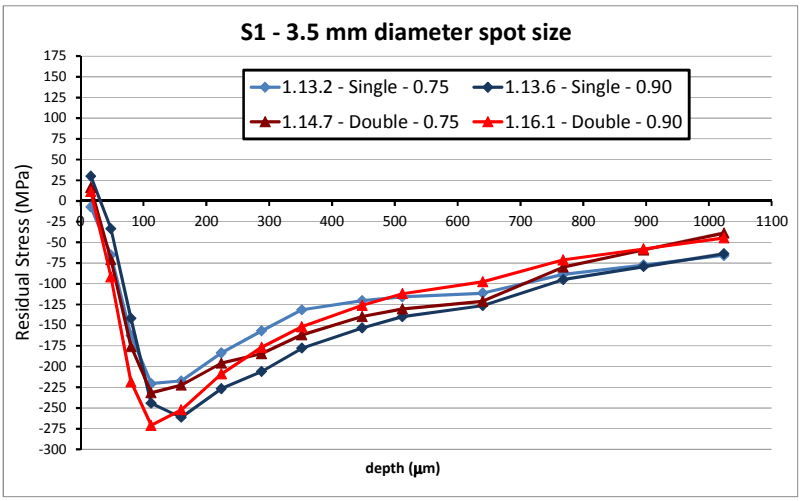

Fig. 9.48 Point 2 – S1 RS profile through thickness for single and double-peened samples with different overlapping distance and same spot diameter – 3.5 mm

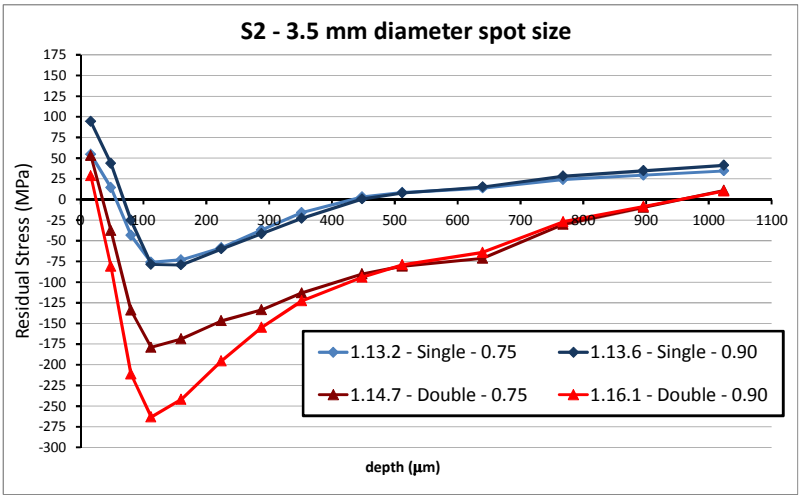

Fig. 9.49 Point 2 – S2 RS profile through thickness for single and double-peened samples with different overlapping distance and same spot diameter – 3.5 mm

In Fig. 9.44, Fig. 9.46 and Fig. 9.48, the measurements made in the S1 direction at point 2 for all the samples are presented, according to spot diameter. Similarly Fig. 9.45, Fig. 9.47 and Fig. 9.49 show the RS profile in the S2 direction. It's possible to see from the graphs that in the S1 direction the overlapping distance is not a as important parameter as the spot diameter. All the RS profiles start in the tensile region at around 50 MPa and a compressive peak is reached around 180 µm and the values are lying between –200 and –250 MPa. Approaching the middle thickness, the RS profiles are still in compression (beside sample 1.15.4) and the values are very similar around –50 MPa. In S2 though, the difference between the single and double-peened samples is more noticeable and in particular it shows that by increasing the spot diameter, the double-peened samples present a deeper compressive RS than the single peened and simultaneously decrease the tensile peak at the surface.

9.4 UPM Samples – BESSY II results

As described already in chapter 4, the UPM thin samples were also measured at the BESSY II synchrotron at the EDDI beamline which uses the Energy Dispersive X-ray

Diffraction (EDXRD) technique. For this experiment there are two important characteristics:

1. The measurement of the unstressed lattice parameter d_0 is not necessary;
2. Several diffracting peaks are detected, each of them coming from a different depth;

The result is that the experiment with the EDDI instrument is very fast and gives as the result a RS profile up to 500 μm in depth. The samples subjected to the measurements were sample 2.7 and 2.10 supplied by UPM. Laser parameters can be found in Table 9.1.

9.4.1 Sample 2.7

The schemes of the measurement points can be found in the following pictures:

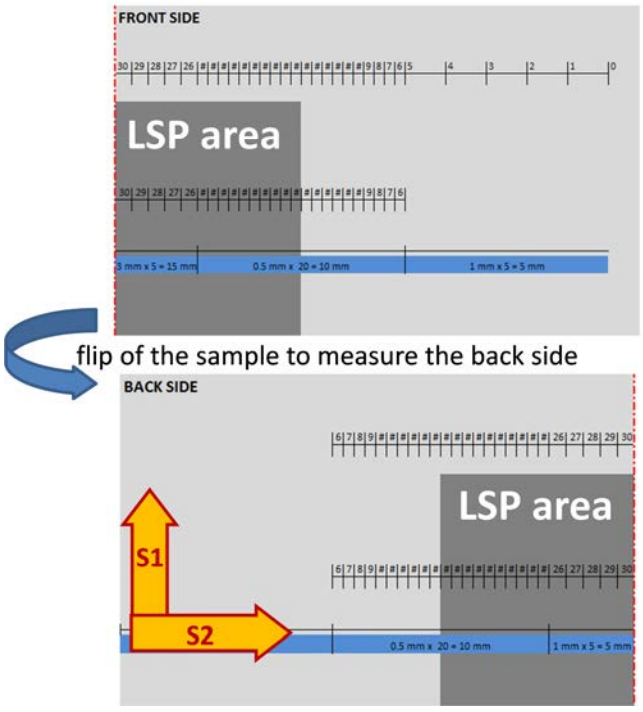

Fig. 9.50 measurement patterns for the front and back side of sample 2.7

As is possible to see from Fig. 9.50, the measurement started outside the peened area and was carried out up to half of its width for both the front and back face. A further line was added outside the peened area, before its start, since has been shown previously, the

behaviour of the RS in S1 and S2 directions are completely different. Before showing the final results, a generic RS obtained inside and outside the peened area is shown. This RS profile is compared with the ICHD measurements:

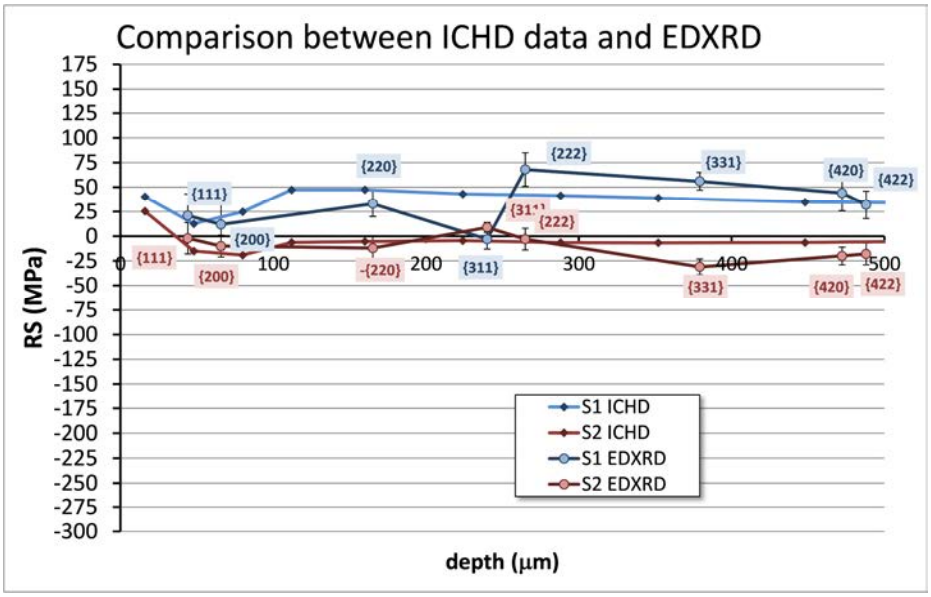

Fig. 9.51 comparison between the ICHD and EDXRD data, outside the peened area

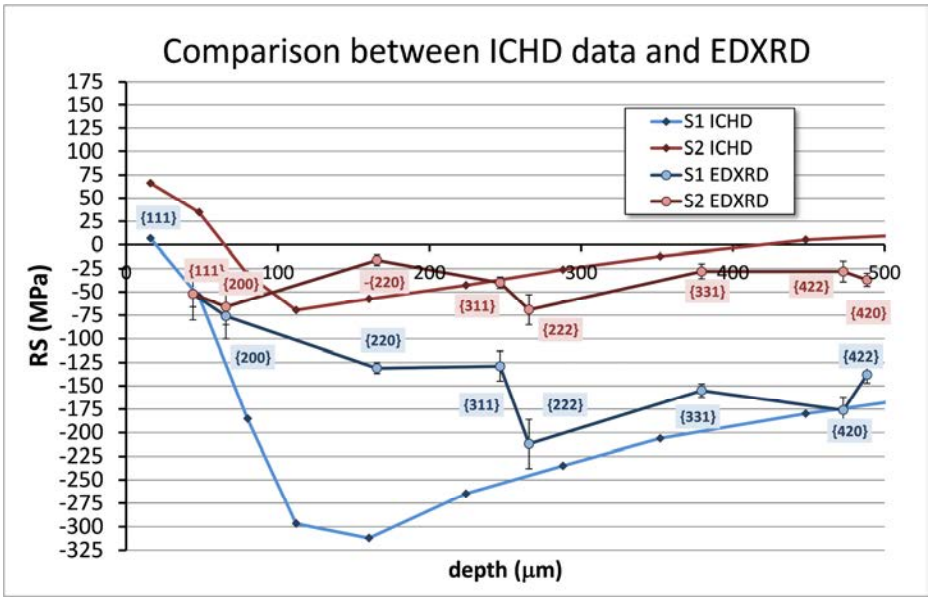

Fig. 9.52 comparison between the ICHD and EDXRD data, inside the peened area

As it is possible to see from Fig. 9.51 and Fig. 9.52, the data coming from EDDI are scattered as it was expected and each point is labelled with the referred lattice plane. It is

also worth noting that the ICHD data are distributed similarly to the average of the EDDI data even though in Fig. 9.52 it is possible to see that the S1 components measured with ICHD show deeper compressive RS than the data collected with EDDI.

Since, as shown previously, the data collected at the EDDI beamline are scattered, a function that smoothed the data was firstly calculated and then all the smooth functions were used to create a 2D map of the RS vs. depth which are shown here:

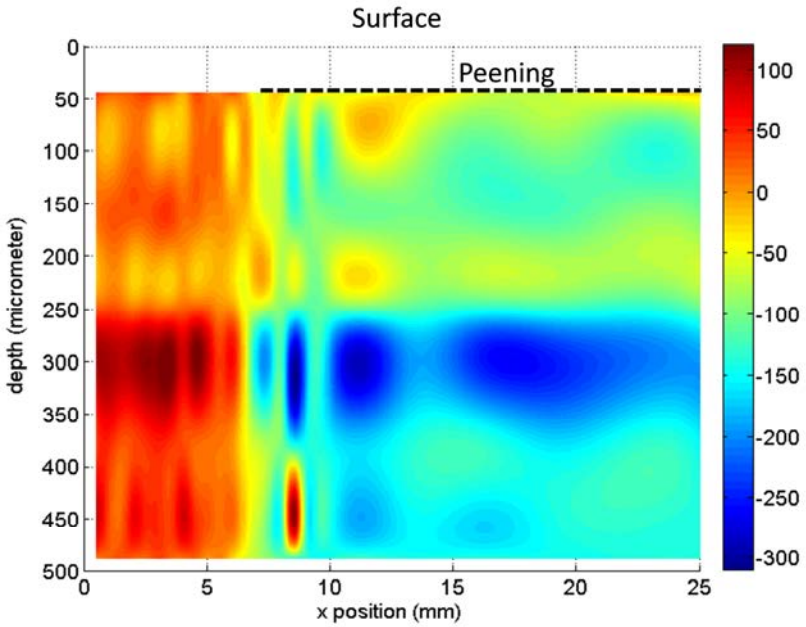

Fig. 9.53 RS map along the thickness, S1 direction of the stress

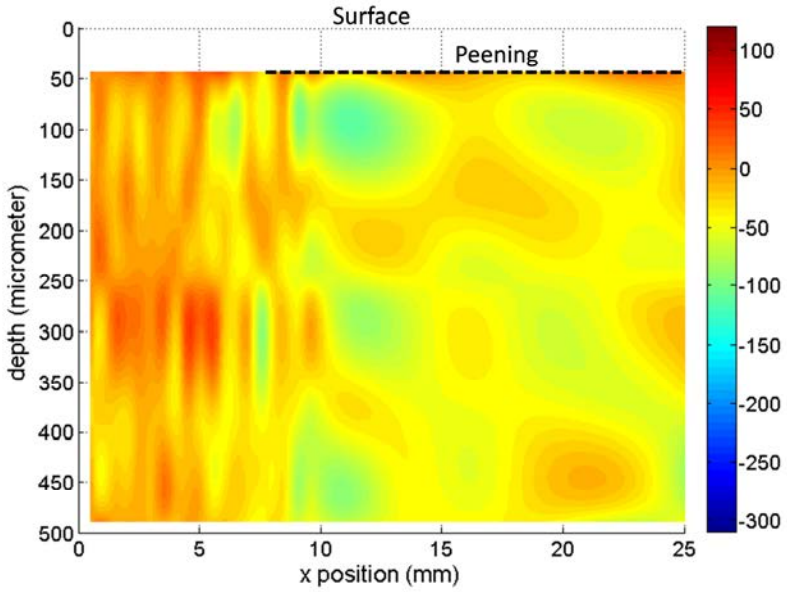

Fig. 9.54 RS map along the thickness, S2 direction of the stress

As it can be seen in Fig. 9.53 and Fig. 9.54, the EDXRD data confirm the hole-drilling results. In particular, along the S1 direction through the thickness of the peened area compressive RS are present even if the distribution is slightly different from the one measured with the ICHD. Outside the peened area, the stresses are in tension and it confirms the measurements made previously at point 5 (see Fig. 9.14 for example) even if in this sample the stresses look higher, up to 100 MPa (against 60 MPa measured in previous samples). In the S2 direction the same conclusion can be outlined: through the thickness of the peened area the stresses are compressive and their value is lower than in the S1 direction; similarly outside the peened area, where the stress are in tension.

The sample was then rotated 180° in order to measure the RS through the thickness starting from the back face. In this case some strange results were obtained as shown in the following pictures:

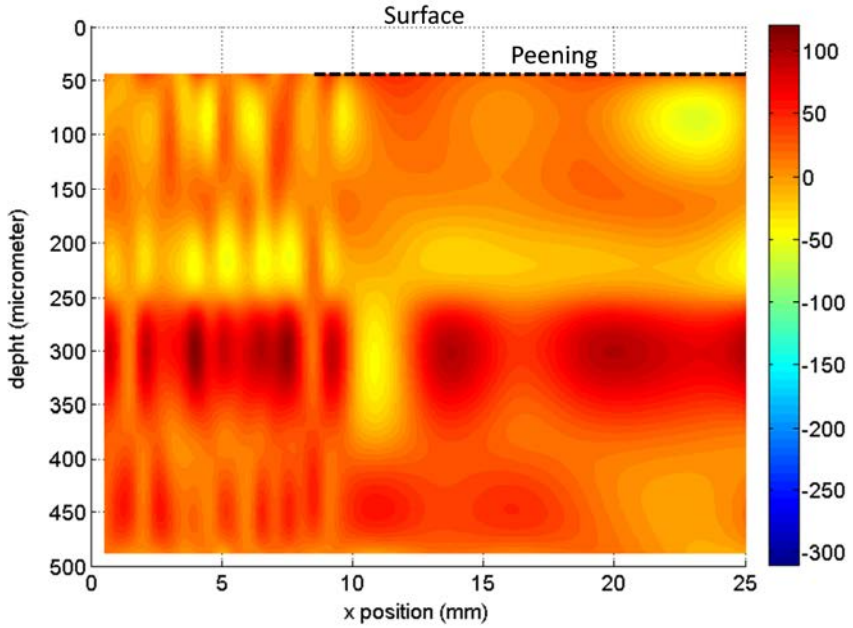

Fig. 9.55 RS map along the thickness, S1 direction of stress

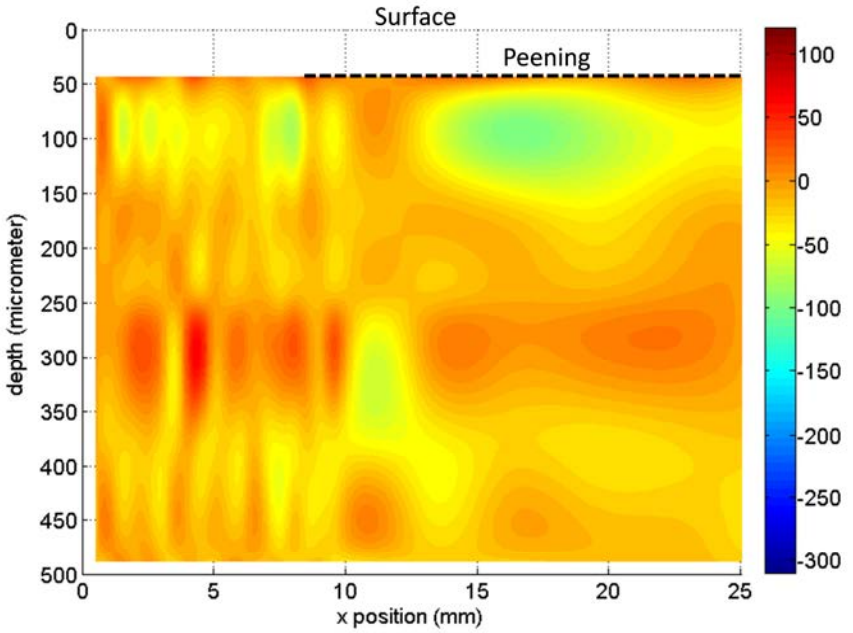

Fig. 9.56 RS map along the thickness, S2 direction of stress

Both graphs do not agree with the previous results. In particular, in the S1 direction there is compressive RS up to 200 μm which does not go beyond 50 MPa and then a peak in tension up to 60 MPa. Furthermore it is impossible to distinguish where the laser

peened area is located from the graph, due to the fact that the whole profile seems to be in compression. Similarly in the S2 direction where the stresses lie in a range of 0 to –40 MPa. A separate ICHD test that starts from the back face shows that the RS profile has a similar behaviour of the front face RS as shown in the picture below:

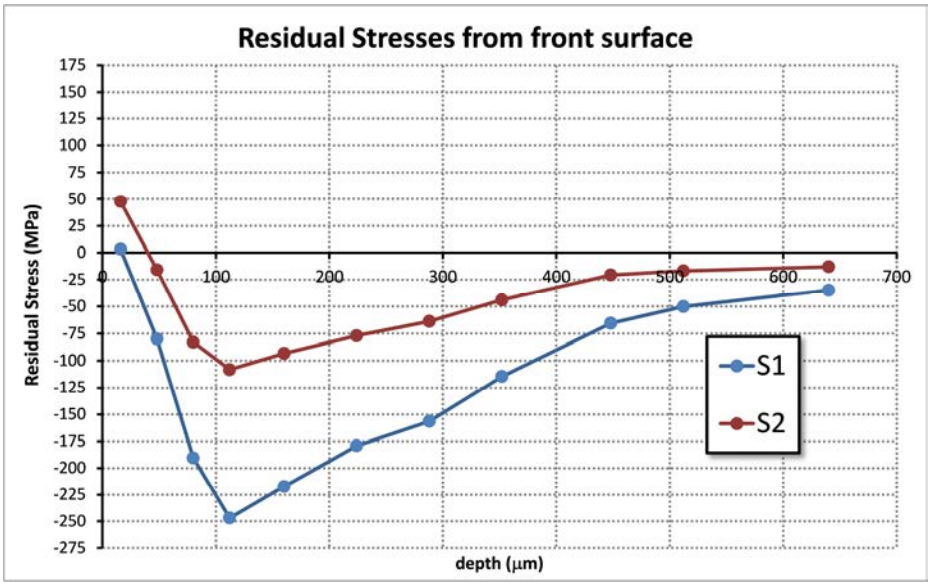

Fig. 9.57 ICHD results from the front face

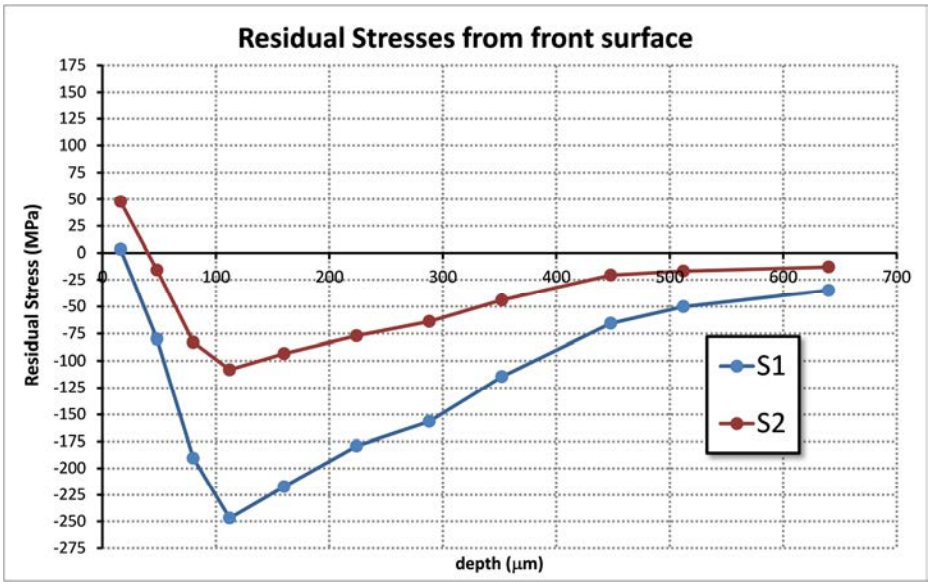

Fig. 9.58 ICHD results from the back face

Fig. 9.57 and Fig. 9.58 show the RS profile measured from the front and back faces. It is possible to see how the profiles are different in values: in particular from the back face the maximum value reached by the RS profile is –150 MPa against the –250 MPa reached by measuring from the front face. This is a behaviour that was already seen in the total RS profile measured in the double-peened samples (see Fig. 9.34) even though in this case the difference between the two minimum values is higher than before (–100 MPa). We believe that this difference is due to the sequence of peening: as the second peen treatment is applied after the first one, the shock waves propagating through the thickness are deteriorating the previous RS profile (generated from the front surface treatment).

The experiment was also conducted outside the peened area, before the LSP strip starts (see Fig. 9.50):

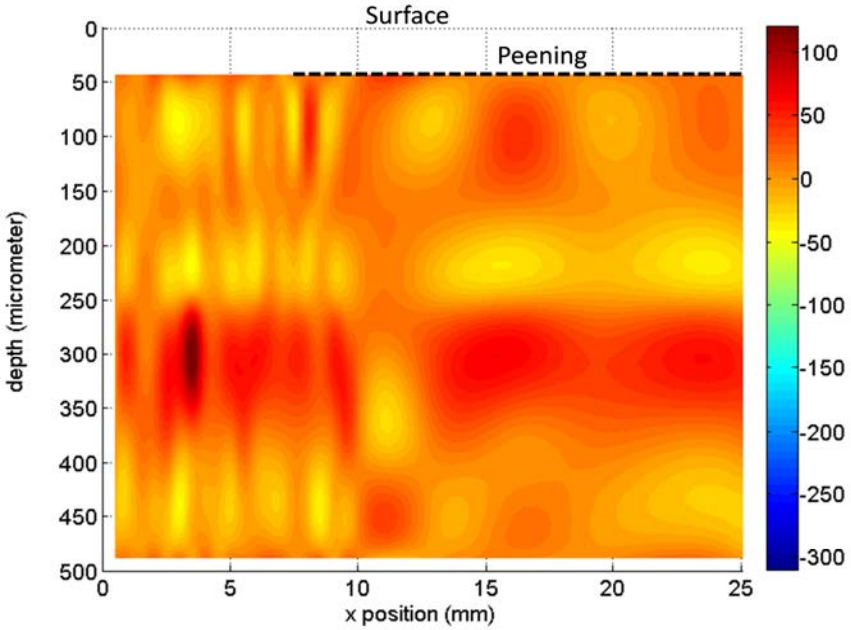

Fig. 9.59 RS map along the thickness, S1 direction of stress

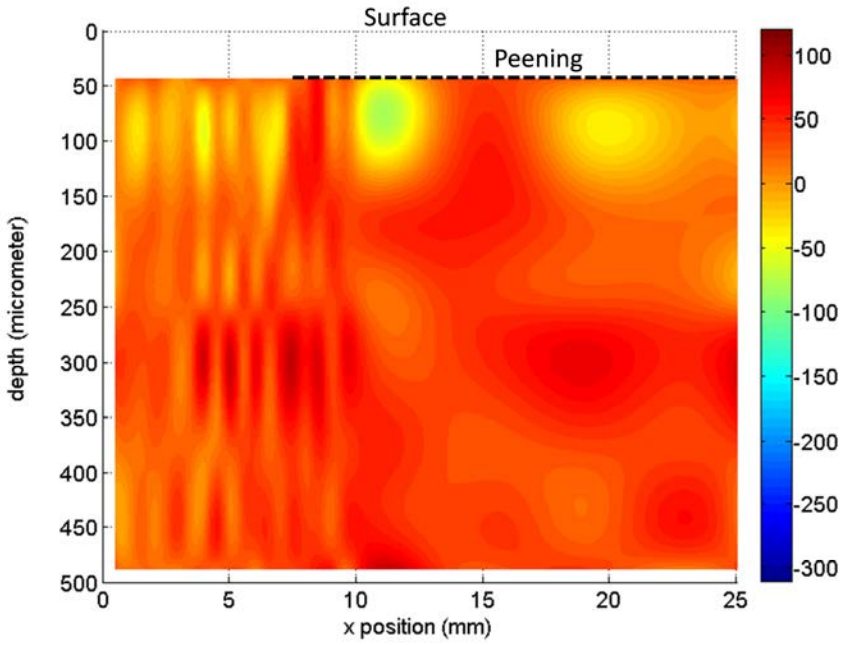

Fig. 9.60 RS map along the thickness, S2 direction of stress

The results again are confirming the ICHD results (see Fig. 9.12 and Fig. 9.13 as reference): in the S1 direction outside the peened area compressive RS are present and they are constantly distributed through the thickness even if there is a tensile peak around 300μm which is not expected and is believed to be one of the limitation of EDDI beamline because only one lattice plane is reflecting at that particular depth. Similarly it happens in the S2 direction where the RS are in tension.

9.4.2 Sample 2.10

The measurements scheme used for the second sample can be found in the following picture:

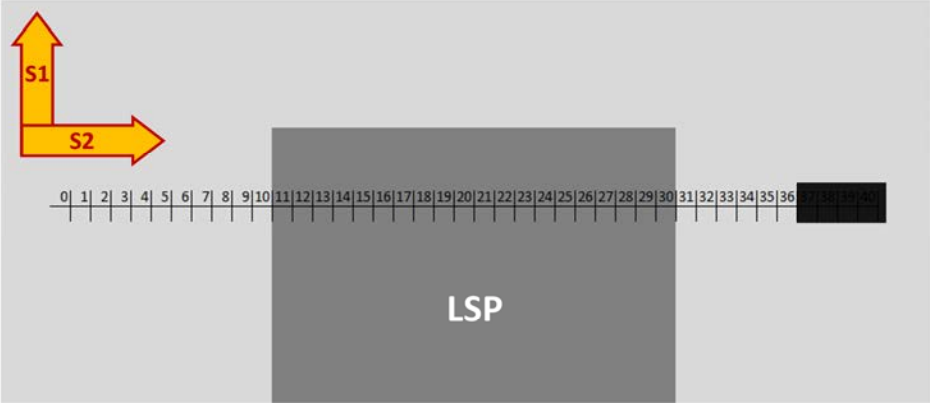

Fig. 9.61 Scheme of the measurement points for sample 2.10

As can be seen in Fig. 9.61, the measurements were made for the entire width of the laser peened area and some points were also taken outside it. Unfortunately, due to lack of time was not possible to measure the RS outside the peened area as was done for sample 2.7. The following pictures show the RS results:

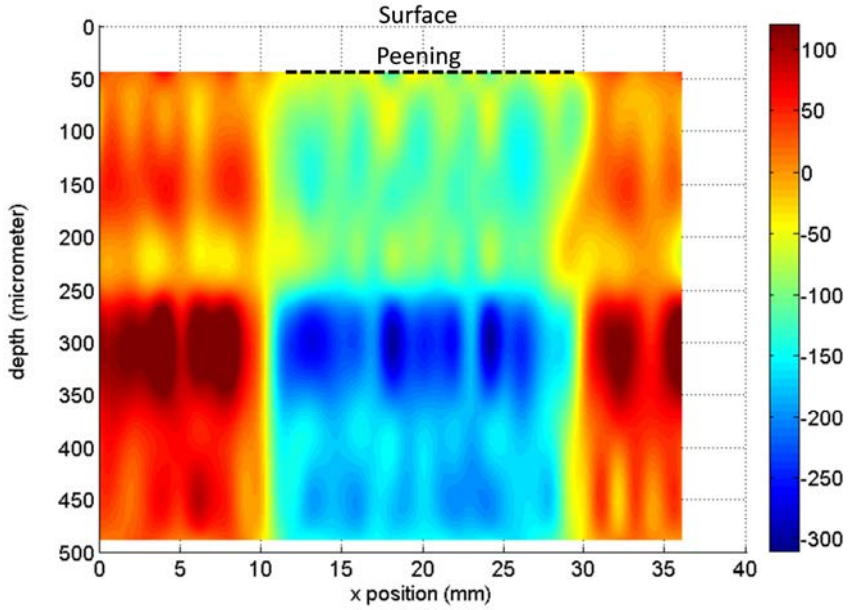

Fig. 9.62 RS map along the thickness, S1 direction of stress

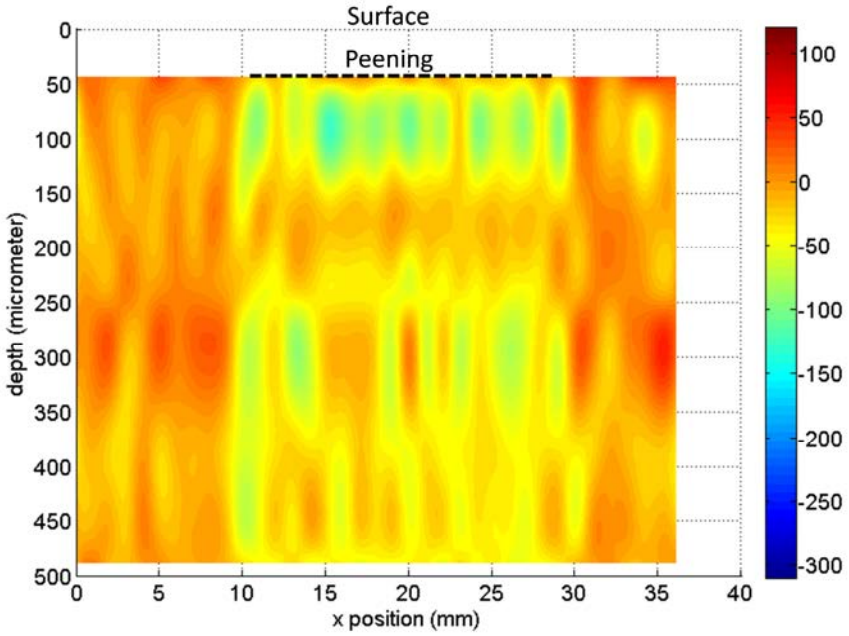

Fig. 9.63 RS map along the thickness, S2 direction of stress

The results in Fig. 9.62 and Fig. 9.63, show that the measurements at EDDI confirm the ICHD results. In the S1 direction it is possible to see how the RS are in compression where the sample was peened and how the tension is distributed outside the peened area. Similarly along S2, the RS are still compressive through the thickness of the peened area and outside of it the stresses are in tension but both of them are lower in module than the stresses in the S1 direction.

To have a second measurement of the back face for the sample 2.10, surface X-ray measurements were carried out and the results are reported here for both the front and back face:

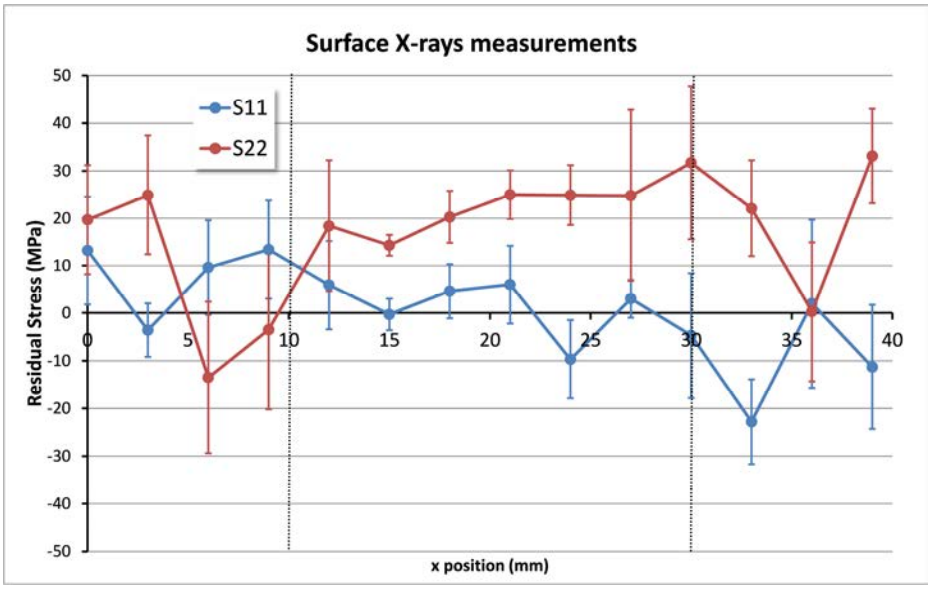

Fig. 9.64 RS measured with XRD – front face

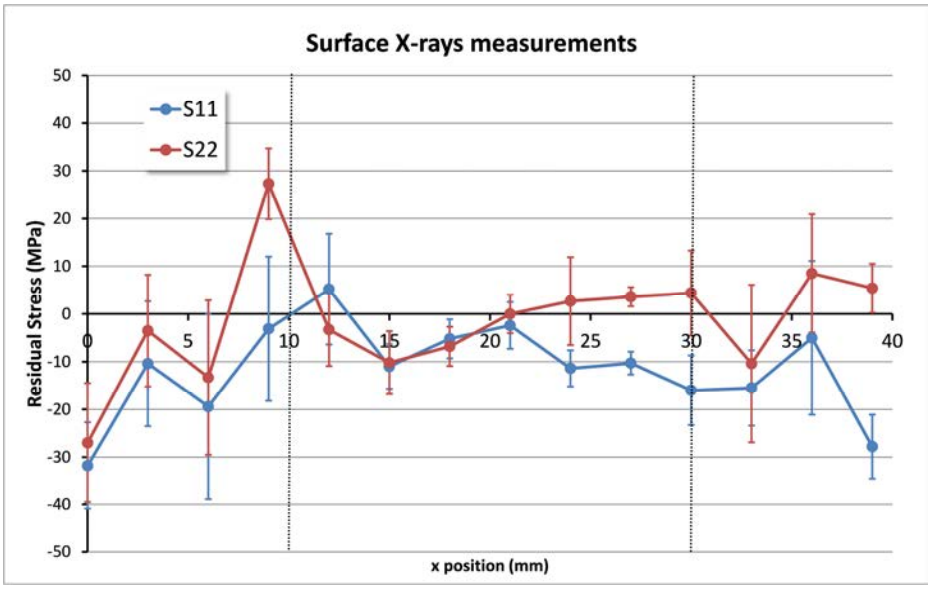

Fig. 9.65 RS measured with XRD – back face

As it is possible to see in Fig. 9.64 and Fig. 9.65, the two surfaces show a different distribution of RS. At the front face, the RS measured at around 40 μm depth (which is considered the depth of the measurement for XRD technique in aluminium) are completely in tension with a value not higher than 30 MPa and similar to the S2 stresses but with lower values. On the other face of the sample, the measured stresses are in compression region, even if within a region of 0-10 MPa.

To conclude this section it is worth noting that some preliminary results on the fatigue tests of these sample were reported in [6] and the conclusion is that the crack growth slows down before entering the LSP strip and then speeds up again which is not the behaviour which was expected and which led to the double side treatments. Further investigation is ongoing.

9.5 Toshiba thin double-peened sample – APS results

The sample T1, supplied by TOSHIBA, is another thin aluminium alloy AA2024-T351 double-peened sample that was the object of RS measurements. In this case, the 1-ID beamline at the Argonne Photon Source (Angle Dispersive XRD – ADXRD) in USA was used to measure the RS profile through the entire 2 mm thickness. As described in chapter 4, conical slits were used at the APS allowing us to collect data with a good spatial resolution and through the entire thickness. A picture of the sample is shown here:

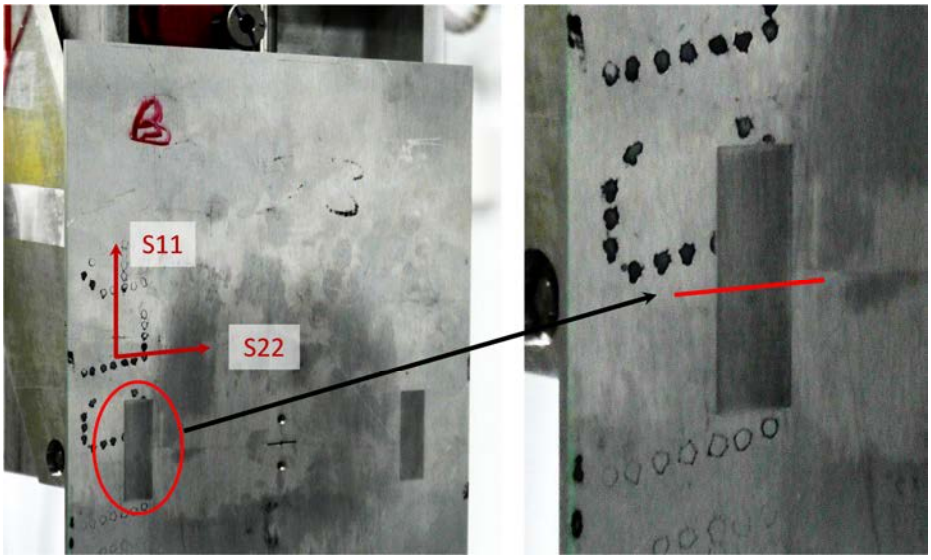

Fig. 9.66 picture of the Toshiba sample with two LSP areas and a magnification of the one which was measured at APS. The line indicates where the measurements were taken

Furthermore, during the measurements a misalignment occurred and was not possible to calculate precisely the position of the entering surface[1] once the sample was flipped with the purpose of calculating the strains to eliminate the pseudo-strains during the post-processing of the data. In order to get a rough estimation of the distribution of the RS close to the back surface, an ICHD measurement was carried out and the data are shown in the next graph:

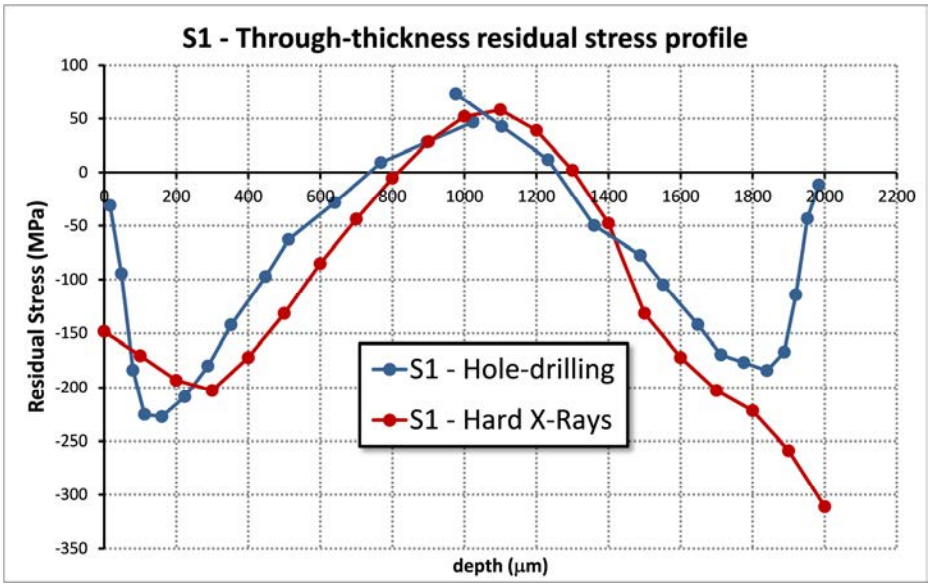

Fig. 9.67 RS distribution comparison between the ICHD and ADXRD

As can be seen in Fig. 9.67, the RS profile close to the back surface is close to 0 MPa if we consider the ICHD measurements, but it is more than –300 MPa if we consider the ADXRD data. This value is unlikely since at the surface a low value of RS is expected due to the presence of a clad layer on top of both surfaces. The cladding is a thin layer that is present to prevent the AA2024 from corrosion. If the RS profile of the ADXRD was correct,

[1] The entering surface is considered the first surface of the sample that the beam encounters during the test. During the first round of measurement, the sample was set up with the front surface facing the beam directly (while the back surface was facing the detector). Once the sample was flipped, the entering surface was the previous back surface. For this reason the data collected were not sufficient to calculate the exact position of the back surface, nor to eliminate the pseudo strains.

it would have meant that the yield strength of the clad layer (i.e. pure aluminium) was at least 300 MPa, while, as reported in [7], the yield stress of the clad layer is 110 MPa.

To better visualize the entire RS profile, the first 4 points measured close to the front face of the sample (on the left side of Fig. 9.67) were pasted on the right side of the back face. The results are reported in next graph:

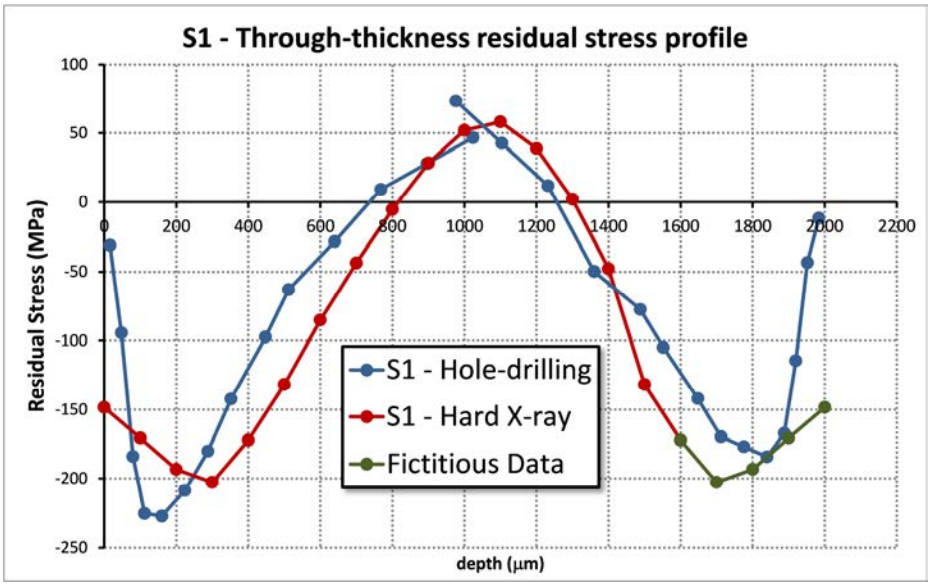

Fig. 9.68 New RS profile

Again, the points after a depth of 1600 µm are a fictitious adjustment of the RS profile and they won't be taken into consideration during the subsequent analysis.

The adjusted data were then smoothed using MATLAB software in order to obtain a complete RS 2D and 3D surface rather than the 1D profile presented up to now.

Here follow the results:

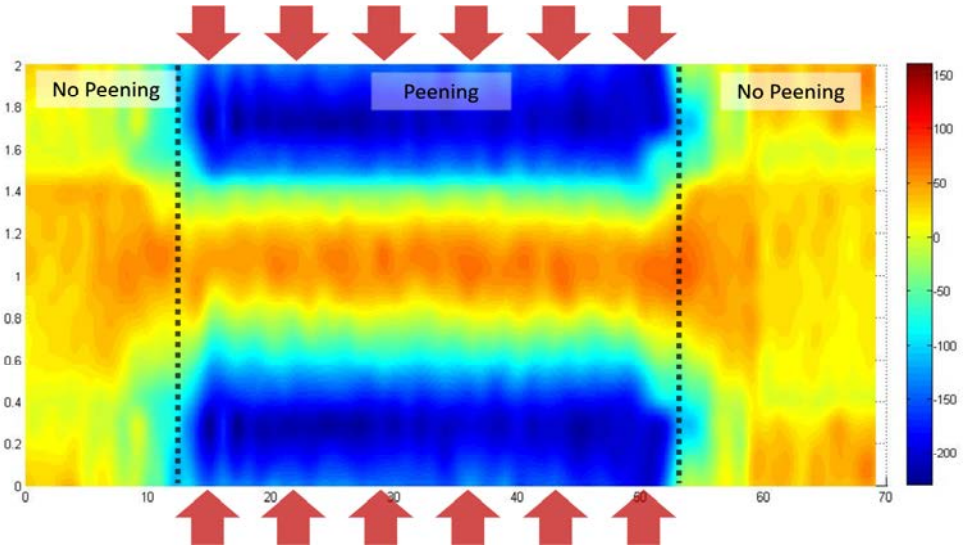

Fig. 9.69 RS 2D plot– S1 direction of stress. X axis represents the length of the area subject of the experiment in mm while y axis represents its width which is the entire thickness (2 mm). The colours indicate the quantity of RS according with the coloured legend on the right hand side

Fig. 9.69 shows the 2D map of the through-thickness RS in the S1 direction. On the left side it is possible to see the variation of the thickness depth, from 0 to 2 mm and the red arrows indicate the action of the peening treatment, perpendicular to the sample surfaces. To allow a perfect view of the distribution of the RS, the picture is not to scale. Considering only the bottom side of the picture, it is possible to see how the compressive RS are distributed close to the surface. In this area the values of the RS are around –50 to –100 MPa while at a depth of 200 µm a peak in compression is reached with a value of -250 MPa. The RS then increase to tension region and they reach a peak around 50-60 MPa in the middle of the thickness. The tensile value is homogenous along the entire peened area. Outside the peened area, an homogenous distribution of tensile stresses is present with an average value <50 MPa. It is also possible to notice that, where the maximum value of compressive RS is reached in the peened area, outside the peened a value around 0 MPa is reached.

A similar description can be done for the RS 2D map in the S2 direction:

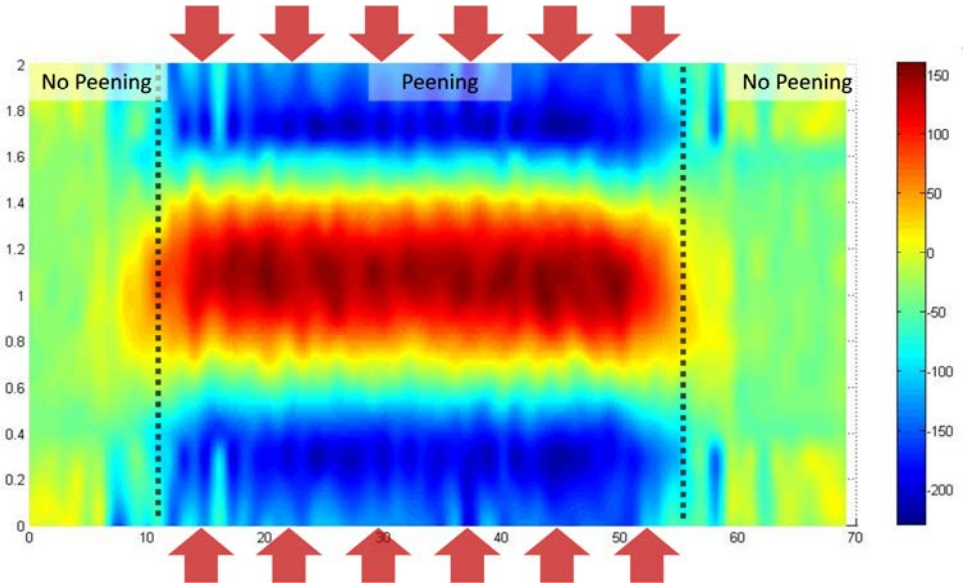

Fig. 9.70 RS 2D plot – S2 direction of stress. X axis represents the length of the area subject of the experiment in mm while y axis represents its width which is the entire thickness (2 mm). The colours indicate the quantity of RS according with the coloured legend on the right hand side

In Fig. 9.70 the RS distribution is reported in a 2D map for the S2 direction. Again, close to the surface a compressive region is present as expected. The peak value is close to the one reached in the S1 direction in this case. In the middle of the thickness, a core of tensile stress is present with a peak value >100 MPa. Outside the peened area, the RS are mostly in compression with a value around –50 MPa and close to the surface this value goes up to 0 MPa.

In order to give the reader a better visualization on how the RS are distributed through the thickness, the following 3D maps of the RS distribution were plotted for both the stress directions:

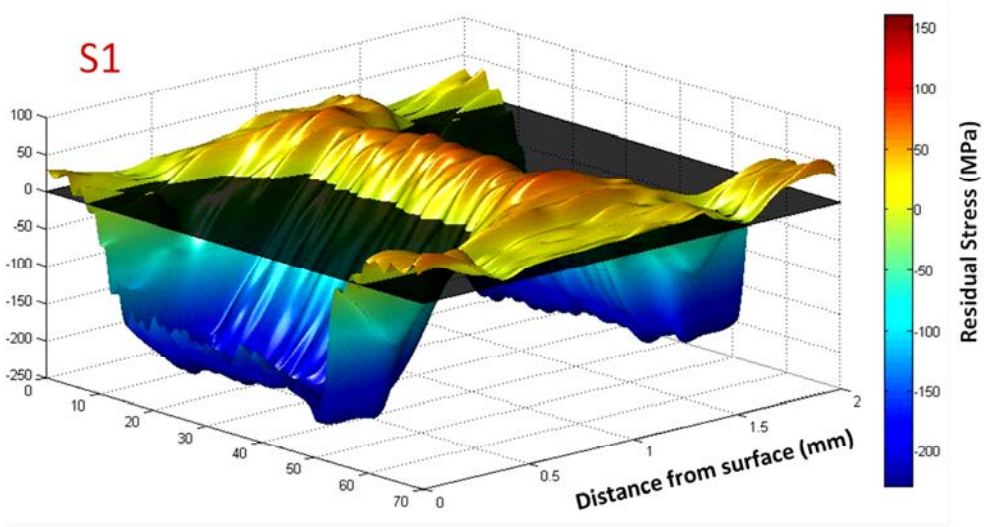

Fig. 9.71 RS distribution in a 3D map – S1

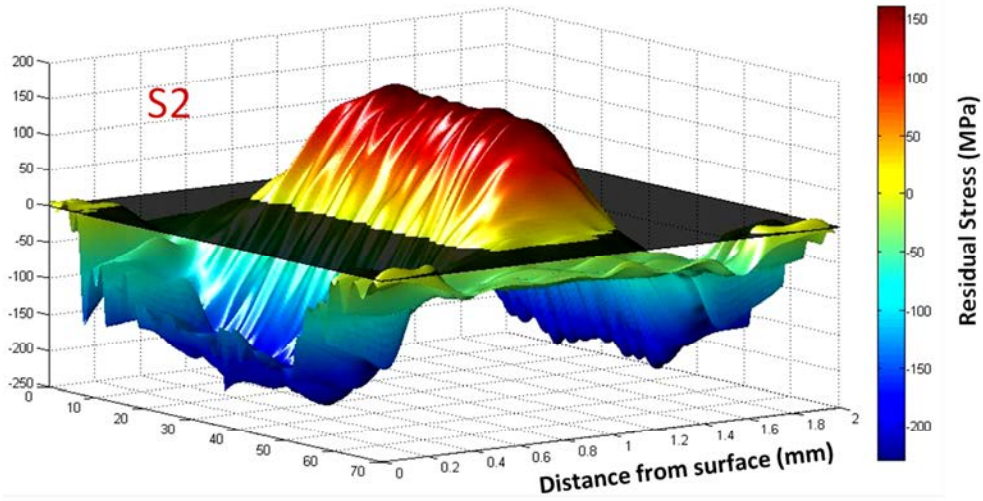

Fig. 9.72 RS distribution in a 3D map – S2

Fig. 9.71 and Fig. 9.72 were presented to give a better visual comprehension of the distribution of the RS within a thin sample when both faces were laser peened. The black semi-transparent planes indicate the 0 MPa level: in this way all the stresses above this

level are in tension and all the stresses below this plane are in compression. Since both graphs share the same legend, it is possible to see how easily the tensile stresses in the middle of the thickness in the S2 direction are higher than the ones in the S1 direction and similarly, the compressive RS in the S1 direction are higher than the RS in the S2 direction.

9.6 Conclusions

In this chapter the RS generated by a double-side treatment on thin aluminium AA2024 samples were measured and compared. The parameters taken into account were the overlapping distance and the spot diameter size for all the UPM-peened samples. After the previous discussions these are the final conclusions:

1. the RS generated by a two-sided treatment are very similar to the ones generated by a single surface treatment if we consider the result up to 700 μm in depth from the surface; differences are present after this depth up to 1 mm;
2. the compressive peak reached by the double-peened sample is similar to the single-peened one and it is around –250 MPa at a depth of 180 μm;
3. outside the peened area, the double-peened samples show a RS trend similar to the single-peened samples: along the S1 direction there is still compression while along S2 there is tension. In the double-peened sample though, the RS tends to stay constant at a certain value of tension rather than showing a linear decay. This is mostly due to balance the compressive RS in the thickness;
4. alongside the peened area the RS along the S1 direction are in tensile and constant along the thickness while in the S2 direction the stresses are close to 0 MPa;
5. along the S1 direction the double-peened samples show a deeper compressive RS profile in most cases: in particular this phenomenon is more evident when the

spot diameter size is smaller while when its size is increased, both double and single peened samples tend to present the same RS distribution;

6. along the S2 direction the differences between the single and double-peened samples are more evident: while the single peened samples do not show any significant difference when the spot diameter is increased, the double-peened samples are positively affected by the larger spot size since the RS profile lies entirely in compression;
7. the sequence of the peening treatment might affect the RS profile since two RS profiles measured on the opposite faces of the same sample show similar RS trends but different values, in particular one of them presents lower (in magnitude) RS profiles; unfortunately this research needs more investigations since the sequence of the peening was not disclosed by the suppliers;
8. the results coming from the EDXRD show that the tension outside the peened area is distributed up to 10 mm far away from the peened area;
9. TOSHIBA samples present both compression and tension through the thickness; this is due to a different use of the laser peening parameters; at the surface compressive RS is present; this different distribution is reflected also in the RS distribution aside the peened area as expected: in particular in this case the stress is tensile in the S1 direction and in compression in the S2 direction (while in the UPM sample this component resulted to be around 0); again the balancing tensile stresses are constant up to a distance of 10 mm away from the peened area.

Reference

[1] G. Ivetic, I. Meneghin, E. Troiani, G. Molinari, J. Ocaña, M. Morales, J. Porro, A. Lanciotti, V. Ristori, C. Polese, J. Plaisier, and A. Lausi, "Fatigue in laser shock peened open-hole thin aluminium specimens," *Mater. Sci. Eng. A*, vol. 534, pp. 573–579, Feb. 2012.

[2] C. A. Rodopoulos, A. T. Kermanidis, E. Statnikov, V. Vityazev, and O. Korolkov, "The Effect of Surface Engineering Treatments on the Fatigue Behavior of 2024-T351 Aluminum Alloy," *J. Mater. Eng. Perform.*, vol. 16, no. 1, pp. 30–34, Jan. 2007.

[3] Q. Liu, C. H. Yang, K. Ding, S. A. Barter, and L. Ye, "The effect of laser power density on the fatigue life of laser-shock-peened 7050 aluminium alloy," *Fatigue Fract. Eng. Mater. Struct.*, vol. 30, no. 11, pp. 1110–1124, Nov. 2007.

[4] A. H. Clauer and D. F. Lahrman, "Laser Shock Processing as a Surface Enhancement Process," in *Key Engineering Materials*, 2001, vol. 197, pp. 121–144.

[5] M. B. Toparli, "Analysis of Residual Stress Fields in Aerospace Materials After Laser Peening," PhD Thesis, The Open University, 2012.

[6] U. C. Heckenberger, E. Hombergsmeier, and D. Furfari, "Residual stress fields in LSP and SP treated aluminium specimens after fatigue testing," in *4th International Conference on Laser Peening and Related Phenomena;*, 2013.

[7] M. K. Khan, S. V. Hainsworth, M. E. Fitzpatrick, and L. Edwards, "Application of the work of indentation approach for the characterization of aluminium 2024-T351 and Al cladding by nanoindentation," *J. Mater. Sci.*, vol. 44, no. 4, pp. 1006–1015, Jan. 2009.

10 Conclusions and Future Works

This 3-year research project was aimed to demonstrate both the possibility to apply Eigenstrain in order to predict the RS field introduced by the LSP technology and to explore the potential of this surface treatment when it is applied on thin samples.

Based on the results and the further discussion reported in chapters 6 to 9 the following conclusions can be outlined:

10.1 Eigenstrain modelling of the stepped coupon and SEN

1. The Eigenstrain theory has been revealed to be an easy-to-use approach once its background theory is fully understood. The application of the Eigenstrain with ABAQUS software has a low computational cost which makes the Eigenstrain approach competitive among the RS prediction methods. The results revealed that the Eigenstrain approach is able to predict correctly the RS profiles in sections where the thickness is greater than the section where the Eigenstrains were measured, even close to the surface. Furthermore, the prediction with Eigenstrain matches within ±20 MPa the measurements of the RS in curved geometries even if, as it was demonstrated in chapter 6, more than one measurement in necessary where convex geometries are present due to the limitations of each singular RS measurement method.
2. The Eigenstrains were used also for the SEN sample which is 10 mm thick and was subjected to a double surface treatment. In this case only a preliminary study was done and further investigation is necessary to outline a complete conclusion. However, it is possible to say that the Eigenstrains calculated from the flat sample that was LSP'ed only were the ones which best predicted the RS profiles measured with neutron diffraction, even if, due to the Eigenstrain theory, the Eigenstrain

calculated from the flat sample both LSP'ed and SP'ed were the ones supposed to predict better the RS profile. One possible reason why this happened is because the SEN was laser peened on three different faces of the sample and also at 45° at the round edges. This particular distribution of treatment makes the prediction of plasticity (i.e. Eigenstrain) quite a challenge. The SP treatment instead affects the RS profile only within the first millimetre under the surface without changing the entire distribution of RS internally. And again, it was not possible to determine how the plasticity is distributed at such a sharp edge after this surface treatment, which is necessary to fully understand the correct Eigenstrain distribution.

10.2 Thin samples

1. The measurements carried out on the single-peened samples demonstrated that with the proper choice of laser setting parameters it is possible to introduce a compressive RS stress profile up to the first millimetre underneath the surface. At the same time the damage of the surface due to the interaction of the laser with the surface can be detrimental for the surface RS. The campaign of measurements outlined that, in order to get a beneficial RS profile, a large spot is required when the laser energy per pulse is kept constant. At the same time, increasing the distance between the laser spots seems to be beneficial for the sample in particular in terms of deeper and higher RS obtained even if this dependency decreases when the laser spot size is increased. Due to the lack of a sacrificial overlay, local melting is expected to occur at the surface, particularly when the spot size was small and the energy was more focused, i.e. when an higher power density is involved.
2. The measurements demonstrated how the RS are distributed through the thickness in several regions of the samples: in more details, compressive RS are obtained through the thickness in both the directions perpendicular to the LSP

stripe (S2) and parallel to it (S1). Outside the LSP'ed stripe compression is measured in the S1 direction while tension is present in S2 direction. Alongside the peened area, tension is present in the S1 direction while low tension or compression is present along the S2 direction. This indicates that most of the tensile stresses are stored alongside the peened area rather than at the end of the LSP'ed strips.

3. The measurements of the RS made on the double-peened samples demonstrate how it is possible, with a proper set of laser parameters, to introduce a fully-compressive RS profile within the samples. The RS profile generated first seems to not be affected by the second treatment made on the opposite face of the sample, or it is slightly affected when the laser energy was higher. Using the TOSHIBA technology, with a laser energy a fraction of the one used by UPM, it was possible to introduce compressive RS at the surface but at the middle thickness tension is present.

In all the samples the lowest compressive value was reached at 180 μm that is at the interface between the AA2024 and the clad layer and this is due to the fact that the yield strength of the clad layer is much lower than the yield strength of the AA2024.

10.3 Future Works

The study of the LSP parameters involved in thin samples and the subsequent distribution of RS, as well as the application of the Eigenstrain approach leads to possible developments for future research:

1. The Eigenstrain approach highlighted the difficulties in predicting the RS when a round edge is present. This difficulty can be overcome by intensifying the research on this field, in particular more measurements of RS on curved samples (or part of

samples) are necessary in order to establish a reliable basis for the future predictions, it being understood that the more RS measurements are done on a certain shape, the more reliable the data become.

2. Further research can be driven toward a better understanding of the interaction of the laser shock peening when the shot is directed toward a curved surface. If the laser spot is small enough to consider the interaction between the beam and the sample surface quasi-perpendicular, no major differences are expected from the peening of a flat surface. But when a laser spot is the same order of magnitude as the curved edge, a prediction of the generation of the shock waves and their mutual interactions within the sample is difficult to outline. Furthermore, these shock wave interactions could lead to a different plasticity distribution, which can be analyzed as well;
3. The Eigenstrains have to be more properly linked with the plasticity introduced by the LSP and SP. Generally the plasticity results in dislocation generation during a surface treatment and they can be measured either through a transmission electron microscopy (where a proper preparation on the sample is needed) or by measuring the peak broadening in measurements with diffraction techniques. This latter approach has demonstrated [1], [2] to give a good approximation of the dislocations after a certain treatment. This approach could lead to better understand the redistribution of plasticity and thus the redistribution of Eigenstrains. In the case of a sample as thick as the SEN, coupling both the Synchrotron X-ray diffraction and neutron diffraction measurements could lead to a better understanding of the distribution of both the RS close to the surface, within the sample and the distribution of plasticity after coupling LSP and SP.
4. The thin samples are extremely interesting from an aerospace point of view due to the low thickness of most of airframe sections, e.g. the fuselage and wing skin. The

distribution of the RS is strictly linked to the improvement of the fatigue life of a sample where the LSP stripe could work as crack-stopper or as a crack retarder. This task is generally accomplished by the stringers (which are needed to avoid the buckling effect as well), but the introduction of a LSP'ed stripe could lead to a better prediction of the crack evolution without adding further weight, which is one of the most challenging tasks that structural engineers have to deal with. The research in this topic is wide. LSP parameter for thin samples can be linked with fatigue life results in order to obtain the best parameters in terms of fatigue life. The double treatment of these samples was introduced with the aim of slowing down the crack propagation by introducing a full-compressive RS profile. Some investigations are still going on in this field.

References

[1] W. Woo, T. Ungár, Z. Feng, E. Kenik, and B. Clausen, "X-Ray and Neutron Diffraction Measurements of Dislocation Density and Subgrain Size in a Friction-Stir-Welded Aluminum Alloy," *Metall. Mater. Trans. A*, vol. 41, no. 5, pp. 1210–1216, Aug. 2009.

[2] T. Ungár, "Strain Broadening Caused by Dislocations," in *Materials Science Forum*, 1998, vol. 278–281, pp. 151–157.